DISS. ETH NO. 23549

Molecular resonances in the Rydberg-excitation spectrum of an ultracold Cs gas

A thesis submitted to attain the degree of

DOCTOR OF SCIENCES of ETH ZURICH
(Dr. sc. ETH Zurich)

presented by

HEINER SAßMANNSHAUSEN
MSc ETH Chemistry

born on 18.02.1989
citizen of Germany

accepted on the recommendation of

Prof. Dr. F. Merkt, examiner
Prof. Dr. T. Esslinger, co-examiner
Dr. J. Deiglmayr, co-examiner

2016

Meinen lieben Eltern

Abstract

This thesis is devoted to studies of Rydberg states of Cs generated in dense (density $> 10^{11}\,\mathrm{cm}^{-3}$) ultracold ($T \approx 40\,\mu\mathrm{K}$) gas-phase samples by photoexcitation with narrow-bandwidth laser radiation and millimetre waves. The emphasis is on systematic investigations of the interactions of the Rydberg atoms with their environment, be it other Rydberg atoms or ground-state atoms located in their vicinity, or external electric and magnetic fields. These interactions and their effects on the Rydberg atoms are studied by high-resolution spectroscopy and manifest themselves as level shifts, line broadenings and, most importantly, by the appearance of additional lines in the Rydberg-excitation spectrum of Cs that can be attributed to the formation of highly excited Cs_2 molecules. At the positions of these resonances, the ultracold atoms are transferred into bound states by the narrow-bandwidth radiation, in a process known as photoassociation. Metastable molecules are formed, which eventually decay by ionisation, dissociation or the emission of a photon.

Depending on the intensity, the frequency and the temporal shape of the photoexcitation radiation pulses used in the experimental studies, very different families of molecular states could be produced: *i*) Molecular states in which one Cs Rydberg atom is bound to a ground-state Cs atom by the low-energy scattering of the Rydberg electron off the ground-state atom. The contribution made to the understanding of these states in the realm of this thesis was the experimental discovery of the importance of the singlet scattering channels next to the triplet scattering channels. *ii*) Molecular states in which one Cs Rydberg atom interacts with another Cs Rydberg atom through long-range electrostatic interactions. Here, the main contributions made in the realm of this thesis were *ii*a) the experimental discovery of molecular resonances caused by the dipole-quadrupole interaction, which violates the electronic parity of the Rydberg-atom dimer, *ii*b) the unambiguous identification of the contributions of terms as high as the octupole-octupole interaction to the spectral signatures of the Rydberg-atom dimer, and *ii*c) the investigation of diverse dynamical phenomena such as Penning ionisation of the dimer, the aggregation of several Rydberg atoms by intentionally catalysing the excitation process, and the spontaneous ionisation of the entire Rydberg-atom sample induced by the long-range interactions.

A prerequisite to a careful study of interactions between Rydberg atoms is a de-

tailed and accurate characterisation of the properties of the individual non-interacting atoms. The first part of this thesis describes high-resolution spectroscopic experiments, which enabled the determination of the ionisation energy of Cs and the values of the quantum defects of the s, p and d Rydberg series of Cs with unprecedented accuracy. Related experiments also led to a characterisation of the effects of electric and magnetic fields on the spectral properties of the Rydberg atoms (Chapters 2 and 3). A second essential aspect of the studies presented in this thesis is the complete first-principles modelling of the interactions using tools borrowed from molecular physics and spectroscopy, including the calculation of molecular potential curves and the analysis of the angular-momentum coupling schemes.

Millimetre-wave-radiation–induced transitions between Rydberg states of Cs were recorded at a resolution of better than 20 kHz, which enabled the observation of the hyperfine splitting of $ns_{1/2}$ Rydberg states up to $n = 90$. These experiments also enabled the accurate characterisation of stray electric and magnetic fields in the photoexcitation region, and their subsequent compensation to below 1 mV/cm and 2 mG, respectively. Absolute transition frequencies from the $6s_{1/2}$ ground state to $np_{3/2}$ and $np_{1/2}$ Rydberg states were measured to an accuracy of ~60 kHz by referencing the frequency of the Rydberg-excitation laser to a frequency comb. Extrapolation of the measured transition frequencies using Rydberg's formula yielded an improved value of $E_I = hc \cdot 31\,406.467\,732\,5(14)\,\mathrm{cm}^{-1}$ for the first ionisation energy of Cs, and improved values of the quantum-defect values of the ns, np, and nd Rydberg series converging to the $Cs^+(5p)^6\,(^1S_0) + e^-$ ionisation threshold.

The interactions of the Rydberg atoms with their environment were revealed as additional weak resonances close to $np_{3/2} \leftarrow 6s_{1/2}$ atomic Rydberg transitions when exciting dense ultracold samples of Cs with intense laser radiation. These resonances are the signature of the long-range interactions between the ultracold Cs atoms and the families of molecular states described above. The interaction of ground-state atoms with Rydberg atoms gave rise to photoassociation resonances which were attributed to the formation of long-range Rydberg molecules. The binding in these molecules is a result of low-energy scattering of the quasi-free Rydberg electron off the ground-state atom. In the experiments, long-range Rydberg molecules correlated to $Cs(np_{3/2}) + Cs(6s_{1/2}, F = 3, 4)$ dissociation asymptotes were studied in the range of principal quantum numbers n between 26 and 34 (Chapter 4). The spectra revealed two types of molecular states recently predicted by D. A. Anderson, S. A. Miller, and G. Raithel [Phys. Rev. A **90**, 062518 (2014)]: states bound purely by triplet s-wave scattering with binding energies ranging from 400 MHz at $n = 26$ to 80 MHz at $n = 34$, and states bound by mixed singlet-triplet s-wave scattering with smaller and F-dependent binding energies. The experimental observations were accounted for by an effective Hamiltonian including s-wave scattering pseudopotentials,

the hyperfine interaction of the ground-state atom, and the spin-orbit interaction of the Rydberg atom. To reproduce the measured binding energies in the model, the singlet and triplet scattering lengths of electron-cesium scattering were adjusted to $a_{T,0} = -21.8 \pm 0.2\ a_0$ and $a_{S,0} = -3.5 \pm 0.4\ a_0$, respectively. The long-range molecules were detected *via* their ionic decay product Cs_2^+. The lifetime at $n = 33$ was measured as $(0.5 \pm 0.2)\,\mu s$, significantly shorter than the lifetime of corresponding molecular resonances in Rb and Sr. Possible decay mechanisms induced by couplings to molecular Rydberg series converging to vibrationally excited states of Cs_2^+ and to Cs^+Cs^- ion-pair states are discussed.

The interactions between two Rydberg atoms were revealed in the observation of resonances attributed to the photoassociation of two ground-state Cs atoms to Rydberg-atom-pair states (also refered to as "macrodimers" in the literature) in two-photon transitions. Two different excitation schemes were applied to study these Rydberg-atom-pair states: one-colour two-photon excitation using a pulse-amplified laser (Chapter 5) and a sequential, resonant two-colour two-photon excitation (Chapter 6). The results of both experiments were accurately reproduced by a potential model based on the determination of the eigenvalues and eigenenergies of a long-range multipole-multipole-interaction Hamiltonian in a large atom-pair basis set.

In the first excitation scheme, resonances correlated to $ns_{1/2}(n+1)s_{1/2}$ (with $n = 22-34$) and $n's_{1/2}n''f_j$ (with $n = 22-32$) dissociation asymptotes were studied at a spectral resolution of 130 MHz (Chapter 5). These resonances revealed dipole-dipole and dipole-quadrupole interactions in pairs of ultracold Cs Rydberg atoms. The occurrence of both electronic-parity-conserving (*e.g.* dipole-dipole) and electronic-parity-violating (*e.g.* dipole-quadrupole) interactions betrayed the coupling between electronic and nuclear motion in the Rydberg-atom pairs, which is facilitated by the quasi-degeneracy of their rotational levels. "Window" resonances observed on the high-frequency side of $np_{3/2} \leftarrow 6s_{1/2}$ transitions are linked to avoided crossings between potential functions correlated to the $np_{3/2}np_{3/2}$ and higher-lying $n'f_jn''f_j$ pair-dissociation asymptotes. The position of these resonances could be reproduced by the calculations only after inclusion of terms up to the octupole-octupole contribution in the interaction Hamiltonian. Rydberg-atom pairs excited to attractive molecular states were observed to decay *via* Penning ionisation within 1 μs. The Penning-ionisation process was studied with delayed pulsed field ionisation and was accounted for by a model treating the motion of the Rydberg atoms, which is governed by the long-range potentials, classically.

Using a sequential, resonant two-colour excitation, the resolution of the spectra of the interacting Rydberg-atom-pair states was improved to ~3 MHz (Chapter 6). The experiment relied on the resonant excitation of a few ground-state atoms to Rydberg states, which subsequently acted as seed atoms for further excitation and thus

“facilitated” the off-resonant Rydberg excitation of additional atoms in their vicinity. The increased resolution and the possibility to excite the two Rydberg atoms to states of opposite parity (using a two-photon transition for one atom and a one-photon transition for the other) led to the observation of resonances linked to long-range potential wells correlated to $n\mathrm{p}_{3/2}(n+1)\mathrm{s}_{1/2}$ pair-dissociation asympotes with $n = 43, 44$. These states correspond to “bound macrodimers”, which were observed under field-free conditions for the first time in the realm of this thesis. The sequential two-colour excitation also resulted in the formation of Rydberg-excitation aggregates. These occur under conditions where every resonantly excited Rydberg atom triggers the excitation of a large number of additional spatially correlated Rydberg excitations.

Zusammenfassung

Die vorliegende Arbeit ist der Untersuchung hoher Rydbergzustände in Cs gewidmet, welche durch Anregung mit schmalbandiger Laserstrahlung und Millimeterwellen in einem dichten (Dichte $> 10^{11}\,\mathrm{cm}^{-3}$), ultrakalten ($T \approx 40\,\mu\mathrm{K}$) Gas erzeugt werden. Der Fokus liegt dabei auf systematischen Untersuchungen der Wechselwirkungen dieser Rydbergatome mit ihrer Umgebung, welche aus anderen Rydbergatomen, Atomen im Grundzustand, oder externen elektrischen und magnetischen Feldern bestehen kann. Die Wechselwirkungen und ihre Auswirkungen auf die Rydbergzustände wurden mittels hochaufgelöster Spektroskopie untersucht. Sie offenbaren sich in Form von Linienverschiebungen und -verbreiterungen und im Auftreten zusätzlicher Resonanzen im Rydberganregungsspektrum von Cs, welche der Bildung hochangeregter Cs_2 Moleküle zugeschrieben werden. An den Positionen dieser Resonanzen werden die ultrakalten Atome mit schmalbandiger Strahlung in gebundene molekulare Zustände überführt, die daraufhin durch Ionisation, Dissoziation oder Fluoreszens wieder zerfallen.

Abhängig von Intensität, Frequenz und zeitlichem Profil der verwendeten optischen Anregungspulse konnten unterschiedliche molekulare Zustände prepariert werden: *i*) Molekulare Zustände, in denen ein Cs Rydbergatom durch Niedrigenergie-Streuung des Rydberg-Elektrons an einem Cs Grundzustandsatom an dieses gebunden ist. Der Beitrag zum Verständnis dieser Zustände, der durch die vorliegende Arbeit erbracht wurde, ist die experimentelle Entdeckung der Bedeutung von Singulett-Streukanälen zusätzlich zu den Triplett-Streukanälen. *ii*) Molekulare Zustände, in denen ein Cs Rydbergatom mit einem weiteren Cs Rydbergatom über langreichweitige elektrostatische Wechselwirkungen interagiert. Bezüglich dieser Zustände liegen die wichtigsten Beiträge dieser Arbeit in *ii*a) der experimentellen Entdeckung von molekularen Resonanzen, hervorgerufen durch die Dipol-Quadrupol-Wechselwirkung, welche die elektronische Parität des Rydbergatom-Paarzustandes nicht erhält, *ii*b) der eindeutigen Beobachtung von Beiträgen bis zur Oktupol-Oktupol-Wechselwirkung zu den spektralen Signaturen der Rydbergatom-Dimere, und *ii*c) der Untersuchung von dynamischen Prozessen wie der Penning-Ionisation der Dimere, der katalysierten Aggregation von Rydberganregungen und der spontanen Ionisation des gesamten Rydberggases, welche durch die langreichweitigen Wechselwirkungen induziert wird.

Eine Vorausetzung für die sorgfältige Untersuchung von Wechselwirkungen zwischen Rydbergatomen ist die detaillierte und genaue Charakterisierung der Eigenschaften der einzelnen (nicht wechselwirkenden) Atome. Der erste Teil dieser Arbeit beschreibt daher hochaufgelöste spektroskopische Messungen, die zur Bestimmung der Ionisationsenergie von Cs und Werten der Quantendefekte der s, p und d Rydbergserien in Cs mit höchster Genauigkeit geführt haben. Im Zuge dieser Messreihen konnten auch die Auswirkungen von elektrischen und magnetischen Feldern auf die spektralen Signaturen der Rydbergatome untersucht werden (siehe Kapitel 2 und 3). Ein weiterer zentraler Aspekt der hier gezeigten Studien ist die vollständige theoretische Beschreibung der experimentellen Beobachtungen mittels Methoden der Molekülphysik und Spektroskopie, welche die Berechnung von Molekülpotentialen und die Analyse von Drehimpuls-Kopplungsschemata beinhalten.

Millimeterwellenstrahlungsinduzierte Übergänge zwischen Rydbergzuständen von Cs wurden mit einer Auflösung von besser als 20 kHz gemessen, was die Beobachtung der Hyperfeinaufspaltung von $ns_{1/2}$ Rydbergzuständen bis zu $n = 90$ ermöglichte. Diese Experimente erlaubten weiterhin die Messung der elektrischen und magnetischen Streufelder im Anregungsvolumen und die darauffolgende Kompensation dieser Felder zu weniger als 1 mV/cm, beziehungsweise 2 mG. Die Übergangsfrequenzen vom $6s_{1/2}$ Grundzustand zu $np_{3/2}$ und $np_{1/2}$ Rydbergzuständen in Cs wurden dank der Kalibration der Frequenz des Anregungslasers mittels eines Frequenzkamms mit einer Genauigkeit von ~60 kHz gemessen. Durch Extrapolation der gemessenen Übergangsfrequenzen auf Grundlage der Rydbergformel wurden der verbesserte Wert von $E_\mathrm{I} = hc \cdot 31\,406.467\,732\,5(14)\,\mathrm{cm}^{-1}$ für die erste Ionisierungsenergie von Cs und verbesserte Werte für die Quantendefekte der ns, np und nd Rydbergserien, welche zur $\mathrm{Cs}^+(5\mathrm{p})^6\,(^1\mathrm{S}_0) + \mathrm{e}^-$ Ionisationsschwelle von Cs konvergieren, bestimmt.

Die Wechselwirkungen der Rydbergatome mit ihrer Umgebung offenbarten sich als zusätzliche schwache Resonanzen nahe der atomaren $np_{3/2} \leftarrow 6s_{1/2}$ Rydbergübergänge, wenn das dichte ultrakalte Cs Gas mit intensiver Laserstrahlung angeregt wurde. Diese Resonanzen sind der beobachtbare Effekt der langreichweitigen Wechselwirkungen zwischen den ultrakalten Cs Atomen, die zu den oben erwähnten Klassen molekularer Zustände führen. Die Wechselwirkung von Grundzustandsatomen mit Rydbergatomen führt mittels Photoassoziationsresonanzen zur Bildung langreichweitiger Rydbergmoleküle. Die Bindung in diesen Molekülen resultiert aus der Niedrigenergiestreuung des beinahe freien Rydbergelektrons am Grundzustandsatom.

In den Experimenten wurden diese langreichweitigen Rydbergmoleküle in der Nähe der Dissoziationsschwellen $\mathrm{Cs}\,(np_{3/2}) + \mathrm{Cs}\,(6s_{1/2}, F = 3, 4)$ (mit Hauptquantenzahl n zwischen 26 und 34) untersucht (Kapitel 4). Die experimentellen Spektren offenbaren zwei Typen molekularer Zustände, die kürzlich von D. A. Anderson, S. A. Miller und G. Raithel [Phys. Rev. A **90**, 062518 (2014)] vorhergesagt wurden: Zustände, welche aus-

schliesslich durch Triplett-Streuung gebunden sind und Bindungsenergien zwischen 400 MHz bei $n = 26$ und 80 MHz bei $n = 34$ aufweisen, und Zustände, welche durch gemischte Singulett-Triplett-Streuung gebunden sind und deutlich kleinere und F-abhängige Bindungsenergien aufweisen. Die experimentellen Beobachtungen konnten mit einem effektiven Hamiltonoperator beschrieben werden, welcher ein Pseudopotential für die Beschreibung der s-Wellenstreuung, die Hyperfeinwechselwirkung im Grundzustand und die Spin-Orbit-Wechselwirkung im Rydbergzustand enthält. Um gemessene Bindungsenergien in diesem Modell zu reproduzieren, wurden die Werte der Singulett- und Triplettstreulängen auf $a_{\mathrm{T},0} = -21.8 \pm 0.2\ a_0$, beziehungsweise $a_{\mathrm{S},0} = -3.5 \pm 0.4\ a_0$, festgelegt. Die langreichweitigen Moleküle wurden mittels ihres ionischen Zerfallproduktes Cs_2^+ detektiert. Deren Lebenszeit bei $n = 33$ wurde zu (0.5 ± 0.2) µs bestimmt. Sie ist damit bedeutend kürzer als die Lebenszeiten vergleichbarer molekularer Zustände in Rb und Sr. Kopplungen an zu hochangeregten Vibrationszuständen von Cs_2^+ konvergierende molekulare Rydbergserien, sowie Kopplungen an Cs^+Cs^- Ionenpaarzustände werden als mögliche Zerfallsmechanismen diskutiert.

Die Wechselwirkungen zwischen Rydbergatomen offenbarten sich in der Beobachtung von Resonanzen, welche der Photoassoziation von zwei Cs Atomen im Grundzustand zu Rydbergatom-Paarzuständen (in der Literatur auch Rydberg-«Makrodimere» genannt) durch Zwei-Photonen-Anregung zugeordnet wurden. Zwei unterschiedliche Anregungsschemata wurden zur Untersuchung dieser Rydbergatom-Paarzustände angewendet: Ein-Farben-Zwei-Photonenanregung mittels eines pulsverstärkten Lasers (Kapitel 5) und eine sequenzielle, resonante Zwei-Farben-Zwei-Photonen-Anregung (Kapitel 6). Die Ergebnisse beider Experimente wurden durch ein Modell der langreichweitigen Potentiale, das auf der Berechnung der Eigenwerte und -energien des Multipol-Multipol-Wechselwirkungs-Hamiltonoperators in einem grossen Basissatz von Atom-Paarzuständen basiert, genau reproduziert.

Durch die Anwendung des ersten Anregungsschemas wurden mit $ns_{1/2}(n+1)s_{1/2}$ (mit $n = 22 - 34$) and $n's_{1/2}n''f_j$ (with $n = 22 - 32$) Dissoziationsasymptoten verbundene Resonanzen mit einer Auflösung von 130 MHz undersucht (Kapitel 5). Diese Resonanzen sind die Folge von Dipol-Dipol- und Dipol-Quadrupol-Wechselwirkungen in Dimeren von ultrakalten Cs Rydbergatomen. Die Beobachtung sowohl von Wechselwirkungen, welche die elektronische Parität erhalten (z.B. die Dipol-Dipol-Wechselwirkung), als auch von solchen, die die elektronische Parität nicht erhalten (z.B. die Dipol-Quadrupol-Wechselwirkung), ist ein eindeutiger Hinweis auf die Kopplung der elektronischen Bewegung und der Kernbewegung in Rydbergatom-Paaren. Diese Kopplung wird durch die Beinahe-Entartung der Rotationszustände in diesen Dimeren ermöglicht. «Fensterresonanzen» wurden bei höheren Frequenzen relativ zu atomaren $np_{3/2} \leftarrow 6s_{1/2}$ Übergängen beobachtet und vermiedenen Kreuzungen zwischen Poten-

tialkurven zugeordnet, welche mit $np_{3/2}np_{3/2}$ und mit energetisch höher liegenden $n'f_j n''f_j$ Dissoziationsasymptoten korrelieren. Die Positionen dieser Resonanzen konnte erst nach Aufnahme von Termen bis zur Oktupol-Oktupol-Wechselwirkung in den Wechselwirkungs-Hamiltonoperator des Modells reproduziert werden. Der Zerfall innerhalb von 1 µs *via* Penning-Ionisation wurde bei Rydbergatom-Paarzuständen mit anziehenden Potentialkurven beobachtet. Der Prozess der Penning-Ionisation wurde mittels verzögerter gepulster Feldionisation untersucht und in einem Modell beschrieben, welches die Bewegung der Rydbergatome, die durch die langreichweitigen Potentiale bestimmt ist, klassisch beschreibt.

Mittels der sequenziellen, resonanten Zwei-Farben-Anregung konnte die Auflösung, mit der die wechselwirkenden Rydbergatom-Paarzustände untersucht werden konnten, auf ~3 MHz verbessert werden (Kapitel 6). Die in diesem Kapitel beschriebenen Experimente basieren auf der resonanten Anregung einiger Grundzustandsatome zu Rydbergzuständen. Diese fungieren dann als «seed» (engl. für «Keim») Atome, welche die Anregung weiterer Rydbergatome in ihrer Umgebung bewirken. Die verbesserte Auflösung und die Möglichkeit, Rydbergatome mit unterschiedlicher Parität anzuregen (so z.B. mittels einer Zwei-Photonen-Anregung eines Grundzustandsatoms und einer Ein-Photonen-Anregung eines weiteren), führte zur Beobachtung von Resonanzen, deren Positionen direkt mit Potentialminima von $np_{3/2}(n+1)s_{1/2}$ Potentialkurven, die zu Dissoziationsasymptoten mit $n = 43, 44$ korrelieren. Die Resonanzen entsprechen somit «gebundenen Makrodimeren», welche unter feldfreien Bedingungen zum ersten Mal in dieser Arbeit nachgewiesen wurden. Die sequenzielle, resonante Zwei-Farben-Anregung führte auch zur Bildung von Rydberganregungs-Aggregaten. Zur Bildung dieser Aggregate kam es dann, wenn jedes resonant angeregte «seed» Rydbergatom die Anregung von einer grossen Zahl weiterer, räumlich korrelierter Rydbergatome bewirkte.

Contents

Chapter 1

Introduction

Rydberg excitation of ultracold atoms [1–7] at temperatures below 1 mK results in the creation of a "frozen Rydberg gas" [8, 9]. The most intriguing physical property of such a system is that the thermal energy of the gas, corresponding to ∼1 MHz or 0.3 mJ/mol for Cs atoms at the temperature of ∼40 μK, is negligible compared to the long-range interactions between the excited atoms. Consequently, the dynamics of the system is governed by long-range forces instead of the random thermal motion.

The laser-cooling technique by which these ultra-low temperatures can be reached is only applicable to a limited number of atomic (primarily the alkali-metal atoms, the earth-alkali-metal atoms, the rare-gas atoms in metastable states [10] and a few other atoms) and very few molecular species [11–13]. However, for experiments on high Rydberg states this is of no particular disadvantage because the properties of the frozen Rydberg gas are predominantly governed by the Rydberg-electron quantum numbers n and l and not by the nature of the ion core.

Rydberg states consist of a positively charged ion core and an excited electron (the Rydberg electron) located in a large orbit of dimension given approximately by the Bohr radius $a_0 n^2$, where n is the principal quantum number. At sufficiently high values of n, the Rydberg electron is insensitive to the structure of the positively charged ion core, and the Rydberg-level structure becomes similar to that of the hydrogen atom. High Rydberg states of all atoms and molecules can be described in good approximation by Rydberg's empirical formula [14, 15]

$$E(n,l) = E_{\mathrm{I}}(\alpha^+) - \frac{R_M h c}{(n-\delta_{lj})^2} \tag{1.1}$$

where h, c, $E_{\mathrm{I}}(\alpha^+)$, R_M, and δ_{lj} are Planck's constant, the speed of light in vacuum, the energy of the ionic state α^+ relative to the neutral ground state, the mass-dependent Rydberg constant and the quantum defect, respectively. In any non-hydrogenic atom and in molecules, the quantum defect depends on the orbital-angular-momentum

quantum number l (and on the total-electronic-angular-momentum quantum number j for states subject to a spin-orbit interaction) and deviates significantly from zero in penetrating low-l states. The specific value of the quantum defect is determined by the structure of the ion core of the Rydberg atom or molecule. Atoms in high Rydberg states have a large orbital radius (scaling as $a_0 n^2$) and are weakly bound (the binding energy scales as n^{-2}), long lived (the lifetime scales as n^3), highly polarisable (the polarisability scales as n^7), and easily perturbed by ground-state atoms or Rydberg atoms in their vicinity. Consequently, the values of specific physical properties of an atom such as its effective size, its lifetime and the magnitude of interactions with the surrounding (external fields or neigbouring atoms) can be adjusted over very large ranges by the choice of the principal quantum number. Several excellent textbooks are devoted to a comprehensive description of atomic Rydberg states [15–17], and I refer to these textbooks rather than dublicating the information they contain.

The rapid scaling with n of most physical properties of Rydberg atoms implies that high Rydberg states have very unusual properties. In recent years, these properties have been used in an increasing range of scientific applications, in diverse fields including quantum optics [18–24], quantum information processing [25, 26], quantum simulation [27–29], and investigations of many-body interactions and entanglement [30–32]. For most applications, the interactions between the Rydberg atoms play a crucial role, for example by defining the blockade radius of excitation used to generate quantum gates [25, 33, 34]. Often, this interaction is treated using rather simple models, which extract some of the main features of the physical behaviour of the systems. However, a detailed understanding with a complete model enables one to recognise when simple models apply or break down.

The experiments described in this thesis are performed on ultracold samples of Cs atoms with the goal of investigating in detail the weak long-range interactions between Rydberg atoms and between Rydberg atoms and ground-state atoms. The advantages of using Cs in these studies are *i*) that Cs is easily laser cooled and *ii*) that its Rydberg series are completely unperturbed. The lowest electronically doubly excited levels are far above the first ionisation threshold [35] and do not influence the Rydberg series of the neutral atom. The Rydberg series (of different l and j) in Cs can be described very accurately with Rydberg's formula (see Eq. 1.1) because no channel interactions occur below the first ionisation threshold. It is shown in this thesis that the description of level positions is accurate to better than $\sim 50\,\mathrm{kHz}$ (see results presented in Section 3.2), if the (small) energy dependence of the quantum defects is neglected.

Interactions involving high Rydberg states have been at the focus of scientific investigations for almost a century [36, 37], and improved experimental tools and techniques have continuously provided new insights, *e.g.* on the mechanisms responsible

for pressure shifts in Rydberg spectra [36–50], on elastic and inelastic collisions in Rydberg-atom samples [15, 51, 52], on the evolution of a dense Rydberg gas into a cold plasma [51, 53, 54], on the generation of unusual quantum phases [55–57], and on the aggregation of highly-excited atoms and molecules [58–65].

The focus in this theses is on two classes of weakly interacting systems involving Rydberg states: *i*) long-range Rydberg molecules consisting of a Rydberg atom and a ground-state atom located within the Rydberg-electron orbit. The binding results from the (short-range) scattering interaction betweeen the Rydberg electron and the ground-state atom, and *ii*) Rydberg-atom-pair states interacting through their electric multipole moments, which are also referred to as Rydberg macrodimers.

Weakly bound molecular systems are typically made of two or more distant constituents that are predominantly held together by long-range forces. Their physical properties depend on the nature of the constituents, *e.g.*, whether these are atomic or molecular species, or a nucleus, or an electron, *etc.*, and whether the constituents are in their electronic ground state or in an electronically excited state. They also depend on the nature of the interactions that hold the constituents together, *e.g.* magnetic or electric interactions involving charges, dipoles, quadrupoles, *etc.* These interactions, which are sufficiently weak not to significantly alter the properties of the constituents, give rise to a long-range potential $V_{\rm inter}(\vec{R}_{i\,j,i\neq j};i;j=1,...,N)$. The relative motion of the N constituents can be described by the Hamiltonian

$$\hat{H} = \hat{H}_1^0 + \hat{H}_2^0 + \cdots + \hat{H}_N^0 + V_{\rm inter}(\vec{R}_{ij}), \tag{1.2}$$

where $\hat{H}_i^0$ represents the Hamiltonian operator of the isolated i-th constituent and $\vec{R}_{ij}$ the position vector of constituent j relative to constituent i.

A third factor of importance in describing the behaviour of weakly-bound systems is the amplitude of the wavefunction in short-range regions, where the potential deviates from the analytic form adequate to describe the long-range region. In pure long-range states [66], this amplitude vanishes, usually because a high potential barrier separates the short- and the long-range regions. Even small amplitudes in short-range regions significantly modify the structure and dynamics of long-range systems. In molecular Rydberg states, the amplitude of the Rydberg-electron wavefunction near the ion core determines the quantum defect and the rate of decay by predissociation, autoionisation and radiative processes. In the long-range Rydberg molecules introduced above, the short-range interaction of the Rydberg electron with the ground-state atom located within the Rydberg-electron orbit determines the binding energy [38] and the dipole moment [38, 42, 47]. In Rydberg-atom pairs, almost immediate ionisation takes place when the orbitals of the two Rydberg atoms start to overlap.

High-resolution photoassociation spectroscopy of ultracold atoms is ideally suited for the investigation of weakly bound systems made of at least one Rydberg atom and other atoms. In photoassociation, photons are used to excite and at the same time induce a chemical bond between two atoms, which are unbound in the lower quantum state of the transition. Photoassociation was first introduced as laser-induced radiative association by Thorsheim *et al.* [67] and was systematically exploited to generate cold molecules since the pioneering work of Pillet and coworkers [68, 69]. Since the first experiments, photoassociation has been applied as a powerful tool to study electronically excited long-range molecular states [70].

At high-resolution, the line shifts and line broadenings resulting from the interactions can be precisely measured in dependence of the sample temperature and density. In a very dilute gas, the experimental linewidth of atomic transitions measured in the gas phase is determined by the laser-excitation bandwidth, the Doppler width, which is a function of the transition wavelength and the temperature of the gas, and the lifetime of the excited state. For high-n Rydberg states, the lifetime is determined by radiative decay and blackbody-radiation-induced transitions to other Rydberg states [15, 71–73]. The natural linewidths of $n\mathrm{p}_{3/2}$ Rydberg states of Cs with $n > 26$ are below 10 kHz [73], and do not contribute significantly to the experimental linewidths. The motion of the atoms resulting from the finite temperature of $\sim 40\,\mu\mathrm{K}$ of the sample causes a Doppler broadening of the $n\mathrm{p}_{3/2} \leftarrow 6\mathrm{s}_{1/2}$ transitions in the ultraviolet with an estimated full width at half maximum of 500 kHz. In millimetre-wave transitions between high-n Rydberg states, the Doppler broadening, which is proportional to the frequency, is negligible and the linewidths are limited by inhomogeneous broadenings induced by external field gradients (see Section 3.1).

Because photoassociation involves a transition between a dissociation continuum and an upper bound state, the widths of photoassociation lines include the width of the continuum, *i.e.* the Boltzmann energy distribution over translational states. The atoms in the dissociation continuum can be treated as scattering states which are themselves conveniently expressed as sums of partial waves. An important quantity is the maximal angular momentum of the collision complex, which depends on the internuclear separation given by the specific molecular state to which photoassociation takes place, and the temperature of the gas. For a collision at the energy $E_{\mathrm{collision}}$, the relation between the largest angular momentum $\hbar L$ and the outer classical turning point R associated with the centrifugal barrier in the ground-state potential is given

by the simple approximate expressions

$$E_{\text{collision}} \approx k_{\text{B}}T \approx \frac{\hbar^2}{2\mu}\frac{L(L+1)}{R^2} \tag{1.3}$$

$$L = -\frac{1}{2} + h \cdot \sqrt{\frac{1}{4} + \frac{32 k_{\text{B}} T \pi^2 \mu R^2}{4h^4}} \approx \frac{2\sqrt{2}\pi}{h} R \sqrt{k_{\text{B}}T \cdot \mu}$$

$$\Rightarrow \hbar L = R\mu\sqrt{\frac{2k_{\text{B}}T}{\mu}} = \mu R v. \tag{1.4}$$

In photoassociation experiments carried out in an ultracold Cs gas at 40 μK, the width of the energy distribution is only ~1 MHz, as mentioned above, and very few partial waves contribute to the photoassociation processes relevant to the present investigation.

These advantages were exploited in the present thesis, which is structured as follows: After a detailed description of the experimental methods and the apparatus in Chapter 2, Chapter 3 summarises the characterisation of the properties of individual, non-interacting Cs atoms by high-resolution UV and millimetre-wave spectroscopy. Chapter 4 is devoted to the study of long-range Rydberg molecules with emphasis on the role of singlet scattering channels on the photoassociation dynamics. The fifth chapter summarises the investigation of molecular resonances corresponding to Rydberg-atom pairs by one-colour two-photon excitation using intense UV laser pulses. This chapter emphasises the importance of long-range electrostatic interactions on the spectral and dynamical properties of the Rydberg-atom pairs; in particular, the role of interactions beyond the dipole-dipole interactions is identified in the long-range interaction series. The sixth chapter presents the results of studies of Rydberg-atom-pair states with a narrow-bandwidth UV laser and demonstrates how specific two-colour two-photon excitation sequences can be applied to generate pairs of Rydberg atoms and even aggregates of such atoms in a controlled manner. The thesis ends with short conclusions and an outlook. Each chapter contains a separate introduction, highlighting specific aspects most relevant to the topics covered and I refer the reader to these introductory parts for additional references.

Chapter 2

Experimental setup & methods

In this chapter, the experimental setup and the main experimental procedures are presented. The experiments are performed on ultracold Cs gas-phase samples in an ultrahigh-vacuum (UHV) chamber (Section 2.1). A generic experimental cycle followed in most of the experiments presented in this thesis consists of a loading phase of the magneto-optical trap (MOT), during which room-temperature Cs ground-state atoms from the very dilute background vapour are laser cooled and accumulated close to the magnetic-field minimum of the MOT (Section 2.2). To increase the density of the ultracold sample, the MOT is either magnetically compressed or the atoms are transferred into an optical dipole trap (Section 2.3). The atoms are prepared in one hyperfine component (or, in some experiments, one specific magnetic sublevel) of the $6s_{1/2}$ ground state before all trapping fields are turned off and the atoms are released from the trap. A typically small fraction of the ultracold ground-state atoms is then excited to a selected np Rydberg state using pulsed ultraviolet (UV) laser radiation of different bandwidths (Section 2.4). In most experiments, a delay time is introduced between Rydberg-state excitation and detection. During this time, millimetre-wave transitions between Rydberg states can be induced (Section 2.4.2) or the spontaneous decay of the photoexcited species can occur. The initial excitation to Rydberg states and all subsequent processes are observed *via* pulsed field ionisation (PFI), followed by the detection of the ion yield with a charged-particle detector (Section 2.6).

This generic cycle is repeated at a rate of 10 Hz while experimental parameters, such as the frequency of the UV laser, the frequency of the millimetre-wave radiation, the delay time between the laser excitation and detection or external-field strengths, are varied. The control over magnetic and electric stray fields is an important prerequisite for high-resolution spectroscopic studies of high Rydberg states. Therefore, the methods used to measure and compensate the stray fields in the photoexcitation region are presented in detail in a separate section (Section 2.7).

2.1 Experimental chamber

The operation of a magneto-optical trap (see Section 2.2.1) requires ultra-high vacuum conditions. The stainless-steel chamber in which the experiments are performed is schematically depicted in Fig. 2.1, which also contains the definition of the laboratory-fixed coordinate system (in the lower left corner) which will be used throughout this thesis. A base pressure of less than 10^{-10} mbar is maintained in this chamber with an ion-getter pump and a titanium-sublimation pump. A schematic diagram of the laser beams used to trap the Cs ground-state atoms and to excite them to Rydberg states is presented in Fig. 2.2. The detector assembly, consisting of an ion lense and a microchannel-plate (MCP) detector shielded by an metallic grid and an ion lense, is mounted is mounted at the end of a short time-of-flight (in y direction) region. The Rydberg-excitation laser (blue colour in Fig. 2.2) enters the chamber along the x axis (for the experiments described in Chapter 3.1) or along the z axis (for all other experiments presented in this thesis). The laser beams of the magneto-optical trap are indicated as red arrows in Fig. 2.1 and in light orange in Fig. 2.2.

2.1.1 Electric-field control

The electrode structures for electric-field control in the photoexciation region consist of a pair of segmented, ring-shaped electrodes (called “field plates” in the following) spaced by 40 mm, and an ion lense for imaging the Cs^+ ions onto the MCP detector. The shape and positions of the field plates are indicated in Fig. 2.1, Fig. 2.2 and in Fig. 2.3 and are designed for the creation of homogeneous fields at the position of the MOT. Each field plate consists of four electrodes. These electrodes can be used to apply electric potentials for stray-field compensation, for studies of the Stark effect, for pulsed field ionisation of Rydberg states and for ion extraction. For the generation of compensation and polarisation fields, potentials of a few volts are generated by a computer-controlled DAQ-Card (Measurement Computing USB-3105) and are applied to the electrodes after analogue filtering and down-scaling by a 1:6 voltage divider. The potential configurations used to apply compensation electric fields along the z, x and y directions are schematically depicted in Figs. 2.3a, b and c, respectively.

2.1.2 Magnetic-field control

Three pairs of coils have been installed around the chamber to compensate stray magnetic fields or to apply well-defined magnetic fields in the experimental volume. The compensation field in z direction is produced by a pair of coils in Helmholtz configuration. The coils are wound around the gradient coils of the MOT and consist

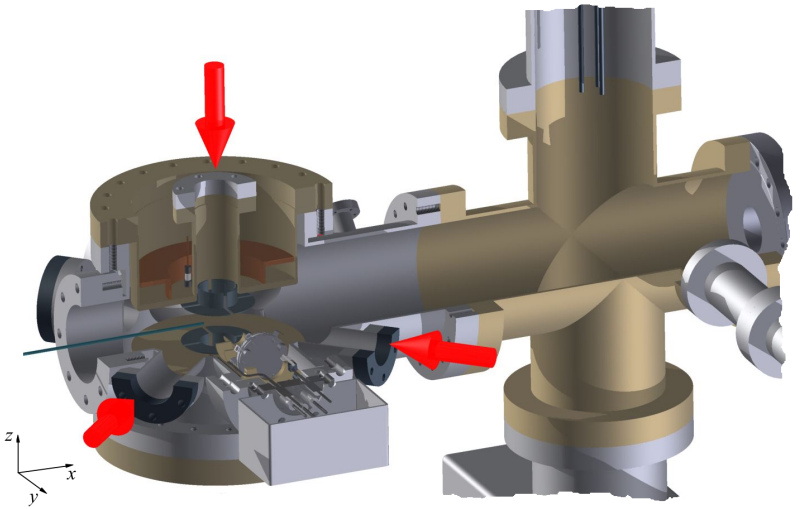

Figure 2.1: Schematic drawing of the experimental chamber. The right-hand side of the chamber is connected to an ion-getter pump (bottom) and a titanium-sublimation pump (top). A pressure gauge is installed at the flange on the right-hand side. The magneto-optical trap (MOT) is located on the left-hand side. The magnetic coils of the MOT are mounted in the re-entrant flanges aligned along the z axis. The IR laser beams of the MOT are schematically indicated by thick red arrows. The UV-laser beam (blue line) is sent into the chamber either along the x axis or along the z axis. A set of segmented ring electrodes (shown in dark grey) for electric-field control is located in the immediate vicinity of the centre of the MOT. The detector assembly, consisting of a multichannel-plate detector (light grey) and an electrostatic lense (light brown), is installed at the flange in the positive y direction. The light grey box contains the read-out electronics of the detector.

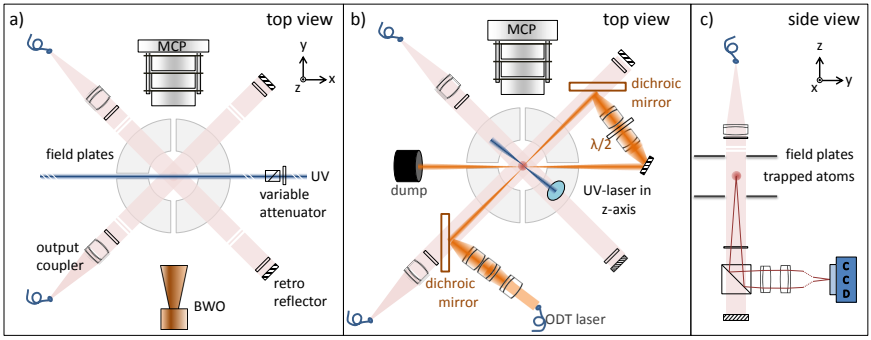

Figure 2.2: a) Schematic top view of the setup used in the experiments described in Chapter 3.1. Pairs of fiber output couplers and retro reflectors deliver the cooling and repumping laser radiations (see text for details). UV laser radiation excites ground-state atoms into Rydberg states, and millimetre-wave radiation from a backward-wave oscillator (BWO) drives transitions between Rydberg states. Field plates (see Fig. 2.3) can be used to apply electric fields across the photoexcitation region. b) Schematic top view of the setup used in the experiments described in Chapters 4, 5 and 6. The UV laser enters the chamber along the z axis, and an optical dipole trap in crossed-beam configuration is indicated in brown. c) Schematic side view of the setup illustrating how the atom cloud is imaged onto a charge-coupled-device (CCD) chip by a matched pair of achromatic lenses.

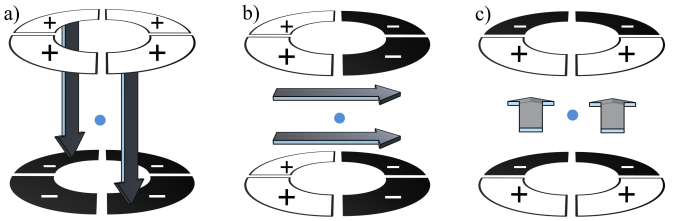

Figure 2.3: Schematic description of the three potential configurations of the eight electrodes used to generate homogeneous electric fields at the position of the MOT (blue circle). Electrodes with positive potentials are presented in white and electrodes with a negative potential in black. The arrows indicate the direction of the electric field vectors. The configurations used to generate electric fields in z, x and y directions are presented in a), b), and c), respectively.

of 13 copper-band windings with a radius of 67.5 mm located at a distance of 33 mm from the centre of the MOT.

In the y direction, the coils are mounted on flanges of the vacuum chamber. The coils consist of 64 windings of wire (ribbon cable) with a radius of 57 mm located at a distance of 63 mm from the centre of the MOT. Because of the geometry of the chamber, a pair of asymmetric coils is used to apply magnetic fields in the x direction. The first (second) coil consists of 27 windings (150 windings) with a mean radius of 57 mm (78 mm) located at a distance of 100 mm (195 mm) from the centre of the MOT. The ratio of the number of windings of these two coils has been chosen so as to obtain a homogeneous magnetic field at the position of the atom cloud when the same current passes through both coils. The number of windings of the two pairs of coils in the x and y dimension has been chosen to generate a magnetic field of about 1 G at the position of the MOT for a current of 1 A passing through each pair of coils. The magnetic coils in the z axis generate a field of 1.82 G at the position of the MOT when a current of 1 A is applied. The typically applied currents used for compensation of external magnetic fields or for the creation of small bias fields cause a magnetic-field variation of ≈ 0.5 mG over the typical size of 100 μm of the ultracold Cs sample.

2.2 Laser cooling and magneto-optical trapping

The central element of the experimental setup is a magneto-optical trap (MOT) for cesium atoms. The idea of using near-resonant laser light to cool atoms was first proposed by Hänsch and Schawlow [1] and independently by Wineland and Dehmelt [2]. Shortly afterwards, the technique of laser cooling was experimentally demonstrated with atomic ions [74, 75]. Magneto-optical trapping of neutral atoms was first demonstrated by Raab *et al.* [4] and has since then been developed to a standard laboratory technique, which has been applied to many different research areas. The possibility to routinely produce atom gas-phase samples at ultracold temperatures (below 1 mK) has led to a revival of interest in many research fields related to atomic physics, including Rydberg physics.

In the experiment described in this thesis, Rydberg excitation of ultracold samples has the important advantage that the thermal energy in the gas (for Cs atoms at a temperature of 40 μK) is completely negligible compared to interaction effects between Rydberg atoms (see Chapters 5 and 6) and also between Rydberg atoms and ground-state atoms (see Chapter 4).

The mechanisms of laser cooling are the subject of textbooks [76] and are not repeated here. The presentation of the magneto-optical trap for Cs atoms in this

section is restricted to the specific technical realisation in our experiment and the scientific research applications.

2.2.1 Laser system for the magneto-optical trap

The optical layout is shown schematically in Fig. 2.4a) and in Fig. 2.5. The main source of narrow-band laser light at 852.3 nm is a master-oscillator power-amplifier (MOPA) system (maximal output of ~ 800 mW with a bandwidth of ~ 500 kHz). The laser frequency of the MOPA laser system is stabilised *via* frequency-modulation spectroscopy of the $6p_{3/2}, F' = 4/5 \leftarrow 6s_{1/2}, F = 4$ crossover resonance measured by Doppler-free saturated-absorption spectroscopy in a Cs cell (see **3** in Fig. 2.5). Repumping light is provided by an additional external-cavity diode laser (ECDL). The laser frequency of the ECDL is stabilised in a lock-in detection scheme to a crossover resonance ($6p_{3/2}, F' = 2/4 \leftarrow 6s_{1/2}, F = 3$), also measured using Doppler-free saturated-absorption spectroscopy in a Cs cell (see **6** in Fig. 2.5).

Various polarising beam-splitter cubes and acousto-optical modulators (AOMs) are used to generate intensity- and frequency-controlled light from these two lasers. The optical setup exploits the linear polarisation of the IR-laser light to split and to recombine the laser beams. Each optical "branch" in the laser setup presented in Fig. 2.5 consists of a polarising beam-splitter cube in combination with a half-wave plate to separate a fraction of the radiation and an RF-frequency-driven AOM in double-pass configuration. This results in frequency shifts $\delta\nu = \pm 2 \cdot \nu_{\mathrm{RF}}$ of the IR light, where ν_{RF} is the frequency of the RF signal applied to the AOM.

The light for cooling (see (C) in Fig. 2.4b) and **4** in Fig. 2.5) is detuned by -11.5 MHz ($\approx 2.1\Gamma$) from the $6p_{3/2}, F' = 5 \leftarrow 6s_{1/2}, F = 4$ transition and is split into three beams with intensity ratios of 1:1:1.5 for the x, y and z directions (see Table 2.1). These beams are coupled into three polarisation-maintaining single-mode fibers. The repumping light is resonant with the $6p_{3/2}, F' = 4 \leftarrow 6s_{1/2}, F = 3$ transition (see (R) in Fig. 2.4b) and **7** in Fig. 2.5). It is spatially overlapped with the two beams used for cooling in the horizontal xy plane and is coupled into the same fibers. Before traversing the vacuum chamber along three mutually orthogonal optical axes, the three laser beams for cooling (and the two for repumping) are coupled out of the fibers, expanded to a diameter of roughly 20 mm, and changed to circular polarisation by quarter-wave plates. The beams are retro reflected outside of the vacuum chamber.

Another fraction of the light provided by the MOPA laser system is shifted into resonance with the $6p_{3/2}, F' = 5 \leftarrow 6s_{1/2}, F = 4$ transition and only coupled into the optical fiber for the z direction (see (A) in Fig. 2.4b) and **5** in Fig. 2.5). This laser light is used to acquire absorption images (explained further in Section 2.2.3). This laser can also be used for optically pumping the Cs atoms into the $6s_{1/2}, F = 4, M_F = 4$ state.

Table 2.1: Typical power levels $P_{x,y,z}$ measured for the different light fields after the optical fibers providing light in the x, y, and z directions.

	P_x (mW)	P_y (mW)	P_z (mW)
Cooling	33	33	45
Repumping	8	8	–
Depumping	0.2	–	–
Absorption	–	–	0.5–5

For rapid pumping of the atoms from the $F = 4$ to the $F = 3$ hyperfine component of the $6s_{1/2}$ ground state, a process referred to as "depumping" in the following, a small fraction of the light is shifted into resonance with the $6p_{3/2}, F' = 3 \leftarrow 6s_{1/2}, F = 4$ transition (see (D) in Fig. 2.4b) and **9** in Fig. 2.5). An additional repump laser beam (see (DR) in Fig. 2.4b) is derived from the ECDL, but detuned by about +13 MHz from the $6p_{3/2}, F' = 4 \leftarrow 6s_{1/2}, F = 3$ transition. This detuning matches the light shift of the atoms in the crossed optical dipole trap (see Fig. 2.6 in Section 2.3), and is used in the experiments to selectively pump atoms located at the position of the dipole trap to the $6s_{1/2}, F = 4$ state.

All AOMs used to generate the light of the respective frequencies are also used to modulate the intensity of the light. In particular, following a MOT-loading phase of ~ 75 ms, and a transfer phase to a compressed MOT or the optical dipole trap for ~ 20 ms, all IR-laser beams are extinguished before Rydberg excitation. This measure is taken to avoid direct photoionisation of atoms in the $6p_{3/2}$ state by the Rydberg-excitation laser.

2.2.2 Magnetic-field configuration and Cs-atom source

The magnetic-field gradient for the MOT is produced by a pair of coils in anti-Helmholtz configuration. Each coil consists of 35 windings of copper band (width 15 mm, thickness 0.45 mm) with a mean radius of 53 mm. The coils are mounted at a distance of 65 mm from each other outside of the vacuum chamber in the re-entrant view ports aligned along the laboratory z axis. To produce gradients on the order of 10 G/cm, a current of 8.0 A is passed through the coils. For the magnetic compression of the ultracold atom cloud (compressed MOT), the current is increased to 13 A for ten milliseconds, while at the same time the detuning and the intensity of the cooling light and the intensity of the repumping light is reduced. Before Rydberg excitation, the current in the magnetic-field-gradient coils is turned off. Eddy currents, which are induced by the change in the magnetic field, have decayed after 5 ms.

In the first experiments, cesium atoms were provided by high-purity resistively-

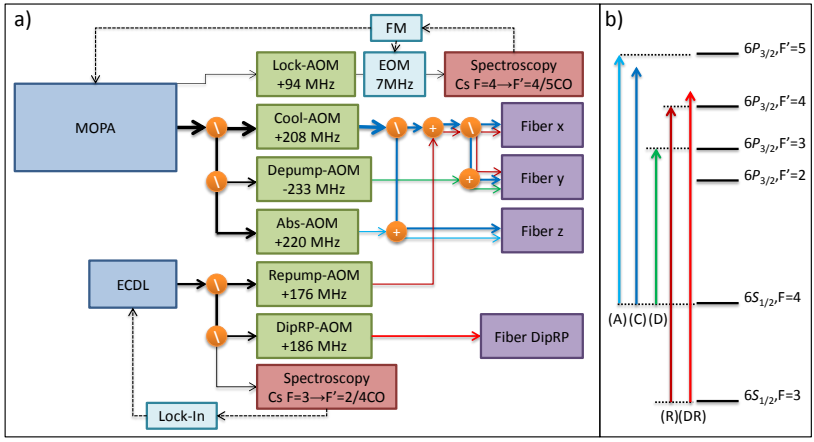

Figure 2.4: a) Schematic overview of the laser setup for laser cooling of cesium. Acousto-optic modulators are indicated in green, optical fibers in violet, and the laser systems in light blue. The frequency of the master-oscillator power-amplifier (MOPA) system (Toptica TA-Pro) is stabilised by frequency-modulation (FM) spectroscopy [77] of a saturated-absorption line of atomic cesium. The frequency modulation of the laser light required for the FM scheme is performed by a resonantly-driven electro-optical modulator (EOM, 7.7 MHz driving frequency). The main output of the MOPA system of ~ 800 mW is divided into three branches used for cooling, depumping and absorption measurements. Repumping light is provided by an external-cavity diode laser (ECDL, Toptica DL-Pro), which is stabilised to a second saturated-absorption line of cesium atoms using a lock-in detection scheme, and coupled into the optical fibers for the light in the xy plane. b) Overview over the relevant transitions coupling the hyperfine components F of $6s_{1/2}$ and F' of $6p_{3/2}$: (A) light for absorption imaging, (C) light for laser cooling, (D) light for depumping, (R) light for repumping, (DR) light for repumping atoms in the dipole trap. See text for details and Fig. 2.5 for the optical setup used to implement the scheme presented here.

heated dispensers (Alvasource AS-3-Cs-100-F) placed at a distance of roughly 15 cm from the MOT. The MOT was then loaded from cesium vapour produced by light-induced atomic desorption (LIAD) [78] of cesium atoms from the walls and view ports of the chamber. The UV light for the LIAD process was produced by three high-power light-emitting diodes (LEDs, Edixeon EDEV-SLC1-R), each emitting approximately 580 mW of light at a central wavelength of 402 nm. The LEDs were installed outside of the vacuum chamber and the light entered the chamber through a fused-silica window. This loading scheme led to a significant increase in the number of trapped atoms over a direct loading from the dispensers.

In the majority of the measurements presented in this thesis, however, a reservoir containing metallic Cs is connected to the UHV chamber by a valve. The vapour pressure of Cs at room temperature is sufficient to load the MOT directly from the thermal background gas, which resulted in higher particle numbers and densities than were obtained with the dispensers/LIAD setup described above.

2.2.3 Absorption imaging

The number, the density, and the temperature of the trapped atoms is determined by saturated-absorption imaging of the atom cloud [79]. The radiation resonant with the $6p_{3/2}, F' = 5 \leftarrow 6s_{1/2}, F = 4$ transition for absorption imaging is provided by the MOPA laser and can be independently modulated in frequency and intensity by an AOM (see also Figs. 2.4 and 2.5). It is spatially overlapped with the cooling laser beam in the vertical z direction, and the two light fields are coupled into the fiber with orthogonal polarisation. In front of the chamber, these polarisations are converted into left- and right-handed circular polarisations by a quarter-wave plate (see Fig. 2.2b) for a schematic drawing). After the chamber, a combination of a quarter-wave plate and a polarising-beamsplitter cube is used to separate the two frequency components based on their state of polarisation. The plane containing the trapped atoms is imaged by a pair of identical achromatic lenses onto a charge-coupled-device (CCD) chip. The scale of the acquired image was calibrated before the final assembly by imaging a ruler at the position of the MOT. In order to obtain an absorption image, the cooling light is switched off using an AOM and an exposure of the CCD chip is triggered. Then, the absorption light is switched on for about $2 - 40\,\mu s$ and the image of the atom cloud is read out digitally and processed by software. All timing sequences for controlling the MOT are generated by a data-acquisition card (National Instruments PCI-6259) which is programmed using LabView. The atomic samples released from the compressed MOT and used for the spectroscopic measurements described in this thesis had a typical peak density of 2×10^{11} atoms/cm^3, a $1/e$ sample diameter of 150 μm, and a temperature of 40 μK, as determined from the analysis of the absorption images.

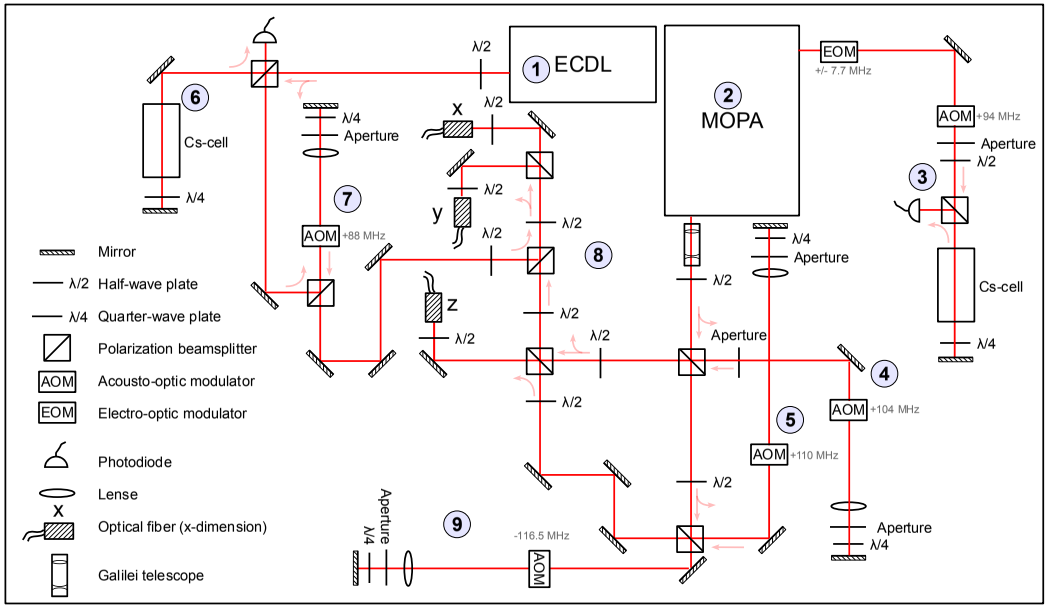

Figure 2.5: **1** External-cavity diode laser (Toptica DL-100 pro). **2** Master-oscillator power-amplifier (MOPA) laser system (Toptica TA pro). **3** Optical setup for Doppler-free frequency-modulation saturated-absorption spectroscopy of the hyperfine-structure-resolved $6p_{3/2} \leftarrow 6s_{1/2}$ transition, which is used to lock the MOPA frequency. Optical branches including the acousto-optical modulators for the cooling light (**4**) and for absorption measurements (**5**) in double-pass configuration. **6** Optical setup for Doppler-free saturated-absorption spectroscopy to lock the frequency of the ECDL. **7** AOM in double-pass configuration to shift the frequency of the ECDL to the $6p_{3/2}F' = 4 \leftarrow 6sF = 3$ transition. **8** Polarisation optics to distribute, combine and couple the light of the laser beams for cooling (x, y, z), repumping (x and y), absorption (z) and depumping (mainly x) into optical fibers, which guide the light to the experimental chamber. **9** AOM in double-pass configuration to shift a fraction of the light of the MOPA laser system into resonance with the $6p_{3/2}F' = 3 \leftarrow 6sF = 4$ transition. This light is used to "depump" atoms rapidly from the $F = 4$ to the $F = 3$ hyperfine component of the $6s_{1/2}$ ground state.

2.3 Far-detuned optical dipole trap

In a magneto-optical trap, the atom-number density is limited to typical peak values of about $10^{11}\,\mathrm{cm}^{-3}$ because of the rescattering of photons emitted by excited atoms from other ultracold atoms (which leads to heating and atom loss) [80, 81]. In a harmonic trap and assuming a non-interacting gas, the density is limited only by the temperature of the sample. This argument is based on the equipartition theorem, which reads

$$\frac{1}{2}k_\mathrm{B}T_d = \frac{1}{2}\kappa_d \langle r_d \rangle \tag{2.1}$$

for one dimension $d = x, y, z$, assuming a harmonic trapping potential with a spring constant κ, a spatial displacement from the centre of the trap r_d and a temperature T_d. The maximal, temperature-limited density in a harmonic trap is consequently

$$\rho_\mathrm{max} = \frac{N}{\sqrt{(2\pi)^3}\langle r_x \rangle \langle r_y \rangle \langle r_z \rangle} \propto N \left(\frac{\kappa}{k_\mathrm{B}T}\right)^{3/2}. \tag{2.2}$$

In experiments on photoassociation of ultracold atoms, one important factor is the mean nearest-neighbour separation r_NN in the gas, which is related to the atomic density ρ by $r_\mathrm{NN} = (2\pi\rho)^{-1/3}$ [82]. Typically, molecules formed *via* photoassociation have an equilibrium internuclear separation which is smaller than the mean nearest-neighbour distance. In this regime, the probability of finding a pair of atoms at a given separation increases linearly with the atomic density. A higher density of ground-state atoms thus enhances photoassociation rates and leads to an increased sensitivity of photoassociation spectroscopy. This is the main motivation to use a far-detuned optical dipole trap (ODT) in the experiments. An additional advantage of confining the ground-state atoms in an ODT is the reduced spatial extend of the sample, which reduces the effects of electric- and magnetic-field gradients in spectroscopic investigations.

The trapping potential in an ODT, which is briefly discussed in the following, can be "steeper" (larger values of the spring constant κ) than the trapping potential in a MOT. In this case, following Eq. (2.2), an increase in density is expected if the atoms can be transferred into the ODT without significantly increasing the temperature. In the calculation of the trapping potential, an approximate model can be applied that treats the atoms as oscillators in a classical radiation field [83]. In this model, the oscillating electric field $\mathbf{E}$ of the far-off-resonant light interacts with the complex dipole moment $\mathbf{d}$ induced by the electric field in the atom with polarisability α. The amplitude of the dipole moment $\tilde{d} = \alpha\tilde{E}$ is proportional to the atomic polarisability and the amplitude $\tilde{E}$ of the electric field. The trapping potential for an alkali-metal

atom in a far-detuned optical field can in this model be written as

$$U_{\mathrm{dip}} = -\frac{1}{2}\langle \mathbf{dE} \rangle = -\frac{1}{2\epsilon_0 c}\mathrm{Re}(\alpha) I = \frac{3\pi c^2}{2\omega_0^3}\frac{\Gamma}{\Delta} I(\mathbf{r}), \tag{2.3}$$

where the atomic polarisability is expressed as a function of the detuning Δ, the spontaneous-emission rate Γ of the excited state of the transition, and the angular frequency ω_0 of the electromagnetic driving field. Equation 2.3 reveals that the potential depth of an ODT is proportional to the intensity of the light field. The expression of Eq. (2.3) applied to the specific case of Cs yields

$$U_{\mathrm{dip}} = -\frac{\pi c^2}{2}\left[\frac{\Gamma_{\mathrm{D1}}}{\omega_{\mathrm{D1}}^3}\left(\frac{1}{\omega_{\mathrm{D1}}-\omega}+\frac{1}{\omega_{\mathrm{D1}}+\omega}\right)\right] I(\mathbf{r}) - \frac{\pi c^2}{2}\left[\frac{\Gamma_{\mathrm{D2}}}{\omega_{\mathrm{D2}}^3}\left(\frac{1}{\omega_{\mathrm{D2}}-\omega}+\frac{1}{\omega_{\mathrm{D2}}+\omega}\right)\right] I(\mathbf{r}), \tag{2.4}$$

where only the D1, *i.e.* $6p_{1/2} \leftarrow 6s_{1/2}$, and the D2, *i.e.* $6p_{3/2} \leftarrow 6s_{1/2}$, transitions (with angular transition frequencies ω_{D1} and ω_{D1}, respectively) are relevant for trapping in light fields with red-detuned frequencies ω. Indeed, the $6p_{1/2}$ and the $6s_{3/2}$ states are the lowest-lying optically accessible states of Cs.

In the experiments, light derived from a diode-pumped 1064 nm fiber laser (3SP Group, Manlight, 10 W continuous-wave output) is used to implement the ODT, in a similar configuration as described in Ref. [84]. The linearly polarised laser radiation is superimposed on one of the MOT IR-laser beams using a dichroic mirror and focused at the centre of the MOT to a beam waist of $\sim 80\,\mu$m. The laser beam exiting the chamber is again separated from the MOT beam using a dichroic mirror. It is then collimated, its polarisation is turned by 90°, and it is finally re-focused and sent into the experimental chamber a second time, crossing the first beam at the position of the MOT at an angle of 45° (see Fig. 2.2b)). The change of the polarisation direction is necessary to avoid interference between the two laser beams, which would create unstable trapping potentials. The power of the fiber laser is reduced to a minimal value of 300 mW during the MOT-loading phase. It is switched on for typically 25 ms during which the MOT is first compressed by ramping up the magnetic field, which is then turned off after 10 ms. The ultracold atoms are then transferred into the ODT during an optical-molasses phase. The power of the ODT laser is reduced to 300 mW again prior to the spectroscopic experiments and the ultracold atoms are released from the trap. This loading into the crossed-beam ODT increases the atom-number density to up to $10^{12}\,\mathrm{cm}^{-3}$.

As mentioned above, for technical reasons, the power of the laser forming the

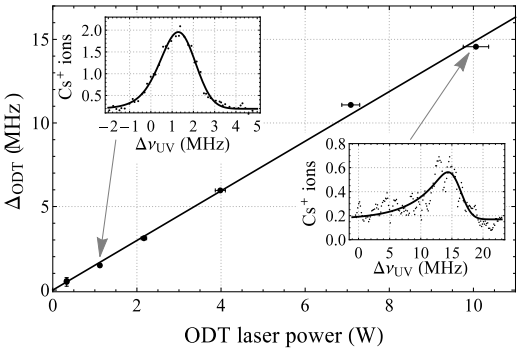

Figure 2.6: AC-Stark shift of the $70p_{3/2} \leftarrow 6s_{1/2}$ transition of Cs measured in the ODT at different power levels of the ODT laser during excitation. Experimentally determined peak positions are displayed as full circles. The horizontal and vertical error bars indicate the estimated standard deviation of the peak position and a 3% uncertainty in the determination of the laser power, respectively. The full line represents the fitted linear model. The upper and lower insets show experimental spectra (black points) and a fit of Eq. (2.6) to the spectrum (solid lines) for ODT laser powers of 1.1 W and 10.0 W, respectively. All frequencies are given relative to the extrapolated zero-power peak position.

ODT cannot be turned off completely but can only be reduced to a minimum value of 300 mW. The residual optical potential leads to an AC Stark shift of the Rydberg-transition frequencies to higher values. For one-photon Rydberg transitions of the type $np_{3/2} \leftarrow 6s_{1/2}$, the influence of the residual light field on both the ground state and the Rydberg state has to be considered. The shift of the $6s_{1/2}$ state is given by the trapping potential U_{dip} (see Eq. (2.4)) and is ~320 kHz for 300 mW and a beam waist of 80 μm. The shift of the Rydberg levels can be approximated with the ponderomotive potential U_{pond} of a free electron in an oscillating field, which is given by [85]

$$U_{\mathrm{pond}} = \frac{e^2}{2c\epsilon_0 m_e \omega^2} I \tag{2.5}$$

and corresponds to ~ 160 kHz for the residual ODT-laser field. The ponderomotive shift is assumed to be identical for transitions to different Rydberg states and is of relevance in absolute-transition-frequency measurements (Chapter 3.2). This shift is characterised by performing measurements at different ODT-laser powers and extrapolating the shifts to zero ODT-laser power. The intensity gradient in the ODT does not only shift the resonances but also causes red-degraded line shapes, which we model by an exponentially modified Gaussian line-shape function [86]

$$g_s(\nu) \propto \frac{1}{\tau} \exp\left(\frac{\sigma^2}{2\tau^2} + \frac{\nu - \nu_0}{\tau}\right) \mathrm{erfc}\left(\frac{\sigma}{\sqrt{2}\tau} + \frac{\nu - \nu_0}{\sqrt{2}\sigma}\right) . \tag{2.6}$$

In Eq. (2.6), ν_0 and σ are the central frequency and the width, respectively, of the unperturbed Gaussian line profile and the parameter τ describes the line asymmetry. An exemplary set of measurements at $70p_{3/2}$ is presented in Fig. 2.6. The line-shape parameters are fitted in a non-linear least-squares fit to the experimental spectral intensities and the intensity maxima are extracted from the model. For an ODT-laser power of less than ~ 0.5 W, the extracted position of the intensity maximum coincides with the central transition frequency obtained by the fit of a symmetric Gaussian distribution to the spectral line shape within the statistical uncertainty, justifying the use of Eq. (3.5) in the determination of the transition frequencies (see Section 3.2.2). By linear extrapolation of this peak position to zero ODT-laser power, the shift Δ_{ODT} of the transition frequency is determined at the residual ODT-laser power of 300 mW. This characterisation measurement is repeated at seven different values of n in the range from 27 to 74 and no systematic variation with n is observed. The experimentally determined shift of a transition at the residual ODT power of 300 mW is $\Delta_{\mathrm{ODT}}(0.30\ \mathrm{W}) = 0.485(16)$ MHz, where the given uncertainty is the statistical standard deviation of the seven independent measurements. This result is in agreement with the combined estimates for the shift of the ground state ($U_{\mathrm{dip},6s_{1/2},0.3\,\mathrm{W}} = 320$ kHz) and the ponderomotive shift of the Rydberg state ($U_{\mathrm{pond},0.3\,\mathrm{W}} = 160$ kHz).

2.4 Light sources

2.4.1 UV-laser sources for one-photon Rydberg excitation

In the literature, the majority of the experiments involving Rydberg excitation of ultracold atoms relies on two-photon transitions. There are two main reasons for this: Firstly, the laser used to drive the first transition to the 5p state in Rb or the 6p state in Cs (Rb and Cs are used in the vast majority of experiments with ultracold Rydberg atoms) is already present in the setups of the corresponding magneto-optical traps. Therefore, only one additional excitation laser is required for the two-photon Rydberg excitation. Secondly, two-photon excitation from the $5s_{1/2}$ and $6s_{1/2}$ ground states of Rb and Cs, respectively, enables the excitation of $ns_{1/2}$ Rydberg states. This is important for investigations and applications of the Rydberg-excitation blockade, for which $ns_{1/2}$ Rydberg states offer the advantage of isotropic long-range interactions [87] (see also the results in Chapter 5).

For the spectroscopic investigations performed in the course of this thesis, an alternative one-photon excitation scheme is chosen, using UV light around 319 nm to excite np Rydberg states directly from the $6s_{1/2}$ ground state of Cs. In the following subsections, the different setups used for the generation of UV-laser light are presented.

Pulsed UV laser with 1.5 GHz bandwidth

In the first experiments, a pulsed frequency-doubled double-grating dye laser (Radiant Dyes, NarrowScan, DCM in ethanol, 0.05 cm^{-1} bandwidth) is used to excite a fraction of the ultracold cesium atoms to high $np_{3/2}$ Rydberg states. The two dye cells of the dye laser are pumped by the second harmonic of a Q-switched Nd:YAG laser (Coherent Surelight I-10) at a wavelength of 532 nm and a pulse energy of ~40 mJ. The repetition rate of the Nd:YAG laser is 10 Hz, which sets the repetition rate of the experiment. The dye laser is operated at a wavelength of about 639 nm and its output is sent through a β-barium borate (BBO) crystal for second-harmonic generation. After second-harmonic generation, the laser wavelength is centred around 319 nm and can be tuned to induce transitions from the $6s_{1/2}$ electronic ground state of cesium to the np Rydberg series converging to the $^1S_0$ ground state of Cs^+. The pulsed ultraviolet (UV) radiation is linearly polarised along the y axis and the pulse energy can be adjusted between 5 and 80 µJ/pulse by using an attenuator consisting of a half-wave plate and a UV polariser. The laser beam is sent into the experimental chamber unfocused along the laboratory x axis.

The ~ 1.5 GHz bandwidth of the laser is sufficient to resolve Rydberg states up to $n \approx 140$. This laser is applied only in the measurements described in Chapter 3.1 in UV–millimetre-wave double-resonance spectroscopy. Because the laser excitation selectively populates a single $np_{3/2}$ Rydberg state, the resolution of Rydberg-Rydberg millimetre-wave transitions is given only by the bandwidth of the millimetre-wave radiation and the instrinsic atomic transition linewidth under the given experimental conditions (see Section 2.4.2 for technical details and Section 3.1 for measured spectra). Direct investigations of interaction effects between ultracold Rydberg atoms are not possible with this laser because of the large bandwidth of the UV-laser pulses. Firstly, interaction effects in higher-lying manifolds ($n > 20$) cannot be resolved, and secondly, the large frequency bandwidth of the laser pulses results in a small overlap with the narrow (typically a few kHz for $n \approx 30$) Rydberg transitions, and in reduced effective coupling strengths.

Fourier-transform-limited UV laser with 130 MHz bandwidth

To obtain high-intensity pulses with a smaller bandwidth than described above, the single-mode output of a narrow-bandwidth continuous-wave (cw) laser is pulse amplified (see, *e.g.*, [88, 89]). Here, a ring dye laser (Coherent 899) is used to generate about 500 mW of cw radiation at a wavelength of 639 nm and a bandwith of about 1 MHz. The ring laser is pumped by the second harmonic of a diode-pumped Nd:YVO_4 (Laser Quantum, finesse, 10 W maximal output at a wavelength of 532 nm) at a power of 5 W. A fraction of the light emitted by the ring laser, corresponding to power levels of

about 100 mW, is coupled into a polarisation-maintaining single-mode fiber and then sent through two dye cells which are transversally pumped by the 532 nm output of a seeded, Q-switched Nd:YAG laser (Continuum Surelight I-10). The seeding 639 nm radiation is pulse amplified in these dye cells. To prevent perturbations of the ring laser by back-reflections, an optical isolator is placed between the fiber output coupler and the amplification line. In order to reduce amplified spontaneous emission (ASE), apertures of 100 μm diameter are placed behind the first and the second dye cell, and 150-mm-focal-length lenses are used to focus the laser beam onto these apertures. One final lense is used to collimate the pulse-amplified beam again. The laser pulses are sent through a BBO crystal for frequency doubling *via* second-harmonic generation. The obtained laser pulses have a temporal shape that reflects the pulse shape of the seeded Nd:YAG laser. The frequency bandwidth of the laser pulses is then given by the Fourier transformation of the temporal pulse shape which corresponds to an almost perfect Gaussian function. The pulse lengths (Gaussian full width at half maximum) in the UV were measured with a fast photodiode to be $\delta t \approx 4.4$ ns, which corresponds to a frequency bandwidth of $\delta\nu = \frac{2\mathrm{Log}(2)}{\delta t \pi} = 100$ MHz. The bandwith determined in spectroscopic experiments on high Rydberg states in Cs is 130 MHz, close to the Fourier-transform limit.

The UV-laser pulses are sent through a variable attenuator (consisting of a half-wave plate and a Glan-Taylor UV polariser) to adjust the pulse energy between zero and 100 μJ and through a Berek compensator to adjust the polarisation. The UV-laser beam enters the experimental chamber along the z axis and is focused to a beam-waist radius of ~ 100 μm at the position of the ultracold Cs sample.

For the experiments presented in Chapter 6, the pulse-amplification line is seeded by the cw output of a diode laser at a wavelength of 639 nm and power levels of about 20 mW. The resulting visible and UV pulses have a slightly reduced intensity stability as a result of the lower input power, but are otherwise very similar to those obtained by pulse amplification of the cw output of the ring dye laser. The reason for this observation is that frequency and intensity characteristics of the pulses are mainly determined by the laser used to pump the dye cells, which is the same in both cases (see above).

Continuous-wave UV-laser radiation with 1 MHz bandwidth

A much higher frequency resolution than the 130 MHz of the pulse-amplified laser system described above is required in the experiments described in Chapters 4 and 6. To this end, the output of the ring dye laser is coupled into an external enhancement cavity (Coherent MBD-200) containing a BBO crystal at the position of the intracavity focus. In this way, second-harmonic conversion efficiencies up to 37% could be

achieved in continuous-wave operation, corresponding to a power of up to 300 mW (at ~850 mW of fundamental radiation). To achieve these levels, the output of the ring laser is sent through a telescope arrangement and a focusing lense for mode-matching to the cavity, and its polarisation is adjusted using a half-wave plate. The intracavity BBO crystal is cut and aligned under Brewster's angle. Therefore, light reflected from the cavity acquires a frequency-dependent change in the polarisation. The light reflected from the cavity is sent through a polarising beam-splitter cube and detected on two photodiodes. From these measured signals, an error signal is derived, which is used to lock the length of the cavity (modulated by a piezo-mounted cavity mirror) to the frequency of the ring laser in a Hänsch-Couillaud locking scheme [90]. This locking scheme does not require the modulation of the laser frequency. This is very important for the experiments presented in Chapters 4 and 6, which are extremely sensitive to sidebands in the frequency spectrum of the Rydberg-excitation laser. Most experiments described in this thesis concentrate on interaction-induced satellite peaks next to atomic transitions which are stronger by many orders of magnitude. Even very weak frequency sidebands in the Rydberg-excitation laser spectrum could lead to the excitation of the atomic transition when the centre frequency is detuned. Consequently, sidebands in the frequency spectrum of the Rydberg-excitation lasers could generate artefacts in the experimental spectra and thus need to be avoided.

By locking the length of the frequency-doubling cavity to the frequency of the ring dye laser, cw UV radiation with power levels up to 300 mW and a frequency bandwidth of ~1 MHz is obtained.

2.4.2 Millimetre-wave sources for transitions between Rydberg states

Spectra of transitions from the initially prepared Rydberg state to higher-lying Rydberg states were recorded with millimetre-wave radiation. As continuous millimetre-wave–radiation source, the phase-locked backward-wave oscillator (BWO) described in Ref. [91] is used. Its frequency can be continuously tuned in the range of 240 – 380 GHz and its bandwidth is narrower than 1 kHz [91]. The output horn of the BWO is placed 40 cm away from the centre of the MOT and the millimetre-wave radiation intersects the UV-laser beam at right angles (see Fig. 2.2a)).

The output of the BWO is stabilised in a phase-lock loop to $f_{\mathrm{RF}} + N f_{\mathrm{LO}}$, where $N f_{\mathrm{LO}}$ is the Nth harmonic ($N = 10 - 15$) of the frequency of a local oscillator (Wiltron 6769B, discontinued product) and f_{RF} is the frequency of an additional radio-frequency (RF) generator (Agilent 8647A, Palo Alto, USA). The output frequency is tuned by changing f_{LO} between 22.8 GHz and 25.1 GHz in minimum frequency steps of 1 kHz. Because the 10th to 15th harmonics of f_{LO} are used for the frequency stabilisation, the minimum step size by which the output frequency can be varied is 10 – 15 kHz, which

is too large for the narrowest lines observed in the experiments (see Chapter 3.1). As an extension of the performance of this source as compared to the description in reference [91], a frequency step size below 1 kHz could be obtained by scanning the frequency f_{RF} of the reference signal (350 MHz in normal operation) instead of f_{LO}. In this way, the frequency step size could be reduced to 1 Hz.

A second source of narrow-bandwidth millimetre-wave radiation (used in the experiments described in Chapter 5) consists of the same frequency synthesiser (Wiltron 6769B) connected to an amplifier-multiplier chain (Virginia Diodes, WR6.5AMC, tunable range 110 - 170 GHz). The 12th harmonic of the incoupled microwave radiation is directly generated and no additional locking electronics (which is the crucial element in the operation of the BWO described above) is required.

Typical interaction times with the millimetre-wave radiation are between 1 µs and 60 µs. The transitions are detected using state-selective pulsed field ionisation (PFI) and separately monitoring the ionisation signals of initial and final Rydberg states in the Cs^+-ion time-of-flight (TOF) traces (see Section 2.6).

2.5 Frequency calibration

2.5.1 Scanning-cavity transfer lock

In order to improve the frequency stability of the continuous-wave ring dye laser, a scanning-cavity transfer lock (SCTL) is implemented. This frequency stabilisation scheme was first described by Lindsay *et al.*[92] and has since then been used in numerous laboratories (see, *e.g.*, [93–95]). It is based on the combination of a stable optical frequency reference (often, as in our case, a stabilised HeNe laser) with a scanning Fabry-Pérot interferometer (FPI). The experimental setup is depicted in Fig. 2.7a). The light from the stabilised HeNe reference laser (Thorlabs HRS015, specified stability of ±1 MHz over one hour) and the light from the dye laser with unknown frequency are superimposed with orthogonal polarisations on a polarising beam-splitter cube and copropagate through the FPI (Thorlabs SA200-5B). One of the FPI mirrors is mounted on a piezo-electric actuator, which allows for a variation of the cavity length. As the length of the confocal FPI is varied, the laser light is transmitted when

$$l_{\mathrm{FPI}} = n\frac{\lambda_\alpha}{4},\ n \in \mathbb{N}, \tag{2.7}$$

i.e., whenever the cavity length l_{FPI} is an integer multiple of the fourth of the wavelength λ_α of that laser. The difference in frequency between two transmission maxima is the free spectral range (FSR) of the FPI, which is given by $\Delta_f\mathrm{FSR} = c/(4l_{\mathrm{FPI}})$, where c is the speed of light in vacuum. For the cavity employed in this setup,

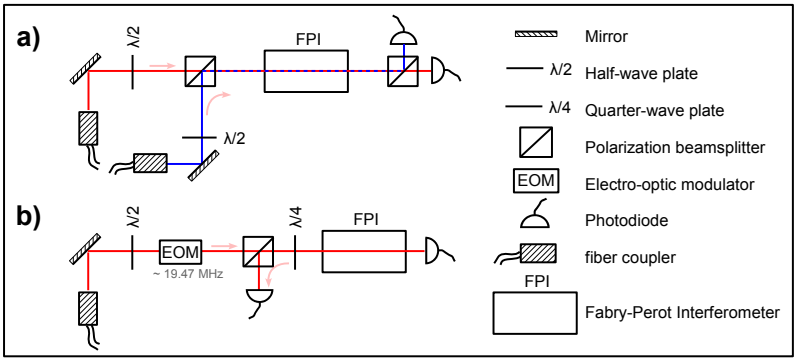

Figure 2.7: Schematic representation of the implementations of a scanning-cavity transfer lock (a) and a Pound-Drever-Hall lock (b). In the setup a), the half-wave plates are used to adjust the relative polarisation of the dye-laser radiation and the HeNe-laser radiation, such that the two beams can be merged before and separated behind the Fabry-Pérot interferometer using polarising beam-splitter cubes.

the manufacturer specified a free spectral range of 1.5 GHz. The transmitted light from the two lasers is separated again by another polarising beam-splitter cube and is detected on separate photodiodes. For scanning the cavity length, a multifunction data-acquisition card (DAQ, National Instruments PCI-6281) is used to apply a triangular voltage ramp to the piezo-electric actuator of the FPI with a repetition rate of 10 Hz. The voltage levels from the two photodiodes are digitised simultaneously by the same DAQ card. Synchronisation of the voltage-ramp generation and the analogue-waveform acquisition ensures that every time position in the waveform corresponds to a well-defined electric-potential difference applied to the FPI. The time traces are then analysed by a program written in Labview, which uses a peak-finding algorithm to determine the positions $t_{\alpha,i}$ at which the cavity is resonant with the frequency of the laser α (see Fig. 2.8). A feedback algorithm, acting on the offset of the potential ramp applied to the FPI, is then used to stabilise the position $t_{\mathrm{HeNe},1}$, and thus the length of the cavity at that position, to a fixed value. Stabilisation of the time delay

$$\Delta t = t_{\mathrm{Dye},1} - t_{\mathrm{HeNe},1}, \tag{2.8}$$

between the transmission of the light from the reference laser and the dye laser is achieved by acting on the external-scan control input of the Coherent-899 control box and allows the stabilisation of the dye-laser frequency to the same level as the reference-laser frequency.

The SCTL can also be used in a “non-locking” mode, which facilitates the measurement of relative frequency changes during a frequency scan of the dye laser, if

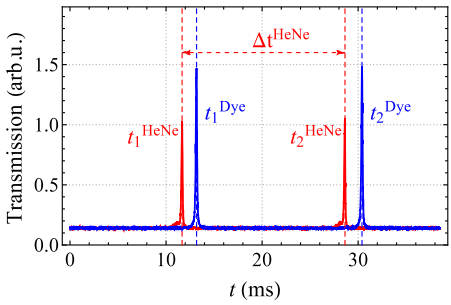

Figure 2.8: Transmission spectrum of the HeNe laser (red trace) and the fundamental laser beam of the ring dye laser (blue trace) though the scanning Fabry-Pérot interferometer. The time on the horizontal axis is proportional to the cavity length, which is scanned by the application of a increasing potential to the piezo-electrical actuator of the cavity (see text for details).

an accuracy of about 2 MHz is sufficient. In this mode, the time interval between two transmission maxima of the reference laser Δt_{HeNe} (see Fig. 2.8), the free spectral range of the cavity, and the wavelengths of the two lasers, λ_{Dye} and λ_{HeNe} as measured by a wavelength meter (HighFinesse, WS-7), are used to determine a conversion factor c^{Dye} between the time interval Δt (see Eq. (2.8)) and a relative frequency change of the dye laser following

$$c^{\mathrm{Dye}} = \frac{\Delta_f \mathrm{FSR}}{\Delta t_{\mathrm{HeNe,FSR}}} \frac{\lambda_{\mathrm{Dye}}}{\lambda_{\mathrm{HeNe}}}$$
$$\Delta f = c_{\mathrm{Dye}} \Delta t \quad . \tag{2.9}$$

This model assumes a linear relationship between the potential difference applied to the piezo-electrical actuator and the length of the cavity. These assumptions are found to be justified over the relevant range of parameters by comparing wavelength-meter readings and detunings given by Eq. (2.9) for many frequency scans over the course of our measurements. Frequency intervals larger than Δ_fFSR are determined by scanning the dye laser continuously over the frequency interval, following the evolution of the values given by Eq. (2.9), and reconstructing the total frequency range by post-analysis in Mathematica. The value of Δ_fFSR is determined by comparing a precisely known frequency interval (in this case the hyperfine splitting of the $6s_{1/2}$ ground state of cesium) to the value given by Eq. (2.9) and was found to be within 2% of the specified value of the FSR. While this frequency-stabilisation scheme is more stable than the calibration based only on the readings of the wavelength meter (HighFinesse WS7), the remaining long-term fluctuations, dominated by drifts of the reference laser, still exceed the linewidth of the dye laser and thus limit the achievable resolution of the spectroscopic experiments. Referencing the frequency of the dye

laser to an optical frequency comb, as described in Section 2.5.3, is found to be more reliable.

2.5.2 Pound-Drever-Hall lock to an external cavity

The highest level of stability and accuracy in the frequency calibration of the ring dye laser was achieved in a three-step locking scheme. First, the frequency of the dye laser is directly stabilised to a mode of the external FPI (Thorlabs SA200-5B) in the experimental configuration shown in Fig. 2.7b). The error signal for the stabilisation is derived using the Pound-Drever-Hall technique [96] by modulating a small part of the fundamental output of the ring laser with an electro-optical modulator (EOM). The EOM consists of a 30 mm long $LiNbO_3$ crystal in a resonant tank circuit and is driven directly by an RF signal at about 20 MHz (peak amplitude 20 V) obtained from a dual-channel function generator (Rigol DG1022). Light reflected from the cavity (see Fig. 2.7b)) is detected by a fast photodiode (Thorlabs PDA10A-EC) and is amplified by a low-noise broadband amplifier (MiniCircuits ZFL-500LN-BNC+) after low-pass filtering by a filter with a passband from DC to 5 MHz (MiniCircuits BLP-5+). The amplified signal is mixed with the local oscillator RF signal, obtained from the second channel of the function generator, on a phase detector (MiniCircuits ZRPD-1+). An analogue proportional-integral (PI) controller feeds the resulting error signal (see Fig. 2.9) back to the electronic control box of the ring laser, which was modified according to Ref. [97]. The closed-loop bandwidth of this lock is ~8 kHz. To reduce the influence of acoustic vibrations and thermal fluctuations, the external FPI was installed in a massive, air-tight enclosure.

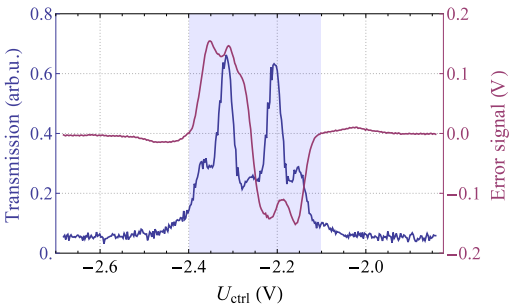

Figure 2.9: Transmission signal (blue trace) and error signal (purple trace) of the frequency-modulated dye-laser radiation reflected from the Fabry-Pérot cavity as a function of the potential applied to the piezo-electrical actuator of the cavity (see text for details), and measured with the setup schematically shown in Fig. 2.7. The shaded area indicates the capture range of about 100 MHz of the locking setup.

Second, slow drifts of the length of the reference cavity are observed by measuring the laser frequency with a wavelength meter (HighFinesse WS-7). The measured frequency is stabilised to a chosen set point by applying a variable voltage to the piezo-electrical actuator of the reference cavity. The closed-loop bandwidth of this lock is ~10 Hz. The frequency of the laser is scanned in steps of typically 150 kHz by varying the lock set point. While the absolute accuracy of the wavelength meter is specified as 60 MHz (3σ), the intrinsic Allan deviation of the wavelength meter measurements is typically around 300 kHz over periods shorter than one minute [98], which was confirmed by our measurements.

In a third step, the readings of the wavelength meter are calibrated to the measurements using a frequency comb following the procedures described in [99–102].

2.5.3 Referencing to an optical frequency comb

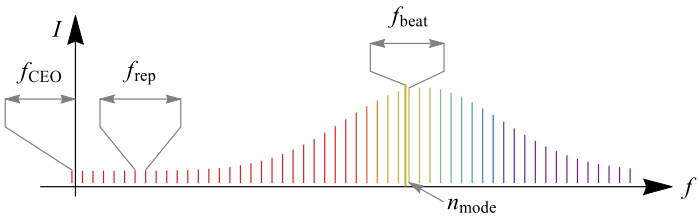

Figure 2.10: Schematic and purely illustrative representation of the frequency spectrum of a frequency comb. The repetion rate f_{rep} determines the comb spacing and is shown here enlarged for the sake of clarity. Frequency bandwidth filtering ensures that the detected beat frequency results only from interference of the laser light with the next tooth of the comb (see text for details).

The absolute frequency of the excitation laser radiation is determined by overlapping a small part of the fundamental beam at ~640 nm with light from a frequency comb (Menlo Systems FC1500-250-WG) on a fast photodiode and counting the frequency of the resulting beat note f_{beat}. The absolute accuracy of the wavelength meter is sufficient to unambiguously determine the mode number n of the beating comb tooth. The frequency of the dye laser is then obtained from measurements of the carrier-envelope-offset frequency f_{CEO} and the repetition rate f_{rep} of the comb (see also Fig. 2.10) by

$$f_{dye} = n \cdot f_{CEO} \pm 2 \cdot f_{CEO} \pm f_{beat} \quad . \tag{2.10}$$

All frequencies are measured by direct comparison with the frequency of a Rb oscillator (Stanford Research Systems FS725) having a stability of 1×10^{-11} over a typical measurement time of 10 s and being disciplined by a GPS receiver (Spectrum Instruments TM-4) with a specified long-term stability of 1×10^{-12}. The accuracy of

this clock yields directly the accuracy of the optical frequency measurements [103]. The RF signal of the beat note f_{beat} is strongly filtered by the control electronics of the frequency comb. To ensure that the frequency of the beat note is always in the detection window from about 55 to 65 MHz during a scan, the repetition rate of the comb is controlled by the data-acquisition program. Because the remote execution of the command for changing the repetition rate takes about one second, such changes are performed as rarely as possible: whenever the frequency of the beat note approaches the lower (upper) limit of the detection window, the repetition rate is set such that the new beat note is close to the upper (lower) limit of the detection window.

In a final step of the stabilisation and calibration scheme, the readings of the wavelength meter can be constantly calibrated to the readings from the frequency comb, such that the frequency of the dye laser can be stabilised to an absolute accuracy of about 100 kHz over the course of several hours.

2.6 Detection of the Rydberg transitions

Even though recently all-optical detection schemes relying on electromagnetically-induced transparency [104–106] have been applied to the detection of Rydberg transitions [107–110], in the experiments described here, Rydberg atoms are detected using pulsed electric-field ionisation (PFI) [15]. PFI is a very powerful detection method because it is *i*) background free, *ii*) very efficient (the ionisation rates scale exponentially with the applied field strengths [111] so that the ionisation yield is 100% for sufficiently high electric-field strengths), *iii*) very sensitive (to levels much below a single Rydberg excitation on average per experimental cycle because a charged particle is detected and this can be done with high efficiency [112]) and *vi*) state selective (because the threshold ionisation field is a function of the principal quantum number n of the Rydberg state, and depends also on l and even on m_l [113], see Ref. [] for more details).

In the experimental setup, the Rydberg atoms are field ionised by applying either a positive potential pulse to the four field plates located on the opposite side of the MCP (generating a homogeneous electric field in y direction, see Fig. 2.3) or a negative potential pulse to the ring electrodes and the metallic grid in front of the MCP. In the former case, four home-built high-voltage switches are used to switch from the potential configuration used to compensate stray electric fields (see Section 2.7) to a potential configuration for the ionisation of Rydberg atoms. Applying the field-ionisation pulses to the ring electrodes enables one to avoid applying pulsed potentials to the field plates, which reduces transient stray fields in the region where the atom cloud is located. The ionisation fields resulting from the application of pulsed negative po-

tentials on the ring electrodes are smaller and only suitable to detect Rydberg states with $n > 50$. Consequently, the ionisation pulses are applied to the ring electrodes to detect Rydberg states with $n > 50$ and to the field plates for the detection of Rydberg states in the range $50 > n > 26$. Electric fields of sufficient strength to field ionise Rydberg states below $n \approx 26$ cannot be generated. Fortunately, transitions to Rydberg states below $n = 26$ can also be detected by monitoring spontaneously produced ions following Rydberg excitation (see, *e.g.*, the spectra shown in Fig. 5.3a)).

In the experiments described in this thesis, the Rydberg atoms were detected state selectively by monitoring the field-ionisation signals induced by slowly rising potentials U_{ion} applied over a simple RC low-pass filter, *e.g.*, with $R = 8.2\,\text{k}\Omega$, $C = 100\,\text{pF}$. The resulting field ramp (see Fig. 2.11) ionises the Rydberg atoms in the volume of the MOT and extracts the positively charged Cs^+ ions towards the MCP detector. The detector consists of a matched pair of MCPs with 18 mm active diameter in chevron configuration. The front plate is typically held at a potential of $-2.1\,\text{kV}$ and the backplate is grounded. The ion–time-of-flight traces are read out by an oscilloscope (LeCroy, Waverunner 606Zi, 600 MHz, 20 G/s) and processed further using a LabView program. U_{ion} is adjusted to the n values of the investigated Rydberg states such that, *e.g.* in millimetre-wave transfer, initial and final Rydberg states appear at distinct positions in the time-of-flight spectra.

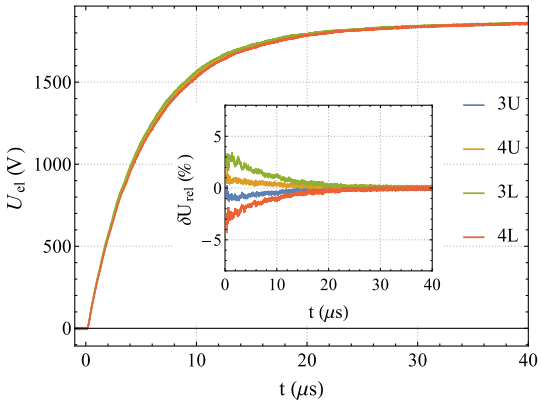

Figure 2.11: Time dependence of the electric potentials applied to the four field plates (red, blue, yellow, and green traces, respectively) to field ionise Rydberg states. Home-built high-voltage switches were used in this experiment and the electric potential $U_{\text{ion}} = 1.8\,\text{kV}$ was applied over a RC low-pass filter ($R = 8.2\,\text{k}\Omega$, $C = 100\,\text{pF}$) with a time constant of $\sim 8\,\mu\text{s}$. The traces were measured with a high-voltage probe. The relative deviations of the potentials applied to the four field plates from the mean potential are shown on a magnified scale in the inset and never exceed 4%.

In the ion–time-of-flight spectra, spontaneously produced ions are separated from ions resulting from PFI, and signals corresponding to Cs^+ ions are separated by Cs_2^+

ions. The times of flight $t_{Cs_2^+}$ of Cs_2^+ ions are longer than the times of flight t_{Cs^+} Cs^+ ions when accelerated by the same potential difference ($t_{Cs_2^+} \propto t_{Cs^+}$). Consequently, in addition of being state selective, the method of PFI in combination with an ion-time-of-flight spectrometer provides also information of the photoexcited species and their decay into charged fragments. This advantage turned out to be very useful in the investigations of the decay of long-range Rydberg molecules (see Chapter 4.6) and of interacting Rydberg-atom-pair states (see Chapter 5.3.5).

2.7 Measurement and compensation of stray fields

2.7.1 Compensation of electric stray fields

Because of their very large polarisabilities, which scale with the principal quantum number n as n^7 [15], atoms and molecules in high Rydberg states are extremely sensitive to external electric fields. This sensitivity has been can be exploited to measure stray electric fields with extreme precision [114] but also imposes great demands on the electric-field control in experiments investigating the properties of high Rydberg states, such as these presented in this thesis.

The experimental chamber has been designed under the constraint that electric stray fields must be minimised. To meet this constraint, all materials in the immediate vicinity of the photoexcitation region are conductive. Their electric potentials are either precisely controlled or grounded. For example, the field plates described in Section 2.1.1 are contacted from the back to prevent electric fields originating from the leads from penetrating into the photoexcitation region. Despite the efforts invested in the design of the experimental chamber, a stray electric field of $\sim 300\,\mathrm{mV/cm}$ was consistently observed in the photoexcitation region using Rydberg-Stark spectroscopy. Possible origins of this stray electric field are charges accumulating on the surface of the fused-silica view ports of the chamber; the largest one is located at a distance of about 4 cm from the photoexcitation region. Charges are generated in our experiments by direct or stray (UV) laser radiation incident on any material and by the ionisation of Cs Rydberg atoms. Fortunately, this stray field can be compensated.

The compensation fields are determined by minimising the Stark shifts of $n's_{1/2} \leftarrow np_{3/2}$ transitions recorded with the millimetre-wave radiation (see Section 2.4.2) or of $np \leftarrow 6s_{1/2}$ transitions recorded with a narrow-band UV laser (see Section 2.4.1). Because the low-angular-momentum states have a non-zero quantum defect, they experience a quadratic Stark effect at small field strengths [15, 115]. Consequently, the stray field can be compensated in each spatial dimension independently. First, a rough compensation of the stray field is performed at low n values. Then, the

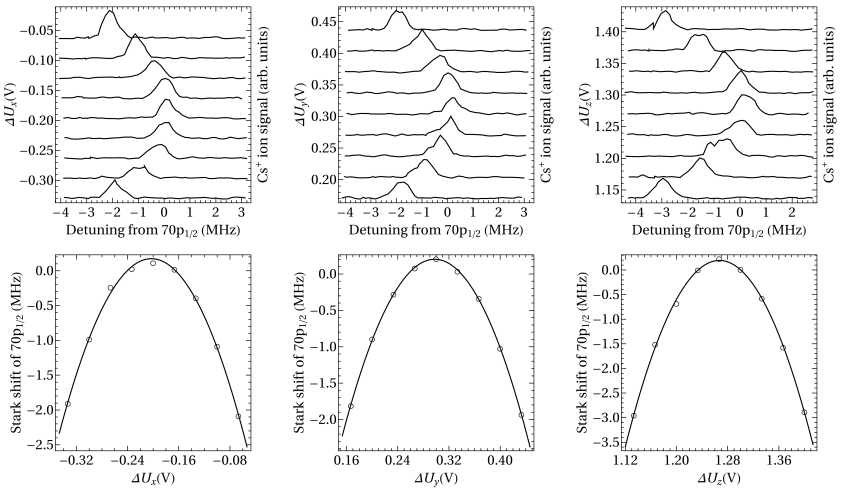

Figure 2.12: Measurement of the Stark effect of the $70p_{1/2}$ Rydberg state. The homogeneous electric fields in x, y and z dimension (left, middle and right panels, respectively) have been applied using the three different potential configurations depicted in Fig. 2.3. Spectra of the $70p_{1/2} \leftarrow 6s_{1/2}$ transition are depicted in the upper row. The spectra are shown with a vertical offset corresponding to the potential difference ΔU_d applied between the two sets of field plates in d dimension. The resonances are fitted with Gaussian line-shape functions and the centre frequencies are plotted as a function of ΔU_d in the bottom row. The position of minimal Stark shift is determined in a parabolic fit (solid black line) to these positions (open black circles).

procedures are repeated at progressively higher n values, exploiting the increasing sensitivity to stray fields resulting from the n^7 scaling of the polarisability [15].

The results of an exemplary measurement of the stray electric field is presented in Fig. 2.12. The three sets of spectra displayed in the upper row correspond to the $70p_{1/2} \leftarrow 6s_{1/2}$ transition recorded in external electric fields applied along the x, y and z axis (from left to right). The vertical offset of the spectra is chosen to correspond to the potential difference ΔU_d applied to the field plates depicted in Fig. 2.3. The quadratic Stark shift of the $70p_{1/2}$ state is negative and the potentials $\Delta U_{d,0}$, corresponding to minimal Stark shift and, thus, minimal residual electric field in direction d corresponds to a maximal transition frequency. The maximal transition frequencies are determined by fitting parabolic curves to the positions of the $70p_{1/2} \leftarrow 6s_{1/2}$ resonance as a function of the applied potentials. The values of $\Delta U_{d,0}$ correspond to the position of the apex of each fitted parabolic curve. The field created by applying the set of compensation potentials $\Delta U_{d,0}$ was calculated using the experimental geometry and the software package SimIon to be $\vec{E} = (E_x, E_y, E_z) = (-44, 65, 317)$ mV/cm.

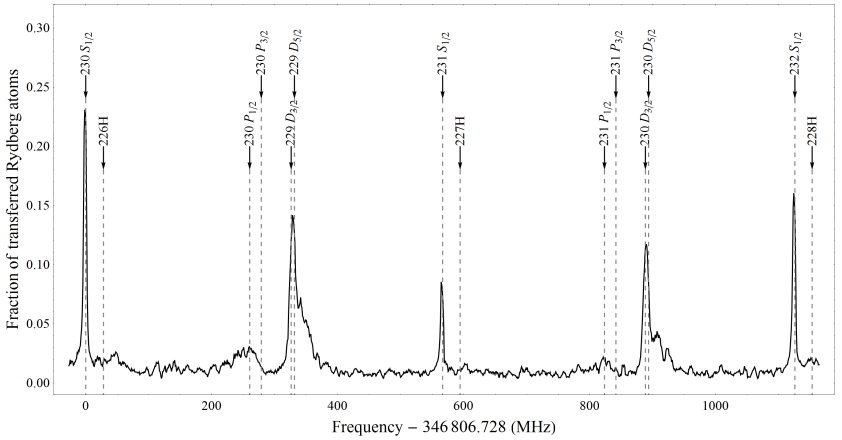

Figure 2.13: Millimetre-wave spectrum of Rydberg states around $231s_{1/2}$ from the initial $93p_{3/2}$ state. The dashed vertical lines are calculated line positions based on the extrapolated quantum defects of Ref [116]. The appearance of the dipole-forbidden transitions $np_{1/2,3/2} \leftarrow 93p_{3/2}$ and the asymmetric line broadenings are caused by the electric-field gradients.

Once the stray electric fields are compensated, transitions to high-n Rydberg states can be observed. A millimetre-wave spectrum of transitions from the $93p_{3/2}$ state to well-resolved Rydberg states with $n \sim 230$ is presented in Fig. 2.13. At such high n values, the linewidths and shifts cannot be reduced by varying the compensation potentials and are found to be independent of the ground- and Rydberg-state density. Moreover, the linewidths increase with increasing polarisability differences of the coupled states. Consequently, the line broadening is attributed to an electric-field gradient originating from the applied compensation field or from ions embedded in the atom cloud. Ions can be formed by collisions of Rydberg atoms, by blackbody-radiation-induced ionisation, and by two-photon ionisation of ground states atoms with UV and IR radiation (all IR beams are turned off by AOMs, but a small amount of IR light can leak through). From the experimental linewidth of ∼2 MHz for the $230s_{1/2} \leftarrow 93p_{3/2}$ transition and calculated Stark shifts of the Rydberg states involved, it can be excluded that the residual electric stray field varies by more than 1 mV/cm over the atomic sample. Thus, initial stray fields of about 300 mV/cm could be reduced to less than 1 mV/cm. Moreover, the spectrum displayed in Fig. 2.13 illustrates the possibility to fully resolve Rydberg states of very high principal quantum numbers.

2.7.2 Compensation of magnetic stray fields

The sensitivity of high Rydberg states to external magnetic fields is similar to the sensitivity of ground-state atoms. Accurate spectroscopic measurements also require the suppression of Zeeman shifts and splittings of the transitions, and, consequently, a compensation of stray magnetic fields. The magnetic stray field is compensated using the three pairs of magnetic coils described in Sect. 2.1.2. The procedure followed to characterise and minimise the magnetic stray field and illustrated in the first set of experiments presented in Section 3.1.4 (see Fig. 3.5) is presented here for completeness.

First, the mechanical Hanle effect [117] is exploited in a coarse compensation of the magnetic field in two directions. To this end, an additional laser beam, resonant with the transition $6p_{3/2}, F' = 4 \leftarrow 6s_{1/2}, F = 4$ and circularly polarised, is passed through the atom cloud in x direction (see Fig. 2.2). By applying a bias magnetic field of 100 mG in x direction, a quantisation axis is defined for the total angular momentum $\vec{F}$ of the atoms. If the magnetic-field components perpendicular to this axis are significantly smaller than the quantisation field, the circular polarised light drives predominantly $\sigma^{+/-}$ transitions and thus optically pumps the atoms into one of the maximally stretched states $F = 4, M_F = \pm 4$, which are dark states in this configuration. Thus, the atoms scatter only few photons before decoupling from the light field. Any component of the magnetic field perpendicular to the quantisation axis weakens the efficiency of the dark-state pumping because π transitions become allowed. In this case, the atoms scatter photons continuously and thus experience a mechanical force in the direction of the laser beam, resulting in a displacement of the atom cloud. The displacement is observed by imaging the fluorescence of the cloud on a CCD camera. Stray magnetic fields in y and z direction are compensated by reducing the observed displacement by modifying the currents applied to the compensation coils.

The remaining magnetic stray field is compensated by measuring the Zeeman effect of high Rydberg states using millimetre-wave spectroscopy (see Fig. 3.5). In this way, an initial magnetic stray field of about 550 mG could be reduced first to approximately 70 mG using the mechanical Hanle effect and then to below 2 mG using millimetre-wave spectroscopy. The latter value is estimated by comparing spectra calculated for different magnetic field strengths to experimental millimetre-wave spectra (see Chapter 3.1.4) and is limited by the accuracy of 1 mA with which the currents applied to the compensation coils can be adjusted.

The hyperfine interaction and the sensitivity to electric stray fields complicates the compensation of magnetic stray fields using millimetre-wave spectroscopy of transitions between Rydberg states. A simpler and faster way to compensate magnetic

stray fields, which was also used in the experiments described in this thesis, relies on Zeeman spectroscopy of the $6s_{1/2}, F = 4 \leftarrow 6s_{1/2}, F = 3$ magnetic-dipole transition. Small magnetic fields result in a splitting of the $F = 3, 4$ hyperfine levels into the different M_F magnetic sublevels, with a spacing of $\sim 0.35\,\mathrm{kHz/mG}$ between adjacent magnetic states [118]. Because the Landé g_F factors are $g_{F=3} = -1/4$ and $g_{F=4} = +1/4$, the Zeeman effect in the $F = 3$ level is inverted and a simple comb-like Zeeman spectrum consisting of equally spaced lines is expected for microwave spectrosocpy of the hyperfine transition in an external magnetic field. The selection rules regarding ΔM_F determine whether the observable splittings between adjacent lines is $2 \cdot 0.35\,\mathrm{kHz/mG}$ (for π transitions with $\Delta M_F = 0$, or for $\sigma^{\pm}$ transitions with $\Delta M_F = \pm 1$) or $0.35\,\mathrm{kHz/mG}$ (when both types of transition are driven).

A schematic overview of the principles underlying a magnetic-field measurement using the Zeeman-split $F = 4 \rightarrow F = 3$ transition is depicted in Fig. 2.14. First, the atoms are prepared in the $F = 4$ hyperfine component of the $6s_{1/2}$ state using a repump-laser pulse. Additionally, in some experiments, the atoms are pumped into the $F = 4, M_F = 4$ magnetic sublevel with an IR-laser pulse resonant with the $6p_{3/2}, F' = 5 \xleftarrow{\sigma^+} 6s_{1/2}, F = 4$ transition. After the state preparation, the microwave radiation is turned on for $300\,\mu\mathrm{s}$. The microwave radiation with a frequency of $\sim 9.2\,\mathrm{GHz}$ is derived from a local oscillator (Wiltron 6769B, discontinued product), the output of which is sent to a waveguide connected to a microwave horn antenna. In the setup, the microwave radiation enters the chamber along the laboratory-fixed x axis and is linearly polarised, with the polarisation vector aligned along the z axis. The microwave radiation induces $6s_{1/2}, F = 4, M_F \rightarrow 6s_{1/2}, F = 3, M_F$ transitions, when its frequency is resonant with one of the Zeeman-split transitions. The atoms remaining in the $F = 4$ hyperfine component are subsequently detected by absorption imaging. To account for microwave-frequency-independent fluctuations of the atom number in the dipole trap, a background measurement is performed by measuring the atom number at every second experimental cycle without turning the microwave radiation on. Because of the short lifetime of the electronically excited $6p_{3/2}$ level and the resulting linewidth of the optical absorption transition of $\sim 5.4\,\mathrm{MHz}$, the Zeeman-split magnetic sublevels are not resolved directly in the absorption measurement for magnetic fields below 5 G.

In the experiments presented in Fig. 2.15a)-c), a small magnetic bias field was applied along the z axis. This magnetic field was generated by increasing the compensation current applied to the corresponding magnetic coils by 150 mA. Considering the geometry of the coils and the applied current, a magnetic field of $\sim 270\,\mathrm{mG}$ at the centre of the coils can be calculated using the Biot-Savart equations (see, *e.g.*, [119]). With the polarisation of the microwave radiation parallel to the quantisation axis, only π transitions with $\Delta M_F = 0$ are expected to occur. The seven lines observed in

the spectra presented in Fig. 2.15a)-c) therefore correspond to $\Delta M_F = 0$ transitions with $M_F = -3, -2, ..., +3$ (see also Fig. 2.14). The observed frequency spacings between adjacent lines are $2 \cdot 0.35\text{kHz/mG} \cdot B_z = 181\,\text{kHz}$, which yields a magnetic-field strength of 258 mG. Considering the uncertainties in the input parameters, this value is in agreement with the calculated value of 270 mG.

The spectra depicted in Fig. 2.15a) show the Cs-atom number in the $6s_{1/2}, F = 4$ levels measured by absorption imaging. The thin red trace was measured without the microwave radiation and the blue trace shows the signal obtained with a 300-μs-long microwave-radiation pulse applied before measuring the $6p_{3/2} \leftarrow 6s_{1/2}$ absorption. Transitions to the $6s_{1/2}, F = 3, M_F$ levels induced by the microwave radiation are revealed by a reduction of atom numbers in the $6s_{1/2}, F = 4$ level. The background-corrected trace (obtained by dividing the signal shown in blue by the signal shown in red in Fig. 2.15a)) is presented in Fig. 2.15b). A spectrum taken under the same experimental conditions, but with an additional 50-μs-long IR pulse resonant on the $6p_{3/2}, F' = 5 \xleftarrow{\sigma^+} 6s_{1/2}, F = 4$ transition applied before the microwave transfer, is shown in Fig, 2.14c. In this way, most of the atoms are transferred to the $F = 4, M_F = 4$ magnetic sublevel of the $6s_{1/2}$ ground state, which is a "dark" state for the microwave transfer, because of the $\Delta M_F = 0$ selection rule. Consequently, the effect of the optical pumping is observed as a reduced integrated line intensity in the microwave spectrum presented in Fig. 2.15c). Only the $\Delta M_F = 0$ transitions at positive detunings corresponding to the $M_F = 3, 2$ states are still observed. Once measured, the magnetic fields can be compensated. After compensation, the spectrum depicted in Fig. 2.15d) is obtained, which consists of a single Lorentzian line with a centre frequency of 9.1926317(1) GHz and a full width at half maximum of 6.5 kHz.

These results demonstrate that Zeeman spectroscopy of the ground-state hyperfine transition in Cs (and in the other alkali-metal atoms) can be used to *i*) determine (and compensate) magnetic stray fields and *ii*) to characterise the effects of optical-pumping processes in the ground state.

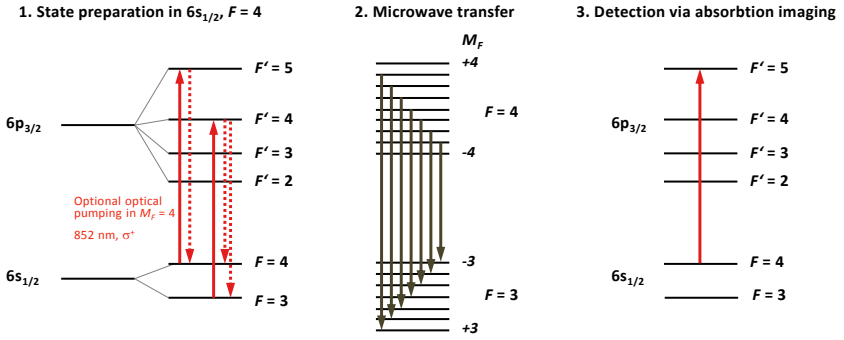

Figure 2.14: Schematic energy-level diagrams of the $6s_{1/2}$ and $6p_{3/2}$ states including their hyperfine and magnetic sublevels relevant for Zeeman spectroscopy of the $6s_{1/2}, F = 3, M_{F=3} \leftarrow 6s_{1/2}, F = 4, M_{F=4}$ magnetic-dipole transition in Cs. Solid vertical arrows denote electric- and magnetic-dipole transitions induced by electromagnetic radiation, whereas dashed vertical arrows denote decay by fluorescence. The left-hand-side scheme (1.) illustrates that the atoms are first prepared in the upper $F = 4$ hyperfine component using the repump laser resonant with the $6p_{3/2}, F' = 4 \leftarrow 6s_{1/2}, F = 3$ transition. Additionally, the atoms can be prepared in a single magnetic sublevel by further optical pumping using circularly polarised σ^+ light with the frequency tuned to the $6p_{3/2}, F' = 5 \xleftarrow{\sigma^+} 6s_{1/2}, F = 4$ transition. Magnetic-dipole transitions with $M_F = 0$ induced by the microwave radiation are indicated by vertical arrows in the middle energy-level diagram (2.). These transitions are detected by monitoring the number of Cs atoms remaining in the $F = 4$ hyperfine component of the $6s_{1/2}$ electronic ground state after absorption using a laser resonant with the $6p_{3/2}, F' = 5 \leftarrow 6s_{1/2}, F = 4$ transition (3.).

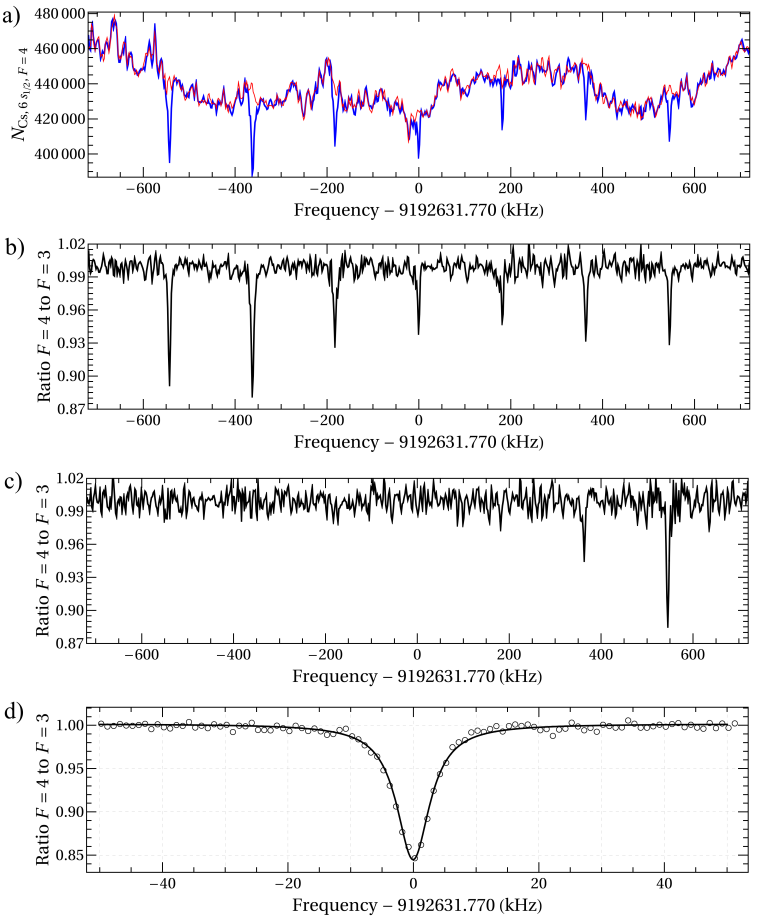

Figure 2.15: a) to c) Experimental microwave spectra of the clock transition in Cs in an external magnetic field of 258 mG. The microwave radiation is linearly polarised, with the polarisation vector parallel to the quantisation axis. The panel in a) shows the number of Cs atoms in the $6s_{1/2}, F = 4$ level a function of the microwave-radiation frequency with the microwave radiation turned on (blue trace) or off (thin red trace) prior to the absorption measurement. The division of the signal shown in blue by the signal shown in red yields the ratio of detected Cs atoms in the $F = 4$ hyperfine level to the $F = 3$ level, and is depicted in panel b). The spectrum depicted in panel c) is obtained with the optical puming on the $6p_{3/2}, F' = 5 \xleftarrow{\sigma^+} 6s_{1/2}, F = 4$ transition before the microwave transfer. When all stray magnetic fields are compensated, only one single resonance with a Lorentzian full width at half maximum of 6.5 kHz at a microwave-radiation frequency of 9.192 631 7(1) GHz is observed (see panel d).

Chapter 3

High-resolution spectroscopy of Cs Rydberg states

The weakly bound nature of the Rydberg electron and the resulting high sensitivity of high Rydberg states to their environment are simultaneously a curse and a blessing: A blessing, because it is the origin of most applications of high Rydberg states, and a curse, because artefacts can easily mask the effects one desires to study. For instance, the presence of only a few ions in the measurement volume can alter the line shapes and line positions in spectra of high Rydberg states [114, 120], which in turn may be interpreted as arising from other effects. Thus, in the spectroscopy of Rydberg states a thorough investigation of all line-broadening mechanisms is required.

The investigation of line shapes and line-broadening mechanisms in spectra of high Rydberg states is the subject of this chapter. It is carried out through high-resolution UV and millimetre-wave spectroscopy of high Rydberg states of Cs under low-density conditions where the interactions between Rydberg atoms and between Rydberg atoms and ground-state atoms can be safely neglected.

Apart from characterising the experimental conditions and their effects on the measured transitions, high-resolution spectroscopy on atomic Rydberg levels yields accurate information on the atomic Rydberg energy-level structure, needed for many subsequent studies, *e.g.* in experimental and theoretical investigations of long-range Rydberg molecules (see Chapter 4) and of pairs of Rydberg atoms interacting *via* long-range forces (see Chapters 5 and 6). The same information can also be used to derive thermodynamically relevant quantities such as ionisation and dissociation energies with high precision [121]. The experimental investigations presented in this chapter exploit laser cooling to generate ultracold samples of atoms in the gas phase and a frequency comb and frequency-stabilised millimetre-wave radiation for the precise measurement of transition frequencies between Rydberg states of Cs.

In the first part of this chapter, transitions between high Rydberg states of ^{133}Cs atoms have been studied by high-resolution millimetre-wave spectroscopy of an ultracold sample. The spectroscopic measurements were performed after releasing the atoms from a magneto-optical trap. Switching off all trapping fields and compensating the stray electric and magnetic fields to below 1 mV/cm and 2 mG, respectively, prior to the spectroscopic measurement enabled the recording of millimetre-wave spectra of Rydberg states with principal quantum number beyond $n = 100$ under conditions where the inhomogeneous broadening by stray fields is minimal and no dephasing of the Rydberg-atom sample can be detected over measurement times up to 60 μs. The Fourier-transform-limited linewidths of better than 20 kHz enabled the observation of the hyperfine structure of $ns_{1/2}$ and $np_{3/2}$ Rydberg states of Cs beyond $n = 90$. The analysis of the lineshapes of transitions to high-n Rydberg states indicated that field inhomogeneities across the atomic sample represent the dominant cause of spectral broadening at high n values. The analysis also revealed that the initial polarisation of the atomic sample ($F = 4$, $M_F = 4$) is preserved for several tens of microseconds, the depolarisation being caused by slow precession induced by magnetic stray fields.

In the second part of the chapter, absolute-frequency measurements of the transitions from the $6s_{1/2}$ ground state of ^{133}Cs to $np_{1/2}$ and $np_{3/2}$ Rydberg states are presented. The transition frequencies are determined by single-photon UV spectroscopy in ultracold samples of Cs atoms using a narrow-bandwidth laser system with its frequency referenced to a frequency comb. Extrapolation of the Rydberg series in a global fit of the ionisation energy E_I of Cs yielded an improved value of $E_\mathrm{I} = hc \cdot 31\,406.467\,732\,5(14)\,\mathrm{cm}^{-1}$ with a relative uncertainty of 5×10^{-11}.

Improved values for the quantum defects of the $np_{1/2}$, $np_{3/2}$, $ns_{1/2}$, and $nd_{5/2}$ series of Cs are derived by considering the results obtained in the first two sections of this chapter and the data reported in Ref. [122].

Section 3.1 of this chapter is adapted from the article H. Sassmannshausen, F. Merkt, and J. Deiglmayr: "High-resolution spectroscopy of Rydberg states in an ultracold cesium gas", *Phys. Rev. A* **87**, 032519 (2013). Dr. Johannes Deiglmayr has contributed the main part to the results presented in Section 3.2, which is adapted from J. Deiglmayr, H. Herburger, H. Sassmannshausen, P. Jansen, H. Schmutz, and F. Merkt: "Precision measurement of the ionisation energy of Cs I", *Phys. Rev. A* **93**, 013424 (2016) and is presented here for the sake of completeness.

3.1 Millimetre-wave spectroscopy of transitions between Rydberg states

This section presents a spectroscopic study of very high Rydberg states of ^{133}Cs in a magneto-optical trap (MOT) under conditions where Doppler broadening and line broadening caused by the finite transit time (see, *e.g.*, Ref. [114]) of the atoms in the measurement region are negligible. The residual line broadening is exclusively caused by residual stray electric and magnetic fields and by transitions induced by blackbody radiation. Under these conditions, Rydberg series, including their hyperfine structures, are resolved up to high values of the principal quantum number. The analysis of line shapes and line positions also enabled the quantification of the effects of weak electric and magnetic fields and the compensation of these fields.

3.1.1 Experiment

The spectroscopic measurements presented in this section are performed on ultracold Cs-atom gas-phase samples released from a vapour-loaded magneto-optical trap (see Chapter 2). These samples have a Gaussian density distribution with a typical peak density of 5×10^9 atoms/cm^3, a $1/e$ sample diameter of 150 μm, and a temperature of 10 μK, as determined from the analysis of the absorption images. To obtain a purely oriented sample of ground-state atoms in the $M_F = 4$ state, the atomic sample is exposed to a beam of circularly polarised laser light propagating along the z direction (see Figs. 2.1 and 2.2 for the definition of the space-fixed axis system) and resonant with the $6p_{3/2}, F = 5 \leftarrow 6s_{1/2}, F = 4$ transition for 100 μs. This laser is then turned off 20 μs prior to Rydberg excitation. A pulsed frequency-doubled dye laser (Radiant Dyes, DCM in ethanol, 0.05 cm^{-1}(1.5 GHz) bandwidth, ∼ 5 ns pulse length) is used to excite a small fraction, typically much less than 10 %, of the ultracold cesium atoms to $np_{3/2}$ Rydberg states. All hyperfine components in the Rydberg-excitation transition allowed by electric-dipole selection rules are excited within the laser bandwidth. Under these conditions, the number of atoms excited to Rydberg states remains low and Rydberg-atom-pair interactions are negligible. The pulsed UV radiation is linearly polarised and the pulse energy is adjusted between 5 and 80 μJ. The UV-laser-radiation frequency is measured with a wavelength meter (HighFinesse, WS-6) at an accuracy sufficient to unambiguously assign the principal quantum number to $np_{3/2}$ series up to $n \approx 120$. For the experiments described here, the UV-radiation frequency is kept fixed at the positions of selected $np_{3/2} \leftarrow 6s_{1/2}$ resonances.

Spectra of transitions from the selected $np_{3/2}$ Rydberg state to higher-lying $ns_{1/2}$ or $nd_{3/2,5/2}$ Rydberg states are recorded with millimetre-wave radiation. As continuous millimetre-wave source, a phase-locked backward-wave oscillator (BWO) is used as

described in Ref. [91, 123] and in the Section 2.4.2 of this thesis. Its frequency can be continuously tuned between 240 and 380 GHz and its bandwidth is below 1 kHz [91]. The output horn of the BWO is placed 40 cm away from the centre of the MOT and the millimetre-wave radiation intersects the UV-laser beam at right angles.

The interaction time of the continuous-wave millimetre-wave radiation and the Rydberg-atom sample is determined by the delay time between the UV-laser pulse used for the initial excitation and the application of the electric-field pulse used for detection of the transitions. Because the laser pulse is short compared to this delay time and the electric-field pulse immediately shifts the transitions out of resonance, the temporal structure of the interaction between the millimetre-wave radiation and the Rydberg atoms can be described to a good approximation by a square pulse.

The maximal output power of the millimetre-wave source is on the order of tens of milliwatts [91]. The transition dipole matrix elements for transitions between Rydberg states scale as n^2. To avoid saturation broadening of the investigated transitions the BWO output power had to be lowered to its minimum and the intensity of the millimetre-wave radiation had to be further reduced by placing a stack of 500 sheets of paper between the source and the atom cloud. This measure effectively blocked the direct optical path, and the transitions were induced by reflected or scattered radiation. Under these conditions, the intensity was low enough to avoid saturation broadening and the narrow bandwidth of the millimetre-wave source could be fully exploited. However, the polarisation of the millimetre-wave radiation interacting with the Rydberg atoms was not well defined.

The Rydberg atoms were detected by monitoring the field-ionisation signal induced by a slowly rising negative potential U_{ion} applied *via* a RC low-pass filter (with $R = 8.2$ kΩ, $C = 100$ pF) to all ring electrodes and the grid in front of the MCP. The resulting field ramp ionised all Rydberg states in the volume of the MOT and extracted the positively charged Cs^+ ions towards the MCP detector. U_{ion} was adjusted to the n values of the investigated Rydberg states such that initial and final Rydberg states appeared at separate positions in the time-of-flight spectra. To reduce the effects of shot-to-shot intensity and frequency fluctuations of the UV laser, the field-ionisation signal of the final state of the transitions was normalised to the total ion yield. At low number densities of excited atoms, the normalisation factor is independent of the absolute number of excited Rydberg atoms. To increase the signal-to-noise ratio, the signal of 80 experimental cycles was averaged at each spectral position.

3.1.2 Line-shape model of transitions between Rydberg states

The simulation of the experimental spectra requires the calculation of line positions and line intensities and a convolution with the instrumental line profile. In order to calculate the line positions, the energies of the hyperfine levels in a magnetic field of the initial and the final Rydberg state are obtained by diagonalising the Hamiltonian matrix [124]

$$\hat{H} = \hat{H}_{\mathrm{hfs}} + \hat{H}_{\mathrm{Z}} = A_{\mathrm{hfs}}(\hat{\vec{I}} \cdot \hat{\vec{J}}) + g_J \mu_{\mathrm{B}} B_z \hat{J}_z. \tag{3.1}$$

The Hamiltonian consists of the hyperfine-structure Hamiltonian $\hat{H}_{\mathrm{hfs}}$ in the magnetic-dipole approximation and the Zeeman Hamiltonian $\hat{H}_{\mathrm{Z}}$ for the electron spin. Neglecting the Zeeman effect of the nuclear spin is justified because the electron g-factor is three orders of magnitude larger than the g-factor of the proton. Neglecting higher multipoles in $\hat{H}_{\mathrm{hfs}}$ is also justified, because the magnetic-quadrupole coupling constant of Cs is two orders of magnitude smaller than the magnetic-dipole coupling constant [125]. The Hamiltonian matrix is evaluated in the coupled $|I, J, F, M_F\rangle$ basis, called $|F, M_F\rangle$ basis hereafter, in which $\hat{H}_{\mathrm{hfs}}$ is diagonal, with matrix elements

$$\langle F|\hat{H}_{\mathrm{hfs}}|F\rangle = \frac{1}{2} A_{\mathrm{hfs}}[F(F+1) - I(I+1) - J(J+1)]. \tag{3.2}$$

The Zeeman Hamiltonian $\hat{H}_{\mathrm{Z}}$ is diagonal in the uncoupled basis $|I, M_I, J, M_J\rangle$ and the matrix elements in this basis are given by

$$\langle I, M_I, J, M_J|\hat{H}_{\mathrm{Z}}|I, M_I, J, M_J\rangle = g_J \mu_{\mathrm{B}} B_z M_J, \tag{3.3}$$

where the Landé g-factor is taken as $g_J = 1 + \frac{J(J+1)+S(S+1)-L(L+1)}{2J(J+1)}$ [126]. The basis transformation from the $|I, M_I, J, M_J\rangle$ to the $|F, M_F\rangle$ basis is then applied to $\hat{H}_{\mathrm{Z}}$, the resulting matrix is added to $\hat{H}_{\mathrm{hfs}}$, and the eigenvalues and eigenstates of the Hamiltonian matrix $\hat{H}$ (Eq. 3.1) are determined numerically. The transition frequencies were obtained as differences between the eigenenergies of the final and initial states.

For the calculation of line intensities, the initial distribution of M_F levels in the $F = 4$ hyperfine component of the $6s_{1/2}$ state of cesium and the ΔM_F selection rules for both Rydberg excitation and Rydberg-Rydberg transitions must be taken into account. The UV laser is linearly polarised with it polarisation axis perpendicular to the quantisation axis of the atoms after optical pumping. Consequently, the UV laser drives $\Delta M_F = \pm 1$ transitions. The polarisation of the millimetre-wave radiation interacting with the cesium atoms was not controlled in the experiments and the ratio of $\Delta M_F = \pm 1$ to $\Delta M_F = 0$ transitions was determined empirically in a global analysis of all spectra. A ratio of 70% $\Delta M_F = 0$ and 30% $\Delta M_F = \pm 1$ yielded best overall agreement with the experimental results. This ratio was kept unchanged in the simulation

of all spectra presented in Figs. 3.1, 3.2, and 3.4. The transition strengths are then evaluated using the dipole-matrix elements

$$\langle FM_F|er_q|F'M_F'\rangle = \langle J||e\mathbf{r}||J'\rangle(-1)^{2F'+J+M_F+I}\sqrt{(2F+1)(2F'+1)(2J+1)}\begin{pmatrix} F' & 1 & F \\ M_F' & q & -M_F \end{pmatrix}\begin{Bmatrix} J & J' & 1 \\ F' & F & I \end{Bmatrix}. \tag{3.4}$$

Because only the relative strengths of transitions between the different $|F, M_F\rangle$ levels is observable in the experimental spectra, and the reduced matrix element $\langle J||e\mathbf{r}||J'\rangle$ only gives a constant contribution for all transitions with given $|\Delta l| = 1$ and $|\Delta J| = 0, 1$ values, this term was not evaluated in the calculation of the transition dipole moments. The line intensities were obtained as the product of the relative population in a given M_F level of the $p_{3/2}$ Rydberg state and the squared matrix elements of the transitions to the $ns_{1/2}$ and nd_J states. For calculations including a non-zero magnetic field, the line intensities were further weighted by the admixture of initial and final states (in the unperturbed $|F, M_F\rangle$ basis) to the eigenstates of $\hat{H}$ in the magnetic field. The magnitude of the residual magnetic field was treated as global fit parameter. The best agreement between experimental spectra and simulation was obtained for a residual magnetic field of 2 mG.

The convolution of the Fourier transform of the square excitation pulse (a sinc function) and the Lorentzian line-profile of the atomic transition was found to be adequately described by a Lorentzian line-profile. Thus, the stick spectra obtained with the calculated line positions and intensities were convoluted with this line-profile function. The overall amplitude and an arbitrary frequency shift of the resulting spectra were fitted separately to each experimental spectrum, as well as the magnetic dipole constants of the initial and final state and the Lorentzian linewidth.

3.1.3 Measurement of the hyperfine structure of high Rydberg states

Before the experiments described in this section were carried out, the stray electric field of $\sim$ 250 mV/cm in the photoexcitation region was reduced to values below 1 mV/cm by measuring the Stark effect of high n Rydberg states beyond $n = 200$ (see Section 2.7 for details), the stray magnetic field was reduced to 2 mG (see Section 3.1.4) and the power of the millimetre-wave radiation was reduced to levels at which no power broadening of the transitions could be observed. Exemplary millimetre-wave spectra of $n's_{1/2} \leftarrow np_{3/2}$ transitions recorded under such conditions are presented in Figs. 3.1 and 3.2. In these experiments, the UV-laser frequency was tuned to the selected $np_{3/2} \leftarrow 6s_{1/2}$ transition and the frequency of the millimetre-wave radiation was scanned around the position of the $n's_{1/2} \leftarrow np_{3/2}$ resonances. Because the band-

width of more than 1 GHz of the UV laser is too large to resolve the hyperfine splitting of the $n\mathrm{p}_{3/2}$ Rydberg states, all possible $F_{n\mathrm{p}_{3/2}} = 3, 4, 5$ hyperfine components are populated. Because of the optical pumping in the ground state and the selection rule $\Delta M = \pm 1$ for the Rydberg-excitation transition, primarily $M_F = 3, 5$ states are populated (see also discussion in Section 3.1.2). The hyperfine splitting of the $F' = 3$ and the $F' = 4$ components of the $n'\mathrm{s}_{1/2}$ Rydberg states is, however, clearly resolved in the millimetre-wave spectra, up to $n = 90$ and leads to the observation of a "doublet" in the spectra, *e.g.* with a splitting of $\sim$ 180 kHz in the case of the spectrum depicted in Fig. 3.1. The two components are broadened by the hyperfine structure of the initial $n\mathrm{p}_{3/2}$ state, which is only partially resolved for $n \lesssim 70$.

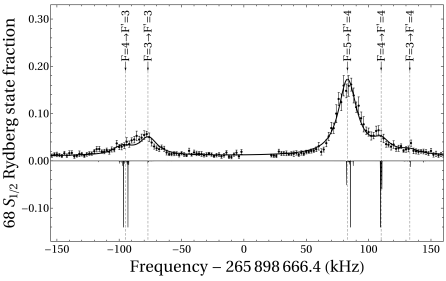

Figure 3.1: Millimetre-wave spectrum of the $68\mathrm{s}_{1/2} \leftarrow 59\mathrm{p}_{3/2}$ including a fitted simulation (thick black line) and an assignment of the single hyperfine transitions (black arrows on dashed vertical lines). The inverted stick spectrum, on which the simulation is based, is presented in arbitrary intensity units and shows the splitting of the $F' \leftarrow F$ transitions into their M_F components at the residual magnetic field of 2 mG.

Stray electric and magnetic fields below 1 mV/cm and 2 mG, respectively, have almost no detectable effect on Rydberg states with $n < 100$ at the experimental resolution. Consequently, the hyperfine structure of high-lying Rydberg states could be investigated with high precision. The experimental spectra (black dots with error bars in Figs. 3.1, 3.2, and 3.4) could be modeled accurately by taking into account the hyperfine and the Zeeman interactions of initial and final states, and a finite Lorentzian line profile, as described above. The adjustment of the calculated spectra (see solid black lines in Figs. 3.1, 3.2, and 3.4) to the measured spectra allowed the determination of the spectral resolution, the hyperfine-coupling constants of the states involved, and the initial polarisation of the atomic sample. As an example, the experimental spectrum of the $68\mathrm{s}_{1/2} \leftarrow 59\mathrm{p}_{3/2}$ transition is compared to a calculated spectrum in Fig. 3.1 which also provides an assignment of the different spectral features. The effect of the residual magnetic field of 2 mG is explicitly taken into account in the calculations. Such a small field only causes a small broadening of the hyperfine-resolved spectra, because the Zeeman splittings are below 10 kHz (see in-

verted stick spectrum in Fig. 3.1). A line profile with a full width at half maximum (FWHM) of 17(3) kHz is obtained for the experimental spectra by fitting the theoretical line-shape function. This is in good agreement with the convolution of the Fourier transform of the 60-µs-long millimetre-wave pulse and a natural linewidth (including the effect of blackbody-radiation-induced transitions) of 2.5 kHz [73], which yields a FWHM of 17.0 kHz. The experimental linewidth increases from 17(3) kHz to 19(3) kHz and 24(3) kHz for the millimetre-wave spectra of the transitions to the $81s_{1/2}$ and $90s_{1/2}$ states, respectively. This is in qualitative agreement with a Stark broadening caused by a residual electric field gradient of 100 mV/cm^2 in the measurement volume.

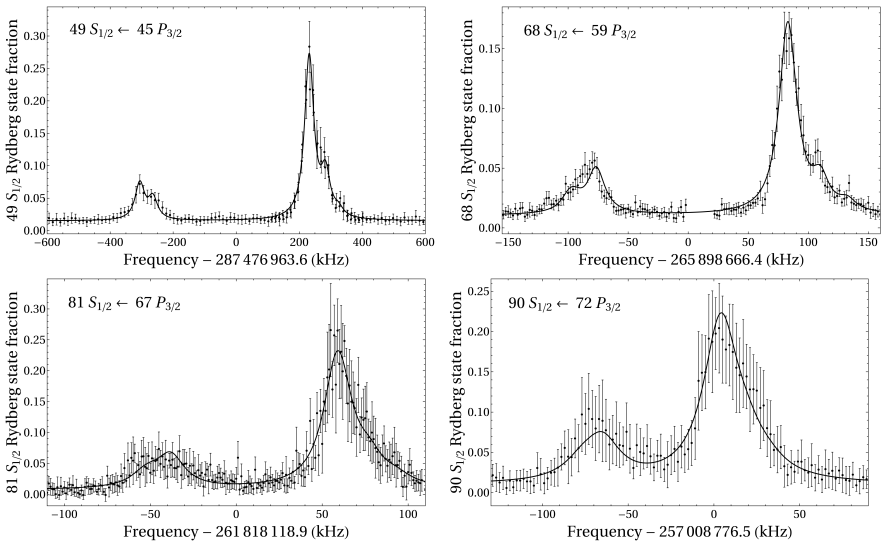

Figure 3.2: Experimental and simulated spectra of millimetre-wave transitions between $np_{3/2}$ and $n's_{1/2}$ Rydberg states of cesium ($49s_{1/2} \leftarrow 45p_{3/2}$, $68s_{1/2} \leftarrow 59p_{3/2}$, $81s_{1/2} \leftarrow 67p_{3/2}$, $90s_{1/2} \leftarrow 72_{3/2}$). Each point represents an average over 80 experimental cycles. The error bars correspond to the standard deviation of the average values of the single measurements. The black line is a simulated spectrum that has been fitted according to the model described in Subsection 3.1.2.

For each spectrum depicted in Fig. 3.2, the magnetic-dipole hyperfine coupling constants $A_{\mathrm{hfs},p_{3/2}}$ of the $np_{3/2}$ states were obtained by adjusting the model to the two $F = 3$ and $F = 4$ hyperfine components of the $ns_{1/2}$ state separately. The hyperfine coupling constants $A_{\mathrm{hfs},s_{1/2}}$ of the $ns_{1/2}$ states were then obtained in a second step by leaving $A_{\mathrm{hfs},p_{3/2}}$ unchanged and fitting the overall amplitude and frequency shift to the complete experimental spectrum. The hyperfine coupling constants of these high Rydberg states can be compared to reported values measured at lower

principal quantum number [116, 127–134] because of its scaling with the effective principal quantum number. The hyperfine structure results from the Fermi-contact-type interaction of the Rydberg electron with the nucleus and is therefore proportional to the probability density of the Rydberg electron at the nucleus. It scales with $(n^*)^{-3}$, where $n^* = n - \delta_\ell$ is the effective principal quantum number and δ_ℓ is the ℓ-dependent quantum defect. One can thus introduce a reduced hyperfine coupling $A^*_{\mathrm{hfs},\ell}$ constant as $A_{\mathrm{hfs},n^*,\ell} = \frac{A^*_{\mathrm{hfs},\ell}}{n^{*3}}$. The so-obtained reduced coupling constants were compared to previously published values [116, 127–134] in Fig. 3.3 (quantum defects are taken from [116]). Because the hyperfine structure of the $n\mathrm{p}_{3/2}$ states could not be resolved, the magnetic-dipole coupling constants of the $n\mathrm{p}_{3/2}$ states were only deduced from the line shape and linewidth and are therefore associated with larger uncertainties, whereas the hyperfine coupling constants of the $n\mathrm{s}_{1/2}$ states could be determined with an accuracy comparable to, or exceeding the accuracy of the measurements at low n^*. The weighted averages of the reduced coupling parameters for $n\mathrm{p}_{3/2}$ and $n\mathrm{s}_{1/2}$ states are $A^*_{\mathrm{hfs,p}_{3/2}} = 0.80(8)\,\mathrm{GHz}$ and $A^*_{\mathrm{hfs,s}_{1/2}} = 13.53(12)\,\mathrm{GHz}$, respectively. For $A^*_{\mathrm{hfs,p}_{3/2}}$, systematically higher values are obtained than previously reported for lower n values. The discrepancy could be the result of line-broadening effects by the residual electric field and the gradients of both electric and magnetic fields, which are not included in the model.

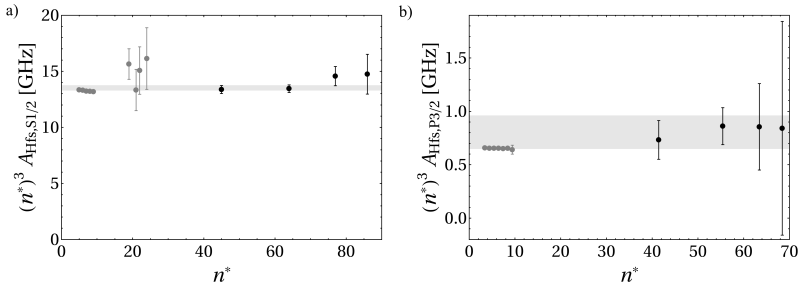

Figure 3.3: Plot of the fitted magnetic-dipole coupling constants of the hyperfine structure of $n\mathrm{s}_{1/2}$ (a) and $n\mathrm{p}_{3/2}$ (b) Rydberg states of cesium atoms weighted by $(n^*)^3$ vs n^* (the data obtained in measurements presented here are shown in black). The grey bar represents a weighted average including a 95% confidence interval of all four measurements and should guide the eye for the comparison with the literature data [116, 127–134] (shown in grey) at lower principal quantum number.

The modeled line shapes are sensitive to the initial population of M_F states in the $6s_{1/2}, F = 4$ ground state, *i.e.*, to the orientation of the initial atomic sample before Rydberg excitation. Experimentally, the sample is polarised by applying a circularly polarised pump laser pulse, which is switched off 20 µs before the excitation to Rydberg states. In the model, the initial polarisation was treated as a global parameter

being constant for all spectra presented in Figs. 3.2, 3.1, and 3.4. The optimal agreement with the experimental spectra was obtained assuming that 95% of the atoms remain in the $M_F = 4$ component until excitation to Rydberg states. The timescale for depolarisation is limited in the experiment by the precession of the magnetic moment of the cesium atoms around the axis of the stray magnetic field with the Larmor period $T_L = \left(\frac{\mu_B g_F B_{\mathrm{res}}}{h}\right)^{-1}$, where μ_B is the Bohr magneton, and $g_F = 1/4$ the g-factor of the $6s_{1/2}, F = 4$ state. A value of $B_{\mathrm{res}} = 2$ mG for the residual magnetic field leads to $T_L = 1.4$ ms, which explains why no significant depolarisation of the atomic sample is observed during the 20 µs delay between optical pumping and Rydberg excitation.

Spectra of transitions from the $59p_{3/2}$ state to the $66d_{3/2}$ and $66d_{5/2}$ states are depicted in Fig. 3.4. The asymmetric line profiles result from the combined hyperfine structure of the initial and final states, which is not resolved. However, because the hyperfine coupling constant of the $59p_{3/2}$ state was independently determined, the hyperfine coupling constants of $A_{\mathrm{hfs},66d_{3/2}} = 2.6(5)$ kHz and $A_{\mathrm{hfs},66d_{5/2}} = 0.10(45)$ kHz can be extracted.

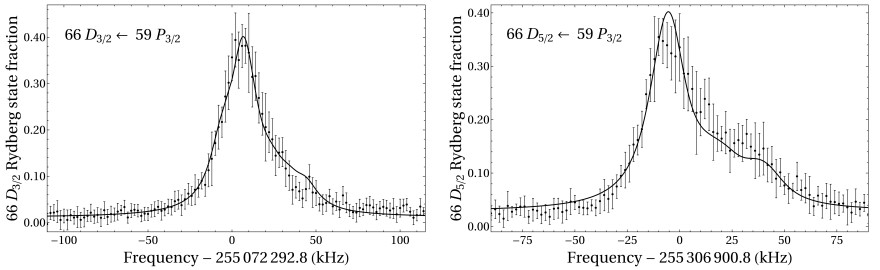

Figure 3.4: Experimental and simulated spectra of millimetre-wave transitions from the $59p_{3/2}$ Rydberg state to the $66d_{3/2}$ and $66d_{5/2}$ states of cesium.

3.1.4 Zeemann effect of high Rydberg states

This subsection is dedicated to an investigation of the Zeeman effect in high Rydberg states, which was studied using millimetre-wave spectroscopy with the example of the $49s_{1/2} \leftarrow 45p_{3/2}$ transition. Care was taken to apply magnetic fields of well-defined strength and direction. The resolution of the millimetre-wave spectra presented in this subsection was limited to ∼ 50 kHz by the applied effective millimetre-wave pulse length of 20 µs .

The Zeeman effect of high Rydberg states has been studied previously, *e.g.*, by Ryabtsev and Tret'yakov [135] in sodium for fields about 7 G. Unlike the Stark effect, the Zeeman effect in Rydberg states has no strong dependence (see Eq. (3.3)) on

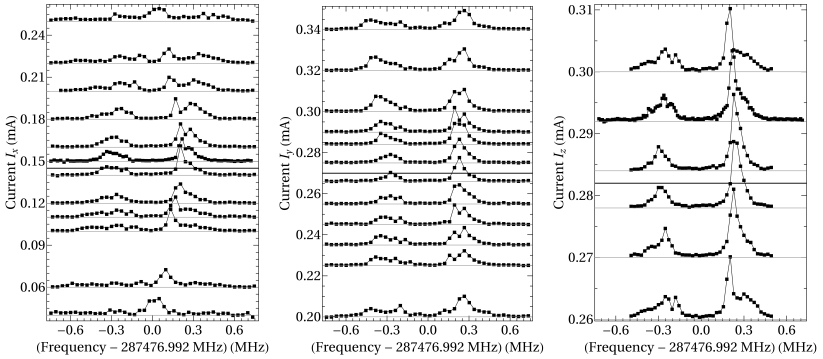

Figure 3.5: Compensation of magnetic stray fields with the example of the $49s_{1/2} \leftarrow 45p_{3/2}$ millimetre-wave transition of Cs. The magnetic field along the x, y and z axis (left-, middle- and right-hand-side panel, respectively) was changed by varying the currents applied to the respective magnetic compensation coils. In each panel, the spectra have been shifted along the vertical axis by a value corresponding to the applied current in mA. The horizontal line in each panel indicates the current at which the stray magnetic field is compensated.

the principal quantum number n and is consequently similar to that in the ground-state of Cs. However, the relative strength compared to the hyperfine interaction depends on n because the magnetic-dipole hyperfine coupling strength decreases with $(n^*)^{-3}$. Consequently, the "strong-field" regime is already reached at small values of the magnetic-field strength in high Rydberg states. In Ref. [135], the magnitude of the Zeeman splittings was comparable to the fine-structure splitting of the $37p_{3/2}$ state in sodium and the hyperfine structure of the Rydberg states was neglected. Here, the high spectral resolution of the experiment enables the observation of the Zeeman effect of Rydberg states at $n = 49$ in a low-field regime where the Zeeman shifts are comparable to the hyperfine splittings.

Using the magnetic compensation coils introduced in Chapter 2, the stray magnetic field of $\sim 550\,\mathrm{mG}$, which is attributed to earth's magnetic field ($\sim 480\,\mathrm{mG}$ on the ground around Zürich [136]) and magnetic fields emanating from the experimental equipment (especially the BWO containing a 2 T permanent magnet placed at $\sim 40\,\mathrm{cm}$ distance from the sample), was compensated to $\sim 2\,\mathrm{mG}$. Millimetre-wave spectra of the $49s_{1/2} \leftarrow 45p_{3/2}$ transition were recorded in magnetic fields of various strengths applied along the laboratory-fixed x, y and z axes. These spectra are presented in the three panels of Fig. 3.5. The amplitude offset of the spectra depicted in Fig. 3.5 corresponds to the current I_d send through the coils aligned along the d axis. The currents of $I_x = 145\,\mathrm{mA}$, $I_y = 270\,\mathrm{mA}$ and $I_z = 282\,\mathrm{mA}$ corresponding to the smallest magnetic fields in the photoexcitation region (see horizontal lines in Fig. 3.5) are determined by comparing the measured spectra to calculated line-shape functions (see Section 3.1.2

and Fig. 3.6). These magnetic-stray-field–compensation currents were applied during all measurements presented in the previous section.

The data presented in the left-hand-side panel of Fig. 3.5 is compared in Fig. 3.6 to a simulation based on the model presented in Section 3.1.2. The qualitative agreement shows that the effects of small magnetic fields on high Rydberg states can be reliably modelled. When the stray magnetic field is compensated to ∼2 mG, the Zeeman effect is not expected to have any influence on the results of laser-spectroscopic experiments, even those carried out at a spectral resolution of ∼1 MHz (see Chapters 4 and 6 and in Section 3.2 described below).

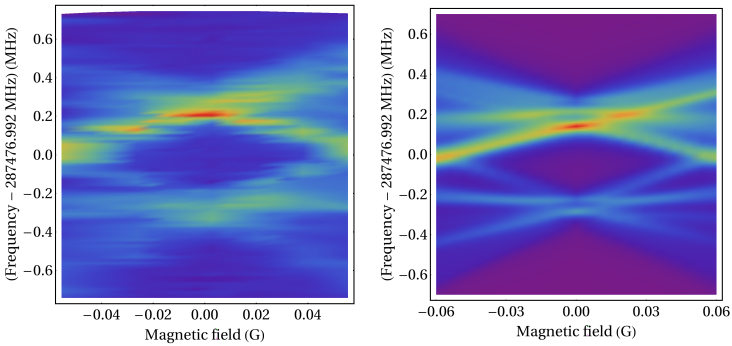

Figure 3.6: Millimetre-wave spectra of the $49s_{1/2} \leftarrow 45p_{3/2}$ transition recorded for different values of the magnetic field applied along the x axis. The spectra are presented in a 2-dimensional colour plot, where the x and y axes correspond to the magnetic-field strength and the frequency of the millimetre-wave radiation, respectively, and the colour indicates the Cs^+-ion signal resulting from pulsed field ionisation of $49s_{1/2}$ Rydberg atoms. The horizontal stripes in the panel on the left-hand side are an artefact of the interpolation of the experimental data. The panel on the left-hand side shows the experimental data and the panel on the right-hand side shows a simulation based on the model described in Section 3.1.2.

3.2 Absolute-frequency measurement of $n\mathrm{p}_{1/2}$ and $n\mathrm{p}_{3/2}$ Rydberg states

Ionisation energies represent important thermochemical quantities and serve as reference data to test *ab-initio* quantum chemical calculations of atomic and molecular structure. Numerous methods can be employed to measure ionisation energies, including photoelectron spectroscopy in numerous variants [137, 138], photoionisation spectroscopy [139–141], photodetachment microscopy [142], and Rydberg-state spectroscopy in combination with Rydberg-series extrapolation [143].

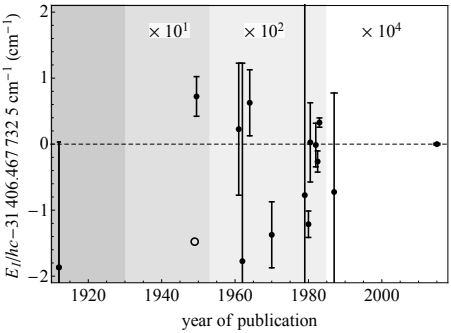

Figure 3.7: History of measurements of the first ionisation energy of ^{133}Cs. Shown is the deviation of values reported in Ref. [116, 144–146] from the value determined in this work. Error bars indicate the 1σ uncertainties given in the respective references. Open symbols indicate that no uncertainty was given. For clarity, the regions shaded in different shades of gray have been scaled differently as indicated at the top of each region.

In this section, a determination of the first ionisation energy of ^{133}Cs at an accuracy of 40 kHz (see Fig. 3.7) is presented. This determination is based on high-resolution single-photon measurements of the Rydberg spectrum from the ground $6s_{1/2}$ state using an ultracold Cs sample and a frequency-comb-based calibration procedure. The ionisation energy is then obtained by extrapolation of the Rydberg series. The most precise determination of the ionisation energy prior to this work was that reported by Weber and Sansonetti [122], who also presented a complete overview of measurements of the ionisation energy of Cs before 1987.

3.2.1 Experiment

The experiments are performed using a sample of ultracold ^{133}Cs atoms, released from a far-off-resonant optical dipole trap (ODT) inside an ultrahigh-vacuum chamber. The small size of typically $\sim$ 150 µm full width at half maximum (FWHM) of the sample in the ODT reduces the influence of electric-field gradients on the measured transition frequencies. Typical samples contain $4 \cdot 10^5$ atoms and have a translational temperature of 70 µK and a peak density of $6 \cdot 10^{10}$ cm^{-3}. Details of the experimental setup can be found in Chapter 2. Only the aspects relevant for the measurements presented in this section are presented here. The electric field is controlled by a set of eight electrodes in the vacuum chamber, which allows for independent adjustment of the field in all three spatial directions. Stray electric fields are canceled by using a procedure based on the measurement of the quadratic Stark effect of $np_{3/2}$ Rydberg states (see Section 2.7). The procedure is repeated regularly (at least daily) to ensure that residual electric fields never exceed 1 mV/cm. Similarly, stray magnetic fields

are measured by radio-frequency (RF) recordings of the $F = 4 \leftarrow F = 3$ transition in the $6s_{1/2}$ ground state of Cs and are reduced to below 2 mG by three external pairs of coils as described in Section 2.7.

The atoms in the ODT are first prepared in the upper hyperfine component of the $6s_{1/2}$ ground state ($F = 4$) by spatially-selective optical pumping. They are then excited in a single-photon transition to np_J ($J = 1/2, 3/2$) Rydberg states. A Cooper minimum in the photoexcitation cross section from the $6s_{1/2}$ ground state of Cs to the $np_{1/2}$ Rydberg states just above the ionisation threshold leads to a strong reduction of the absorption cross section for these states at high values of n [147]. The power and the pulse length of the excitation laser is increased to compensate for this effect.

For $n \geq 42$, the Rydberg atoms are detected by switching the electric potential at an additional electrode to a high value, which field ionises the Rydberg atoms and accelerates the resulting ions toward a micro-channel-plate detector [148]. The detector signal is recorded with a digital-storage oscilloscope. The digitised trace is transferred to a computer and is analyzed by a peak-finding algorithm to determine the number of detected ions. At values of n lower than 42, field-ionisation is not efficient in the same configuration of applied electric potentials. An additional delay of 100 µs is introduced between excitation and the application of the pulsed potential. During this delay, Rydberg atoms can spontaneously ionise and the resulting ions are then extracted and detected as described above. Possible ionisation mechanisms include direct ionisation by black-body radiation or black-body-radiation-enhanced field ionisation [72], interaction-induced Penning-ionisation of pairs of Rydberg atoms [65], and collisions between Rydberg atoms and hot atoms from the background gas in the chamber.

For the here presented precise measurement of the transition frequencies to np Rydberg states, the continuous-wave UV laser system described in Section 2.4.1 was employed. Laser radiation at wavelengths around 319 nm with a spectral bandwidth of less than 1 MHz is obtained by stabilising the laser frequency to an external reference cavity and a wavelength meter as explained in Section 2.5.2. The central frequency of the narrow-bandwidth UV radiation is determined to an absolute accuracy of better than 60 kHz by measuring the laser frequency using an optical frequency comb (see Section 2.5.3). The continuous UV light is chopped into short pulses of 3 to 20 µs length using the negative first diffraction order of an acousto-optic modulator (AOM) in single-pass configuration. The RF signal driving the AOM is derived from a stable quartz oscillator at 110.000(1) MHz. Its frequency was repeatedly controlled by recording and analyzing RF-leakage signals with an antenna and a Fast-Fourier transformation on a digital oscilloscope (LeCroy WaveRunner 604Zi, specified clock accuracy at time of measurement: 4 ppm).

3.2.2 Line-shape model and transition frequencies

The experimentally observed line widths are on the order of 1.2 MHz (FWHM). Possible contributions to the widths are the spontaneous decay of the Rydberg states, the Doppler broadening of the transitions, inhomogeneous broadening caused by residual electric fields, broadenings induced by Rydberg-Rydberg-interactions, the hyperfine splitting of the Rydberg states, and the bandwidth of the excitation radiation. The natural line widths of transitions to np Rydberg states scale with the principal quantum number n approximately as n^{-3} and are less than 10 kHz for $n \geq 27$ [73]. Their contributions to the experimental line widths are thus negligible. The motion of the atoms resulting from the finite temperature of the sample causes a homogeneous Doppler broadening of the transitions in the ultraviolet with an estimated FWHM of 600 kHz.

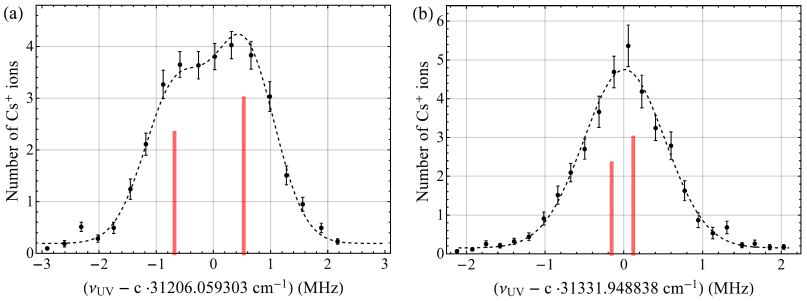

Figure 3.8: (a) Spectrum of the $27p_{1/2} \leftarrow 6s_{1/2}(F = 4)$ transition with partially resolved hyperfine structure: (red lines) Positions and relative weights of hyperfine components, (dashed line) fit of the line model of Eq. (3.5) to the raw data, (black points) binned raw data for visualisation (error bars show the standard error of the mean). (b) Spectrum of the $42p_{1/2} \leftarrow 6s_{1/2}(F = 4)$ transition with unresolved hyperfine structure. Legend as in (a).

Because the polarisability of Rydberg states with non-zero quantum defect scales as n^7 [149], the inhomogeneous line broadening resulting from electric-field gradients is most severe at high n values. The same holds for inhomogeneous broadenings by Van der Waals interactions between Rydberg atoms, which scale as n^{11} [149] and with the Rydberg-atom density ρ as ρ^2. After reducing the number of excited Rydberg atoms per shot to below 10 atoms, an almost constant line width in the range $27 \leq n \leq 74$ is observed. A significant contribution from these two mechanisms to the observed line widths can thus be excluded.

The hyperfine interaction is a Fermi-contact-type interaction and the coupling strength scales as n^{-3}. In the case of Cs, the nuclear spin ($I = 7/2$) and the magnetic-

dipole hyperfine coupling constants are large ($A_{6s_{1/2}} = 2.298\,157\,942\,5$ GHz) [124], leading, at the experimental resolution, to significant hyperfine splittings even for high Rydberg states, as demonstrated in the Section 3.1. Using experimentally determined hyperfine splittings for selected $np_{1/2}$ states from Ref. [116] and for $np_{3/2}$ states from Ref. [148], the hyperfine coupling constants A_{hfs} of the investigated Rydberg states are predicted. For $27p_{1/2}$, the $F = 3$ to $F = 4$ interval is 1.2 ± 0.1 MHz and for $27p_{3/2}$ the $F = 3$ to $F = 5$ interval is 0.6 ± 0.1 MHz. The hyperfine structure must thus be taken into account explicitly at least for lower values of n. Weighting the different hyperfine transitions by their statistical factor of $(2F + 1)$ results in the following line-shape model

$$g(\nu) \propto \sum_F (2F+1) \exp\left(-\frac{(\nu - \nu_F - \nu_0)^2}{2\sigma^2}\right) \tag{3.5}$$
$$\nu_F = \frac{A_{\mathrm{hfs}}}{2} F(F+1) - \frac{A_{\mathrm{hfs}}}{4}\left(F_<^2 + F_> (F_> + 2)\right),$$

which includes all hyperfine components of a given transition. In Eq. (3.5), A_{hfs} is the magnetic-dipole coupling constant, $F_<$ ($F_>$) is the smallest (largest) allowed value of the quantum number F, ν_0 is the centre of gravity of the hyperfine structure, and the residual width σ accounts for the finite bandwidth of the excitation laser and the Doppler width of the transition. The central frequency ν_0 and the residual width σ are the only free parameters of this model. The partially resolved hyperfine structure of the $27p_{1/2} \leftarrow 6s_{1/2}(F = 4)$ transition allows us to confirm the validity of the line-shape model, see Fig. 3.8 (a). This model is then also applied to resonances with non-resolved hyperfine structures, see Fig. 3.8 (b). For transitions from the $6s_{1/2}(F = 4)$ state to $np_{3/2}$ states, only the optically accessible hyperfine components $F = 3 - 5$ are considered in the line-shape model. The hyperfine shift $\nu_{6s_{1/2}(F=4)}$ of the hyperfine component of the $6s_{1/2}$ ground state with $F = 4$ is taken into account by adding $\nu_{6s_{1/2}(F=4)} = 4.021\,776\,4$ GHz to the observed transition frequencies.

In order to determine the frequency of a given $np_j \leftarrow 6s_{1/2}$ transition, the laser frequency is scanned stepwise over the resonance and typically 150 consecutive excitation-detection cycles are performed at each position. Without prior averaging, the model of Eq. (3.5) is fitted to the raw data using a non-linear least-squares-fit algorithm. For several transitions, the transition frequencies are determined up to five times in separate measurements. This procedure yields the most reliable estimate of typically 60 kHz for the statistical uncertainty of the determination of the transition frequencies ν_0. This corresponds to approximately $1/20^{\mathrm{th}}$ of the typical experimental line width. The wavenumbers of all observed transitions are listed in Table 3.1. They are in agreement with the respective transition wavenumbers reported in Ref. [122] within the stated uncertainties, but are more precise by about two orders of magni-

Table 3.1: Wavenumbers $\tilde{\nu}$ (in cm^{-1}) and fit residuals δ_{fit} (in kHz, see Sect. 3.2.4) of all observed transitions to $np_{1/2}$ and $np_{3/2}$ Rydberg states with respect to the centre of gravity of the $6s_{1/2}$ ground state. In case a transition was measured several times the mean of all determined wave numbers and fit residuals, weighted by the statistical uncertainties of the fit of Eq. (3.5), is considered. The estimated standard deviation of all line positions is $2 \cdot 10^{-6}$ cm^{-1}.

n	$\tilde{\nu}_{p1/2}$ / cm^{-1}	δ_{fit} / kHz	$\tilde{\nu}_{p3/2}$ / cm^{-1}	δ_{fit} / kHz
27	31 206.189 769 8	14	31 206.744 750 5	−3
30	31 249.111 102 0	−27	31 249.497 750 0	35
33	31 279.579 380 2	−35	31 279.859 432 4	−49
36	31 301.984 579 8	12	31 302.193 882 3	43
39	31 318.939 791 8	32	31 319.100 300 8	15
42	31 332.079 304 8	−10	31 332.205 082 9	11
45	31 342.467 758 4	42	31 342.568 141 1	−24
47	31 348.229 448 9	43	31 348.316 589 8	−83
50	-	-	31 355.586 932 3	−20
54	-	-	31 363.336 799 2	22
56	31 366.514 426 8	−14	31 366.563 956 6	−18
59	31 370.723 748 8	44	31 370.765 664 1	49
62	31 374.301 268 8	−17	31 374.337 055 9	59
64	31 376.395 953 5	−6	31 376.428 301 8	9
66	31 378.292 494 8	−56	31 378.321 835 7	51
70	31 381.584 461 0	−110	31 381.608 817 4	70
74	31 384.331 466 9	−36	31 384.351 900 1	−17

tude.

3.2.3 Systematic frequency shifts

All measurements are performed with samples released from an ODT. As explained in Chapter 2, the residual IR light of 0.30 W of the optical dipole trap induces a shift $\Delta_{ODT}(0.30\ W) = 0.485(16)$ MHz of the $np_{3/2} \leftarrow 6s_{1/2}$ transition frequencies that is independent of the principal quantum number n. The value of Δ_{ODT} is subtracted from all measured transition frequencies.

The AC-Stark shift induced by the excitation laser was found to be negligible by varying the power of this laser while maintaining the same number of excited Rydberg atoms by either adapting the length of the excitation laser pulse or the number of ground-state atoms. The positions of the Rydberg levels are also shifted by the AC-Stark effect induced by the thermal radiation from the room-temperature environment. However, the magnitude of this effect, measured to be about 2.4 kHz at $T = 300$ K [71], is negligible compared to the uncertainties of the measurements.

Rydberg states of atoms in dense gases experience a pressure shift resulting from collisions of the Rydberg electron with ground-state atoms located within the electron

orbit [36, 37], which arises from the same interaction that leads to long-range Rydberg molecules discussed in Chapter 4. For a maximal ground-state-atom density of 10^{11} cm^{-3} and a triplet s-wave scattering length of $a_T = -21.7\ a_0$ (see Chapter 4 and also Refs. [65, 150]), an upper limit for the pressure shift is estimated to -13 kHz at high values of n. Reducing the ground-state-atom density by a factor of two did not lead to observable shifts of the transition frequencies at $n = 74$ and, thus, a possible pressure shift is neglected.

Electric-field gradients and long-range Van der Waals interactions do not only lead to a line broadening, as discussed above, but also to a shift of the observed line centres. Electric-field gradients always lead to a shift of $np_j \leftarrow 6s_{1/2}$ transition frequencies to lower values, whereas the interaction-induced shift of np states is positive for $n < 42$ and negative for $n \geq 42$ (see Ref. [151] and Chapter 5). Although no systematic shifts were observed when varying the experimental parameters (*e.g.* the number of Rydberg atoms), line shifts up to $\sigma_{\mathrm{ryd}} = 20$ kHz at the highest values of n cannot be excluded.

3.2.4 Ionisation energy and quantum defects of np$_{1/2,3/2}$ series in Cs

The term values of the Rydberg levels of Cs are accurately described by the extended Ritz formula [152]

$$\tilde{\nu}_{n\ell j} = \frac{1}{hc}E_{\mathrm{I}} - \frac{R_{\mathrm{Cs}}}{n^{*2}} = \frac{1}{hc}E_{\mathrm{I}} - \frac{R_{\mathrm{Cs}}}{\left(n - \delta_{\ell j}(n)\right)^2}, \tag{3.6}$$

with

$$\delta_{\ell j}(n) = \delta_{0,\ell j} + \frac{\delta_{2,\ell j}}{\left(n - \delta_{\ell j}(n)\right)^2} + \frac{\delta_{4,\ell j}}{\left(n - \delta_{\ell j}(n)\right)^4} + \cdots, \tag{3.7}$$

where E_{I} is the lowest ionisation energy of Cs, R_{Cs} is the reduced Rydberg constant of Cs, and $\delta_{\ell j}(n)$ are the energy-dependent quantum defects of the respective series. Using the currently recommended values of fundamental constants [153] and the Cs mass [154], the Rydberg constant of the Cs atom is obtained as $R_{\mathrm{Cs}} = 109\,736.862\,733\,9(6)$ cm^{-1}. A global fit based on Eq. (3.6) was performed to all measured transition wavenumbers (weighted by their statistical uncertainties) by truncating the expansion of the energy-dependent quantum defects after the linear term:

$$\delta_{\ell j}(n) = \delta_{0,\ell j} + \frac{\delta_{2,\ell j}}{\left(n - \delta_{0,\ell j}\right)^2}. \tag{3.8}$$

Table 3.2: Quantum-defect expansion coefficients for the np series of Cs determined from a global fit to the observed transitions. The uncertainties are the statistical standard deviations extracted from the global fit.

	$np_{1/2}$	$np_{3/2}$
δ_0	3.591 587 1(3)	3.559 067 6(3)
δ_2	0.362 73(16)	0.374 69(14)

Note the replacement of $\delta_{\ell j}(n)$ by $\delta_{0,\ell j}$ in the denominator of the δ_2 term. As Drake *et al.*[155] discuss, this modified expression allows for a simultaneous fit of the quantum defects and the ionisation energy at the cost of a loss of physical meaning for the expansion coefficients $\delta_{k,\ell j}$. However, it was verified that an iterative fit of the quantum defects using Eq. (3.7) (restricted in the expansion to δ_0 and δ_2) to the data leads to results identical to the ones obtained by the global fit using Eq. (3.8) within the experimental uncertainty. It was also verified that the inclusion of higher-order terms in Eq. (3.7) (*i.e.*, $\delta_{4,\ell j}$, $\delta_{6,\ell j}$, ...) does not reduce the residuals of the global fit.

The first ionisation energy of Cs resulting from the fit is

$$E_{\mathrm{I,Cs}} = hc \cdot 31\,406.467\,732\,5(14)\,\mathrm{cm}^{-1}$$

where the quoted uncertainty is found by adding σ_{ryd} and the statistical uncertainties of E_{I} and Δ_{ODT} in quadrature. This result is in agreement with the ionisation energy reported by Weber and Sansonetti [122] ($hc \cdot 31\,406.467\,66(15)\,\mathrm{cm}^{-1}$), however, its uncertainty is reduced by two orders of magnitude. The parameters for the expansion of the quantum defect (Eq. (3.8)) are given in Table 3.2. A direct comparison with previously reported values is difficult because of the different orders in the series expansion of the quantum defects. However, the transition frequencies predicted by combining our values for the ionisation energy with the quantum defects reported in Ref. [122] for the $np_{1/2}$ series deviate from our experimental observations by up to 200 kHz for the lowest $n \sim 30$, which is significantly more than the residuals obtained with the quantum defects of Table 3.2 (see Fig. 3.9).

All residuals δ_{fit} of the global fit (see Fig. 3.9) are below 10% of the experimental line width. The standard deviations of the transition frequencies, extracted from the fits of Eq. (3.5) to the raw data, seem to underestimate the true uncertainties by roughly a factor of two. They are nevertheless a good measure of the quality of the fit, justifying their use as weights in the global fit. The standardised fit residuals are almost symmetrically distributed around zero, which indicates that the systematic shifts discussed in Sec. 3.2.3 are small. The estimated statistical uncertainties of the parameters obtained from the global fit are dominated by correlations between the values of the parameters. If the quantum defects obtained from the global fit

are used to calculate the ionisation energy separately from every observed transition using Eq. (3.6), an estimate for the error of the average value of about $2.5 \cdot 10^{-7}\,\mathrm{cm}^{-1}$ is obtained, *i.e.* four times smaller than the uncertainty of $E_{\mathrm{I,Cs}}$ resulting from the global fit.

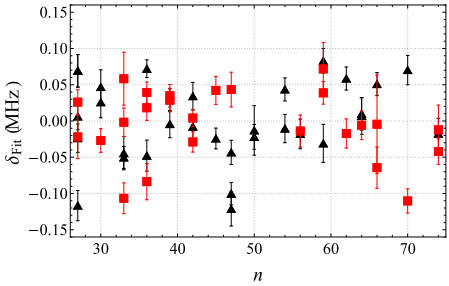

Figure 3.9: Fit residuals of the global fit based on Eq. (3.6) and (3.8) to the observed frequencies of the $n\mathrm{p}_{3/2} \leftarrow 6\mathrm{s}_{1/2}$ (black triangles) and $n\mathrm{p}_{1/2} \leftarrow 6\mathrm{s}_{1/2}$ (red squares) transitions. The error bars give the estimated standard deviations of the centre frequencies resulting from the fit of Eq. (3.5) to the raw data (see Sec. 3.2.2).

3.3 Quantum defects for $n\mathrm{s}_{1/2}$ and $n\mathrm{d}_{3/2,5/2}$ Rydberg series of Cs

In the previous section (see also Ref. [148]), frequency measurements of interseries transitions (*i.e.* $\mathrm{p}_{3/2} \rightarrow \mathrm{s}_{1/2}$ and $\mathrm{p}_{3/2} \rightarrow \mathrm{d}_{3/2,5/2}$) using millimetre-wave radiation were reported. The values of selected intervals, for which the transition frequency relative to the centre of gravity of the hyperfine-split resonances could be determined with an absolute accuracy of 10 kHz, are summarised in Table 3.3. By combining these intervals, the observed transition frequencies to the $n\mathrm{p}_{3/2}$ states from Table 3.1, and the ionisation energy determined above, the binding energies $t^{b}_{n,\ell j} = \tilde{\nu}_{n\ell j} - \frac{E_{\mathrm{I}}}{hc}$ of several $n\mathrm{s}_{1/2}$ and $n\mathrm{d}_{5/2}$ Rydberg states are obtained and listed in Table 3.3. Binding energies are less sensitive to absolute calibration errors than transition frequencies and are best suited to combine measurements from different sources. The binding energies for the transitions to the $n\mathrm{s}_{1/2}$ and $n\mathrm{d}_{5/2}$ series are extracted from Ref. [122] by subtracting the ionisation energy of the respective series from the reported transition energies. Using these binding energies and the binding energies of Table 3.3 with their respective uncertainties ($\sigma = 2 \cdot 10^{-4}$ cm^{-1} for data from Ref. [122] and $\sigma = 2 \cdot 10^{-6}$ cm^{-1} for our data), the energy dependence of the quantum defects (Eq. (3.7)) is determined in a non-linear least-squares fit. To reach convergence of the

Table 3.3: Interseries intervals from determined by high-resolution millimetre-wave spectroscopy [148], and binding energies of the final Rydberg state obtained as described in the text.

Transition $f \leftarrow i$	Interval / MHz	$t^b_{n_f,\ell_f j_f}$ / cm^{-1}
$49s_{1/2} \leftarrow 45p_{3/2}$	287 476.992(10)	−54.310 390 4
$68s_{1/2} \leftarrow 59p_{3/2}$	265 898.688(10)	−26.832 644 6
$81s_{1/2} \leftarrow 67p_{3/2}$	261 818.142(10)	−18.532 264 3
$90s_{1/2} \leftarrow 72p_{3/2}$	257 008.756(10)	−14.854 382 7
$66d_{5/2} \leftarrow 59p_{3/2}$	255 306.920(10)	−27.185 947 9

Table 3.4: Quantum-defect expansion coefficients of the $ns_{1/2}$ and $nd_{5/2}$ series obtained by combining data from Ref. [122] (for $11 \le n \le 31$ and $9 \le n \le 36$, respectively) and the measurements presented here (see text for details). The quoted uncertainties are the estimated standard deviations from the fit.

	$ns_{1/2}$	$nd_{5/2}$
δ_0	4.049 353 2(4)	2.466 314 4(6)
δ_2	0.239 1(5)	0.013 81(15)
δ_4	0.06(1)	−0.392(12)
δ_6	11(7)	−1.9(3)
δ_8	−209(150)	

fit residuals, it was necessary to include higher-order terms up to δ_8 in the expansion, although the values of several parameters, such as $\delta_4 - \delta_8$ for the $ns_{1/2}$ series, remain poorly defined. The values of the fitted parameters are listed in Table 3.4. These parameters simultaneously reproduce the high-resolution data obtained in the measurements presented in Section 3.1 (see also Table 3.3) within the experimental uncertainty and the transition frequencies of Ref. [122] with a similar sum of squared errors as the parameters reported in Ref. [122].

3.4 Conclusions

In a first set of measurements, the hyperfine structure of $ns_{1/2}$ Rydberg states of Cs within the range $n = 45 - 90$ could be resolved using millimetre-wave spectroscopy of transitions between high Rydberg states of Cs. From the modelling of the experimental spectra, magnetic-dipole coupling constants for the hyperfine structure of the $ns_{1/2}$ and $np_{3/2}$ states were obtained which are in agreement with measurements at lower n values. To achieve the required resolution, electric and magnetic stray fields of 250 mV/cm and 560 mG were compensated to residual fields below 1 mV/cm and 2 mG, respectively. The experiments exploited the fact that the factors usually

limiting the resolution of spectroscopic measurements are negligible in our setup. Indeed, the Doppler broadening is well below 1 kHz in samples of ultracold atoms in the millimetre-wave range of the electromagnetic spectrum. Moreover, the low temperature of the atomic sample enables measurement times extending beyond 100 μs. The control over the stray electric and magnetic fields demonstrated in this chapter was essential for the determination of the hyperfine structure of Rydberg states of Cs at high n values and to avoid a significant depolarisation of the atomic sample over a time scale of up to 60 μs. This field control is also essential for the experiments described in the following chapters of this thesis, which focus on weak interaction effects that would be either unobservable or strongly modified in the presence of the uncompensated stray fields.

In a second set of experiments, the lowest ionisation energy of ^{133}Cs was determined to be $E_\mathrm{I} = hc \cdot 31\,406.467\,732\,5(14)$ cm^{-1} with a relative uncertainty of $5 \cdot 10^{-11}$, using narrow-bandwidth UV-laser radiation and a frequency-comb-based frequency-calibration procedure. The uncertainty of ∼ 50 kHz is two orders of magnitude smaller than the best previous result [122] and is limited by experimental sources of error and to a lesser extent by correlations of the parameters in the quantum-defect model of the Rydberg-atom term values and the ionisation energy. The experimental uncertainties, especially those resulting from the laser bandwidth and from the determination of the residual AC Stark shifts of the atoms in the ODT, might be reduced by a factor of at least three by using a UV laser with a narrower bandwidth than the laser available for the present investigation, and by performing the experiment with a small sample of atoms in a completely field-free environment. The correlations of the parameters in the global fit might be reduced by increasing the number of fitted Rydberg series to include, *e.g.*, $n\mathrm{s}_{1/2}$ and $n\mathrm{d}_{3/2,5/2}$, for which unfortunately no data of comparable precision is available. The analysis also resulted in improved energy-dependent quantum defects for the $n\mathrm{s}_{1/2}$, $n\mathrm{p}_{1/2}$, $n\mathrm{p}_{3/2}$, and $n\mathrm{d}_{5/2}$ series of Cs.

These results demonstrate that ionisation energies can be determined with a precision of $1.4 \cdot 10^{-6}$ cm^{-1} (46 kHz) by combining (ultra)cold atoms, frequency-comb-based calibration and Rydberg-series extrapolation. Given the improvement margins of the experiment, a precision on the order of 10 kHz seems possible in the near future.

Cs presents distinct advantages for a precise measurement of ionisation energies. It can be easily laser cooled to sub-mK temperatures; its first ionisation is reachable from the ground state with a single UV photon; its large mass reduces the Doppler broadening, and the closed-shell nature of the Cs^+-ion core facilitates the Rydberg-series extrapolation. It is therefore an ideal system to test experimental precision limits. Unfortunately, Cs possesses too many electrons for being an attractive system for accurate *ab-initio* quantum-chemical calculations in the near future.

On the basis of the results presented in this chapter it can be anticipated that new methods of generating cold samples in few-electron molecules [156, 157] and advances towards extending frequency combs to the far-UV range of the electromagnetic spectrum [158, 159] will soon permit measurements of few-electron molecules with a similar accuracy. The most accurate determination of the ionisation energy in a molecular system, H_2, has an uncertainty of 12 MHz [160] and has stimulated advances in the *ab-initio* calculations of molecular energies including adiabatic, non-adiabatic, relativistic and quantum-electrodynamics corrections [161–163]. Such calculations can now reach an accuracy comparable to that of the experiments. The uncertainty in the electron-proton mass ratio (currently $5.446\,170\,213\,52(52) \cdot 10^{-4}$, *i.e.*, a fractional uncertainty of $9.5 \cdot 10^{-11}$ [153]) imposes a fundamental limit of a few kHz to the accuracy of theoretical determinations of the ionisation energy of H_2 [164]. The results presented in this chapter suggest that precision spectroscopy of Rydberg states of H_2 in combination with Rydberg-series extrapolation has the potential to be even more accurate, and to thus provide a route to determine fundamental constants.

Chapter 4

Long-range Rydberg molecules bound by electron-Cs scattering

4.1 Introduction

Long-range molecular states supported by a Fermi-contact-type potential [37] describing the interaction of a Rydberg electron and a ground-state atom *via* electron–neutral-atom scattering were first predicted by Greene *et al.* [38]. In these states, an atom in its electronic ground state is located inside the large electron orbit of a Rydberg atom with which it interacts *via* the slow Rydberg electron. This binding mechanism does not fit into any of the usual categories of chemical bonds, namely covalent, ionic, metallic or van der Waals [165].

Two main sub-classes of these long-range molecular states were already predicted in Ref. [38]: Molecular states asymptotically correlated to low-l Rydberg states with bond strengths of typically a few MHz, and states correlated to high-l atomic Rydberg states with bond strengths of several GHz for Rydberg states around $n = 30$. Because the binding energies are much lower than the thermal energy at room temperature, the observation of such metastable molecules is only possible through photoassociation of ultracold atoms in the gas phase. Even though the effect of the perturbation of Rydberg series by ground-state atoms was observed early through line broadenings and line shifts [36], the preparation of the long-range Rydberg molecules in well-defined quantum states requires ultracold samples. Experimentally, the long-range Rydberg molecules were first observed through photoassociation of ultracold Rb atoms using $n\mathrm{s}_{1/2} \leftarrow 6\mathrm{s}_{1/2}$ two-photon transitions [40]. Since then, they have also been observed using nd [44, 46] and np [48] Rydberg states of Rb and in Cs [47, 166, 167] and Sr [49]. Molecular resonances originating from electron–neutral-atom scattering were also observed in transitions from the electronic ground state of Rb_2 to np Rydberg states [168]. Further experiments revealed additional proper-

ties of these long-range molecules. Long-range states correlated asymptotically with $ns_{1/2}$ Rydberg states in Rb were found to be bound by internal quantum reflection at a steep drop of the molecular potential towards smaller internuclear separation [41]. Recently, high-l-mixed molecules were observed with very large induced dipole moments [47, 169]. The lifetimes of Rb_2 [170] and Sr_2 [171] molecules have been investigated, and values similar to the parent atomic Rydberg state were found.

Most of the experiments have focused so far on the alkali-metal atoms Cs and Rb, for which singlet and triplet scattering channels for electron-atom scattering exist. Because the singlet scattering length is one order of magnitude shorter than the triplet scattering length in all alkali-metal atoms [150], its effects were initially not observed experimentally and were also neglected in the first theoretical models. Recently, it was pointed out that the hyperfine interaction of the ground-state atom leads to a mixing of singlet and triplet scattering channels in these molecules, giving rise to molecular states in which the binding results from mixed singlet and triplet e^--Cs scattering [39]. These states were predicted to have even weaker binding energies and were first observed in the experiments in Cs [167] described in this chapter and, more recently, also in Rb [50]. The experimental observation of Cs_2 long-range molecules bound by mixed singlet and triplet scattering and their theoretical modelling resulted in the first determination of a zero-energy singlet s-wave scattering length for electron–alkali-metal-atom collisions [167].

This chapter is an adapted version of the article H. Sassmannshausen, F. Merkt, and J. Deiglmayr: "Experimental characterisation of singlet scattering channels in long-range Rydberg molecules", *Phys. Rev. Lett.* **114**, 133201 (2015). The introduction and the final section of this chapter have been adapted from H. Sassmannshausen, J. Deiglmayr, and F. Merkt: "Long-range Rydberg molecules, Rydberg macrodimers and Rydberg aggregates in an ultracold Cs gas", submitted to *Eur. J. Phys. ST*, (2016).

4.2 Model for long-range Rydberg molecules

The total Hamiltonian of long-range Rydberg molecules asymptotically correlated to one atom in a high Rydberg state and one atom in the electronic ground state can be written as

$$\hat{H} = \hat{H}_\mathrm{r} + \hat{H}_\mathrm{g} + V_{\mathrm{r-g}}(\boldsymbol{R}, \boldsymbol{r}) \tag{4.1}$$

with

$$V_{\mathrm{r-g}}(\boldsymbol{R}, \boldsymbol{r}) = V_{\mathrm{Cs-Cs^+}}(\boldsymbol{R}) + V_{\mathrm{e^- - Cs}}(\boldsymbol{R}, \boldsymbol{r}), \tag{4.2}$$

where $\hat{H}_\mathrm{r}$ and $\hat{H}_\mathrm{g}$ are the Hamiltonian operators of the unperturbed Rydberg atom and the ground-state atom, respectively, and $V_{\mathrm{r-g}}(\boldsymbol{R},\boldsymbol{r})$ accounts for the interactions between the two atoms. In Eq. (4.1), $V_{\mathrm{r-g}}(\boldsymbol{R},\boldsymbol{r})$ is expressed as the sum of the interaction terms $V_{\mathrm{e^-\!-Cs}}(\boldsymbol{R},\boldsymbol{r})$ and $V_{\mathrm{Cs-Cs^+}}(\boldsymbol{R})$. $V_{\mathrm{e^-\!-Cs}}(\boldsymbol{R},\boldsymbol{r})$ accounts for the interaction of the Rydberg electron at position $\boldsymbol{r}$ with the ground-state Cs atom at position $\boldsymbol{R}$ (relative to the Cs^+ ion) and $V_{\mathrm{Cs-Cs^+}}(\boldsymbol{R})$ accounts for the interaction of the Cs^+ ion with the neutral Cs atom. The Born-Oppenheimer approximation has been applied to obtain Eq. (4.1), in which R only appears as a parameter. The Born-Oppenheimer approximation is valid, even though the electronic level density is very high and the electronic dynamics is slow in high Rydberg states. Indeed, the nuclear motion in the long-range molecules is still much slower. In high Rydberg states, the Rydberg electron occupies a large and diffuse orbit and the terms in $V_{\mathrm{r-g}}(\boldsymbol{R},\boldsymbol{r})$ can be approximated by their long-range potential forms. Explicit electron-correlation effects are neglected and the interaction is reduced to the long-range interaction of the induced dipole moments of the neutral atoms with the charged particles. The leading long-range term is

$$V_{\mathrm{r-g}}(\boldsymbol{R},\boldsymbol{r}) \approx \frac{|e|^2}{(4\pi\epsilon_0)^2}\cdot\left(-\frac{\alpha_\mathrm{g}}{2|\boldsymbol{r}-\boldsymbol{R}|^4}-\frac{\alpha_\mathrm{g}}{2|\boldsymbol{R}|^4}\right). \tag{4.3}$$

The contribution $V_{\mathrm{Cs-Cs^+}}(\boldsymbol{R}) = \frac{|e|^2}{(4\pi\epsilon_0)^2}\cdot\left(-\frac{\alpha_\mathrm{g}}{2R^4}\right)$ can be estimated from the typical equilibrium internuclear separation in a long-range Rydberg molecule ($R_\mathrm{eq} \approx 2a_0(n^*)^2$, where n^* is the effective principal quantum number). The polarisability $\alpha_\mathrm{g} = 4\pi\epsilon_0 \cdot 59.39(9)\cdot 10^{-30}\,\mathrm{m}^3$ of the ground-state Cs atom is taken from Ref. [172]. $V_{\mathrm{Cs-Cs^+}}(R_\mathrm{eq})$ is depicted in Fig. 4.1 as a function of the principal quantum number of $n\mathrm{p}_{3/2}$ Rydberg states of Cs. For the range of n values considered in this chapter, *i. e.* $n = 26-34$, the contribution of $V_{\mathrm{Cs-Cs^+}}$ is smaller than the laser-excitation bandwidth and is neglected.

The second term of the interaction Hamiltonian, $V_{\mathrm{e^-\!-Cs}}(\boldsymbol{r}-\boldsymbol{R})$, is larger. The polarisability potential is of short range compared to the $1/r$ dependence of the Coulomb attraction between electron and Cs^+ ion and compared to the de Broglie wavelength of the Rydberg electron (at the values of the principal quantum number considered here). This justifies the treatment of the interaction using scattering theory instead of evaluating $V_{\mathrm{e^-\!-Cs}}(\boldsymbol{r}-\boldsymbol{R})$ explicitly. This approach was first suggested and successfully applied by Fermi to describe the effects of ground-state atoms located within Rydberg-electron orbits [37]. The electron–neutral-atom scattering problem is solved using a partial-wave analysis, in which the incoming wave is decomposed into partial waves labelled by the scattering angular-momentum quantum number l. Each partial wave is characterised in good approximation by one parameter, *e.g.*, the s-wave ($l = 0$) scattering length a and the p-wave ($l = 1$) scattering volume. At the classical

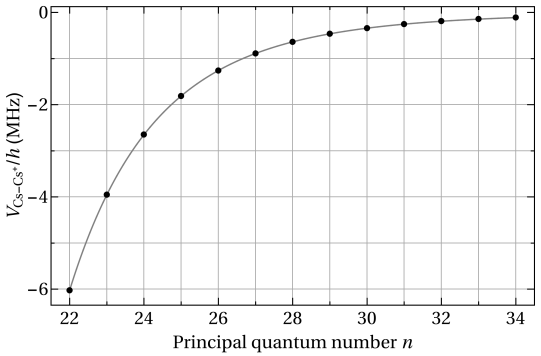

Figure 4.1: Interaction strength of a Cs^+ ion with a Cs atom with polarisability α_g at internuclear separations $R = 2a_0(n^*)^2$ corresponding approximately to the region of the outermost lobe of the radial wavefunction of the Rydberg electron.

turning point of the Rydberg electron, where its kinetic energy vanishes, and beyond, only s-wave scattering needs to be considered, because the centrifugal barriers of higher-l partial waves render the short-range-scattering region inaccessible. Under these conditions, the interaction potential takes the simple form of a Fermi-contact pseudo-potential [37, 38]

$$V_{r-g}(\boldsymbol{R},\boldsymbol{r}) \approx \frac{|e|^2}{(4\pi\epsilon_0)^2} \cdot \left(-\frac{\alpha_g}{2|\boldsymbol{r}-\boldsymbol{R}|^4}\right) \Rightarrow 2\pi a_{S/T}(k)\,\hat{\delta}^3(\boldsymbol{r}-\boldsymbol{R}), \tag{4.4}$$

where $a_{S/T}(k)$ are the singlet (index S) and triplet (index T) energy-dependent s-wave scattering lengths for e^--Cs scattering.

Now, the different terms in the Hamiltonian operators of the unperturbed atoms are considered and their relevance to the theoretical description of long-range Rydberg molecules is accessed. The spin-orbit-interaction and the hyperfine-interaction Hamiltonians, $\hat{H}_{SO}$ and $\hat{H}_{HF}$, respectively, are treated separately for the ground-state atom and the Rydberg atom

$$\hat{H}_r = \hat{H}_{0,r} + \hat{H}_{SO,r} + \hat{H}_{HF,r} \approx \hat{H}_{0,r} + \hat{H}_{SO,r} \tag{4.5}$$

$$\hat{H}_g = \hat{H}_{0,g} + \hat{H}_{SO,g} + \hat{H}_{HF,g} = \hat{H}_{0,g} + \hat{H}_{HF,g}, \tag{4.6}$$

where $\hat{H}_{0,x}$ ($x = g, r$) are the Hamiltonians without spin-orbit and hyperfine interaction terms. For the np Rydberg states with $n > 26$ studied here, the spin-orbit interaction, even though scaling as $A_{SO,r}/n^{*3}$, is still larger than the Fermi-contact interaction in the long-range Rydberg molecules and needs to be considered in the model. The hyperfine interaction, which scales as $A_{HF,r}/n^{*3}$, can be neglected in the

model because it corresponds to splittings of less than 1 MHz (see Section 3.1 and Ref. [148]) for the Rydberg states discussed here and is therefore much weaker than the Fermi-contact interaction. The splittings are also too small to be resolved in our experiments. In the $6s_{1/2}$ electronic ground there is no spin-orbit interaction, but the hyperfine interaction is much stronger than the binding energies of the long-range molecules that are investigated in this chapter.

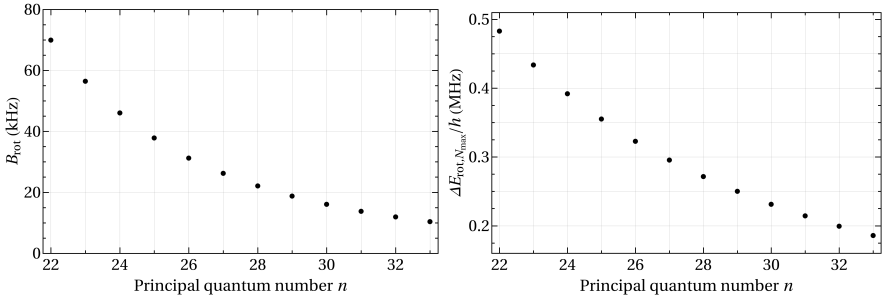

Figure 4.2: Rotational constants B_{rot} (left panel) and maximal rotational energy-level splittings $\Delta E_{\mathrm{rot},N_{\mathrm{max}}}$ (right panel) of long-range Rydberg molecules correlated to Cs $(6s_{1/2})$ + Cs $(np_{3/2})$ dissociation asymptotes as a function of the principal quantum number n.

Implementing these approximations, the total molecular Hamiltonian [39] is written as

$$\hat{H} = \hat{H}_0 + \hat{H}_{\mathrm{SO,r}} + \hat{H}_{\mathrm{HF,g}} + \hat{P}_{\mathrm{S}} \cdot \hat{V}_{\mathrm{S}} + \hat{P}_{\mathrm{T}} \cdot \hat{V}_{\mathrm{T}}, \tag{4.7}$$

where $\hat{H}_0$ is the Hamiltonian of the Rydberg atom without spin-orbit interaction, $\hat{H}_{\mathrm{SO,r}} = A_{\mathrm{SO}} \boldsymbol{\ell}_r \cdot \boldsymbol{s}_r$ is the spin-orbit interaction of the Rydberg electron with angular momentum $\boldsymbol{\ell}_r$ and electron spin $\boldsymbol{s}_r$, and $\hat{H}_{\mathrm{HF,g}} = A_{\mathrm{HF}} \boldsymbol{i}_g \cdot \boldsymbol{s}_g$ is the hyperfine interaction of the ground-state atom with nuclear spin $\boldsymbol{i}_g$ and electron spin $\boldsymbol{s}_g$. Separate terms for singlet (S) and triplet (T) scattering are obtained by using the projection operators $\hat{P}_{\mathrm{S}} = -\boldsymbol{s}_r \cdot \boldsymbol{s}_g + \frac{1}{4} \cdot \hat{\mathbb{1}}$ and $\hat{P}_{\mathrm{T}} = \boldsymbol{s}_r \cdot \boldsymbol{s}_g + \frac{3}{4} \cdot \hat{\mathbb{1}}$ and representing the corresponding Fermi-contact-interaction operators by $\hat{V}_i = 2\pi a_i \hat{\delta}^3(\boldsymbol{r} - R\hat{\boldsymbol{z}})$, with $i = \mathrm{S,T}$, for s-wave scattering between the Rydberg electron at position $\boldsymbol{r}$ and the ground-state atom located at distance R along the molecular z axis [173].

The rotational motion of the long-range molecules is neglected because their rotational constants B_{rot} are below 100 kHz (see left-hand-side panel in Fig. 4.2). Because only low rotational levels, labelled with the rotational angular momentum quantum number N, are accessible in the photoassociation from an ultracold sample (see Eq. (1.3)), the maximal spacings $\Delta E_{\mathrm{rot},N_{\mathrm{max}}}$ between accessible rotational states are only on the order of a few hundred kHz. The rotational constants of the long-range Rydberg molecules have been calculated using the model described in this section and

Table 4.1: Asymptotes and binding mechanism. First column: fine-structure asymptote of the Rydberg atom. Second column: symmetries contributing to the molecular state. Third and fourth column: degeneracies g_3 and g_4 of the molecular states associated with Cs np_j,$6s_{1/2}(F=3,4)$ asymptotes. Last column: s-wave scattering lengths contributing to the binding.

Rydberg asymptote		Contributions	g_3	g_4	Binding via
$np_{1/2}$	$\lvert\omega_r\rvert = 1/2$	$^1\Sigma^+$, $^3\Sigma^+$, $^1\Pi$, $^3\Pi$	8	8	a_S, a_T
		$^3\Sigma^+$, $^1\Pi$, $^3\Pi$	6	10	a_T
$np_{3/2}$	$\lvert\omega_r\rvert = 1/2$	$^1\Sigma^+$, $^3\Sigma^+$, $^1\Pi$, $^3\Pi$	8	8	a_S, a_T
		$^3\Sigma^+$, $^1\Pi$, $^3\Pi$	6	10	a_T
	$\lvert\omega_r\rvert = 3/2$	$^1\Pi$, $^3\Pi$	14	18	—

their values are depicted on the left-hand side of Fig. 4.2. The maximal rotational spacings (assuming photoassociation of two Cs atom in an ultracold gas at a temperature of 40 μK and an internuclear distance corresponding to the Bohr radius of the excited atomic Rydberg state) are presented on the right-hand side of Fig. 4.2. Both $B_{\rm rot}$ and $\Delta E_{{\rm rot},N_{\rm max}}$ decrease with increasing values of the principal quantum number, which is an effect of the increasing bond lengths in the molecules. The rotational spacings are smaller than the experimental resolution for $n > 22$. The results presented in Figs. 4.1 and 4.2 indicate that a simple model of long-range Rydberg molecules, neglecting the interaction between the ion and the ground-state atom as well as the molecular rotation, is suitable for high-n levels at a resolution of ~ 1 MHz and a temperature of 40 μK. More complicated molecular structures are expected when the molecular rotation energy levels become resolvable (for $n < 20$) and the ion–ground-state interaction becomes relevant (for $n < 26$).

To reproduce experimental binding energies, the zero-energy limits of the singlet and triplet energy-dependent scattering lengths (Ref. [174], Eqs. (1,4-6)) are adjusted. The spin-orbit coupling constants $A_{\rm SO}$ are extracted from experimental fine-structure splittings [116] and the hyperfine coupling constant $A_{\rm HFS}$ is taken from Ref. [124]. The Hamiltonian matrix corresponding to Eq. (4.7) is set up in the uncoupled basis $|\ell_r,\lambda_r\rangle\,|s_r,\sigma_r\rangle\,|s_g,\sigma_g\rangle\,|i_g,\omega_{i,g}\rangle$ ($i_g = 7/2$ for ^{133}Cs) for a single np Rydberg state and the energetically closest Rydberg state, $(n-1)$d. The quantum number $\Omega_{\rm tot} \equiv \lambda_r + \sigma_r + \sigma_g + \omega_{i,g}$ of the projection of the total angular momentum on the internuclear axis is a good quantum number. The ground-state atom can be in either of the two $F = 3,4$ ($\boldsymbol{F} \equiv \boldsymbol{i}_g + \boldsymbol{s}_g$) hyperfine levels, and the np Rydberg atom can be in either the $np_{3/2}$ ($\omega_r \equiv \lambda_r + \sigma_r = -3/2, -1/2, 1/2, 3/2$) or the $np_{1/2}$ ($\omega_r = -1/2, 1/2$) spin-orbit levels. The spin-orbit interaction of the Rydberg electron completely mixes the $\lambda_r = 0$ and $|\lambda_r| = 1$ components of the $|\omega_r| = 1/2$ levels, whereas the $|\omega_r| = 3/2$ levels have pure Π character. Because the e^--Cs interaction is restricted to s-wave scattering, only the $\lambda_r = 0$ (Σ^+) components of the Rydberg wavefunction contribute

to the binding [173]. The $|\omega_r| = 3/2$ levels are thus non-bonding and the strength of the bond of the $|\omega_r| = 1/2$ levels is proportional to their $\lambda_r = 0\,(\Sigma^+)$ character. Consequently, the binding energies of long-range molecules asymptotically correlated to Rydberg states with spin-orbit interaction are lowered compared to Rydberg states with pure nl levels without spin-orbit interaction. With spin-orbit interaction, the "total" bond strength of a pure nl level is distributed according to a Clebsch-Gordan coefficient determining the weight of the $\lambda_r = 0$ component of the Rydberg-electron wavefunction. Even though there is no spin-orbit interaction in ns Rydberg states, long-range Rydberg molecules correlated to higher l Rydberg states generally have larger binding energies because of the increasing probability density of the Rydberg electron around the intermolecular axis with increasing angular momentum l, reflected by the $\sqrt{2l+1}$ scaling of the $Y_{l,m_l=0}(\theta = 0)$ angular wavefunctions (see also Ref. [39]).

The selection of the $\lambda_r = 0$ component in the interaction terms $\hat{V}_\mathrm{S}$ and $\hat{V}_\mathrm{T}$ implies that ω_r equals σ_r in all components of the wavefunctions contributing to binding and that s-wave singlet and triplet channels of the e^--Cs scattering interaction are not mixed by $\hat{H}_\mathrm{SO}$. These channels can, however, be mixed by $\hat{H}_\mathrm{HF}$. Remarkably, the eigenstates of Eq. (4.7) form two distinct subgroups, one containing states which do not possess any $^1\Sigma^+$ character (but $^3\Sigma^+$, $^1\Pi$ and $^3\Pi$) and for which the binding is entirely dictated by the triplet s-wave-scattering interaction, and one containing states which possess both $^3\Sigma^+$ and $^1\Sigma^+$ (as well as $^1\Pi$ and $^3\Pi$) character and for which the binding results from both singlet and triplet s-wave scattering interactions. Table 4.1 gives an overview of the character and degeneracy factors of the resulting bound states. For simplicity, the states bound via the $^3\Sigma^+$ component are referred to as $^3\Sigma$ states and those for which the binding results from both $^3\Sigma^+$ and $^1\Sigma^+$ components as $^{1,3}\Sigma$ states. The $^3\Sigma$ states have been observed in previous experiments [40, 46, 168], whereas the $^{1,3}\Sigma$ states are discussed here and in Ref. [167]. They have also recently been observed in Rb_2 [50].

The Cooper minimum in the $n\mathrm{p}_{1/2} \leftarrow 6\mathrm{s}_{1/2}$ photoexcitation cross section of Cs [147] prevents the observation of molecular states correlated to $n\mathrm{p}_{1/2}$ asymptotes and the investigations focus on the states correlated to Cs ($6\mathrm{s}_{1/2}$) + Cs ($n\mathrm{p}_{3/2}$) dissociation asymptotes. Potential-energy curves (PECs) for the long-range molecules are obtained by determining the eigenvalues of the total Hamiltonian (see Eq. (4.7)) as a function of the separation R between the atoms. The mapped Fourier-grid method [175] was used to obtain the vibronic eigenstates of these PECs. The PECs and vibrational wavefunctions of the $26\mathrm{p}_{3/2}$,$^3\Sigma$ and $26\mathrm{p}_{3/2}$,$^{1,3}\Sigma$ states, calculated for parameters derived from the analysis of the spectroscopic data, are depicted in Fig. 4.3.

For the case of the Cs atom and for the other alkali-metal atoms, the triplet electron–neutral-atom scattering lengths are negative and their absolute values are

much larger than those of the singlet scattering lengths, which are positive for all alkali-metal atoms except Cs. Consequently, the s-wave scattering model predicts larger binding energies for the $^3\Sigma$ molecular states than for the $^{1,3}\Sigma$ states. Moreover, $^3\Sigma$ PECs do not depend on the hyperfine state of the ground-state atom, whereas the $^{1,3}\Sigma$ states correlated to the $F = 3$ asymptotes are more strongly bound than the $^{1,3}\Sigma$ states correlated to the $F = 4$ asymptote. The hyperfine state of the ground-state atom thus has an effect on the binding of long-range Rydberg molecules [39]. This effect had not been observed prior to the work presented here.

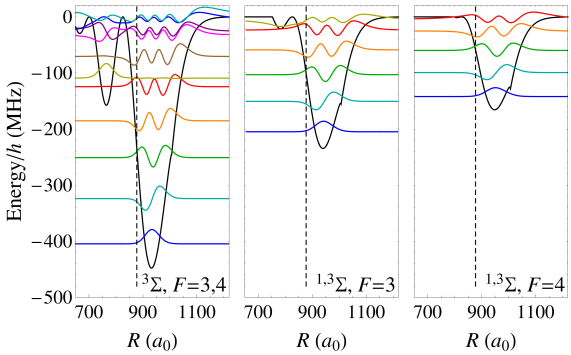

Figure 4.3: Potential-energy curves (black lines) and vibrational wave functions (colored lines) for $^3\Sigma$ states dissociating to the $26p_{3/2}$, $6s_{1/2}(F = 3, 4)$ asymptotes (left panel), $^{1,3}\Sigma$ state dissociating to the $26p_{3/2}$, $6s_{1/2}(F = 3)$ (middle panel), and $26p_{3/2}$, $6s_{1/2}(F = 4)$ (right panel) asymptote. Vertical dashed lines mark the positions where the semiclassical Rydberg-electron kinetic energy equals the energy of the $^3P_0$ Cs-e^- scattering resonance (see text).

4.3 Experiment

The experiments are performed with ultracold samples of Cs atoms released from a vapour-loaded compressed magneto-optical trap (cMOT) (see Chapter 2) at a temperature of 40 μK and a density of 10^{11} cm^{-3}[a]. Temperature and density are estimated on the basis of saturated-absorption images of the ultracold cloud. The preparation of the ultracold sample involves a MOT-loading phase of ∼ 80 ms duration that depends on the repetition rate of typically 10 Hz of the experiment, followed by a compression phase of 10 ms. The magnetic field of the cMOT is switched off and the atoms are cooled during an optical-molasses phase. After 5 ms, magnetic fields caused by eddy

[a]Higher densities of $2 \cdot 10^{12}$ cm^{-3} have been demonstrated in the setup when the atoms are transferred into a crossed far-off-resonance optical dipole trap (FORT) [64]. However, the reduction in atom number is not compensated by the increase in density.

currents have decayed. The atoms are then optically pumped into one of the two hyperfine states ($F = 3, 4$) of the $6s_{1/2}$ electronic ground state and excited to $p_{3/2}$ Rydberg states in single-photon transitions. During the photoassociation experiments, all trapping fields are switched off and stray magnetic and electric fields are suppressed to below 20 mG and 20 mV/cm, respectively.

The UV radiation with a wavelength of about 319 nm necessary to excite high Rydberg states of Cs from the $6s_{1/2}$ ground state is generated with a single-mode cw ring dye laser, the output of which is frequency doubled in a BBO crystal inside an external enhancement cavity. The fundamental frequency of the ring laser is locked to its internal reference cavity, resulting in a bandwith of $\sim$ 3 MHz in the UV. The absolute frequency is calibrated with a wavemeter (HighFinesse, WS-7, 60 MHz accuracy) and relative frequencies with respect to a frequency-stabilised HeNe laser (Thorlabs, 2 mW, stabilised to 2 MHz) are measured with a scanning cavity (see Section 2.5.1). The final calibration accuracy of frequency detunings from the strong atomic transitions is $\sim$ 5 MHz.

This large uncertainty in the relative frequency (which is the direct measure of binding energies in photoassociation experiments) results primarily from the determination of the positions of the saturated and broadened atomic resonances. In the most recent experiments, the frequency of the laser is calibrated using a frequency comb and frequencies relative to atomic Rydberg transitions can be determined to an accuracy better than 100 kHz. The atomic positions are themselves known to an accuracy of $\sim$60 kHz from the quantum defects and the ionisation energy reported in Chapter 3 and Ref. [121]. The improved accuracy is demonstrated in Subsection 4.6.

For the results presented in this section, 40 μs long UV pulses are produced using an electro-optical modulator and the UV-laser beam is focused to a beam-waist radius of $\sim$ 150 μm in the centre of the ultracold Cs atom cloud. All Rydberg-excitation experiments are performed once with all atoms prepared in the $F = 3$ hyperfine component of the $6s_{1/2}$ electronic ground state and once with all atoms pumped to the upper $F = 4$ component. Rydberg atoms and long-range molecules are detected as atomic Cs^+ and molecular Cs_2^+ ions, respectively, on a microchannel-plate (MCP) detector following spontaneous ionisation or pulsed field ionisation. Cs^+ and Cs_2^+ ions are detected separately by setting temporal detection gates at the corresponding positions of the ion-time-of-flight spectrum. On the photoassociation resonances, the spontaneous formation of Cs^+ ions is attributed to Penning ionisation [176], whereas the observation of molecular Cs_2^+ ions is indicative of associative ionisation [177]. The signal strength of the Cs^+ ions relative to the Cs_2^+ ions increases with the density of excited molecules. Most spectra presented in this chapter show the spontaneously formed Cs_2^+ ions because of larger signal-to-noise ratios. However, comparable, though not identical, spectra are obtained when detecting Cs^+ ions resulting

from the field ionisation of Rydberg states (compare Fig. 4.7a) and b)).

4.4 Photoassociation spectra and determination of scattering lengths

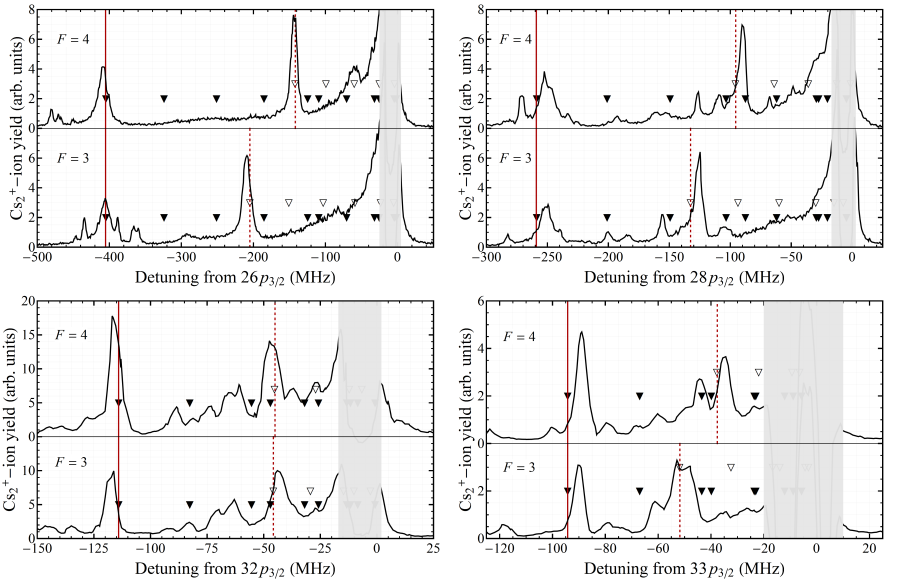

Figure 4.4: Detected Cs_2^+ ions as function of laser frequency near the $np_{3/2}$,$6s_{1/2}(F = 3, 4)$ asymptotes. Solid (dashed) red lines mark the calculated positions of the $v = 0$ levels of $^3\Sigma$ ($^{1,3}\Sigma$) states. Calculated positions of higher vibrational levels are also shown (full and open triangles, respectively). The strongly saturated atomic transitions correspond to the grey areas.

Fig. 4.4 presents photoassociation spectra of Cs atoms prepared in the $F = 3$ and $F = 4$ hyperfine levels to Cs_2 Rydberg molecules correlated to $np_{3/2}$ Rydberg states ($n = 26$, 28, 32, and 33). Several photoassociation resonances are observed on the low-frequency side of the strongly saturated atomic $np_{3/2} \leftarrow 6s_{1/2}$ ($F = 3, 4$) resonances, marked by grey areas. The two most intense photoassociation resonances are assigned to the $v = 0$ levels of the $^3\Sigma$ and $^{1,3}\Sigma$ states, where v denotes the vibrational quantum number. From the positions of the two strongest photoassociation lines in the Rydberg-excitation spectra, the binding energies of the $^3\Sigma(v = 0)$ and $^{1,3}\Sigma(v = 0)$ levels are determined for all n values between 26 and 34. These energies are compared in Fig. 4.5 and in Tables 4.2 and 4.3 to binding energies calculated with the model outlined above after adjustment of the zero-energy

s-wave singlet ($a_{S,0}$) and triplet ($a_{T,0}$) scattering lengths to $a_{T,0} = -21.8 \pm 0.2\ a_0$ and $a_{S,0} = -3.5 \pm 0.4\ a_0$, respectively, in a least-squares fit. If the energy dependence of the scattering lengths is modelled by $a(k) = a_0 + \frac{\pi}{3}\alpha k(R)$ with the ground-state atom polarisability $\alpha = 402.2$ a.u. and the semiclassical electron momentum $k = \sqrt{2/R - 1/n^{*2}}$ [173], the values $a_{T,0} = -20.5 \pm 0.2\ a_0$ and $a_{S,0} = -3.7 \pm 0.4\ a_0$ are found. The fact that the adjustment of only two parameters permits the reproduction of 36 resonances within their experimental uncertainty of 5 MHz leaves no doubt concerning the validity of the assignments. As predicted by the model calculations (see also Fig. 4.3), the positions of the ${}^3\Sigma(v = 0)$ levels are identical for $F = 3$ and $F = 4$ within the experimental uncertainty whereas $(F = 4), {}^{1,3}\Sigma(v = 0)$ levels are less strongly bound than the $(F = 3), {}^{1,3}\Sigma(v = 0)$ levels. An exception is found at $n = 32$, where the ${}^{1,3}\Sigma(v = 0)$ levels correlated to the $32p_{3/2}$, $6s_{1/2}(F = 3)$ and $32p_{3/2}$, $6s_{1/2}(F = 4)$ asymptotes have almost identical binding energies. The effect of this perturbation is also recognisable in the values of the calculated molecular dipole moments, which are listed in the last column of Table 4.2. Whereas the $(F = 4), {}^{1,3}\Sigma(v = 0)$ states typically have dipole moments of about 20 Debye, the ${}^{1,3}\Sigma(v = 0)$ states correlated to the $32p_{3/2}, 6s_{1/2}(F = 4)$ dissociation threshold has a dipole moment of only about 4.5 Debye. The observed irregularity in the binding energies is well described by the model, which indicates that it originates from an accidental perturbation of the $32p_{3/2}, 6s_{1/2}(F = 3)$ state by the almost degenerate $32p_{1/2}, 6s_{1/2}(F = 4)$ state. Indeed, at $n = 32$, the $np_{1/2} - np_{3/2}$ fine-structure splitting, which scales as n^{-3}, almost exactly matches the ground-state hyperfine splitting. The dependence of the ${}^3\Sigma(v = 0)$ binding energies on the effective quantum number n^* deviates from the previously encountered n^{*-6} scaling [40] (see Fig. 4.5). This deviation is also present in the calculated binding energies and is caused by the increasing contribution of higher-order, energy-dependent terms of the s-wave scattering lengths for as n decreases.

The values of the triplet and singlet s-wave scattering lengths are effective, model-based values obtained assuming that p-wave scattering is negligible. This assumption is fulfilled for low electron energies and in the absence of scattering resonances. The lowest p-wave scattering resonance (the ${}^3P_0$ shape resonance in Cs^- [178]) is located at an electron kinetic energy $\frac{p_c^2}{2m_e}$ of 4 meV [166], which is (in a semi-classical description) reached by the Rydberg electron at the critical radius r_c corresponding to $p_c^2 = (-\frac{1}{n^{*2}} + \frac{2}{r_c})$, and marked in Fig. 4.3 for $n = 26$ by vertical dashed lines. Although the minima of the outermost potential wells are located beyond r_c and the $v = 0$ levels should not be strongly affected by p-wave scattering for $n \geq 26$, Fig. 4.3 also indicates that PECs for lower n values and excited vibrational levels of the outermost well should be significantly affected by p-wave scattering channels. We believe this to be the main reason for the inability of the effective s-wave scattering model to reliably

predict the positions of excited vibrational levels, which are marked by triangles in Fig. 4.4, and of further resonances observed in the experiments for $n = 19 - 25$. For the molecular levels below $n = 25$ effects of the ion-ground-state-atom interaction $V_{Cs-Cs^+}(\boldsymbol{R})$ (see Fig. 4.1) could also play a role.

A similar observation was made in studies of long-range ns Rydberg molecules in Rb where pure triplet s-wave scattering was sufficient to describe the observed $^3\Sigma(v = 0)$ binding energies [40], but a more complete model, including p-wave scattering and quantum reflection at short range, was required to reproduce the positions of excited vibrational levels [41].

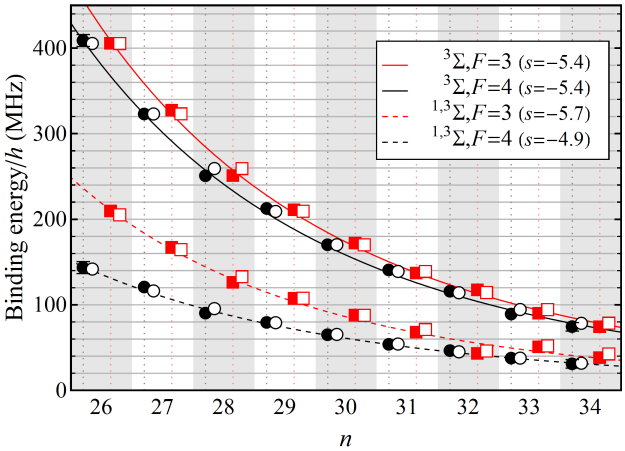

Figure 4.5: Comparison of experimental (full symbols) and calculated (open symbols) binding energies of the $^3\Sigma(v = 0)$ and $^{1,3}\Sigma(v = 0)$ levels. The solid/dashed lines are fits of a $(n^*)^s$ scaling law to the experimental binding energies to guide the eye. Black and red symbols designate states with the ground-state atoms prepared in the $F = 4$ and $F = 3$ hyperfine level of the $6s_{1/2}$ state, respectively.

Fabrikant [174] and, more recently, Bahrim *et al.* [150] calculated the zero-energy s-wave scattering lengths of electron-Cs scattering to be $a_{T,0} = -22.7\ a_0$ and $a_{S,0} = -2.4\ a_0$, and $a_{T,0} = -21.7\ a_0$ and $a_{S,0} = -1.33\ a_0$, respectively, from an effective-range-theory analysis of higher-energy scattering data. As appropriate measure of the deviation between experiment and theory, the absolute error in the zero-energy scattering phase shift $\delta_0 = \arctan(a_i/R_{pol}) + \pi/4$ [179] should be considered, where $R_{pol} = \sqrt{\alpha} = 20.05\ a_0$ is the typical range of the e^--Cs interaction and α is the polarisability of the Cs ground-state atom. The deviation between experiment and theory is at most 0.1 radian and the agreement can thus be regarded as good. The fitted model-based values include possible effects of higher partial waves in the e^--Cs scattering and interactions with Rydberg states other than the neigbouring $(n-1)d_{3/2,5/2}$ states in an effective manner. The fact that the s-wave-scattering model reproduces

Table 4.2: Measured and calculated binding energies of $Cs(np_{3/2}) - Cs(6s_{1/2}, F = 3)$ long-range Rydberg molecules (E^{expt} and E^{theor}, respectively) in units of [MHz $\times$ h]. Average dipole moments $\bar{\mu}^{theor}$ of the corresponding molecular states of different Ω (quantum number of the projection of the total angular momentum onto the molecular axis), which are degenerate in zero electric field, are given in units of Debye and have been calculated at the predicted equilibrium distances R^{eq} (values given in [nm]).

n	$E^{expt}_{^3\Sigma}$	$E^{theor}_{^3\Sigma}$	$R^{eq}_{^3\Sigma}$	$\bar{\mu}^{theor}_{^3\Sigma}$	$E^{expt}_{^{1,3}\Sigma}$	$E^{theor}_{^{1,3}\Sigma}$	$R^{eq}_{^{1,3}\Sigma}$	$\bar{\mu}^{theor}_{^{1,3}\Sigma}$
26	−406	−409	46.8	19.2	−209	−205	47.1	20.5
27	−327	−324	51.1	19.0	−167	−164	51.4	20.6
28	−251	−259	55.6	18.9	−127	−132	55.9	20.5
29	−211	−208	60.3	18.7	−107	−106	60.6	20.0
30	−172	−169	65.2	18.5	−88	−86	65.5	19.3
31	−137	−138	70.4	18.3	−68	−70	70.6	17.6
32	−118	−113	75.7	16.6	−43	−45	76.3	4.5
33	−90	−93	81.2	17.7	−51	−51	81.3	23.8
34	−74	−77	86.9	17.5	−38	−42	87.1	22.0

the experimental observations well over a broad range of n from 26 to 34 suggests that these effects are not dominant.

4.5 Molecular Stark effect

In an externally applied electric field, the widths of the molecular resonances identified as $^3\Sigma(v = 0)$ and $^{1,3}\Sigma(v = 0)$ increase linearly with the magnitude of the electric field E, as illustrated in Fig. 4.6 for the $32p_{3/2}, 6s_{1/2}(F = 4)$ resonances. The molecular dipole moments of the $^3\Sigma$ and $^{1,3}\Sigma$ states arise in the model from the mixing with the neigbouring $(n - 1)d_{3/2,5/2}$ states induced by the Fermi-contact interaction terms in Eq. (4.7). For the $32p_{3/2}, 6s_{1/2}(F = 4), ^3\Sigma(v = 0)$ states, dipole moments are predicted to range from 21.0 to 25.8 D (mean value 24.4 D) for $|\Omega_{tot}|$ values between 1/2 and 9/2. The dipole moments predicted for the $32p_{3/2}, 6s_{1/2}(F = 4), ^{1,3}\Sigma(v = 0)$ states are smaller and range from −0.5 to 12.0 D (mean value 5.6 D) for $|\Omega_{tot}|$ values between 1/2 and 7/2. The polarisation of the excitation laser (linear and parallel to the DC electric field) favours the excitation of molecules which are aligned parallel to the electric-field axis and one expects the zero-field resonance to evolve in a double-peak structure with a splitting of $\Delta\nu \simeq 2d_{mol}E$ (dashed lines in Fig. 4.6), where d_{mol} is the molecular dipole moment. While the observed broadenings and splittings are in qualitative agreement with the predicted Stark shifts, the asymmetric line shape of the $32p_{3/2}, 6s_{1/2}(F = 4), ^3\Sigma(v = 0)$ level is not captured by the model. A correct description would require the explicit consideration of the rotational structure in the

Table 4.3: Measured and calculated binding energies of $Cs(np_{3/2}) - Cs(6s_{1/2}, F = 4)$ long-range Rydberg molecules (E^{expt} and E^{theor}, respectively) in units of [MHz $\times$ h]. Average dipole moments $\bar{\mu}^{theor}$ of the corresponding molecular states of different Ω (quantum number of the projection of the total angular momentum onto the molecular axis), which are degenerate in zero electric field, are given in units of Debye and have been calculated at the predicted equilibrium distances R^{eq} (values given in [nm]).

n	$E^{expt}_{^3\Sigma}$	$E^{theor}_{^3\Sigma}$	$R^{eq}_{^3\Sigma}$	$\bar{\mu}^{theor}_{^3\Sigma}$	$E^{expt}_{^{1,3}\Sigma}$	$E^{theor}_{^{1,3}\Sigma}$	$R^{eq}_{^{1,3}\Sigma}$	$\bar{\mu}^{theor}_{^{1,3}\Sigma}$
26	−409	−409	46.7	26.3	−144	−141	47.5	5.4
27	−323	−324	51.0	26.2	−121	−115	51.7	5.5
28	−250	−259	55.5	26.2	−89	−94	56.2	5.7
29	−212	−208	60.2	25.9	−79	−78	60.9	5.9
30	−170	−169	65.1	25.7	−65	−64	65.7	6.1
31	−141	−138	70.3	25.5	−53	−53	70.8	6.3
32	−116	−113	75.5	25.1	−46	−44	76.1	6.4
33	−89	−93	81.2	24.9	−35	−37	81.6	6.7
34	−74	−77	86.8	24.6	−31	−31	87.3	7.0

model [42].

4.6 Lifetimes of long-range Rydberg molecules

Only two experimental investigations of the lifetimes of long-range Rydberg molecules in Rb and Sr have been reported so far (see Refs. [170, 171]). The lifetimes of Rb_2 long-range Rydberg molecules were found to decrease with increasing ground-state-atom density. The molecular-state lifetimes were reduced compared to those of the correlated atomic Rydberg states, but still were of the order of tens of microseconds [170]. These observations indicated that the dominant decay mechanism in long-range Rydberg molecules correlated to $ns_{1/2}$ Rydberg states in Rb are collisions with cold ground-state atoms. In contrast, the lifetimes of Sr_2 long-range Rydberg molecules were found to be very similar to those of the correlated atomic Rydberg states [171]. Radiative decay to the ground state is therefore dominant for Sr_2 long-range Rydberg molecules with minor contributions of black-body-radiation-induced transitions.

In the experiments on Cs described above, the resonances attributed to the excitation of long-range Rydberg molecules are detected *via* their their ionic decay products. During the 40-µs-long photoassociation phase, the long-range Rydberg molecules were found to predominantly decay into molecular Cs_2^+ ions. These observations indicate that the lifetimes of the detected Cs_2 long-range Rydberg molecules are less than 40 µs in the range of n between 26 and 34. The motivation of the experiments

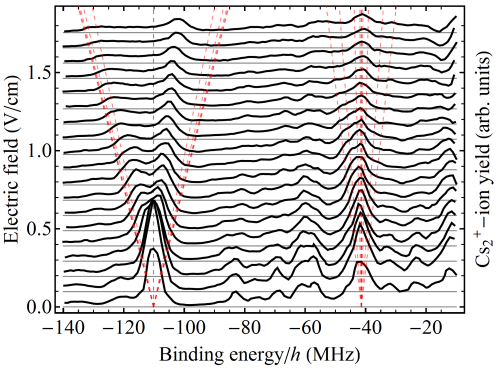

Figure 4.6: Cs photoassociation spectra in different electric fields near the $32p_{3/2},6s_{1/2}(F = 4)$ asymptote. Dashed red lines mark the maximal linear Stark shift of the $^3\Sigma(v = 0)$ and $^{1,3}\Sigma(v = 0)$ levels from calculated molecular electric dipole moments (for all values of $|\Omega_{tot}|$). The quadratic Stark shift of the atomic $32p_{3/2}$ asymptote (*e.g.*, 50 MHz at 1.5 V/cm) was subtracted from the experimental frequencies.

presented in this section was to measure the lifetime of the Cs_2 Rydberg molecules more accurately to allow for a comparison with the previous investigations in Rb and in Sr [170, 171].

In the first part of this section, measurements of the lifetime of the $33p_{3/2},6s_{1/2}$ $(F = 4)$, $^3\Sigma$ $(v = 0)$ state are presented. These experiments rely on the improved frequency-calibration procedure outlined in Section 4.3 and enable the determination of a lower limit of the lifetime from the widths of the photoassociation lines. The lifetimes can also be measured by monitoring spontaneously formed Cs^+ and Cs_2^+ ions and field-ionised Rydberg atoms and molecules as a function of the delay between the laser-excitation pulse and the ion-extraction and field-ionisation pulse. This latter measurement discriminates between decay caused by associative ionisation (leading to molecular ions), collisional ionisation (leading to atomic ions) and radiative decay (leading to ground-state atoms as dissociation products).

The second part of this subsection contains a general discussion of the decay channels in metastable long-range Rydberg molecules. Central to this discussion is the relation between long-range Rydberg molecules, ion-pair states and molecular Rydberg states of Cs_2.

4.6.1 Lifetime measurement of the $33p_{3/2}$, $6s_{1/2}(F = 4)$, $^3\Sigma(v = 0)$ state

The lifetimes of molecular resonances can be determined from photoassociation spectra under conditions where the linewidth of the photoassociation resonances corresponds to the natural linewidth of the molecular states. To reach this limit, the frequency calibration and bandwidth of the UV photoassociation laser is improved (see Sections 2.5.3 and 2.5.2).

The largest contribution to the uncertainty of ~ 5 MHz for the binding energies of the long-range Rydberg molecules as reported in Tables 4.2 and 4.3 was caused by the uncertainty in the positions of the broadened atomic resonances which were used as reference. In the measurement of the high-resolution spectra on the low-frequency side of the atomic $33p_{3/2} \leftarrow 6s_{1/2}, F = 4$ transition presented in Figs. 4.7a) and b), the frequency of the UV laser was calibrated using a frequency comb (see Section 2.5.3). The binding energies are obtained by taking the difference between the accurately known atomic term values (accurate to better than 100 kHz as demonstrated in Section 3.2) and the position of the molecular resonances. Using this procedure, binding energies of the photoassociated long-range Rydberg molecules can be determined with one order of magnitude higher accuracy than in the case of the spectra depicted in Fig. 4.4.

The frequency fluctuations of the UV laser have also been reduced by a more stable locking to an external cavity (see Section 2.5.2) and a better signal-to-noise ratio enabled measurements using UV-laser pulses of 2 μs length. These technical improvements resulted in a better spectra resolution, as can be seen by comparing in the spectrum depicted in Fig. 4.7b) with the corresponding spectrum in Fig. 4.4. The full width at half maximum of the photoassociation resonances is ~ 4 MHz. The observed width is larger than the UV-laser-excitation bandwidth of ~ 1.5 MHz, which includes the Doppler broadening expected from a Cs gas-phase sample at 40 μK and a wavelength of $\sim$ 319 nm. In a photoassociation spectrum, transitions from a scattering continuum to bound states are observed. Consequently, an additional broadening of the expected photoassociation resonances corresponding to the energy width of the distribution of populated continuum states is expected. This width can be estimated to be ~ 1 MHz in the case of Cs atoms at a temperature of 40 μK. The combined width[b] of ~ 2.5 MHz of the two contributions to the photoassociation line width cannot explain the width of 4 MHz that is observed in the experiments. An additional broaden-

[b]The estimation of the linewidth is only qualitative. A quantitative analysis of the linewidth would need to take into account the line shapes of the different contributions, which is Gaussian for the laser width, Lorentzian for the lifetime and more complicated (and asymmetric) for the photoassociation.

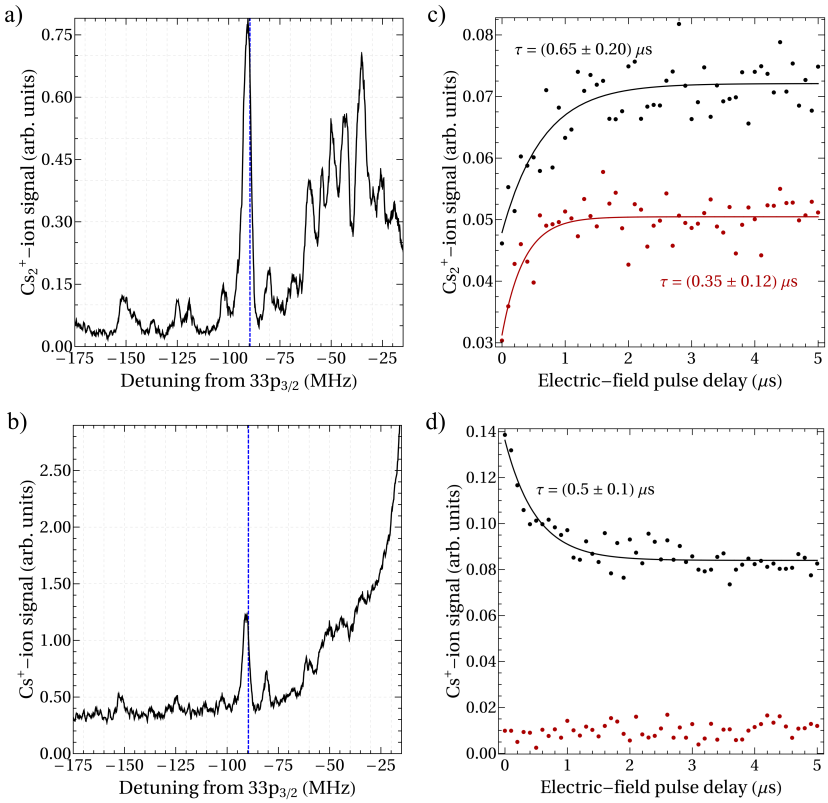

Figure 4.7: Photoassociation spectra of ultracold Cs atoms recorded on the low-frequency side of the $33p_{3/2} \leftarrow 6s_{1/2}, F = 4$ transition in Cs using a 2-µs-long UV-laser pulse. The spectrum in a) corresponds to the Cs_2^+-ion signal resulting from the decay of long-range Rydberg molecules. The spectrum in b) depicts the Cs^+-ion signal resulting from pulsed field ionisation of Rydberg atoms and long-range Rydberg molecules. Panels c) and d) show the results of a lifetime measurement of the $33p_{3/2}, {}^3\Sigma(v = 0)$ state using delayed pulsed field ionisation after photoexcitation with a 0.15 µs-long UV-laser pulse with a central frequency fixed at a detuning of −89.5 MHz (indicated by vertical dashed blue lines in a) and b)) relative to the atomic resonance frequency. The time dependence of the Cs_2^+-ion and the Cs^+-ion signal is presented in c) and in d), respectively. The results of measurements using an extraction-field pulse above (below) the classical ionisation field of $33p_{3/2}$ Rydberg atoms are depicted in black (red) in panels c) and d). Solid lines represent fitted exponential-decay curves to the measured data, with the fitted values of τ given in the panels.

ing of approximately 2 MHz could be interpreted as the contribution from the natural line width of the molecular resonance, which, in turn, leads to the determination of a lower limit of the lifetime of the state of $\tau > 1/(2\pi \cdot 2 \cdot 10^6)\,\mathrm{s} \approx 80\,\mathrm{ns}$.

The selective detection of Cs^+- and Cs_2^+-ion signals enables one to investigate the different channels in which the long-range Rydberg molecule decay. The comparison of Fig. 4.7a) and b) reveals that following the 2-μs-long UV-laser pulse most of the photoassociated Rydberg molecules are detected as Cs_2^+ ions. However, only Cs^+ ions are expected from the pulsed field ionisation of long-range Rydberg molecules because the weak binding in these long-range states is only mediated *via* the Rydberg electron, which is rapidly removed in the pulsed-field-ionisation process. Consequently, the formation of the molecular ions must have occurred before the application of the electric-field pulse and during the 2 μs of the laser pulse, from which an upper limit on the lifetime of the state can be estimated. The lifetime of the $32p_{3/2}, {}^3\Sigma(v = 0)$ resonance is determined from the photoassociation spectra to be within the limits $80\,\mathrm{ns} < \tau < 2\,\mu\mathrm{s}$.

The lifetime of the $33p_{3/2}, {}^3\Sigma(v = 0)$ resonance was measured in a second, time-resolved experiment. With the frequency of the UV laser fixed at the position of the $33p_{3/2}, {}^3\Sigma(v = 0)$ resonance (corresponding to a detuning of ∼89.5 MHz relative to the atomic $33p_{3/2} \leftarrow 6s_{1/2}, F = 4$ transition), the detected ions are monitored as a function of the delay between the laser pulse and the electric-field pulse. The results for Cs^+ ions and for Cs_2^+ ions presented in Fig. 4.7c) and d), respectively, have been obtained with a 150-ns-long UV-laser excitation pulse. The measurement was carried out first with an electric-field pulse sufficient to field ionise an $33p_{3/2}$ Rydberg state (black dots), and then with a pulsed electric field below the classical field-ionisation threshold for this Rydberg state (red dots). Consequently, the signal presented in red colour in Fig. 4.7c) and d) originates from spontaneous ionisation of the sample. The different amplitudes in the signals depicted in Fig. 4.7c) might be just a detection artefact related to the different kinetic energies of the molecular ions impinging on the MCP detector. The different velocities of atomic and molecular ions also render a direct comparison of the absolute signal strengths between the panels c) and d) in Fig. 4.7 difficult.

To extract values for the lifetime of the molecular level, the decay curves depicted in Fig. 4.7d) was analysed with the model

$$S(t) = S_\infty + (S_0 - S_\infty)\, e^{-t/\tau}. \tag{4.8}$$

In Eq. (4.8), S_∞ corresponds to the background ionisation in the limit of infinite delay time t and $(S_0 - S_\infty)$ represents the initial contribution to the signal from the Cs $np_{3/2}$ Rydberg states. The decay time $\tau \approx (0.5 \pm 0.1)\,\mu\mathrm{s}$ represents the decay of Cs

$n\mathrm{p}_{3/2}$ Rydberg states. Fig. 4.7c) indicates that the Cs_2^+-ion signal increases with time according to

$$S(t) = S_0 + (S_\infty - S_0)e^{-t/\tau}, \tag{4.9}$$

where τ^{-1} represents the rate of decay into the molecular channel detected by Cs_2^+ ions. The fitted curves are shown as solid black and red red traces in Fig. 4.7. Comparison of Fig. 4.7c) and d) suggests that the long-range Rydberg molecules decay into Cs_2^+ ions with a rate of $\sim (0.5\mu\mathrm{s})^{-1}$. The data presented Fig. 4.7 allows for the following important conclusions regarding the lifetime and decay channel of the $33\mathrm{p}_{3/2}$,$6\mathrm{s}_{1/2}(F = 4)$, $^3\Sigma(v = 0)$ state in Cs:

1. The molecular Cs_2^+ ions are formed during and after the laser pulse, and the formation mechanisms are not influenced by the electric extraction field. The decay of the long-range Rydberg molecules leads to molecular Cs_2^+ ions.

2. The pulsed field ionisation of long-range Rydberg molecules results in the observation of atomic Cs^+ ions (large signals at smallest delay times in Fig. 4.7d). The decrease of the Cs^+-ion signal occurs on the same timescale as the appearance of the molecular Cs_2^+ ions, because the metastable molecules decay into molecular ions.

3. Only a very small, time-independent Cs^+-ion signal is observed under conditions where the electric-field strength is not sufficient to field ionise the Rydberg molecules. It thus appears that the decay of the $33\mathrm{p}_{3/2}, 6\mathrm{s}_{1/2}, F = 4, ^3\Sigma(v = 0)$ state does not lead to the spontaneously formed Cs^+ ions[c].

4. From all decay curves exhibiting a variation as a function of the delay, a lifetime of $\tau = (0.5 \pm 0.2)\,\mu\mathrm{s}$ of the $33\mathrm{p}_{3/2}$,$6\mathrm{s}_{1/2}(F = 4)$, $^3\Sigma(v = 0)$ state can be extracted. The lifetime of the molecular resonance is therefore two orders of magnitude shorter than the lifetime of the correlated atomic Rydberg state ($\tau(33\mathrm{p}_{3/2}) > 100\,\mu\mathrm{s}$).

The observed decay of the $33\mathrm{p}_{3/2}, 6\mathrm{s}_{1/2}(F = 4)\,^3\Sigma(v = 0)$ state in Cs thus differs from the decay of long-range Rydberg molecules in Rb and Sr, as reported in Refs. [170, 171], both compared to the timescale and the dominant decay channel. This surprising observation motivates the following, more qualitative discussion.

[c] This behaviour observed in the decay long-range Rydberg molecules bound by electron–neutra-atom scattering is different to the decay observed in interacting Rydberg-atom-pair states. Rather generally it was found that the long-range Rydberg molecules primarily decay into molecular ions, whereas interacting Rydberg-atom-pair states were found to decay only decay into Cs^+ ions (see Section 5.3.5). This difference can be used experimentally to distinguish between the two interactions, which can lead to similar resonances in Rydberg-excitation spectra.

4.6.2 Discussion of decay channels of long-range Rydberg molecules

To evaluate which decay channels are open, a global understanding of the molecular structure of Cs_2 is required. Potential curves of representative molecular states of Cs_2 in the energy range between the electronic ground state and the first dissociative-ionisation threshold are presented in Fig. 4.9. The three panels focus on different ranges of the internuclear separation. Panel (a) shows the short range, with covalently bound molecular states; panel (b) shows the long-range region highlighting the three different important dissociation thresholds $Cs(6s_{1/2}) + Cs(6s_{1/2})$, $Cs^+ + Cs^-$, and $Cs(6s_{1/2}) + Cs^+ + e^-$; finally, panel (c) presents the electronic structure of the Cs atom. At short range (see Fig. 4.9a), the Rydberg states of Cs_2 have potential curves that resemble those of the $X^+\ ^2\Sigma_g^+$ and the $A^+\ ^2\Sigma_u^+$ states of Cs_2^+. Interactions between Rydberg states having a repulsive A^+ ion core and those having a X^+ ion core and the resulting avoided crossings are responsible for the appearance of double minima in several curves. This aspect of the electronic structure of Cs_2 is analogous to the situation encountered in molecular hydrogen (see, *e.g.*, Refs. [180–184]). Another common characteristic feature of the electronic structure of Cs_2 and H_2 is the existence of an attractive ion-pair potential curve at long range, represented as a thick black line in Fig. 4.9b. In the discussion of long-range states of Cs_2, it is useful to consider both the internuclear separation R and the distance $r \approx a_0 n^2$ of the Rydberg electron from the centre of charge of the ion core. A classification of the long-range states of Cs_2 on the basis of the relative magnitude of R and r is presented in Fig. 4.8.

Along the bisecting red line in this figure, R is equal to r. For large values of n (and thus of r and R), this case corresponds closely to the long-range Rydberg molecules discussed in section 2 because the Fermi-contact term (see Eq. 4.4) responsible for the binding is proportional to the electron probability density at the position of the ground-state Cs atom. This situation is also realised in ion-pair states if one imagines that the Rydberg electron is "attached" to the ground-state atom in the $6s_{1/2}$ state, forming the $Cs^-\ ^1S_0$ anion. Long-range Rydberg molecules and ion pairs are therefore related: In the former, the attractive interaction between the slow Rydberg electron and the ground-state Cs atom correlates their motion around the Cs^+ ion core, and leads to binding as well as to a partial charge separation. This charge separation has, in previous work, been linked to the existence of a permanent electric dipole moment in a homonuclear diatomic molecule [42, 47], although, of course, an antisymmetrised nuclear wavefunction of the two Cs nuclei makes this dipole moment vanish, both in long-range Rydberg molecules and in Cs^+Cs^- ion pairs.

At low values of n, the molecular states with $R \approx r$ are less isolated from other molecular states and the interactions cannot be conveniently treated with scattering theory because the kinetic energy of the electron markedly deviates from zero

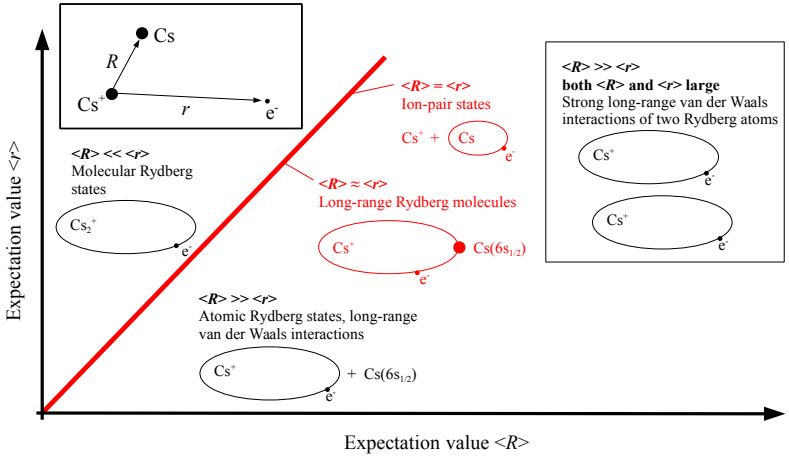

Figure 4.8: Schematic illustration of different molecular regimes as a function of the expectation value of the internuclear distance, $\langle R \rangle$, and the expectation value of the distance of one electron to the Cs^+ ion core, $\langle r \rangle$.

and more partial waves need to be included. Qualitative aspects are, however, preserved [185, 186].

The long-range Cs_2 molecules lie energetically just below the first ionisation energy of Cs ($E_I(Cs)/hc = 31406.4673225(14)\,cm^{-1}$ [121]). Because the electron affinity, $E_{EA}(Cs)$, of Cs is $3804\,cm^{-1}$ [178], the ion-pair dissociation limit is located at the position of $n^* \approx 5.4$ Rydberg states. Long-range Rydberg molecules of the type discussed in section 2 are therefore located in the ion-pair dissociation continuum into which they could, in principle, decay. The kinetic-energy release would roughly correspond to $E_{EA}(Cs)$ and thus to a de Broglie wavelength of $\sim 0.1\,a_0$ for the ionic dissociation products. The overlap of the vibrational wavefunction of the long-range Rydberg molecule with the wavefunction of the dissociated ion pair is therefore expected to be extremely small. Consequently, the decay of the long-range Rydberg molecules into ion-pair states is likely to be of minor importance.

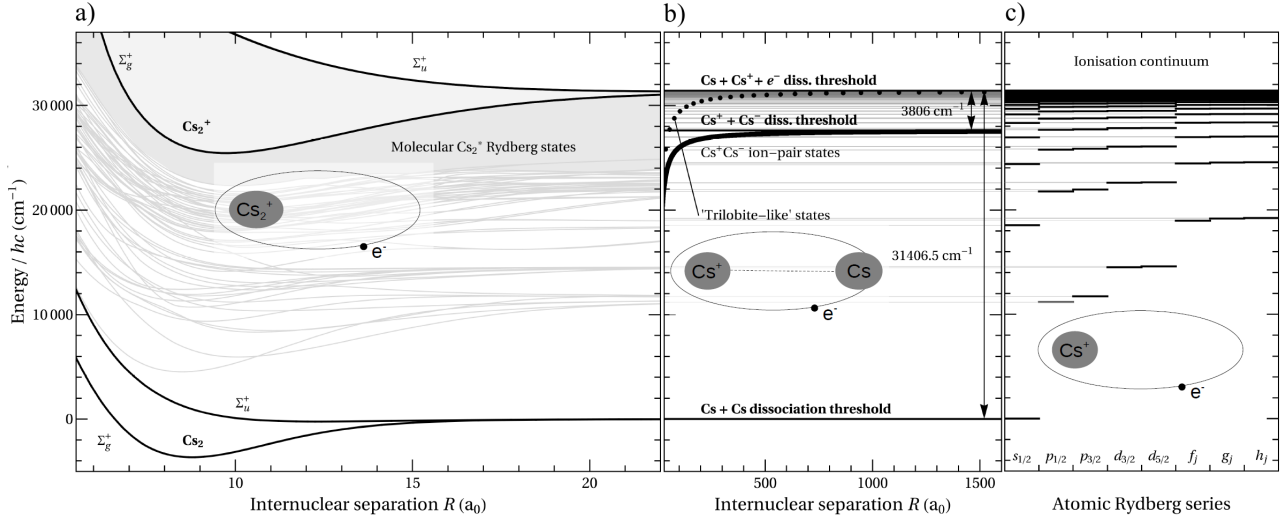

Figure 4.9: Overview of molecular potential functions of Cs_2 and Cs_2^+ below the first dissociative-ionisation threshold of Cs_2 ($Cs^+ (^1S_0) + Cs(6s_{1/2})$) in different ranges of internuclear separation. The electronic structure of isolated Cs atoms consists of Rydberg series of increasing orbital angular momentum and is depicted in panel (c). Panel (a) shows molecular potentials of covalently bound Cs_2 molecules. The lowest two ground-state potentials of g and u symmetry of Cs_2 and Cs_2^+ are depicted in black, whereas the excited states of the Cs_2 dimer having Rydberg character are shown in grey (calculated potentials taken from Ref. [187]). At high n values, the state density is high and the level structure is represented as a pseudo-continuum (grey background). Panel (b) focuses on the long-range regime where orbital overlap of low-lying states of the two atoms is negligible and the Cs_2 ground-state potential is essentially flat. The thick black line corresponds to the Coulomb potential of the Cs^+Cs^- ion pair and the black dots give the energy and average internuclear separation of the long-range Rydberg molecules discussed in section 2. All energies are given with respect to the $Cs(6s_{1/2}) + Cs(6s_{1/2})$ dissociation threshold.

The main decay product of the long-range Rydberg molecules detected in our experiments is the molecular Cs_2^+ ion. To illustrate possible mechanisms for the formation of Cs_2^+, Fig. 4.10 focuses on the energy region just below the first ionisation threshold of Cs_2. The $X^+\Sigma_g^+$ and $A^+\Sigma_u^+$ potential curves of Cs_2^+, taken from [188], are shown as solid black traces. Vibrational levels in these potentials were calculated using the mapped Fourier-grid technique [175] and their energies as a function of the expectation value $\langle 1/R^2 \rangle^{-1/2}$ are indicated as blue and light blue dots for the Σ_g^+ and Σ_u^+ states, respectively. The wavefunctions of the $v^+ = 263$ and the $v^+ = 366$ levels of the Σ_g^+ state are shown as thin blue lines. The molecular potentials have their minima at relatively short ranges, but exhibit a long-range α/R^4 scaling and support a few long-range states that have their peak probability amplitude at internuclear distances $> 200a_0$. Molecular Rydberg series, schematically represented by vertical lines in Fig. 4.10, converge to each of the ionic levels of Cs_2^+. The Rydberg states of Cs_2 have potential functions, and thus vibrational wavefunctions, that closely resemble those of Cs_2^+. The rotational structure adds significantly to the already very high molecular state density of Cs_2 and Cs_2^+ just below the first ionisation energy of Cs, but is omitted here for the sake of clarity.

The energies and internuclear separations of the Cs_2 long-range Rydberg molecules near Cs $np_{3/2}$ + Cs $6s_{1/2}$ dissociation asymptotes are presented as purple dots in Fig. 4.10. The black lines represent the potentials calculated with our s-wave scattering model at $n = 32$. These potentials are shown on an expanded energy scale for visibility and the vibrational wavefunctions of the two vibrational ground states are depicted as purple lines. A multitude of $Cs_2^+(v^+) + e^-$ channels are open at the position of the long-range Rydberg molecular states observed experimentally. However, the overlap of the vibrational wavefunctions of the long-range Rydberg molecules with those of accessible $Cs_2^+(v^+) + e^-$ ionisation continua is also extremely small. It is conceivable that the decay of the long-range Rydberg molecules into Cs_2^+ occurs through sequential couplings to Rydberg states of Cs_2 in successive $\Delta v = -1$ steps starting with the highest ($v^+ = 366$) level, which has a good Franck-Condon overlap with the long-range Rydberg molecular state. Channel interactions in molecular Rydberg states with $\Delta v = -1$ are, indeed, known to be the strongest (see, *e.g.* [189]). The decay of the long-range Rydberg molecules into $Cs_2^+ + e^-$ may also arise from $l \geq 1$ contributions in the e^--Cs scattering [41, 190], which might help bridging the internuclear separation. We are currently extending our potential model of the long-range Rydberg molecules by including p-wave scattering contributions to the interaction Hamiltonian.

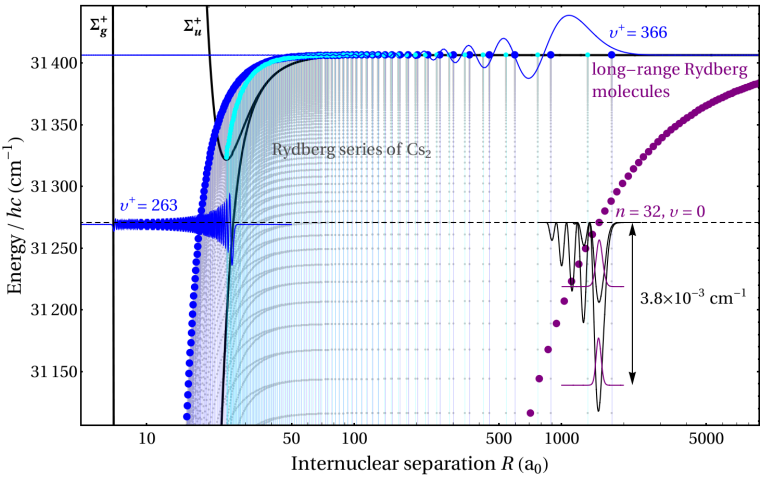

Figure 4.10: Comparison of energetic and structural characteristics of long-range Rydberg molecules and Cs_2^+ ions in high vibrational states. The molecular potentials of the $X^{+\,2}\Sigma_g^+$ and $A^{+\,2}\Sigma_u^+$ states of Cs_2^+ are given as solid black lines (taken from [188]). The energies and the expectation values $\langle 1/R^2 \rangle^{-1/2}$ of the vibrational levels of the X^+ and the A^+ states are marked as dark and light blue dots, respectively. The Rydberg series that converge to each of these v^+ levels are schematically indicated as vertical thin dashed lines. The vibrational wavefunctions of the $v^+ = 263$ and $v^+ = 366$ levels of the X^+ state are drawn as thin dark blue lines. The energies and internuclear separations of the long-range Rydberg molecules discussed in section 2 are given as purple dots. The molecular potentials correlated to the $Cs(32p_{3/2}) + Cs(6s_{1/2})$ dissociation asymptote calculated with our Fermi s-wave scattering model are depicted on an energy scale magnified by a factor of 35000 and the two vibrational ground-state wavefunctions are presented as thin purple traces.

4.7 Conclusions & Outlook

The formation of long-range Cs_2 Rydberg molecules consisting of a Rydberg and a ground-state atom was observed by photoassociation spectroscopy in an ultracold Cs Rydberg gas near $np_{3/2} \leftarrow 6s_{1/2}(F = 3, 4)$ resonances ($n = 26 - 34$). The spectra revealed two types of molecular states recently predicted by D. A. Anderson, S. A. Miller, and G. Raithel [Phys. Rev. A **90**, 062518 (2014)]: Pure triplet ($^3\Sigma$) states with binding energies ranging from 400 MHz at $n = 26$ to 80 MHz at $n = 34$, and states of mixed singlet and triplet ($^{1,3}\Sigma$) character with smaller and F-dependent binding energies. The experimental observations were accounted for by an effective Hamiltonian including Fermi-contact s-wave scattering pseudopotentials, the hyperfine interaction of the ground-state atom, and the spin-orbit interaction of the Rydberg atom. The analysis enabled the characterisation of the role of singlet scattering in the formation of long-range Rydberg molecules and the determination of an effective singlet s-wave

scattering length for low-energy electron-Cs collisions.

The assignment of vibrationally excited states of the $^3\Sigma$ and $^{1,3}\Sigma$ potentials and of molecular resonances observed both at detunings below the vibrational ground state of the $^3\Sigma$ potential and on the high-frequency side of the atomic $np_{3/2} \leftarrow 6s_{1/2}$ transitions is beyond the scope of the s-wave scattering model presented in this chapter. The influence of p-wave scattering on the energy-level structure of long-range Rydberg molecules of the alkali-metal atoms, which have a low-energy ^{3}P shape resonance in electron-atom scattering, is significant already at small displacements from the classical outer turning point of the Rydberg electron [41]. The divergence of the scattering volume $A_{^3\mathrm{P}}$ at the position of the shape resonance leads to the formation of an unusual molecular state, which has been referred to as the "butterfly" state [169, 190]. The $\mathrm{Cs}(6s_{1/2}) + \mathrm{Cs}^*$ dissociation asymptote of this state corresponds to the position of the hydrogenic high-l manifold and its binding energy corresponds to several hundred GHz at $n = 30$. Consequently, the potential of the "butterfly" state undergoes avoided level crossings with lower-lying molecular states correlated to $\mathrm{Cs}(6s_{1/2}) + \mathrm{Cs}(nl_j)$ dissociation asymptotes with $l = 0, 1, 2, 3$. Resonances on the high-frequency side of the atomic resonance could originate from the upper branches of the avoided curve crossings and are thus similar to the long-range molecular states reported on the high-frequency side of $6s_{1/2} + ns_{1/2}$ asymptotes in Cs [166]. Regular weak series of molecular states observed at large negative detunings are likely to result from almost harmonic potential wells of the "butterfly" potential. Experiments on the Stark shifts and broadenings of these levels indicate larger dipole moments than observed for the vibrational ground states in the outer wells of s-wave-scattering potentials, in accordance with the high-l-mixed character of a "butterfly-like" molecular state. These effects could be accounted for in an extended potential model including the p-wave scattering contributions.

The long-range Cs_2 Rydberg molecules were found to decay into Cs_2^+ molecular ions by autoionisation. Autoionisation processes take place at short range. The mechanism by which the internuclear separation is reduced during the autoionisation process remains to be elucidated in detail.

A qualitative discussion of the long-range Rydberg molecules, Cs_2 Rydberg molecular states and Cs^+Cs^- ion-pair states indicates that these classes of molecular states are related. The decay of Cs_2 long-range molecules in Cs_2^+ ions is either the result of contributions of $l > 0$ partial waves to the e^--Cs scattering or the result of interactions between channels associated with highly-excited vibrational levels of Cs_2^+ and Rydberg series converging to these levels.

Chapter 5

One-colour two-photon excitation of Rydberg-atom-pair states

This chapter presents studies of the long-range interactions between two Rydberg atoms that result in the formation of molecular resonances. Specifically, experiments are presented in which Cs Rydberg-atom pairs are detected as sharp resonances in laser-excitation spectra of ultracold, dense samples of Cs vapour. The resonances are assigned and quantitatively analysed using a model describing the interactions between Cs Rydberg atoms using long-range molecular potential curves that are calculated without any adjustable parameter.

The experiments involve the excitation of pairs of interacting Cs Rydberg atoms with intense pulsed laser fields and enable the observation of long-range molecular states connected to different pair-dissociation asymptotes. Whereas only np Rydberg states are optically accessible in one-photon transitions from Cs $(6_{1/2})$ ground-state atoms because of the electric-dipole approximation for isolated atoms, interacting Rydberg-atom-pair states have been observed as resonances near, *e.g.*, $n\mathrm{s}_{1/2}(n+1)\mathrm{s}_{1/2}$, $n\mathrm{s}_{1/2}(n-3)\mathrm{f}_j$, and $(n-4)\mathrm{f}_j(n-3)\mathrm{f}_j$ asymptotes as a result of dipole-dipole, dipole-quadrupole [64], and higher-order terms of the multipole-expansion series [65]. The observations are related to earlier work describing similar phenomena in ultracold Rydberg gases of rubidium [58–60, 191] and cesium [62, 63] at values of the principal quantum number n around 70. Compared to these previous investigations of molecular resonances, in this work, the resonances were studied at lower principal quantum numbers in the range $22 \leq n \leq 36$. Additionally to pair resonances observed in the immediate vicinity of dissociation thresholds, sharp spectral structures result also from local maxima in the molecular potentials and from avoided crossings between different potential curves for $n < 27$. The positions, widths and relative intensities of these resonances are sensitive to the details of the long-range molecular potentials. This sensitivity is exploited to validate the Rydberg-atom-pair interaction

model (presented in Subsection 5.1), which is then used to describe, in Section 5.3.4, the asymmetric broadening observed in millimetre-wave transitions between pairs of Rydberg atoms. The model also successfully accounts for the Penning-ionisation processes that take place following Rydberg-atom-pair excitation in the dense ultracold Cs gas on timescales of several hundreds of nanoseconds (see Subsection 5.3.5).

This chapter is an adapted version of the articles H. SASSMANNSHAUSEN, F. MERKT, and J. DEIGLMAYR: "Pulsed excitation of Rydberg-atom-pair states in an ultracold Cs gas", *Phys. Rev. A* **92**, 032505 (2015) and J. DEIGLMAYR, H. SASSMANNSHAUSEN, P. PILLET and F. MERKT: "Observation of Dipole-Quadrupole Interaction in an Ultracold Gas of Rydberg Atoms", *Phys. Rev. Lett.* **113**, 193001 (2014).

5.1 Theory of interacting Rydberg-atom-pair states

The molecular resonances encountered in the experiments presented in this chapter originate from long-range interactions between two Cs atoms in high-n Rydberg states. The term "long-range" in this case means that the internuclear distances at which the atoms are excited exceed the LeRoy radius R_{LR} of two Rydberg atoms A and B, which is defined as $R_{\mathrm{LR}} = 2\left(\langle r_{\mathrm{A}}^2\rangle^{1/2} + \langle r_{\mathrm{B}}^2\rangle^{1/2}\right)$ [192], where r_i is the distance of the Rydberg electron from the core of atom i. The LeRoy radius is used as a boundary for the internuclear separation of two atoms beyond which orbital overlap, and therefore contributions from electron exchange and covalent binding, can be neglected. The remaining molecular interactions are induced long-range interactions often called van der Waals interactions.

5.1.1 Long-range potential model

For the theoretical modelling of long-range interacting Rydberg-atom-pair states, the total Hamiltonian is set up as

$$H = H_0^{\mathrm{A}} + H_0^{\mathrm{B}} + V_{\mathrm{inter}}(R), \tag{5.1}$$

where H_0^{A} and H_0^{B} are the Hamiltonian operators describing the unperturbed and non-interacting Cs Rydberg atoms A and B, respectively. H_0^{A} and H_0^{B} include the spin-orbit interaction of the Rydberg electron but neglect the hyperfine interaction (see Section 3.1.3) which is negligible compared to the resolution in the experiments. The long-range interactions are accounted for by $V_{\mathrm{inter}}(R)$, where R is the internuclear distance. Following the generally applied formalism [193, 194] for long-range van der Waals interactions, the Hamiltonian for the Rydberg-Rydberg interaction [58, 62, 195]

is expressed in the multipole-multipole expansion

$$V_{\text{inter}}(R) = \sum_{L_{\text{A/B}}=1}^{\infty} \sum_{\omega=-L_<}^{+L_<} \frac{(-1)^{L_\text{B}} f_{L_\text{A},L_\text{B},\omega}}{R^{L_\text{A}+L_\text{B}+1}} Q_{L_\text{A},\omega}(\vec{r}_\text{A}) Q_{L_\text{B},-\omega}(\vec{r}_\text{B}) \tag{5.2}$$

$$Q_{L,\omega}(\vec{r}) = \sqrt{\frac{4\pi}{2L+1}} r^L Y_{L,\omega}(\hat{r}) \tag{5.3}$$

$$f_{L_\text{A},L_\text{B},\omega} = \frac{(L_\text{A}+L_\text{B})!}{\sqrt{(L_\text{A}+\omega)!(L_\text{A}-\omega)!(L_\text{B}+\omega)!(L_\text{B}-\omega)!}}, \tag{5.4}$$

where $\vec{r}_i$ is the position of the Rydberg electron bound to atom i with respect to the ion core, R is the interatomic separation, and $Q_{L,\omega}(\vec{r})$ are the atomic multipole moments, which are defined in terms of the spherical harmonics $Y_{L,\omega}(\hat{r})$. The order of a given atomic multipole moment is L, and $L_<$ is defined as the smaller of the two L values of the interacting multipole moments of two Rydberg atoms. The quantum number of the projection of the angular momentum associated with $L_<$ onto the molecular axis is ω. The multipole expansion of Eq. (5.2) is an exact description of the long-range interactions in the absence of retardation effects and for distances larger than the LeRoy radius.

For all practical purposes, the infinite multipole expansion must be truncated. Based on the comparison with the experimental results presented in this chapter, it was found that terms up to the octupole-octupole ($L_\text{A} = L_\text{B} = 3$) contribution needed to be included in some calculations. This finding was unexpected because so far observations of interacting Rydberg atoms described in the literature were usually interpreted as arising from the dipole-dipole interaction alone (see, *e.g.*, [9]) and the quadrupole-quadrupole contribution has only been considered in rare cases (see, *e.g.* [196]). The contributions from the dipole-quadrupole and higher-order terms in the multipole expansion, observed for the first time in the realm of this dissertation, are presented in Sections 5.3.2 and 5.3.3, respectively.

The Hamiltonian operator (5.1) is evaluated in matrix form in a product basis

$$|n_\text{A} l_\text{A} j_\text{A} \omega_\text{A}\rangle\, |n_\text{B} l_\text{B} j_\text{B} \omega_\text{B}\rangle \equiv |\gamma_\text{A} j_\text{A} \omega_\text{A}\rangle\, |\gamma_\text{B} j_\text{B} \omega_\text{B}\rangle \tag{5.5}$$

consisting of two non-interacting atoms in states defined by the principal quantum numbers n_i, the orbital-angular-momentum quantum numbers l_i, the total-angular-momentum quantum numbers of the Rydberg electrons j_i and the quantum numbers ω_i of its projection onto the internuclear axis (with $i = \text{A,B}$). The projection of the total angular momentum onto the molecular axis is a constant of motion in a diatomic molecule and is labelled here by the quantum number $\Omega = \omega_\text{A} + \omega_\text{B}$. In this basis, the spin-orbit interaction of the Rydberg electron is taken into account even though it scales with $(n^*)^{-3}$ because it is still larger than, or on the same order

of magnitude as, the interaction-induced effects observed in the experiments. The hyperfine interaction of the Rydberg atoms (see Section 3.1) is, however, much smaller than the experimental laser-excitation bandwidth of $\sim$ 130 MHz and is neglected in the model.

To obtain the molecular eigenstates and eigenenergies of the Hamiltonian matrix, radial and angular parts are separated. The radial matrix elements need to be evaluated by numerical integration [115], using experimental quantum defects [116, 122][a] and an *ab-initio* model core potential. The angular matrix elements can be calculated analytically using standard angular-momentum algebra (see Appendix B for more details). The eigenstates and eigenvalues are determined as a function of the internuclear separation R, which only appears as a parameter in Eq. (5.1), and for different values of Ω because molecular states with different Ω do not interact at zero field.

Intentionally, the molecular basis is not symmetrised with respect to the permutation of the two identical Cs nuclei, which leads to non-zero contributions of the interaction Hamiltonian that mix pair states of different electronic parity. The electronic parity of such a pair state is given by $(-1)^{l_A+l_B}$ and is conserved for all interaction terms with $(-1)^{L_A+L_B} = 1$ (such as the dipole-dipole interaction), whereas terms with $(-1)^{L_A+L_B} = -1$ (the lowest-order contribution is in this case the dipole-quadrupole interaction) require a change in the electronic parity. The role of these electronic-parity-violating interaction terms in the formation of long-range Rydberg-atom-pair states is further discussed in Section 5.3.2.

The molecular eigenenergies $E_\Psi(R)$ of different molecular states Ψ are determined as a function of the internuclear distance and the molecular eigenfunctions are linear combinations of the basis functions $|\Psi(R)\rangle = \sum c_{\gamma_A j_A \omega_A, \gamma_B j_B \omega_B}(R)\,|\gamma_A j_A \omega_A, \gamma_B j_B \omega_B\rangle$. Exemplary potential-energy curves are presented in Fig. 5.1 for interacting Rydberg-atom-pair states of Cs in the vicinity of $n\mathrm{p}_{3/2}n\mathrm{p}_{3/2}$ thresholds with $n = 23, 25, 32$.

The inclusion of higher-order terms in the interaction Hamiltonian of Eq. (5.2) necessitates the extension of the basis set $|n_A l_A j_A \omega_A, n_B l_B j_B \omega_B\rangle$ to include pair states with l_A and l_B values up to 6. Convergence of the eigenvalue calculations was checked by increasing the range of principal quantum numbers n_A and n_B. Because the atomic radial transition matrix elements rapidly decrease with the value of Δn, only states differing in the effective principal quantum number n^* by at most 1 were considered in the calculations. It further turned out to be sufficient to only consider the pair

[a] The improved quantum-defect values for Cs originating from work presented in this thesis (see Chapter 2 and Ref. [121]) were not available at the time the simulations were performed. The improved quantum defects are sufficiently close to the one from Refs. [116, 122], which are used in the calculations, that the difference is not expected to cause significant deviations from the results presented here.

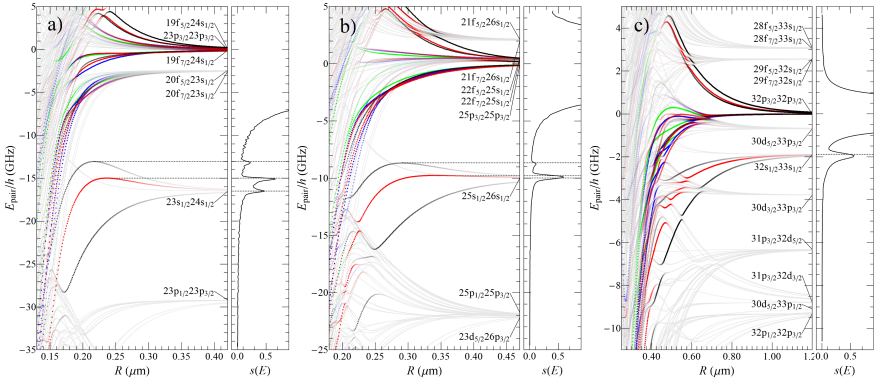

Figure 5.1: Calculated potential-energy curves for long-range Rydberg-atom pairs in the vicinity of $np_{3/2}np_{3/2}$ asymptotes at a) $n = 23$, b) $n = 25$, and c) $n = 32$ and for $\Omega = 0, 1, 2, 3$ (black, red, blue, and green curves, respectively) as obtained from the long-range potential model (details in the text). The intensity of the colour reflects the value of $\overline{p_\Psi}(R)$, grey colour denoting 0% overlap with the atomic $np_{3/2}np_{3/2}$ state, full colour denoting 1% or higher overlap. The simulated spectra plotted in arb. units on the right-hand side of each of the three panels were calculated using Equation (5.9).

states with asymptotes located within an energy window of $0.64 \cdot 4R_{Cs}/(n^*)^3$ around the relevant $np_{3/2}np_{3/2}$ asymptotes. States located outside this range only approach the $np_{3/2}np_{3/2}$ potential curves at short range, where the gradients of the potential-energy curves are large and spectral structures are broad and weak. The majority of the pair states are neglected following these restrictions, but their coupling to the optically accessible states is so weak that they do not contribute significantly to the state mixing and energy shifts of experimentally observable states. The state density in the model is still very high (also because several potential functions correlate to each asymptote, see Fig. 5.1), and even though inclusion of these states is necessary to accurately predict the observations, most of the states only couple indirectly to the optically accessible states and only a small fraction of the molecular states actually contributes to the experimental signals.

5.1.2 Theoretical line profile

The excitation probability $\overline{p_\Psi}(R)$ of a molecular eigenstate $|\Psi\rangle$ at a pair separation R is proportional to the square of the mixing coefficients of the $np_{3/2}np_{3/2}$ basis states. The optically accessible states $|\phi\rangle$ (for $np_{3/2}np_{3/2}$ that is n, $l = 1$, $j_A = j_B = 3/2$) are conveniently expressed in the laboratory-fixed frame as

$$|\phi\rangle = \sum_{m_A, m_B} a_{j_A m_A, j_B m_B} |j_A m_A, j_B m_B\rangle \,. \tag{5.6}$$

To account for the experimental conditions, an isotropic distribution in the $6s_{1/2}$ ground state of the Cs atoms ($m_s = \pm 1/2$) is assumed. σ^+ polarised transitions thus lead to the excitation of four different states $|\phi\rangle$ corresponding to $j_A = j_B = 3/2$ and $m_A = 1/2, 3/2$ and $m_B = 1/2, 3/2$ with equal weights. The intensity is obtained as the squared overlap $p_\Psi(\theta, R) = \left|\langle\Psi(R)|\phi\rangle\right|^2$ between the optically accessible function $|\phi\rangle$ and the function $|\Psi(R)\rangle$ expressed in the molecule-fixed frame with the internuclear axis forming an angle θ with the laboratory-fixed z axis. To calculate $p_\Psi(\theta, R)$, the atomic functions $j_{A,B} m_{A,B}$ are transformed into the molecule-fixed frame using the Wigner $d^j_{\omega m}(\theta)$ rotation matrices and

$$p_\Psi(\theta, R) = \left|\langle\Psi(R)|\phi\rangle\right|^2 = \left| \sum_{\substack{\gamma_A j_A \omega_A, \gamma_B j_B \omega_B \\ j_A m_A, j_B m_B}} \langle\Psi(R)|\gamma_A j_A \omega_A, \gamma_B j_B \omega_B\rangle \, d^{j_A}_{\omega_A m_A}(\theta) \times d^{j_B}_{\omega_B m_B}(\theta) \, \langle j_A m_A, j_B m_B|\phi\rangle \right|^2 . \tag{5.7}$$

is obtained. The θ-dependent probability $p_\Psi(\theta, R)$ is averaged over all orientations θ of the molecular axis relative to the z axis, resulting in $\overline{p_\Psi}(R) = \int p_\Psi(\theta, R) 2\pi \sin(\theta) d\theta$, which is directly proportional to the spectral intensity resulting from excitation of a molecular pair state $|\Psi\rangle$ at the interatomic separation R. The corresponding spectral line profile $s_\Psi(E')$ is then determined as

$$s_\Psi(E') = 4\pi \int_0^\infty \delta(E' - E_\Psi(R)) \frac{4\,\omega_{\mathrm{atom}}^4}{(E_{\mathrm{pp}} - E_\Psi(R))^2} \overline{p_\Psi}(R) R^2 \mathrm{d}R, \tag{5.8}$$

where ω_{atom} is the Rabi frequency of the atomic $np_{3/2} \leftarrow 6s_{1/2}$ transition, E_{pp} the energy of the $np_{3/2}np_{3/2}$ asymptote, and the term $4\,\omega_{\mathrm{atom}}^4/(E_{\mathrm{pp}} - E_\Psi(R))^2$ accounts for the one-colour two-photon excitation of the pair state with an intermediate $np_{3/2}6s_{1/2}$ (or $6s_{1/2}np_{3/2}$) state at a detuning of $\frac{1}{2}(E_{\mathrm{pp}} - E_\Psi(R))$ [60]. The delta function ensures resonance with the molecular state $|\Psi\rangle$ with the energy $E_\Psi(R)$. In a gas of homogeneous density, the number of atom pairs at a separation R is proportional to the volume of the spherical shell $4\pi R^2 \mathrm{d}R$ and this factor is included in Eq.(5.8). In order to compare with experimental spectra, the line profile $s_\Psi(E')$ is convoluted with the laser line profile $G(E)$ and summed over all molecular states $|\Psi\rangle$ to obtain the full

spectrum $s(E)$ as

$$\begin{aligned} s(E) &= \sum_{\Psi} \int_{-\infty}^{\infty} s_{\Psi}(E') \cdot G(E-E')\mathrm{d}E' \\ &= 16\pi \sum_{\Psi} \int_{-\infty}^{\infty} \int_{0}^{\infty} \delta(E' - E_{\Psi}(R)) \frac{\omega_{\mathrm{atom}}^4}{(E_{\mathrm{pp}} - E_{\Psi}(R))^2} \times \\ &\quad \overline{p_{\Psi}}(R) R^2 \cdot G(E-E')\mathrm{d}R\mathrm{d}E' \\ &= 16\pi \sum_{\Psi} \int_{0}^{\infty} \frac{\omega_{\mathrm{atom}}^4}{(E_{\mathrm{pp}} - E_{\Psi}(R))^2} G(E - E_{\Psi}(R)) \times \\ &\quad \overline{p_{\Psi}}(R) R^2 \mathrm{d}R. \end{aligned} \tag{5.9}$$

A Gaussian laser line-shape function with a full width at half maximum (FWHM) of 130 MHz was used for $G(E)$ corresponding closely to the Fourier-transform limit of the pulsed UV laser that was used for the excitation of the interacting Rydberg-atom-pair states (see Section 5.2, and Chapter 2). Consequently, the theoretical line profile $s(E)$ of Eq. (5.9) has no adjustable parameter, with the exception of a global distance- and energy-independent amplitude. The global amplitude includes the atomic Rabi frequency ω_{atom} of $n\mathrm{p}_{3/2} \leftarrow 6\mathrm{s}_{1/2}$ transitions, which is not evaluated quantitatively. The resulting spectra for $n = 23, 25, 32$ calculated with Eq. (5.9) are presented in Fig. 5.1 on the right-hand side of the corresponding potential-energy functions. In this figure, the colours black, red, blue and green indicate molecular potentials characterised by $\Omega = 0, 1, 2, 3$, respectively, and the colour-intensity shading reflects the values of $\overline{p_{\Psi}}(R)$. Full colour was chosen for 1 % or more $n\mathrm{p}_{3/2}n\mathrm{p}_{3/2}$ character and states with zero $n\mathrm{p}_{3/2}n\mathrm{p}_{3/2}$ character are presented in grey in Fig. 5.1.

At large distances, the only non-vanishing contributions are located in the immediate vicinity of the $n\mathrm{p}_{3/2}n\mathrm{p}_{3/2}$ asymptotes. At shorter distances, many more potential curves contribute to the spectral intensity. However, most potential curves are strongly attractive and the large gradients spread the overall intensity over broad spectral ranges, which renders the observation of pair states impossible. Because the spectral line-shape function scales with R^2 (see Eq. (5.9)), the excitation of short-range pairs is additionally suppressed[b]. From the general appearance of the curves depicted in Fig. 5.1, one expects sharp spectral structures to arise from regions where the potential curves that possess some $n\mathrm{p}_{3/2}n\mathrm{p}_{3/2}$ character are flat. Such regions of enhanced intensity are encountered where the curves have local maxima (a good example of such a situation is given by the red and black curves correlated to the

[b] For example, the regime of almost full state mixing in the n range considered here is encountered at internuclear separations $R < 0.2$ µm. The mean internuclear separation at the highest densities is only on the order of $\bar{R} = 1$ µm. The probability of finding a pair of atoms at those distances much smaller than the mean internuclear separation is low.

$23s_{1/2}24sp_{1/2}$ asymptote in the left panel of Fig. 5.1) or closely approach their asymptotic value (examples are the three curves correlated to the $ns_{1/2}(n+1)s_{1/2}$ asymptotes at large R values in Fig. 5.1). In regions where the potential functions are flat atom pairs at many different internuclear distances R contribute to the signal $s(E)$. Sharp spectral structures are also encountered in regions where avoided crossings reduce the spectral density, leading to intensity minima.

Resonances originating from the excitation of interacting Rydberg-atom-pair states are expected to be observable in the range of internuclear distances $0.2\mu m < r < 1.5\mu m$ for the n states around 30 considered in this work. In this range, the van der Waals interactions are strong enough to lead to significant state mixing, but the state density is low enough for the states to be spectrally resolved.

Because the dipole-dipole interaction for the resonant and the non-resonant cases scales with R as $1/R^3$ or $1/R^6$, respectively, the dipole-dipole term is the longest-range contribution in the multipole-multipole expansion and its effects dominate at the largest distances. The dipole-dipole interaction mixes $ns_{1/2}(n+1)s_{1/2}$ states with the $np_{3/2}np_{3/2}$ states[c]. The resonances resulting from this interaction are dominant in Fig. 5.1 and are discussed in Section 5.3.1. At smaller internuclear separations, effects of higher-order multipole-multipole interactions are observable, and these interactions need to be included when modelling the experimental data near $nl_Jn'l'_{J'}$ asymptotes that are not coupled to the optically accessible pair state though a dipole-dipole interaction (see Section 5.3.2). At high n values, the pair-state density, which scales as n^6 becomes so large that it becomes impossible to identify individual resonances resulting from interactions of higher order than the dipole-dipole interaction. Consequently, to study the effects of dipole-quadrupole and higher-order interactions, it is advantageous to carry out the measurements on relatively low-n Rydberg states in the n range between 20 and 30 (see Section 5.3.3).

5.1.3 Non-perturbative calculation of the excitation-blockade radius

On the basis of potential-energy curves such as those depicted in Fig. 5.1 and Eq. (5.9), the two-atom excitation probability for resonant Rydberg excitation can be determined as a function of the internuclear separation (see Fig. 5.2). The reduction of the resonant excitation rate of one atom conditional on the distance to a second excited atom is called the Rydberg-excitation-blockade effect.

The region where the excitation probability approaches zero (see Fig. 5.2) corresponds to the effective blockade radius. The blockade radius is often approximated

[c] In this thesis, the label for the asymptote of a molecular Rydberg-atom-pair state will sometimes be used as a label for the whole molecular function.

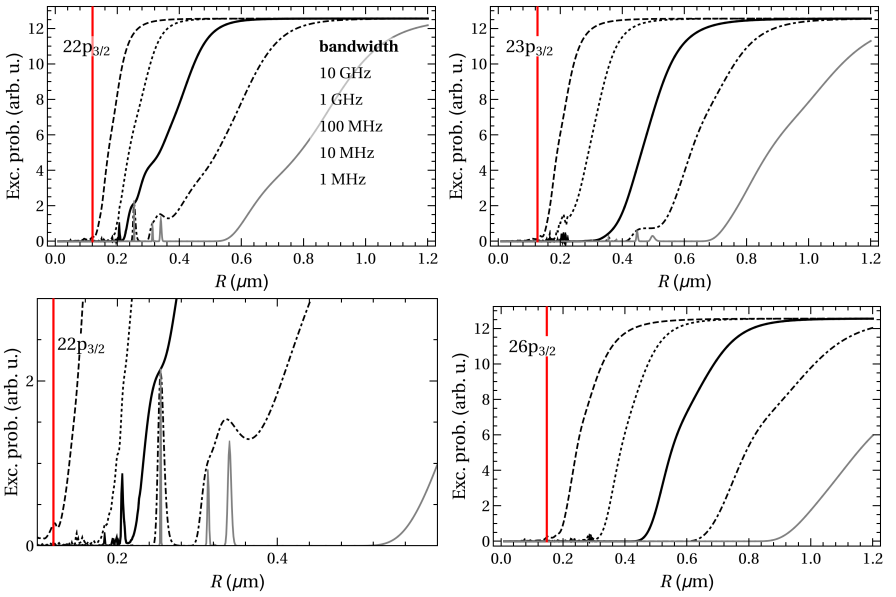

Figure 5.2: The calculated probabilities of resonant $np_{3/2} \leftarrow 6s_{1/2}$ transitions as a function of the internuclear distance to another Cs atoms in an $np_{3/2}$ Rydberg state are presented for different laser bandwidths of 10 GHz (dashed trace), 1 GHz (dotted trace), 100 MHz (thick solid trace), 10 MHz (dotted-dashed trace), and 1 MHz (solid grey trace). The LeRoy radii for the different Rydberg-atom-pair states are indicated by vertical red lines.

by

$$R_B = \sqrt[6]{2C_6/(\delta\nu_L h)}, \tag{5.10}$$

In this approximation, R_B is only a function of the C_6 coefficient of the off-resonant dipole-dipole coupling and the laser-excitation bandwidth is $\delta\nu_L$. Eq. (5.10) is only valid at very long range, where the level shifts can be calculated using perturbation theory and can be described with a single van der Waals parameter.

The more accurate calculation presented in Fig 5.2 reveals that the Rydberg-atom-pair excitation is not necessarily restricted to large internuclear separations (even with very narrow-bandwidth excitation) because of molecular resonances in the excitation probability at short internuclear separations (see, in particular, the panel on the lower left-hand side in Fig. 5.10). These resonances result from avoided crossings between different potential curves and occur relatively randomly when varying n, R and $\delta\nu_L$. Models with large basis sets are required to predict their positions and widths. The interaction-induced shift of Rydberg-atom-pair levels back into resonance, enhancing the signal expected just for atomic excitation, is also called “anti-

blockade" effect in the literature [197, 198]. The molecular resonances occur mostly with $l > 0$ Rydberg pair states [199], which is an effect of the anisotropy of the long-range interactions between atoms in $l > 0$ states (see, *e.g.*, [87, 200, 201]), and can limit the applicability of the Rydberg-excitation blockade. However, the resonances are typically sharp with respect to the internuclear distance (see grey curve in the lower panel on the left-hand side of Fig. 5.2), and their experimental observation can be prohibited, *e.g.*, when loading the ultracold atoms in optical lattices, restricting the internuclear separations to defined values where no resonances occur [202, 203].

In the experiments described here, the two-atom-excitation probability only reaches zero at distances significantly smaller than the mean nearest-neighbour separation in the ultracold gas, both for the pulsed excitation and the cw excitation with 130 MHz and 1 MHz excitation bandwidths, respectively. Consequently, no significant blockade effect is expected in the range of n values measured here[d]. The reason for the small values of R_B encountered here in $np_{3/2}$ Rydberg states are molecular states that experience almost zero level shift even at short internuclear distances. These states have been termed "Förster zero" states and appear in Rydberg states with $l > 0$ [87, 200]. Our calculations show that the negative effects of these "Förster zero" states on blockade experiments are avoided by using excitation to ns Rydberg levels, and indeed, the most successful blockade experiments reported to date rely on ns Rydberg states [30, 31]. However, Rydberg-blockade effects have also been demonstrated with np [204] and nd [205] Rydberg states.

5.2 Experiment

All experiments were performed on ultracold samples of cesium atoms at a density of $\sim 10^{12}\,\mathrm{cm}^{-3}$, a particle number of $\sim 10^6$, and a translational temperature of $\sim 40\,\mu\mathrm{K}$. The samples were released from a far-detuned crossed optical dipole trap (see Section 2.3) which was loaded from a magneto-optical trap (MOT). The transfer of atoms from the MOT to the dipole trap proceeded as follows: After a MOT-loading phase of ~80 ms, the fiber laser used for the dipole trap was turned on and, simultaneously, the magnetic-field gradient was ramped up, compressing the MOT for 10 ms. The magnetic field was then turned off and the atoms were cooled in an optical-molasses phase for 5 ms. The MOT lasers were then turned off and the atoms were optically pumped into the lower hyperfine component of the $6s_{1/2}$ electronic ground state. The atoms were held in the dipole trap for 10 ms, during which time the non-

[d] This theoretical prediction is confirmed experimentally. Both with pulsed and narrow-band cw excitation the atom cloud can be completely depleted when the laser frequency is set to an atomic $np_{3/2}$ resonance (with $22 < n < 34$) and the laser power is gradually increased.

captured atoms left the photoexcitation region. The power of the optical-dipole-trap laser was reduced to its minimum value of 300 mW after the cesium atoms in the optical dipole trap had been selectively pumped optically into the upper hyperfine state of the $6s_{1/2}$ ground state, from where they were photoexcited in single-photon transitions to $np_{3/2}$ Rydberg states. The experimental cycle was repeated at a rate of 10 Hz.

The excitation laser was a frequency-doubled pulse-amplified ring dye laser (see Section 2.4.1), delivering 4.4-ns-long Fourier-transform-limited UV pulses (~319 nm, 140 MHz bandwidth) with pulse energies of up to 100 μJ. The laser was focused to a spot size of ~150 μm ($1/e^2$ radius), resulting in peak irradiances of up to 100 MW/cm^2. The laser frequency was calibrated with a wavelength meter (High Finesse WS6-200). One-colour two-photon $ns_{1/2} \leftarrow 6s_{1/2}$ transitions were driven with the pulse-amplified fundamental output of the ring laser at a wavelength of ~639 nm and a pulse energy of ~0.5 mJ.

The transitions were detected by monitoring the Cs^+ ion signal using a microchannel-plate (MCP) detector[e] after state-selective pulsed-field ionisation (PFI). For PFI, a pulsed electric field with a rise time of 1 μs and maximal field strength $F_{max} = 1.25$ kV/cm was applied. Only np Rydberg states with $n \geq 26$ could be field ionised under these conditions. However, the formation of ions on molecular resonances was also observed for Rydberg states with $n < 26$, but only after introducing some delay between laser and electric-field pulse. After PFI but before the next MOT-loading phase, the atom number and density of the atom cloud were measured using saturated-absorption images (see Section 2.2.3). On the atomic resonances the trap was fully depleted and the resulting ion signals strongly saturated the detection system, which was designed to be sensitive to single ions. The spectral positions of the atomic transitions were obtained from trap-loss spectra based on the saturated-absorption images.

Millimetre-wave transitions between Rydberg states excited on atomic or pair resonances were measured using a millimetre-wave source (see Section 2.4.2) consisting of a swept frequency synthesiser (Wiltron, Model 6769B) connected to an amplifier-multiplier chain (Virginia Diodes, WR6.5AMC, tunable range 110 - 170 GHz). Typical interaction times with the millimetre-wave radiation were 1 μs and the transitions were detected using state-selective PFI and separating initial and final Rydberg states in the Cs^+-ion time-of-flight (TOF) traces.

As described in Section 2.7, regular measurement and compensation of the stray

[e]The MCP detector has a quantum detection efficiency of ~40% limited by the fraction of active to non-active surface area. Together with a Poisson distribution in the counting statistics of laser-excited Rydberg atoms and Rydberg-atom-pair states, the excitation of Rydberg atoms and pair states lead to statistically indistinguishable counting statistics at low laser intensities. With an ideal detector and small signals, the counting statistics of Rydberg-atom-pair states should peak at 0 and 2, with zero probability of detecting only one Rydberg atom.

electric and magnetic fields during the data acquisition period ensured that the magnitude of the stray electric and magnetic fields never exceeded 20 mV/cm and 20 mG, respectively, which is sufficiently low that these fields do not influence the behaviour of the Rydberg states under investigation. The electric field was compensated by measuring and minimising the quadratic Stark effect of high $n\mathrm{p}_{3/2}$ Rydberg states [148] and the magnetic field was compensated by measuring the Zeeman splitting of the $F' = 4 \leftarrow F = 3$ hyperfine transition of the $6\mathrm{s}_{1/2}$ state using microwave spectroscopy.

5.3 Experimental results and discussion

In this section the experimental results obtained following one-colour two-photon excitation of interacting Rydberg-atom-pair states is presented. In the first part, the experimental pulsed-UV-laser-excitation spectra are discussed and interpreted by comparison to simulated line profiles. Several resonances could be assigned as originating from individual terms of the multipole-interaction expansion. Different subsections are dedicated to resonances resulting from the dipole-dipole (Subsection 5.3.1), the dipole-quadrupole (Subsection 5.3.2) and higher-order (Subsection 5.3.3) interaction terms. Experiments are also presented that were carried out to characterise specific properties of the Rydberg-atom-pair states, namely their Stark effect (see Section 5.3.1), their response to millimetre-wave radiation resonant with a transition to another pair state (see Section 5.3.4), and their spontaneous decay by Penning ionisation (see Section 5.3.5). These results have also been published under the Refs. [64, 65].

5.3.1 Dipole-dipole coupling and $n\mathrm{s}_{1/2}(n+1)\mathrm{s}_{1/2}$ resonances

Rydberg-excitation spectra of Cs near $n\mathrm{p}_{3/2} \leftarrow 6\mathrm{s}_{1/2}$ transitions recorded with an intense pulsed UV laser contain resonances that are a manifestation of dipole-dipole interactions in the ultracold Cs Rydberg gas. These resonances occur close to $n\mathrm{s}_{1/2}(n+1)\mathrm{s}_{1/2}$ pair-dissociation asymptotes.

An overview of the experimental spectra (black traces) measured near these asymptotes is presented in Fig. 5.3 in comparison to simulated line profiles (red dashed traces). Single resonances are observed for $n > 27$ and sets of resonances are observed for $22 < n < 28$ on the low-frequency sides of atomic $n\mathrm{p}_{3/2} \leftarrow 6\mathrm{s}_{1/2}$ transitions. Despite the large signal-to-noise ratios, the signals obtained on these resonances correspond to only around 20 ions per laser shot. In comparison, the signals at the atomic resonance frequencies are several orders of magnitude larger, effectively saturating the ion-detection system. Because of this saturation, the atomic resonances

observed by monitoring the ionisation signal cannot be used to calibrate the frequency detunings. However, from the simultaneously recorded saturated-absorption images it is possible to derive the number of ground-state atoms remaining after each laser shot. When the number of ground-state atoms is plotted as a function of the UV-laser frequency, the atomic resonance appears as a dip (*cf.* spectra depicted in Fig. 5.6b). This reveals that the ultracold atom cloud is significantly depleted when the frequency of the intense UV laser is resonant with an atomic $n\mathrm{p}_{3/2} \leftarrow 6\mathrm{s}_{1/2}$ transition. Given the number of ground-state atoms in the trap, which is on the order of 10^6, more than 10^5 Cs^+ ions are generated on the atomic resonances. The resonance features visible in the spectra presented in Fig. 5.3 are, consequently, at least around 10^4 times weaker than corresponding $n\mathrm{p}_{3/2} \leftarrow 6\mathrm{s}_{1/2}$ transitions[f].

The resonances have a red-degraded line shape and split in several components for $n < 28$. However, in each spectrum one resonance is always observed near the asymptotic energy of $n\mathrm{s}_{1/2}(n+1)\mathrm{s}_{1/2}$ pair states (within $2 \times 75\,\mathrm{MHz}$, see Fig. 5.3c). The detunings $\Delta\nu(n)$ of the $n\mathrm{s}_{1/2}(n+1)\mathrm{s}_{1/2}$ from the $n\mathrm{p}_{3/2}n\mathrm{p}_{3/2}$ pair-dissociation asymptotes are calculated with Rydberg's formula and the known quantum defects of Cs (taken from Refs. [116, 122]) using

$$\Delta\nu(n) = \frac{\Delta E(n)}{2h} = \frac{2E_{n\mathrm{p}_{3/2}} - E_{n\mathrm{s}_{1/2}} - E_{(n+1)\mathrm{s}_{1/2}}}{2h} \tag{5.11}$$

with

$$E_{nl_j} = \frac{hR_{\mathrm{Cs}}}{(n - \delta_{l_j}(n))^2}. \tag{5.12}$$

In Equation (5.12), $R_{\mathrm{Cs}} = 3.289\,828\,299(20) \cdot 10^9\,\mathrm{MHz}$ is the Rydberg constant of Cs and $\delta_{l_j}(n)$ are the l- and weakly j- and n-dependent quantum defects. The n dependence of the quantum defects is expressed with the Ritz formula [152]

$$\delta_{l_j}(n) = \delta_{l_j}(\infty) - \frac{a_{l_j}}{(n - \delta_{l_j}(\infty))^2}. \tag{5.13}$$

The detuning $\Delta\nu(n)$ of the molecular from the atomic resonance frequency in the experimental spectra (see Fig. 5.3b) corresponds to a one-photon energy scale. Consequently, the energy defect of the two-photon resonances is divided by two. At low n values, the energy dependence of the quantum defects is significant and $\Delta\nu(n)$ varies considerably with n, as illustrated in Fig. 5.3c. The detuning becomes gradu-

[f] This ratio corresponds roughly to the intensity ratio of $n\mathrm{p}_{3/2} \leftarrow 6\mathrm{s}_{1/2}$ to $n\mathrm{p}_{1/2} \leftarrow 6\mathrm{s}_{1/2}$ transitions at $n = 30$. The reason for this extreme difference in the transition strength from the electronic ground state to the two fine-structure components of the p Rydberg series is a Cooper minimum in the excitation cross section to $n\mathrm{p}_{1/2}$ states just above the ionisation threshold in the $\epsilon\mathrm{p}_{1/2}$ continuum. The similarity in transitions strengths was applied in the measurement of the intensity dependence of the molecular resonance by comparing the signal to that of the weak atomic transition (see Fig. 5.5).

ally smaller with increasing n up to $n = 42$, where the detuning changes sign, and becomes almost independent of n, stabilising at around $+50$ MHz. Below $n = 42$, the increasing detuning of the $ns_{1/2}(n+1)s_{1/2}$ pair states and the reduced strength of the dipole-dipole interaction leads to a continuous reduction of the pair-state signals towards lower n values. By applying more intense UV pulses (see left-hand side of Fig. 5.3a), constant absolute signal strengths and signal-to-noise ratios could be maintained down to $n = 23$.

To quantitatively analyse the origins of the different resonances, their red-degraded line shapes and splittings, the experimental spectra are compared to spectra simulated using Eq. (5.8) (see red dashed lines in Fig. 5.3a). The excellent agreement of the simulation with the experimental observations proves that these resonances originate from the dipole-dipole coupling of the optically accessible $np_{3/2}np_{3/2}$ states with $ns_{1/2}(n+1)s_{1/2}$ levels. With the exception of the spectrum at $n = 22$, the peak positions and line shapes of all spectra are reproduced by the simulation. The experimental peak positions relative to the positions of the $ns_{1/2}(n+1)s_{1/2}$ dissociation asymptotes are presented as a function of the principal quantum number in Fig. 5.3c, where they are compared to the peak positions extracted from simulated spectra. Overall, the experimental peak positions (open circles in Fig. 5.3c) closely match the asymptotic energies at all n values. However, there are small systematic n-dependent deviations (labelled $\Delta E_{\mathrm{int}}/h$ in the inset of Fig. 5.3c) of the experimental peak positions from the asymptotic values. These energy shifts exceed the estimated error bars of the measurements and are reproducible. They are compared to the peak positions determined from the simulated spectra (indicated by the dashed trace in the inset), which reveal the same deviations. These deviations are attributed to an interaction-induced shift ΔE_{int} as schematically illustrated in Fig. 5.3b. The shifts obtained from the spectra have been multiplied by a factor of 2, because they do not represent a one-photon detuning but a detuning from the two-photon energy[g].

Three representative sets of potential-energy functions that give the $ns_{1/2}(n+1)s_{1/2}$ resonances their characteristic interaction-induced shifts (see inset of Fig. 5.3c) and fine structures (see Fig. 5.3a) are depicted in Fig. 5.1 for $n = 23$, 25 and 32. The calculated spectra $s(E)$ are depicted on the right-hand side of each panel, where dashed horizontal lines mark the positions of the relevant dissociation asymptotes. Three states correlating to the $ns_{1/2}(n+1)s_{1/2}$ asymptotes possess a significant admixture of the optically accessible $np_{3/2}np_{3/2}$ pair state, two of which are $\Omega = 0$

[g] The high-resolution spectra presented in Chapter 6 reveal that this shift results from the convolution of a strongly asymmetric line profile with a 130-MHz-broad laser-line-shape function. The sign of the shift therefore indicates blue- and red-degraded lines, whereas the absolute values are both determined by the exact shape of the asymmetric line profile and by the laser width, and are close to its value of the the half width at half maximum

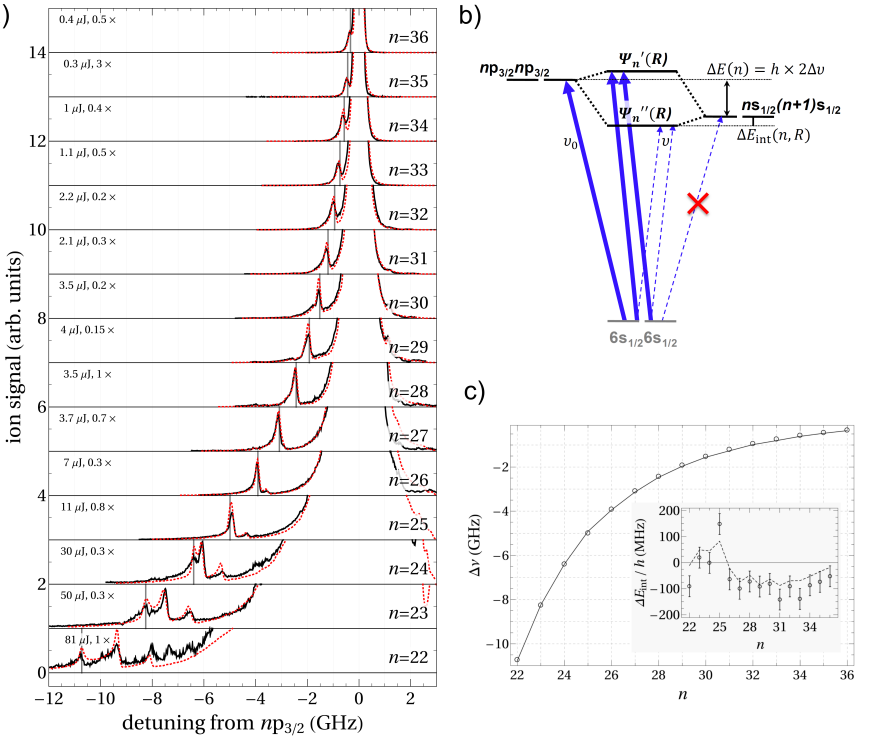

Figure 5.3: a) Spontaneous-ion signals as a function of the detuning of the pulsed UV-laser frequency from $np_{3/2} \leftarrow 6s_{1/2}$ transitions of Cs at ground-state-atom densities of around 10^{12} atoms/cm^3 for n between 22 and 36 (solid black traces). The spectral positions corresponding to the asymptotic energies of $ns_{1/2}(n+1)s_{1/2}$ states are marked with vertical grey bars. The pulse energies for each spectrum and the relative intensity scaling factors of the experimental spectra are given on the left-hand side of each panel. Simulated spectra are shown as red dashed traces. b) Simplified and schematic energy-level diagram of the interaction between the $ns_{1/2}(n+1)s_{1/2}$ states with energetically close-lying $np_{3/2}np_{3/2}$ states. The blue thick and thin dashed lines indicate strong and weak UV transitions. Two-photon transitions are represented by two parallel arrows. c) Peak positions of the resonances correlated to the $ns_{1/2}(n+1)s_{1/2}$ asymptotes as a function of the principal quantum number n. Experimental values are shown as open circles and the asymptotic energy (see vertical grey bar in a)) calculated with the known quantum defects is shown as a thin black line. The inset highlights the deviations from the asymptotic energies of the resonance peak position in the experiment (open dots with error bars) and the simulation (dashed line).

(black curves) states and the third (red curves) is a $\Omega = 1$ state. At the highest n values studied experimentally ($27 < n < 37$) and for which the results obtained at $n = 32$ are representative (see Fig. 5.1), all three states are attractive. The experimentally observed red-degraded line shapes therefore result from the attractive nature of the molecular potentials. The sharp high-frequency edge of the resonances corresponds closely to the asymptotic energy of the pair state. The comparison of calculated potentials and the simulated spectra also reveals the internuclear separation at which the pair states are excited at a given frequency detuning of the laser. This aspect will be discussed further in Section 5.3.5.

In the range of internuclear distances where the $np_{3/2}np_{3/2}$ character of the three states is significant, the dipole-dipole interaction with the $np_{3/2}np_{3/2}$ state is the dominant interaction. The interaction with the $np_{1/2}np_{3/2}$ pair state, which is located more than 10 GHz below the $np_{3/2}np_{3/2}$ asymptote at $n = 32$, does not significantly affect the $ns_{1/2}(n+1)s_{1/2}$ potential curves in this range of n values. In the range $27 < n < 37$, the calculations predict a small red shift of the pair resonance with respect to the $ns_{1/2}(n+1)s_{1/2}$ asymptote and a red-degraded line shape, in excellent agreement with the experimental observations (see Fig. 5.3).

As n decreases below $n = 28$, the position of the $ns_{1/2}(n+1)s_{1/2}$ asymptotes rapidly shifts away from the $np_{3/2}np_{3/2}$ asymptote and toward the $np_{1/2}np_{3/2}$ asymptote. Consequently, the effect of the dipole-dipole interaction with the lower-lying $np_{1/2}np_{3/2}$ pair state becomes important: The $\Omega = 1$ and one of the two $\Omega = 0$ potential functions become repulsive at intermediate distances, beyond about 0.3 μm at $n = 25$ and beyond about 0.20 μm at $n = 22$ (see Fig. 5.1). At shorter range, the interaction with the higher-lying $np_{3/2}np_{3/2}$ pair state is always dominant and makes the $ns_{1/2}(n+1)s_{1/2}$ potentials attractive, resulting in local maxima in these two curves. These two maxima give rise to two additional peaks in the spectra located on the high-frequency side of the $ns_{1/2}(n+1)s_{1/2}$ asymptotes. The position of the asymptote corresponds to the third resonance, which is well resolved below $n < 25$. Overall, the calculated spectra $s(E)$ accurately reproduce the experimental spectra at all n values investigated (see Fig. 5.3). The interaction-induced shifts of the pair resonances extracted from simulated and experimental spectra agree within the experimental uncertainty, as shown in the inset of Fig. 5.3c. Even the positive interaction-induced shift of the $n = 25$ pair resonance with respect to the $25s_{1/2}26s_{1/2}$ asymptote (see Fig. 5.3c) is accounted for by the calculations, which indicate that it results from the overlap of signals originating from the long-range part of the potentials and from the flat potential region near the maximum of the $\Omega = 1$ curve (red trace in Fig. 5.1b).

In the first set of control experiments, the density dependence of the resonance signal strength relative to the strength of an atomic resonance was studied. Because it is possible, but experimentally challenging, to vary the ground-state-atom density

without simultaneously varying the atom number in the photoexcitation region, only two pulsed-UV-laser spectra in the vicinity of the $31p_{3/2} \leftarrow 6s_{1/2}$ transition were measured with the same UV-laser intensity, one at low Cs-atoms density (10^8 cm^{-3}, obtained after thermal expansion of the ultracold cloud released from the MOT, dashed trace in Fig. 5.4) and one at high density (10^{12} cm^{-3}, obtained releasing the atoms from the crossed optical dipole trap, solid trace in Fig. 5.4).

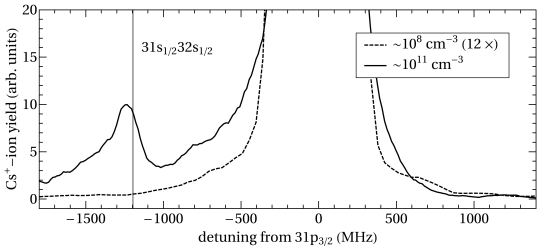

Figure 5.4: UV-laser spectra near the $31p_{3/2} \leftarrow 6s_{1/2}$ transition of Cs at ground-state-atom densities of around 10^8 atoms/cm^3 (dashed trace) and 10^{12} atoms/cm^3.

In Fig. 5.4, the intensity of the spectrum recorded with a low-density sample has been multiplied by a factor of 12 to match the high-frequency wing of the atomic transition observed in the more intense spectrum. One additional peak is observed at a detuning of −1200 MHz in the spectrum recorded at a high ground-state density. The spectral position of the resonance does not correspond to any transition of an isolated Cs atom but matches closely the frequency of the two-photon pair excitation $31s_{3/2}32s_{3/2} \leftarrow 6s_{1/2}6s_{1/2}$, which is weakly allowed because of the long-range configuration interaction of the $31s_{3/2}32s_{3/2}$ pair state with the $31p_{3/2}31p_{3/2}$, as explained in Section 5.1. For this molecular resonance a quadratic dependence on the ground-state density is expected. This strong dependence on the atom density is revealed here by the fact that the resonance is not visible at all in the spectrum recorded with the low-density sample. Taking into account that the $31s_{1/2}32s_{1/2}$ pair resonance is excited at an internuclear separation of ∼0.8 μm, it is not surprising that no signal can be detected in measurements carried out with a dilute gas, where the mean internuclear separation is larger than 20 μm.

In a second set of control experiments, the scaling of the signal intensity with the laser intensity, which is expected to be quadratic for a two-photon excitation process, was investigated. This measurement was performed on the $33s_{1/2}34s_{1/2}$ pair resonance. The corresponding spectrum is depicted in the upper panel of Fig. 5.5, where the peak at a detuning of ∼ −8.4 GHz corresponds to the weak $33p_{1/2} \leftarrow 6s_{1/2}$ transition and the peak at a detuning of ∼ −0.75 GHz to the two-photon transition to the $33s_{1/2}34s_{1/2}$ Rydberg-atom-pair state. The lower panel of Fig. 5.5 shows the results of

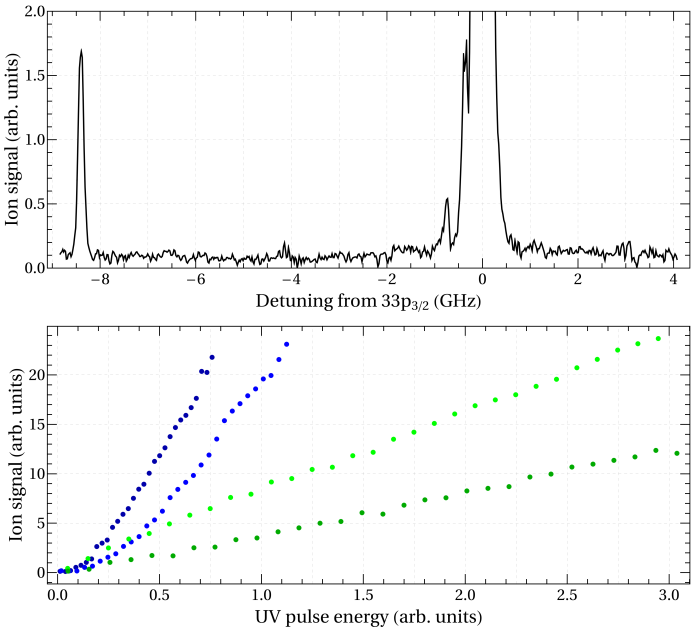

Figure 5.5: Upper panel: Cs^+-ion yield as a function of the detuning of the UV laser from the the $33p_{3/2} \leftarrow 6s_{1/2}$ transition of Cs. The peak at a detuning of $\sim -8.4\,\mathrm{GHz}$ corresponds to the weak atomic $33p_{1/2} \leftarrow 6s_{1/2}$ transition. Lower panel: Dependence of the Cs^+-ion signal on the atomic $33p_{1/2} \leftarrow 6s_{1/2}$ resonance (green points) and the $33s_{1/2}34s_{1/2} \leftarrow 6s_{1/2}6s_{1/2}$ pair resonance (blue points) on the UV-laser intensity. The UV laser was σ^+ polarised and a small magnetic offset field was applied. Two sets of measurement were conducted: One set on a polarised ground-state atom sample prepared by optical pumping in the $6s_{1/2}$, $F = 4, M_F = 4$ state (points shown in dark colour), and the second set with an unpolarised sample (points shown in light colour).

the measurement of the Cs^+-ion signal at the peak of the $33s_{1/2}34s_{1/2}$ resonance (blue points) and at the peak of the $31p_{1/2}$ resonance (green points). In all measurements, a small magnetic quantisation field was applied and the UV laser was σ^+ polarised. Two sets of measurements were conducted, the first one on a polarised ground-state sample in which the Cs atoms were optically pumped into the $6s_{1/2}, F = 4, M_F = 4$ magnetic sublevel (dark blue and dark green dots in Fig. 5.5), and the second one on an unpolarised sample (light blue and light green dots in Fig. 5.5). Because there is no $31p_{1/2} \xleftarrow{\sigma^+} 6s_{1/2}, F = 4, M_F = 4$ transition, the signal obtained in the first set of measurements (dark green dots) is a consequence of the imperfections in the optical pumping and the UV-laser polarisation. The signal is, however, suppressed by a factor of two compared to the measurements carried out with the unpolarised sample (light green dots), and both measurements show a clear linear dependence of the sig-

nal on the UV-laser intensity, as expected for a one-photon transition. The pair-state signals (blue dots) show a quadratic dependence on the laser intensity for low intensities and a linear dependency at large intensities. A quadratic scaling is expected for a two-photon process, the change to a linear scaling could indicate a saturation effect (*e.g.*, related to the available number of atom pairs at suitable distances). The larger signals (compare dark blue points to the light blue points in the lower panel of Fig. 5.5) observed with the sample of polarised ground-state atoms results from the larger electronic coupling matrix elements at the higher m values.

In the last control experiment, the Stark effect of the pair resonances was investigated by recording pulsed UV-laser spectra in the presence of external homogeneous electric fields of different strengths. The spectra of the $32s_{1/2}33s_{1/2} \leftarrow 6s_{1/2}6s_{1/2}$ transition obtained at zero field (black lines) and measured with an externally applied electric field of 10 V/cm (blue lines) are depicted in the upper row of Fig. 5.6. Fig. 5.6a shows the Cs^+-ion signal resulting from the spontaneous ionisation of the sample. The Stark shift of the pair state (sharp line at a detuning of −1 GHz) is negative, but much smaller than the Stark shift of the $32p_{3/2} \leftarrow 6s_{1/2}$ atomic resonance, which appear strongly saturated. The Stark shift of the atomic resonance was determined from trap-loss spectra (see Fig. 5.6b) obtained on the basis of saturated-absorption images, as explained in Subsection 5.3.1. In the trap-loss spectra, the shifts and splittings into the $m_J = 1/2, 3/2$ components of the $31p_{3/2}$ state are clearly resolved at a field of 10 V/cm.

The atomic resonance positions as well as the pair-resonance peak positions were determined and are plotted as a function of the external electric-field strengths in Fig. 5.6c). The splittings and the shifts of the atomic $31p_{3/2}$ Rydberg state were used to calibrate the electric-field strengths by comparison to the calculated Stark shifts. The obtained values for the electric-field strengths are in agreement with a simulation of the electric-field distribution in the photoexcitation region using the programme SimIon and taking the the experimental geometry and the applied electric potentials as input. For the weak electric fields between 0 and 12 V/cm applied in the experiments, quadratic Stark shifts of the atomic s and p Rydberg states are expected because these states have large quantum defects and are energetically well separated from other Rydberg states of opposite parity. The pure quadratic Stark effect of $np_{3/2}$ Rydberg states is given by

$$\Delta E_{\mathrm{Stark}} = \frac{1}{2}\alpha_{\mathrm{p}_{3/2,\mathrm{m}}}(n)F^2. \tag{5.14}$$

At the dissociation asymptote, where the $s_{1/2}$ atoms do not interact, the Stark shift of the $32s_{1/2}33s_{1/2}$ pair state corresponds to

$$\Delta E_{\mathrm{Stark,2-pht}} = \frac{1}{2}F^2\left(\frac{1}{2}\alpha_{\mathrm{s}_{1/2}}(n) + \frac{1}{2}\alpha_{\mathrm{s}_{1/2}}(n+1)\right), \tag{5.15}$$

where the shift is already divided by 2 to account for the experimental two-photon excitation of the pair state. The polarisabilities α_i of both states have been calculated following the procedures outlined in Ref. [115] and are both negative, but much larger for $p_{3/2}$ Rydberg states than for $s_{1/2}$ Rydberg states. A measurement of the Stark effect of a pair resonance can therefore be used to unambiguously distinguish between states of s and p character. According to the long-range potential model, the $32s_{1/2}33s_{1/2}$ pair states are excited mainly at internuclear separations where the admixture of p character is still weak (less than $\sim 5\%$), so that the Stark shift of the pair is well described by Eq. (5.15). The fact that the measured shifts lie within their experimental uncertainty on the curve predicted by Eq. (5.15) (see Fig. 5.6) is thus a proof that the pair resonance actually is the $32s_{1/2}33s_{1/2}$ Rydberg-atom-pair resonance.

Figure 5.6c also demonstrates that external electric fields can be used to adjust the detuning between two pair states, and even bring them into resonance, which happens here at a field of ~ 7 V/cm. To be exact, the resonance condition is met at three different electric-field strengths. Indeed, the Stark effect splits the $np_{3/2}np_{3/2}$ pair state into the three magnetic components $np_{3/2,m=1/2}np_{3/2,m=1/2}$, $np_{1/2,m=3/2}np_{3/2,m=3/2}$ and the $np_{3/2,m=3/2}np_{3/2,m=3/2}$, for which the resonant field is slightly different. Many experimental investigations have focused on such resonances [8, 9, 206–211][h], for which the term "Förster resonances" has been used because the situation is analogous to that leading to Förster resonance energy transfer (FRET) in molecules [216].

Here, the dipole-dipole interaction between the $np_{3/2}np_{3/2}$ and the $ns_{1/2}(n+1)s_{1/2}$ states is non-resonant and the measurement of pair-state Stark shifts requires high atom densities and high laser intensities. At electric field strengths above 7 V/cm the pair resonance is observed on the high frequency side of the atomic $np_{3/2} \leftarrow 6s_{1/2}$ transition and its intensity successively decreases with increasing detuning.

5.3.2 Dipole-quadrupole coupling and $n's_{1/2}n''f_j$ resonances

In this section, experimental observations are presented that are the consequence of a direct dipole-quadrupole interaction between two atoms in the gas phase. This observation is surprising because the dipole-quadrupole interaction does not conserve the electronic parity of an atom-pair state. Because electromagnetic interactions[i] in

[h] Two Rydberg atoms can also exhibit always-resonant dipole-dipole interactions at zero electric field. This happens when they are excited to states of opposite parity (see, *e.g.*, [212–215] and Chapter 6 of this thesis). In this case, resonant "excitation-hopping" process of the type

$$(ns_{1/2})_{\mathrm{atom1}} + (n'p_{3/2})_{\mathrm{atom2}} \longleftrightarrow (n'p_{3/2})_{\mathrm{atom1}} + (ns_{1/2})_{\mathrm{atom2}}$$

can occur and the interaction potential scales with C_3/R^3, where R is the internuclear distance.

[i] The electro-weak nuclear force does not conserve the parity, and its consequences of the resulting parity violation in molecules is discussed in detail in Ref. [217] (see the chapter on symmetry

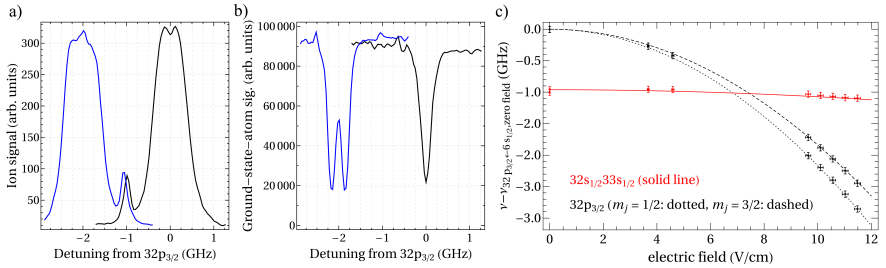

Figure 5.6: Spectra of Cs recorded in the vicinity of the $32p_{3/2} \leftarrow 6s_{1/2}$ atomic transition by monitoring Cs^+ ions produced by spontaneous ionisation (panel a) and by monitoring the depletion of the Cs ground-state population (panel b). In both panels the black and the blue traces were obtained in the presence of electric fields of 0 and 10 V/cm, respectively. In panel c, the experimental (dots with error bars) and calculated (solid and dashed lines) Stark shifts of the atomic $32p_{3/2} \leftarrow 6s_{1/2}$ transition (black) and the two-photon $32s_{1/2}33s_{1/2} \leftarrow 6s_{1/2}6s_{1/2}$ pair-resonance peak position are plotted as a function of the external electric-field strength. The Stark shift of the pair resonance is calculated as the sum of the Stark shifts of two isolated atoms, on in the $32s_{1/2}$ state, the other in the $33s_{1/2}$ state.

a molecule in isotropic space must conserve the total parity, the observation of a dipole-quadrupole interaction necessitates the coupling of electronic and nuclear degrees of freedom and a change in the rotational quantum state to compensate for the change in electronic parity. In the following, the experimental observations are described that lead to the conclusion that dipole-quadrupole interactions play a significant role in the photoassociation of Cs atoms into pairs of interacting Rydberg atom.

The dipole-quadrupole interactions in the ultracold Cs gas are revealed by resonances resulting from Rydberg-atom-pair states asymptotically correlated to $ns_{1/2}(n-3)f_j$ and $(n+1)s_{1/2}(n-4)f_j$ dissociation thresholds. These resonances are observed in experiments identical to the ones leading to the previously described $ns_{1/2}(n+1)s_{1/2}$ resonances and rely in particular on Rydberg excitation with an intense pulsed UV laser. The experimental spectra are presented in Fig. 5.7 as solid black traces for $n = 22-32$, along with simulated spectra (dashed traces). The experimental spectra are compared to spectra simulated on the basis of two types of interaction Hamiltonians, one where the dipole-quadrupole interaction term was artificially removed (left-hand side of Fig. 5.7) and one with the full interaction Hamiltonian including the $L_A = 1, L_B = 2$ dipole-quadrupole interaction term (right-hand side of Fig. 5.7). In both simulations, terms up to the quadrupole-quadrupole interaction were considered. The two different sets of simulated spectra clearly show that the experimen-

and symmetry violation). The effects of parity violation by the electro-weak force is negligible in our experiment.

tally observed molecular resonances are solely the result of the dipole-quadrupole interaction term. The resonances are observed close to the dissociations thresholds of $ns_{1/2}(n-3)f_j$ and $(n+1)s_{1/2}(n-4)f_j$ pair states, which are marked by vertical dashed blue and violet lines, respectively, in Fig. 5.7. Each of these resonances consists of an unresolved doublet corresponding to the two $f_{5/2}$ and $f_{7/2}$ fine-structure components. The n dependence of the detunings relative to the asymptotic energy of the $np_{3/2}np_{3/2}$ pair states is a result of the energy dependence of the quantum defects for s, p and f states. The detuning of the $n's_{1/2}n''f_j$ pair states is negative for $n < 23$ and positive for $n > 24$, and becomes almost independent of n in the range of $n = 29-32$, where the two $ns_{1/2}(n-3)f_j$ and $(n+1)s_{1/2}(n-4)f_j$ pair states have detunings of $\sim$1 GHz and $\sim$1.5 GHz, respectively.

The contrast with which these dipole-quadrupole resonances appear in the experimental and in the simulated spectra gradually decreases with increasing principal quantum number, despite the fact that the coupling strength increases with n. The reason for the decreasing contrast of dipole-quadrupole resonances with increasing n is the increased density of states, many of which are directly or indirectly dipole-dipole coupled. Since the dipole-dipole coupling is of longer range, the effects of the shorter-range dipole-quadrupole coupling are more difficult to observe at higher n values.

Even though agreement with the simulated spectra strongly suggests that these resonances are a result of the direct dipole-quadrupole interaction, the excitation of $n's_{1/2}n''f_j$ pair states with two photons from the $6s_{1/2}6s_{1/2}$ ground state could, in principle, also be the result of l mixing induced by an external electric field. In the experimental setup, the residual electric field was measured to be below 25 mV/cm using Stark spectroscopy of high n Rydberg states. For the investigated quantum numbers ($n = 22-32$) such an electric field causes negligible l mixing. To fully exclude any significant contributions from external electric fields, the Stark effect of the $n's_{1/2}n''f_j$ pair states was studied by measuring Rydberg-excitation spectra in externally applied electric fields. The measured Stark spectra are presented in Fig. 5.8c as solid black lines. The resonance at a detuning of ~ -900 MHz is located very close to the $23s_{1/2}18f_j$ and the resonance at a detuning of ~ -2600 MHz located very close to the $22s_{1/2}19f_j$ pair-dissociation asymptotes. The sum of the expected Stark shifts of two isolated atoms in $n's$ and $n''f$ states, respectively, is indicated by blue (for $s_{1/2}f_{5/2}$ states) and red (for $s_{1/2}f_{7/2}$ states) lines and has been calculated using the same procedure as for the $ns_{1/2}(n+1)s_{1/2}$ pair states (see Eq. (5.15)). The shifts, broadenings and splittings of the molecular resonances observed at different electric-field strengths are in good agreement with the calculated Stark shifts, which strongly supports the assignment of these resonances as originating from the excitation of $n's_{1/2}n''f_j$ atom pairs. Moreover, if the excitation of these $n's_{1/2}n''f_j$ resonances were

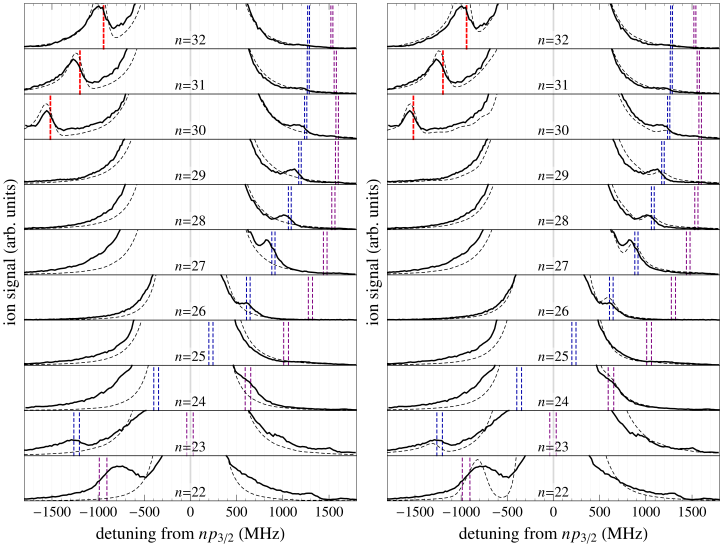

Figure 5.7: Comparison of experimental spectra (thick lines) with simulated line profiles (dashed lines) including the dipole-quadrupole interaction term in the simulation (panel on the right-hand side) or excluding the dipole-quadrupole interaction term (panel on the left-hand side). The dissociation thresholds correlated to $ns_{1/2}(n-3)f_j$ and $(n+1)s_{1/2}(n-4)f_j$ pair states are indicated by vertical dashed blue and violet lines, respectively. The positions of the $ns_{1/2}(n+1)s_{1/2}$ asymptotes are indicated by vertical dashed red lines for $n = 30 - 32$.

caused by a small residual electric field, their intensity should depend on the electric-field strength. The experiment, however, only reveals a broadening and splitting of the resonance by the Stark effect but no increase of the integrated line intensities, even for the highest electric-field strengths (30 V/cm) applied which are almost three orders of magnitude larger than the residual electric stray field. Consequently, l mixing by the stray electric field can be excluded as playing any role in the excitation of these pair states.

Hypothetically, $n's_{1/2}n''f_j$ pair states could also be excited from the $6s_{1/2}6s_{1/2}$ ground state by an electric-dipole transition of one atom and an electric-quadrupole transition of the other atom, rather than by electric-dipole transitions enabled by a weak admixture of $np_{3/2}np_{3/2}$ character induced by the dipole-quadrupole interaction. Even though electric-quadrupole transitions, *e.g.*, of the type $nd_j \leftarrow 6s_{1/2}$ can be observed in the experiments (not shown) and have also been reported in the literature [218], they are much weaker than electric-dipole transitions. Additionally, the excitation of a $n's_{1/2}n''f_j$ pair resonances would be strongly suppressed due to the much larger detuning from intermediate states in the one-colour two-photon ex-

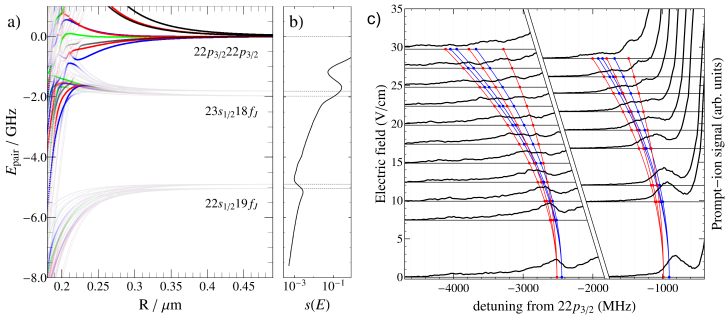

Figure 5.8: a) Calculated potential-energy curves of Cs Rydberg-atom pairs near the $22p_{3/2}22p_{3/2}$ dissociation asymptote for $\Omega = 0, 1, 2, 3$ (black, red, blue, green curves respectively). The intensity of the colour codifies the value of $\overline{p_\Psi}$. Grey corresponds to zero and full colour to a contribution of 5% or more of the $22p_{3/2}22p_{3/2}$ state to the pair state. b) Logarithmic plot of the simulated excitation profile. Dotted lines indicate the asymptotic pair energies. c) Experimental spectra of the $22s_{1/2}19f_j$ and $23s_{1/2}18f_j$ pair states at different electric fields (left and right black traces respectively) and corresponding calculated pair-states asymptotic positions. Blue and red curves corresponds to $s_{1/2}f_{5/2}$ and $s_{1/2}f_{7/2}$ asymptotes, respectively. The experimental spectra are offset by the respective electric field strength in V/cm (marked by the solid base line of each spectrum).

citation scheme. Consequently, electric-quadrupole transitions are negligible in the excitation of $n's_{1/2}n''f_j$ pair states.

Because all alternative excitation mechanisms can be excluded, the dipole-quadrupole interactions are the reason for the observation of the $n's_{1/2}n''f_j$ pair states, even though they do not conserve the electronic parity of the pair state. Consequently, the mixing of electronic states of opposite parity must be caused by a change of the rotational parity of the atom pair which is given by $(-1)^L$, where L is the quantum number associated with the angular momentum of the Cs + Cs collisional complex. This coupling is facilitated in the case of ultracold long-range Rydberg-atom-pair states because of the quasi-degeneracy of rotational levels of the molecular system. Indeed, the interacting Rydberg atoms can be regarded as a colliding pair with reduced mass $\mu = 1/2m_{Cs}$ and relative velocity $v = \sqrt{k_B T/\mu}$. The maximal value $|\vec{L}_{max}|$ of the angular momentum of the collision complex is then given by $\hbar L_{max} = \mu \bar{R} v$, where L_{max} is the corresponding rotational quantum number and $\bar{R}$ is the internuclear separation characteristic of the pair state ($\bar{R} \approx 0.23\,\mu m$ for $n = 22$, see Fig. 5.8). Treating the collision complex as a rotating molecule, one can estimate the rotational constant to be $B_{rot} = \hbar^2/(\mu \bar{R}^2)$ and the spacing between the rotational levels with rotational quantum numbers L (of parity $(-1)^L$) and $L+1$ (of parity $(-1)^{(L+1)}$ to be $2LB_{rot}$. A maximal spacing of $2L_{max}B_{rot}$ of ~ 20 kHz results, which is less than the natural width of $n = 22, l = 0-3$ Rydberg states of Cs. These considerations reveal that rota-

tional states of opposite parity are quasi-degenerate at the internuclear distances and the relative angular momentum of the Rydberg-atom-pair states at low temperatures. Consequently, the relative strengths of electronic-parity-conserving and electronic-parity-violating interaction terms are given by by Eq. (5.2). The inclusion of electronic-parity-violating terms in the interaction Hamiltonian 5.2 is only possible if the basis functions used to set up the Hamiltonian matrix are not symmetrised with respect to permutation of the nuclei, as mentioned in Section 5.1).

5.3.3 Higher-order coupling and window resonances at avoided level crossings

The interaction between the $n\mathrm{p}_{3/2}n\mathrm{p}_{3/2}$ and the $n\mathrm{s}_{1/2}(n+1)\mathrm{s}_{1/2}$ pair states schematically represented in Fig. 5.3b leads to predominantly attractive potential-energy functions correlated to the $n\mathrm{s}_{1/2}(n+1)\mathrm{s}_{1/2}$ dissociation asymptotes and repulsive potential-energy functions correlated to the $n\mathrm{p}_{3/2}n\mathrm{p}_{3/2}$ asymptotes for the range of principal quantum numbers n investigated here. Whereas the former lead to isolated resonances on the low-frequency side of the strong atomic resonances (see, *e.g.*, Figs. 5.4 and 5.3a), the latter lead to dense and complex spectral structures on the high-frequency side of the atomic resonances, which are partially resolved at the lowest n values studied ($n = 22 - 26$). The corresponding spectra are displayed on an expanded scale in Fig. 5.9, where they are compared to numerical simulations performed using the interaction model presented in Section 5.1.

The observed spectral patterns, which are perfectly reproducible in the experiments, are more complex than those observed on the low-frequency side of the atomic resonance and do not reveal any obvious scaling with the principal quantum number. They originate from the interactions of the repulsive $n\mathrm{p}_{3/2}n\mathrm{p}_{3/2}$ pair states with attractive $(n-4)\mathrm{f}_j(n-3)\mathrm{f}_j$ pair states which have their dissociation asymptotes located just above the $n\mathrm{p}_{3/2}n\mathrm{p}_{3/2}$ asymptotes. The numerical simulations of the spectra in these regions indicate that the spectral structures do not only arise from an accumulation of spectral intensity in regions where the potential-energy functions are flat, as in case of the $n\mathrm{s}_{1/2}(n+1)\mathrm{s}_{1/2}$ resonances, but also from a reduction of spectral intensity centred around avoided crossings between states correlated to the $n\mathrm{p}_{3/2}n\mathrm{p}_{3/2}$ and $(n-4)\mathrm{f}_j(n-3)\mathrm{f}_j$ dissociation asymptotes.

The potential-energy functions of the $\Omega = 0$ (black), 1 (red), 2 (blue), and 3 (green) states required to interpret the spectral structures located on the high-frequency side of the $24\mathrm{p}_{3/2}24\mathrm{p}_{3/2}$ asymptotes are depicted in Fig. 5.10. Many pair states correlating to the $20\mathrm{f}_{5/2,7/2}25\mathrm{s}_{1/2}$, $20\mathrm{f}_{5/2,7/2}21\mathrm{f}_{5/2,7/2}$, $22\mathrm{d}_{3/2}24\mathrm{d}_{3/2,5/2}$, $21\mathrm{g}_j24\mathrm{s}_{1/2}$, $20\mathrm{g}_j25\mathrm{s}_{1/2}$ and $21\mathrm{h}_j24\mathrm{s}_{1/2}$ asymptotes are located in this region, but they only possess $24\mathrm{p}_{3/2}24\mathrm{p}_{3/2}$ character near avoided crossings with the $n\mathrm{p}_{3/2}n\mathrm{p}_{3/2}$ ($\Omega = 0-3$) states. In the absence

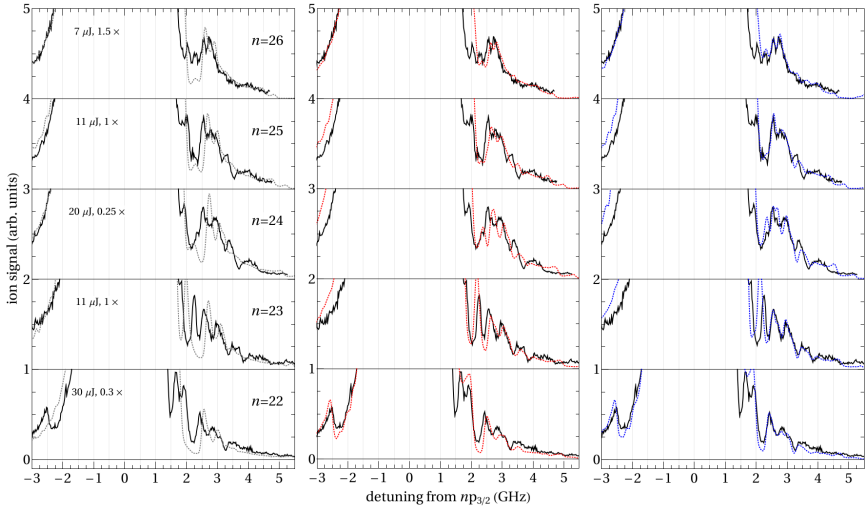

Figure 5.9: UV-laser spectra recorded on the high-frequency side of $np_{3/2} \leftarrow 6s_{1/2}$ transitions of Cs. The experimental spectra (black traces) represent the spontaneously-produced Cs^+ ion signal as a function of the one-photon detuning of the atomic transitions. In the three panels, the same experimental spectra are compared to simulations based on a potential model including successively higher order coupling terms in the multipole-interaction operator (left-hand side: up to dipole-dipole interactions, grey; middle: up to quadrupole-quadrupole interactions, red; right-hand side: up to octupole-octupole interactions, blue). The pulse energies used to record the spectra and the relative intensity-scaling factors are indicted below each experimental trace in the panel on the left-hand side.

of these crossings, the repulsive curves associated with the $24p_{3/2}24p_{3/2}$ asymptote would lead to a broad and structureless high-frequency wing of the atomic transition. However, at the avoided crossings no curve possesses significant $24p_{3/2}24p_{3/2}$ character. Consequently, the spectral excitation function $s(E)$ has minima that can be directly linked to the avoided crossings, as indicated by the horizontal dashed lines in Fig. 5.10.

The simulations of the spectra presented in Fig. 5.9 (and in Fig. 5.10) indicate that a potential model restricted to the dipole-dipole interaction fails to reproduce the details of the spectral structures (left panel) on the high-frequency side of the atomic transitions and that the successive inclusion of interaction terms up to the octupole-octupole term gradually improves the agreement between measured and calculated spectra.

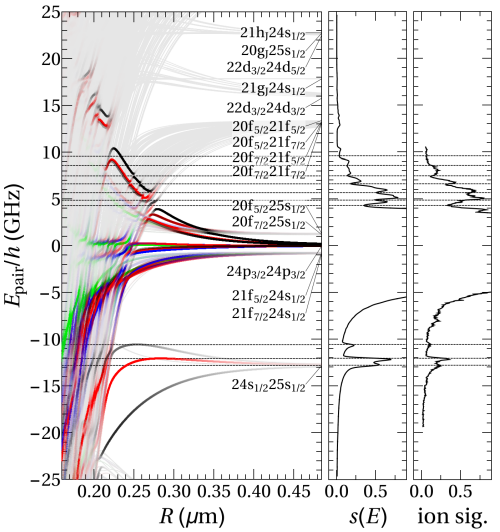

Figure 5.10: Calculated potential-energy functions around the $24p_{3/2}24p_{3/2}$ pair-dissociation asymptote (left panel), simulated spectrum $s(E)$ (middle, arbitrary units), and measured Cs^+-ion signal as a function of the two-photon detuning $2\Delta\nu$ (right panel, arbitrary units). The colour depths of the potential curves (black, red, blue and green for $\Omega = 0, 1, 2, 3$, respectively) represents the $\tilde{p_\Psi}(R)$ values, where full colour indicates 1% $24p_{3/2}24p_{3/2}$ character in the molecular state and grey denotes 0% $24p_{3/2}24p_{3/2}$ character. The horizontal dashed lines indicate the positions of minima and maxima in the simulated spectrum for comparison with the experiment and the calculated potential-energy functions.

5.3.4 Millimetre-wave transitions between Rydberg-atom-pair states

The ability to observe well-resolved transitions to $ns_{1/2}(n+1)s_{1/2}$ dipole-dipole-coupled pair states with good signal-to-noise ratio offers the possibility to further characterise these states by studying transitions to neighbouring dipole-dipole-coupled states using millimetre-wave radiation. In a similar fashion microwave transitions between pairs of Rb Rydberg atoms were studied by Yu *et al.* [219].

Experimental results

At large internuclear distances and for pair states correlated to $ns_{1/2}(n+1)s_{1/2}$ dissociation asymptotes, one expects the most intense transitions to be those to pair states located near $ns_{1/2}n_1p_J$ and $n_2p_J(n+1)s_{1/2}$ asymptotes, where the values of the principal quantum numbers n_1 and n_2 are close to the value of n. The investigation presented here focused on the $32s_{1/2}33s_{1/2}$ pair state and on the millimetre-wave transitions to the pair states near the $32s_{1/2}33p_{3/2}$ and $31p_{3/2}33s_{1/2}$ asymptotes,

which lie 129611 MHz above, and 157962 MHz below the $32s_{1/2}33s_{1/2}$ asymptote, respectively (see Fig. 5.11a)). The detection of the millimetre-wave transitions requires a state-selective detection of Rydberg atoms, which was achieved by delayed pulsed-field ionisation with a slowly rising electric-field ramp (rise time 1 µs) and monitoring the Cs^+-ion time-of-flight (TOF) spectra. To calibrate the TOF spectra, experiments were first performed in low-density samples following single-photon laser excitation to the $np_{3/2}$ ($n = 31, 33$) and non-resonant single-colour two-photon excitation to the $n's_{1/2}$ ($n' = 32, 33$) Rydberg states of Cs. The resulting Cs^+ TOF traces are displayed in the lower panel of Fig. 5.12 and reveal distinct maxima for the four Cs Rydberg states. This state selectivity makes it possible to record millimetre-wave spectra of the $33p_{3/2} \leftarrow 33s_{1/2}$ and $32s_{1/2} \rightarrow 31p_{3/2}$ transitions by monitoring the Cs^+-ion signal at the corresponding TOF positions, as illustrated by the spectra displayed as dotted lines in Fig. 5.11b) and c), respectively. The lines in these spectra have a near-Fourier-transform-limited width of 2 MHz. The Cs^+-ion TOF spectrum obtained at the

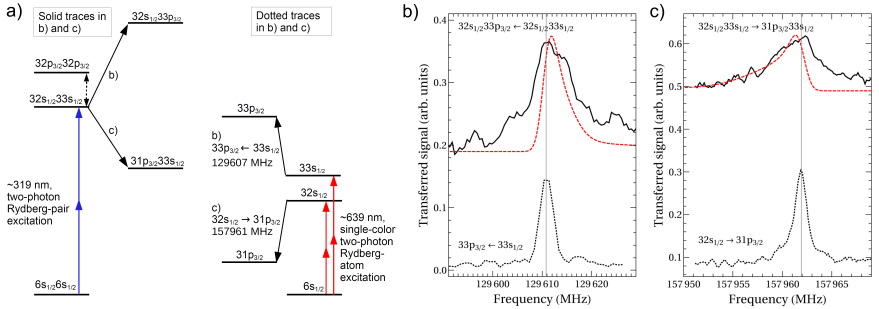

Figure 5.11: a) Schematic energy diagram of the $32s_{1/2}33s_{1/2} \leftarrow 6s_{1/2}6s_{1/2}$ pair-state excitation (left-hand side, blue arrows) and the single-colour two-photon excitation of $ns_{1/2} \leftarrow 6s_{1/2}$ transitions (right-hand side, red arrows). millimetre-wave transitions are indicated with black arrows in the energy-level diagrams. Experimental millimetre-wave spectra of the $33p_{3/2} \leftarrow 33s_{1/2}$ (b) and $32s_{1/2} \rightarrow 31p_{3/2}$ (c) transitions recorded following excitation of the $32s_{1/2}33s_{1/2}$ pair state (solid black traces) and following excitation of the atomic $ns_{1/2} \leftarrow 6s_{1/2}$ transitions (dashed black traces). The spectra represent the ratio of ions detected in the integration window of the relevant final Rydberg states over the ions detected in the integration windows corresponding to both the final and initial Rydberg states (see Fig. 5.12). The red dashed lines are spectra simulated with a model taking into account all relevant Rydberg-Rydberg–pair potentials and considering the Penning-ionisation dynamics, as explained in more detail in the text.

position of the $32s_{1/2}33s_{1/2}$ pair resonance and a delay of 1 µs between the laser and the electric-field pulse is displayed as red trace in the upper panel of Fig. 5.12. It consists of an intense sharp peak at early times which is attributed to Cs^+ ions produced before the electric-field pulse (the dynamics of the ionisation process is discussed in Section 5.3.5), and a broad distribution with only weak maxima at the positions

expected for the pulsed-field ionisation of the atomic $32s_{1/2}$ and $33s_{1/2}$ states.

Compared to the TOF spectra recorded for the non-interacting Cs Rydberg gas, the state selectivity of the pulsed-field-ionisation process is reduced. The reduction is attributed at least in part to adiabatic traversals of the curve crossings between different pair states, *e.g.*, between the $32s_{1/2}33s_{1/2}$ and $32p_{3/2}32p_{3/2}$ states (see Fig. 5.6) before and as the electric field is ramped up. A similar observation was made by Han and Gallagher in their study of the field-ionisation dynamics in an ultracold Rb Rydberg gas (see in particular their Fig. 4 in Ref. [220]). The reduced state selectivity of the field ionisation causes a millimetre-wave-radiation-independent background signal at the TOF positions corresponding to the $31p_{3/2}$ and $33p_{3/2}$ Rydberg states, which makes the recording of millimetre-wave spectra of the $(31p_{3/2}33s_{1/2}, 32s_{1/2}33p_{3/2}) \leftarrow 32s_{1/2}33s_{1/2}$ transitions difficult. However, comparing the Cs^+-ion TOF spectrum recorded with and without millimetre-wave radiation under otherwise identical conditions reveals a weak enhancement of the $33p_{3/2}$ PFI signal and a weak depletion of the $33s_{1/2}$ PFI signal when the millimetre-wave frequency is tuned to the $33p_{3/2} \leftarrow 33s_{1/2}$ resonance (see dark red trace in Fig. 5.12).

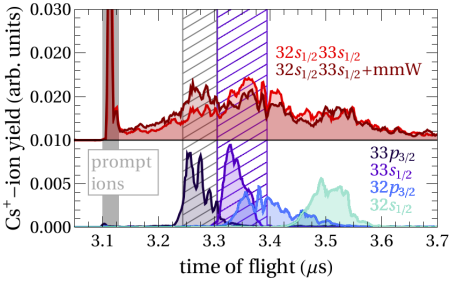

Figure 5.12: Cs^+-ion time-of-flight (TOF) distributions measured using a pulsed extraction field of 1.25 kV/cm with a 1 µs rise time. Top panel: TOF distributions following the two-photon excitation of the $32s_{1/2}33s_{1/2}$ pair state without (red trace) and with millimetre-wave radiation (mmW) with the frequency tuned to the $33p_{3/2} \leftarrow 33s_{1/2}$ transition (brown trace). Bottom panel: TOF distributions following the one-photon excitation of the atomic $33p_{3/2}$ (black trace) and $32p_{3/2}$ (blue trace) states, and the two-photon excitation of the atomic $33s_{1/2}$ (violet trace) and $32s_{1/2}$ (turquois trace) states. The $ns_{1/2}$ states have been excited from the $6s_{1/2}$ ground state in single-colour two-photon transitions. Hatched areas indicate the integration windows used to extract the spectra shown in Fig. 5.11b).

The ion-signal ratios at the TOF positions of the $33p_{3/2}$ and $33s_{1/2}$ states (indicated by hatched grey and violet areas in Fig. 5.12, respectively) and at the positions of the $31p_{3/2}$ and $32s_{1/2}$ states were used to record millimetre-wave spectra of the transitions from the $32s_{1/2}33s_{1/2}$ pair state to regions near the $32s_{1/2}33p_{3/2}$ and $31p_{3/2}33s_{1/2}$ asymptotes, respectively. These spectra are presented as solid lines

in Fig. 5.11b) and c). The observation of a millimetre-wave-dependent PFI signal corresponding to the $31p_{3/2}$ and the $33p_{3/2}$ Rydberg states represents a further experimental verification of the $32s_{1/2}33s_{1/2}$ nature of the laser-excited pair resonance. Compared to the millimetre-wave spectra recorded in the non-interacting Rydberg gas, the transitions are broadened and degraded toward lower (higher) frequencies in the case of the $32s_{1/2}33s_{1/2} \rightarrow 31p_{3/2}33s_{1/2}$ ($32s_{1/2}33p_{3/2} \leftarrow 32s_{1/2}33s_{1/2}$) transition. Although the large background signal and the poor signal-to-noise ratio of the millimetre-wave spectra of the pair states prevent a quantitative analysis, the spectra enable one to draw the following qualitative conclusions: *i*) The weak line broadenings and frequency shifts compared to the transitions recorded in the non-interacting Rydberg gas suggest that the Rydberg-atom pairs contributing to the spectra have a large interatomic separation. *ii*) The red (blue) shift of the transitions to the $31p_{3/2}33s_{1/2}$ ($32s_{1/2}33p_{3/2}$) pair state reveals that the potential curves of the $n'p_{3/2}ns_{1/2}$ pair states are less strongly attractive, at long range, than is the case for the $32s_{1/2}33s_{1/2}$ pair state, despite the fact that the dipole-dipole interaction is resonant ($ns_{1/2}n_2p_j$ and $n_1p_jns_{1/2}$ are degenerate when $n_1 = n_2$).

The observation of a prompt ionisation signal further shows that an important fraction of the initial population in the $32s_{1/2}33s_{1/2}$ pair state decays by ionisation on the sub-microsecond timescale and therefore does not contribute to the millimetre-wave spectra. The millimetre-wave spectra can be adequately modelled (see red dashed traces in Fig. 5.11) by taking into account the motion of the Rydberg-atom pairs on their potential-energy curves, as explained in the following.

Simulation

The potential model and the spectral distribution function $s(E)$ presented in Section 5.1 were also used to calculate the millimetre-wave spectra of the $32s_{1/2}33p_{3/2} \leftarrow 32s_{1/2}33s_{1/2}$ and $32s_{1/2}33s_{1/2} \rightarrow 31p_{3/2}33s_{1/2}$ transitions displayed in Figs. 5.11b) and c). To this end, the relative population in the two $\Omega = 0$ and the $\Omega = 1$ states that are accessed optically at the peak of the $32s_{1/2}33s_{1/2}$ resonance was used as initial distribution of Rydberg-atom–pair states, and transitions from these states to the pair states correlating to the $31p_{3/2}33s_{1/2}$ and $32s_{1/2}33p_{3/2}$ asymptotes that are accessible in a single-photon millimetre-wave transition were considered. The relevant potential-energy functions are displayed in Fig. 5.13.

The attractive nature of the potential functions associated with the $32s_{1/2}33s_{1/2}$ asymptote implies, in a classical description of the nuclear motion, that the internuclear separation decreases with time. Because the potential curves of the states associated with the $31p_{3/2}33s_{1/2}$ and $32s_{1/2}33p_{3/2}$ asymptotes are less attractive than those of the states associated with the $32s_{1/2}33s_{1/2}$ asymptote, the frequency of the

$32s_{1/2}33s_{1/2} \rightarrow 31p_{3/2}33s_{1/2}$ transition decreases, and that of the $32s_{1/2}33p_{3/2} \leftarrow 32s_{1/2}33s_{1/2}$ increases, with time. This evolution (chirp) of the transition frequencies reduces the transition probabilities. The narrow bandwidth (1 MHz) of the millimetre-wave radiation implies that the main contribution to the millimetre-wave spectra originates from pairs with large internuclear separation R, for which the evolution (chirp) of the transition frequency is slow.

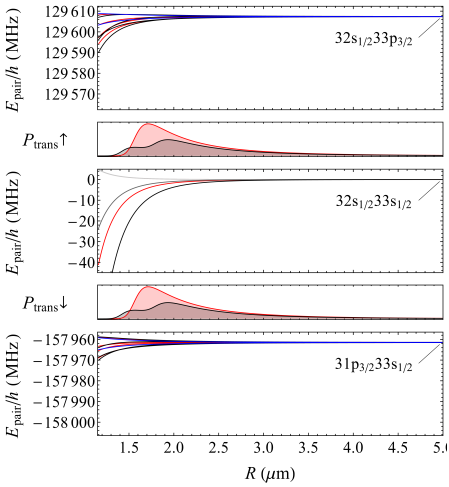

Figure 5.13: Potential-energy curves of the states correlated to the $32s_{1/2}33s_{1/2}$ (middle panel), the $32s_{1/2}33p_{3/2}$ (top panel) and the $31p_{3/2}33s_{1/2}$ (bottom panel) asymptotes used for the simulation of the millimetre-wave spectra presented as red dashed lines in Figs. 5.11b) and c). Black (grey), red and blue designate states with $\Omega = 0, 1$ and 2, respectively. The intermediate panels present the transition probabilities calculated for the absorption ($P_{\text{trans}}\uparrow$) and stimulated emission ($P_{\text{trans}}\downarrow$) out of the $\Omega = 0$ (black) and $\Omega = 1$ (red) states correlated to the $32s_{1/2}33s_{1/2}$ asymptote. All energies are given relative to the energy of the $32s_{1/2}33s_{1/2}$ asymptote. See text for details.

To model the intensity distribution, a cut-off chirp of 2 MHz/µs was introduced, beyond which it is assumed that the transitions are too weak and broad to be observed and determines the range of internuclear separations contributing to the millimetre-wave transition intensities. In this range, the distribution of transition frequencies is calculated from the potential-energy curves. For each frequency, the spectral intensities are determined as sum over products of the initial populations in the $\Omega = 0$ and 1 states correlated to the $32s_{1/2}33s_{1/2}$ asymptote and the relative transition probabilities

$$P_{\text{trans}}(R) = \sum_{i,f} f_{\Psi,i}(R)\overline{p_{\Psi,i}}(R) \; \left|\langle \Psi_f(R)|\hat{\mu}_{0,\pm 1}|\Psi_i(R)\rangle\right|^2 R^2, \tag{5.16}$$

where $f_{\Psi,i}(R)$ is the cutoff function described above, $\hat{\mu}_{0,\pm1}$ is the sum of $\sigma^{\pm}$ and π electric-dipole transition operators, and the double sum runs over all initially excited pair-state Ψ_i for a fixed value of Ω and all dipole-coupled final states Ψ_f.

The calculated spectra, convoluted with the experimental line-shape function of the corresponding atomic transitions, are displayed as dashed red lines in Figs. 5.11b) and c) and are in qualitative agreement with the experimental ones. In particular, the shifts from the asymptotic transition frequencies, which correspond to the spectra of the isolated atoms displayed as lower traces, and the asymmetric line shapes (red-degraded for the $32s_{1/2}33s_{1/2} \rightarrow 31p_{3/2}33s_{1/2}$ transition and blue degraded for the $32s_{1/2}33p_{3/2} \leftarrow 32s_{1/2}33s_{1/2}$) are well described by the calculations. This agreement represents a further illustration of the ability of the potential model to describe the spectral and dynamical properties of Rydberg-atom pairs.

5.3.5 Penning ionisation

The spontaneous ionisation of Rydberg atoms in the gas phase is the first step in the evolution of a dense Rydberg gas towards a plasma. Spontaneous ionisation of a Rydberg gas was first reported by Vitrant *et al.* [51], who pointed out that it reduces the lifetimes of Rydberg states in dense samples. Interest in the ionisation process was renewed with experiments on ultracold atoms which provided detailed information on the evolution from an ultracold Rydberg gas to an ultracold plasma [53]. This evolution can be described by an avalanche-ionisation model [221] that involves an initial seed ionisation process, during which ions are produced in the ultracold gas and the free electrons escape. Once the positive space charge of the ions is sufficiently high to trap low-energy electrons, the remaining Rydberg atoms are rapidly ionised by collisions with the electrons. For the seed-ionisation process, experiments pointed at the importance of a small fraction of hot Rydberg atoms and blackbody-radiation-induced photoionisation [53], static orbital overlap between close-lying Rydberg-atom pairs, sequences of quasi-resonant dipole-dipole transitions [222, 223], and interaction-induced motion leading to Rydberg-Rydberg collisions and Penning ionisation [54, 224, 225].

The dynamics leading to the seed ionisation depends on the density of the excited Rydberg atoms, on the Rydberg state and on the details of the interaction between the Rydberg atoms. At high n values ($n \approx 100$) and high Rydberg-atom densities ($> 10^9\,\mathrm{cm}^{-3}$), the complete ionisation of the Rydberg gas occurs in less than 100 ns, as reported in Ref. [220] and confirmed in the present work (not shown). The theoretical understanding of this fast ionisation process is still incomplete, but a classical simulation [226] suggests that many-body interactions and excitation of closely-spaced pairs of Rydberg atoms play an important role under these conditions. At lower den-

sities and n values, Penning-ionisation processes [54, 176, 224, 225, 227] involving two Rydberg atoms, one atom undergoing a transition to a lower state and the other being ionised, have been identified as the dominant seed-ionisation mechanism.

Experimental results

To characterise the processes leading to the strong prompt Cs^+ ionisation signal in the studies of millimetre-wave transitions between Rydberg-pair states (see upper panel of Fig. 5.12), the ionisation dynamics of the $32s_{1/2}33s_{1/2}$ pair state was studied at a time resolution of 100 ns limited by the temporal resolution of the Cs^+-ion–TOF spectra. The experiments consisted in monitoring the yield of Cs^+ ions produced spontaneously during the delay time between the laser excitation pulse and the application of the pulsed electric field as a function of the UV-laser frequency. The spontaneously formed ions are accelerated from the beginning of the electric-field ramp used for the field-ionisation and thus arrive first on the detector, see the integration-windows labelled “prompt ions” in Fig. 5.12.

The results of this investigation are presented in Fig. 5.14a), which compares spectra of the $32s_{1/2}33s_{1/2}$ pair resonance recorded for several delay times between 200 ns and 9.9 µs. At the shortest delay times, the peaks in the prompt-ion signal are observed $\approx 2 \times 300$ MHz below the $32s_{1/2}33s_{1/2}$ asymptote and are very weak. The intensity of the resonance grows with increasing delay time and its position gradually shifts toward the $32s_{1/2}33s_{1/2}$ asymptote, and stabilises at $\approx 2 \times 75$ MHz below this asymptote at delay times beyond 1 µs. This deviation from the asymptotic pair energy is the interaction-induced shift ΔE_{int} discussed in section 5.3.1 and shown in the inset of Fig. 5.3c. The time dependence of the resonance position is displayed in the upper left inset of Fig. 5.14.

Because the total density of Rydberg atoms in these experiments is still very low (on the order of 10^8 atoms/cm^3), the experimental observations can be qualitatively understood as resulting from the purely pair-wise Penning-ionisation mechanism. Pairs of Rydberg atoms are excited at well-defined initial separations given by the detuning of the excitation laser from the dissociation asymptote and are accelerated on the attractive potential-energy curves. The first pairs that ionise are those characterised by the strongest shifts, *i.e.*, those that correspond to the shortest internuclear distances and are thus subject to the strongest attractive interactions. As the delay time increases, atom pairs subject to smaller shifts and thus weaker attractive interactions start contributing to the prompt-ion signal in the TOF spectra. These pairs have larger initial internuclear separations and require longer times before the motion on the attractive potential leads to ionising collisions. Based on these qualitative interpretation, a quantitative model for Penning ionisation was developed in which

the motion of the atoms on the long-range potentials is calculated classically. This model and its predictions are discussed in the following.

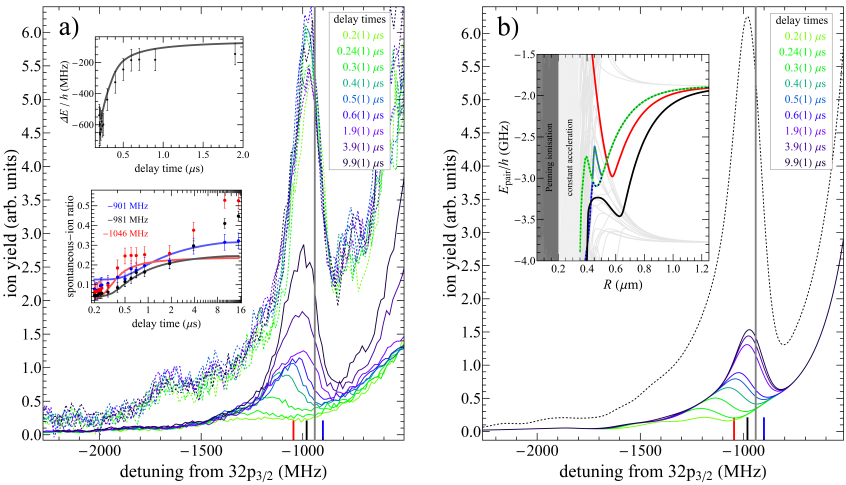

Figure 5.14: a) Spontaneous-ionisation signal as a function of the detuning of the UV-laser frequency from the $32p_{3/2} \leftarrow 6s_{1/2}$ transition and of the delay between laser pulse and pulsed ion-extraction field (solid coloured traces, values for the delay time given in the upper right inset). The spectral position corresponding to the asymptotic energy of the $32s_{1/2}33s_{1/2}$ pair state is shown by a vertical grey bar. Simultaneously recorded spectra of the total ion signal including ions resulting from pulsed-field ionisation are shown as dashed coloured traces on the same scale. The interaction-induced shift (*i.e.*, twice the detuning of the resonance peak from the asymptotic energy of the $32s_{1/2}33s_{1/2}$ pair state) is given in the upper left inset and the fractions of spontaneous ion to the total-ion signals at the detunings indicated by red, black, and blue lines on the horizontal axis are displayed in the lower left inset, as functions of the delay time. Experimental values are shown as dots with error bars and simulated quantities as solid lines. b) Spectra simulated for the same experimental parameters as in panel a), as described in Sec. IV C. The inset shows the potential-energy functions (the two $\Omega = 0$ (green, blue, and black) and the $\Omega = 1$ (red) potentials associated with the $32s_{1/2}33s_{1/2}$ asymptote are shown in colour) of pair states below the $32p_{3/2}32p_{3/2}$ asymptote as a function of the internuclear separation.

Simulation of Penning ionisation with a model based on classical dynamics

To analyze the Penning-ionisation experiments described previously (see in particular Fig. 5.14a), a simple model was set up which relies on the spectral excitation function $s(E)$ and treats the relative motion of the atoms on the two $\Omega = 0$ and the $\Omega = 1$ potential curves associated with the $32s_{1/2}33s_{1/2}$ asymptote classically. All other pair states are excited at short range (*i.e.*, at R values below 0.4 μm) and only contribute to

the spectra weakly on the low-frequency side of the resonance. The potential curves of the relevant molecular states are drawn in colour in Fig. 5.14b). Below 0.7 μm, the potential-energy curves reveal several avoided crossings. Following photoexcitation, the two interacting Rydberg atoms are accelerated towards each other until Penning ionisation takes place, which is assumed, for simplicity, to happen at an interatomic distance of 200 nm that is well below the LeRoy radius of ~ 270 nm for two Cs atoms in $32s_{1/2}$ and $33s_{1/2}$ states. The probabilities of adiabatic traversals of the avoided crossings are estimated with the Landau-Zener formula

$$P_{\mathrm{diab}} = \exp\left\{-2\pi \frac{|V_{12}|^2}{\hbar(\mathrm{d}E/\mathrm{d}t)}\right\}; P_{\mathrm{adiab}} = 1 - P_{\mathrm{diab}}, \tag{5.17}$$

where V_{12} represents the minimal distance between the potential curves and the slew rate $\mathrm{d}E/\mathrm{d}t$ is determined from the relative motion of the two atoms on the potential curves. The first avoided crossing of the $\Omega = 1$ state (see red curve in Fig. 5.14b)) is traversed adiabatically ($P_{\mathrm{adiab}} > 99\%$). The adiabatic potential has a minimum at $R \approx 0.58\,\mu\mathrm{m}$ and the state therefore does not rapidly reach the region where Penning ionisation takes place. The motion on the two $\Omega = 0$ potential curves (black and blue/green lines in Fig. 5.14b)) is such that the regions of short internuclear distances where Penning ionisation takes place is reached rapidly despite several avoided crossings. The simulation of the ionisation dynamics of the $\Omega = 0$ states adequately reproduces both the rise of the spontaneous-ionisation signal and the gradual shift of the peak position (see insets of Fig. 5.14a)) observed experimentally for delay times up to $\approx 2\,\mu\mathrm{s}$. For longer delay times a slower rise of the spontaneous-ionisation signal up to $\approx 10\,\mu\mathrm{s}$ is observed, which is not explained by the model (see lower inset of Fig. 5.14a)). This additional ion signal is attributed to the ionisation of pairs of atoms in the $\Omega = 1$ state. A possible mechanism could be a weak mixing of $\Omega = 0$ and $\Omega = 1$ states (*e.g.* by a residual electric field), which would lead to a small avoided crossing of the two symmetries (see red and green/blue traces in the inset of Fig. 8b) at $R \sim 0.5$ μm) and open a path for ionisation of pairs in the metastable $\Omega = 1$ state. The probability for an adiabatic crossing is inversely proportional to the velocity of the two colliding atoms at the crossing (see Eq. (5.17)). For pairs excited at lower frequencies, this velocity decreases and the ionisation probability thus increases. This is consistent with the observed increase of the deviation between experimental and simulated ionisation signals at longer delays when the excitation laser is tuned to lower frequencies (see lower inset in Fig. 8a)). For long delay times, the experimental spontaneous-ion signal approaches approximately 50% of the initial total ion signal, which indicates that every pair of atoms eventually undergoes a Penning ionisation process.

The model discussed in this section predicts the correct qualitative behaviour of

fast and slow spontaneous ionisation processes, but does not satisfactorily explain the observation of an almost constant total-ion signal for all experimental delay times (see dashed-coloured traces in Fig. 5.14a)). Indeed, one can predict, by considering energy conservation only, that the Rydberg atom undergoing a transition to a lower Rydberg state in the Penning ionisation process must end in a level with $n^* < 21$. The amplitude of the pulsed electric field used for field ionisation (1250 V/cm) should, however, only ionise Rydberg states with $n^* > 22$.

5.3.6 Long-pulse laser excitation of Rydberg-atom-pair states

At higher n values, the $ns_{1/2}(n+1)s_{1/2}$ pair-state can also be excited with a much lower-peak-power continuous-wave UV laser. This is because of the increased coupling strength and, primarily, the small energy defect between the $44p_{3/2}44p_{3/2}$ and the $44s_{1/2}45s_{1/2}$ state, corresponding to a detuning of only 52 MHz in the two-photon pair-state excitation. The measured cw-UV-laser spectrum is depicted in Fig. 5.15 together with a simulation based on Eq. (5.9) (see thick red line). To reproduce the broad atomic transition close to zero detuning, a Lorentzian function with a full width at half maximum of 12 MHz centred at zero detuning was added to the line profile $s(E)$. Apart from two resonances on the low-frequency side of the atomic transition[j], the complete spectrum can be reproduced by the simulation.

The main difference between the spectrum presented in Fig. 5.15 and the spectra presented in Section 5.3.1 is the increased spectral resolution, that enables the observation of the molecular resonance at small detunings. Much better defined is also the interaction-induced shift ΔE_{int} of the resonance peak from the asymptotic energy (vertical grey bar in Fig. 5.15). Since the $ns_{1/2}(n+1)s_{1/2}$ states are found at positive detunings for $n > 42$, the molecular potentials correlated to the $ns_{1/2}(n+1)s_{1/2}$ asymptote are now repulsive, resulting in a blue-degraded line shape, which is well reproduced in the simulation at $n = 44$.

The excitation to repulsive states at long range ($R > 1\,\mu$m) also leads to a reduced ionisation rate of the pair state. Penning ionisation as the main ionisation channel for attractive molecular states should not directly occur in the repulsive Rydberg-atom pair. Nevertheless, increased ionisation rates have also been reported for the excitation to repulsive curves compared to atomic Rydberg excitation because of the interaction-induced motion [228] and heating of the ultracold Rydberg sample and have also been observed in the present work. To obtain a better signal-to-noise ratio, the pulsed-field-ionisation signal is plotted in the spectrum depicted in Fig. 5.15 rather than just the spontaneous-ion signal.

[j] These resonances originate from long-range originate from long-range Rydberg molecules bound by low-energy-electron–neutral-atom scattering (see Chapter 4).

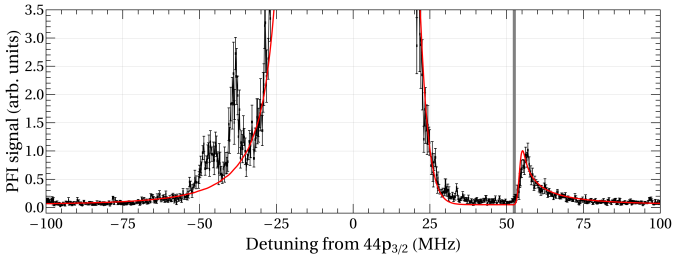

Figure 5.15: Continuous-wave UV-laser Rydberg excitation spectrum of Cs in the vicinity of the $44p_{3/2} \leftarrow 6s_{1/2}$ transition (black dots). A simulated line profile based on Eq. (5.9) is shown as a thick red line. The position of the $44s_{1/2}45s_{1/2}$ pair-dissociation asymptote is indicated by a vertical grey line.

The high-resolution cw-laser excitation of interacting Rydberg-atom-pair states is restricted to states with a small energy detuning from the optically accessible state, which excludes the large majority of the molecular levels. An experimental excitation scheme that enables high-resolution spectroscopy of a wider range of interacting pair states is presented in Chapter 6.

5.4 Conclusions

In this chapter a comprehensive survey of Rydberg excitation spectra in a dense (density $\sim 10^{12}$ atoms/cm^3), ultracold ($T = 40$ μK) Cs gas recorded using an intense (peak intensity 10^8 W/cm^2) narrow-band (bandwidth 140 MHz) UV laser source is presented.

Next to strong lines corresponding to the atomic $np_{3/2} \leftarrow 6s$ transitions, the spectra also exhibit a very rich structure of weaker, sharp spectral features, which are attributed to pairs of Rydberg atoms, also known as Rydberg macrodimers [191, 229], interacting through long-range electrostatic forces. Sharp features of three different origins have been identified: *i*) lines with maxima at positions located very close to $ns_{1/2}(n+1)s_{1/2}$ and $ns_{1/2}(n-3)f_j$ dissociation asymptotes and which correspond to the formation of weakly interacting Rydberg-atom pairs at long range, *ii*) lines with maxima located above the $ns_{1/2}(n+1)s_{1/2}$ dissociation asymptotes and which correspond to excitation to flat potential regions near local maxima of the potentials of $\Omega = 0$ and 1 molecular states correlated with $ns_{1/2}(n+1)s_{1/2}$ dissociation asymptotes, and *iii*) "window" resonances located on the high-frequency side of the atomic transitions, which arise from avoided crossings between repulsive molecular potential curves correlated to $np_{3/2}np_{3/2}$ dissociation asymptotes and attractive potentials near $(n-4)f_j(n-3)f_{j'}$ $(j, j' = 5/2, 7/2)$ dissociation asymptotes. The first category of resonances has been observed in earlier studies (see, *e.g.*, Refs. [58–60, 62, 63]). The

observation of the latter two categories *ii*) and *iii*) represents the first major result of this investigation.

The second major result is the observation of the direct excitation of pairs of cesium atoms from the $6s_{1/2}$ ground state to molecular states correlating asymptotically to $n's_{1/2}n''f_j$ asymptotes. The molecular resonances were interpreted as originating from the dipole-quadrupole interaction between the $n's_{1/2}n''f_j$ pair states and closeby $np_{3/2}np_{3/2}$ asymptotes ($21 \leq n \leq 32$). This interpretation was supported by Stark spectroscopy of the pair states and a detailed modelling of the interaction potentials. It is shown that the dipole-quadrupole interaction mixes electronic states of opposite parity and thus requires a coupling between electronic and nuclear motion to conserve the total parity of the system. This non-Born-Oppenheimer coupling is facilitated in Rydberg-atom-pair states by the near-degeneracy of even and odd ℓ partial waves in the atom-atom scattering which have opposite parity.

The third major result is the demonstration, on the basis of a rigorous comparison of experimental and calculated spectra, that long-range molecular potential models provide a quantitatively correct and accurate description of the behaviour of interacting Rydberg atoms in ultracold gases, provided that a sufficient number of channels and long-range interaction terms are considered. The potential model derived to describe Cs Rydberg-atom pairs adequately reproduces experimental UV-laser photoassociation spectra, millimetre-wave spectra of transitions between different Rydberg-atom–pair states, and the observed Penning-ionisation dynamics of the Rydberg-atom pairs. Given the very high density of electronic states, it first appears astonishing that adiabatic potential models are at all adequate to describe the spectral and dynamical properties of interacting Rydberg-atom pairs. The reason for the usefulness of such models is that, in the range of interaction strengths and internuclear distances that are relevant for most experiments in ultracold Rydberg gases, the heavy nuclei are almost stationary on the time scale associated with the electronic motion, taken as the inverse state density, *i.e.*, about 1 ns at $n \approx 24$.

In the discussion of dipole- and van der Waals-blockade effects in the excitation of Rydberg states, the attractive and repulsive potentials arising from the dipole-dipole interaction near the asymptotes of Rydberg-atom–pair states, are often represented, for clarity and simplicity, as two-level systems of the kind depicted in Fig. 5.3b. The present analysis of Rydberg-atom–pair states of Cs in the range of principal quantum number $n = 22 - 36$, which includes all relevant potential curves and long-range interaction terms, demonstrates the limits of two-level Rydberg-blockade models. Indeed, many interacting molecular potentials give rise to a multitude of avoided crossings, resonances and level shifts. The range of observable phenomena is thus much wider than two-level blockade models predict, which on the one hand reduces their range of applicability, but on the other also offers new opportunities for scientific investi-

gations and applications.

The fact that the calculations almost perfectly reproduce the experimental spectra (see Figs. 5.3 and 5.9) is remarkable and clearly reveals that *i*) the long-range adiabatic potential model is adequate both with respect to the multipole expansion and the basis set, and *ii*) pairwise interactions are sufficient to fully describe the behaviour of the Rydberg gas at the time scale probed by the laser pulses ($\approx$ 5ns) under the experimental conditions used to record the spectra.

Chapter 6

Resonant two-colour excitation of interacting Rydberg atoms

Two-colour laser-excitation schemes of the type depicted in Fig. 6.1b) and c) have been used so far only in a few experiments to study interactions between Rydberg atoms (see, *e.g.*, [225]), and are applied here to study interacting Rydberg-atom-pair states at a spectral resolution of $\sim 3\,\mathrm{MHz}$, almost two orders of magnitude better than in the experiments described in Chapter 5. The main motivation for these experiments is the observation of bound Rydberg macrodimers.

Rydberg macrodimers are formed by two Rydberg atoms interacting at long range *via* van der Waals forces. Their existence [61, 191, 195, 229, 230] as well as some of their unique properties [231] have been predicted theoretically. The bound states are predicted to be localised in long-range potential wells that result from avoided crossings between different molecular potential functions.

So far, molecular resonances were observed following one-colour two-photon excitation of ultracold gases and identified as arising from the correlated excitation of two interacting Rydberg atoms [58–60, 62–65]. Indirect evidence for bound Rydberg macrodimers could be obtained from ion time-of-flight spectra measured following delayed pulsed field ionisation (PFI) of states at a specific electric field [63], and from the dynamics during Penning ionisation of macrodimers under field-free conditions (see Chapter 5 and Ref. [65]). The one-colour two-photon excitation scheme used to study Rydberg macrodimers so far is schematically depicted in Fig. 6.1a). To be in resonance with a molecular state Ψ, which is shifted by Δ from a pair-dissociation asymptote, necessitates a detuning of the laser frequency by $\delta = \Delta/2$ from the intermediate singly excited state. The observation of such transitions requires either the high intensities of pulse-amplified lasers (see Chapter 5 and, *e.g.*, Ref. [58]) with reduced frequency resolution, or the strong long-range coupling of high-n Rydberg levels, where the vibronic state density of the interacting Rydberg-atom pairs is too

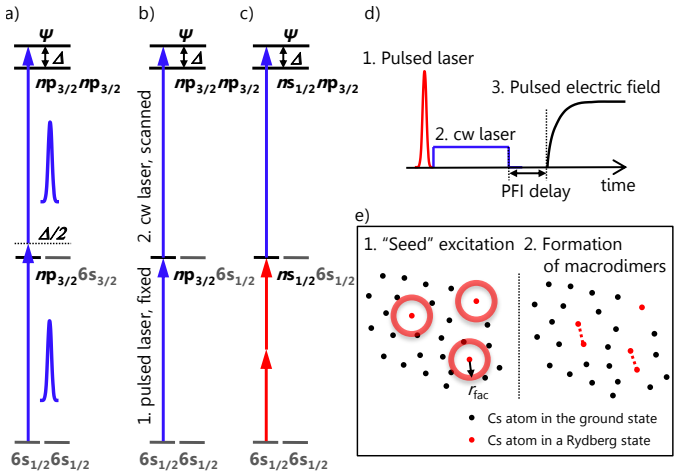

Figure 6.1: Schematic three-level diagram for the single-colour two-photon (a), two-colour two-photon (b) and three-photon (c) excitation of interacting Rydberg-atom-pair states. Panel d) illustrates the time sequence of the experiment, with the two laser pulses separated in time, and a variable PFI delay between the second laser pulse and the electric-field ramp. Panel e) includes a two-dimensional illustration of the effects of the sequential two-colour excitation: The initial excitation generates seed Rydberg atoms surrounded by a sphere of radius $R_{\rm fac}$ [232] in which Rydberg excitation by the second laser is facilitated and leads to the formation of interacting Rydberg-atom pairs or even Rydberg aggregates after excitation with a second laser pulse.

high to be resolved [63]. The very high state density of the interacting Rydberg-atom pairs at high n values and the limited resolution of the laser systems used to study them so far has prevented an unambiguous spectral assignment of bound states so far.

Here, a sequential, resonant excitation of the type

$$nl_Jnl_J \xleftarrow{\nu'=\nu-\Delta E(R)/h} nl_J6s_{1/2} \xleftarrow{\nu} 6s_{1/2}6s_{1/2} \tag{6.1}$$

is applied to the photoassociation of ground-state Cs atoms into interacting Rydberg-atom-pair states. The scheme relies on the population of a singly excited intermediate Rydberg level using a short-pulse laser resonant with one- or two-photon transitions to atomic Rydberg states. A narrow-bandwidth long-pulse laser is used to drive the second, photoassociation step with high spectral resolution (see Fig. 6.1b) and c)). An important further advantage of this excitation scheme is the increased number of accessible molecular states, and that, in particular, Rydberg macrodimers with always-resonant dipole-dipole interactions, *e.g.*, those asymptotically correlated to

states with n'snp and n'dnp configurations, can be accessed. This type of sequential excitation scheme is very similar to laser-induced collisional energy transfer (LICET, see Ref. [233] for a comprehensive review) in ultracold Rydberg gases.

The first experiments implementing this type of excitation scheme were performed by Reinhard *et al.* [225] with the goal of characterising the Rydberg-excitation-blockade effect. A broadening of the Rydberg transitions was observed depending on the first resonant laser pulse. The Rydberg excitation by the second, detuned laser was found to be facilitated by the first, resonant laser because atoms located at the distance R_{fac} [232] from Rydberg atoms produced by the first laser experience a shift of their transition frequency into resonance with the frequency of the second laser. This anti-blockade effect [197, 198] can lead to non-Poissonian counting statistics and bimodal counting distributions in off-resonant Rydberg excitation [57, 234] and to the formation of spatially correlated Rydberg aggregates [232, 235, 236].

Here, experiments on Cs Rydberg atoms are presented that rely on the sequential two-colour excitation (see Eq. (6.1)). The results show that this type of Rydberg excitation results in the formation of bound Rydberg macrodimers or in the formation of Rydberg-excitation aggregates depending on the laser detuning, the selected Rydberg states and the interaction time with the narrow-bandwidth radiation.

6.1 Theoretical considerations

Most of the experimental results presented in this chapter can be accounted for by the model described in Section 5.1. The only necessary modification involves the optically accessible states, $|\Phi\rangle$, which are now dependent on the state of the seed Rydberg atoms. The model is valid for interatomic distances larger than the LeRoy radius $R_{\mathrm{LR}} = 2\left(\langle r_{\mathrm{A}}^2\rangle^{1/2} + \langle r_{\mathrm{B}}^2\rangle^{1/2}\right)$ [192], which is $< 0.25\,\mu$m for the states considered in this chapter. To account for the resonant excitation of the macrodimers, spectra are simulated using

$$s(E) = 16\pi\omega_{\mathrm{atom}}^2 \sum_{\Psi} \int_0^{\infty} G(E - E_{\Psi}(R))\overline{x}_{\Phi,\Psi(R)} R^2 \mathrm{d}R, \tag{6.2}$$

which is a a modified version of Eq. (5.9). In Eq. (6.2), ω_{atom} is the Rabi frequency for the atomic $n\mathrm{p}_{3/2} \leftarrow 6_{1/2}$ transition, $G(E)$ is the laser line profile for which a Gaussian function was chosen, $\overline{x}_{\Phi,\Psi(R)}$ is the generalised overlap of the optically accessible Φ state with the molecular state Ψ. The expression $s(E)$ is proportional to the probability of exciting another Rydberg atom at a distance R to a pre-exicted atom in an $n'l'$ state. These pre-excited Rydberg atoms play the role of seed atoms for subsequent excitation and are referred to as “seed” Rydberg atoms in the following. The modi-

fied model does not account for off-resonant single-colour two-photon excitation (see Fig. 6.1a)). The description of secondary processes, which can occur during the long photoassociation-laser pulse in the experiments, is also beyond the current model of Rydberg-atom-pair excitation.

A simplified model is presented in the following to identify the conditions under which a Rydberg-atom-pair–excitation model (as opposed to a model describing the excitation of aggregates of Rydberg atoms) is adequate to treat the photoexcitation dynamics. The model relies on the concept of a facilitation radius R_{fac} (already introduced above, see also Fig. 6.1e)), assumes isotropic van der Waals interactions and includes only one relevant molecular state. The main condition is that the product between the density of Cs atoms ρ_{Cs} and the volume $4\pi R_{\mathrm{fac}}^2 \Delta R_{\mathrm{fac}}$ over which excitation by the second, detuned laser is facilitated, is much smaller than one

$$P_{\mathrm{exc}} = \rho_{\mathrm{Cs}} \cdot 4\pi R_{\mathrm{fac}}^2 \Delta R_{\mathrm{fac}} \ll 1, \tag{6.3}$$

which is equivalent to assuming that the probability P_{exc} of exciting a Cs atom located within the facilitated volume V_{fac} is much less than one. In Eq. (6.3), ΔR_{fac} is proportional to the excitation bandwidth $\delta\nu$ of the second laser and to the inverse of the slope $((\mathrm{d}V(R)/\mathrm{d}R)_{R_{\mathrm{fac}}})^{-1}$ of the long-range interaction potential at the position of the facilitation radius.

$$\Delta R_{\mathrm{fac}} = \delta\nu \cdot h((\mathrm{d}V(R)/\mathrm{d}R)_{R_{\mathrm{fac}}})^{-1} \tag{6.4}$$

When $P_{\mathrm{exc}} > 1$, the aggregation of Rydberg excitation is possible around an initial seed atom which leads to an excitation avalanche [237], as discussed in more detail in Section 6.5. The effects of off-resonant one-colour two-photon excitation and the occurrence of an excitation avalanche can be related, as the former can act as a "seed" to activate the latter. These processes are expected to play a role at small detunings from the atomic resonances, at which point the pair-excitation model is expected to fail and to underestimate experimental signals.

6.2 Experiment

The experiments are performed on samples of ultracold Cs atoms released from a crossed optical dipole trap at a temperature of ~40 μK and an atom-number density of $10^{12}\,\mathrm{cm}^{-3}$. Only the atoms in the densest centre part (diameter ~30 μm) of the atom sample are pumped into the $F = 4$ hyperfine state with a focused repump laser beam during the operation of the optical dipole trap. To increase the selectivity of the optical pumping of the atoms in the centre of the trap (beyond what is possible by focusing the laser beam), the frequency of the repumping laser is detuned to match

the AC Stark shift in the atoms in the centre of the dipole trap (see Chapter 2). The atoms pumped to the $F = 4$ hyperfine level are selected for Rydberg excitation.

The first Rydberg-excitation transition (see Eq. (6.1)) is driven by a pulse-amplified and frequency-doubled diode laser (Toptica DL-100 pro). The continuous-wave output of the diode laser is sent through two dye cells pumped by the second harmonic of a seeded Nd-YAG laser for amplification. In this way, ~9-ns-long transform-limited laser pulses are generated at a wavelength of ~639 nm. By sending the pulse-amplified radiation through a BBO crystal for second-harmonic generation, UV-laser pulses of 4.4 ns duration with a Fourier-transform-limited bandwidth of ~130 MHz are obtained, very similar to the UV-laser pulses used for the experiments described in Chapter 5. The frequency of this "short-pulse" laser is kept resonant with a selected atomic $n\mathrm{p}_{3/2} \leftarrow 6\mathrm{s}_{1/2}$ one-photon transition or with a selected $n\mathrm{s}_{1/2} \leftarrow 6\mathrm{s}_{1/2}$ two-photon transition (using the pulse-amplified fundamental light at ~639 nm). The power of the short-pulse laser is adjusted to levels resulting in the excitation of typically ~40 atoms per pulse, corresponding to a typical seed-Rydberg-atom density of $\sim 5 \cdot 10^7\,\mathrm{cm}^{-3}$ and a mean nearest-neighbour separation between seed-Rydberg atoms of more than 15 μm. The laser is pulsed after the atoms are released from the optical dipole trap.

The second laser is a single-mode continuous-wave ring dye laser, the output of which is frequency doubled in an external enhancement cavity (Coherent MDB-200), resulting in continuous-wave UV radiation of ~200 mW and a bandwidth of 1.5 MHz. The same laser was used to photoassociate the long-range Rydberg molecules bound by low-energy electron-Cs scattering (see Chapter 4). The frequency of the ring laser is stabilised by a Pound-Drever-Hall lock to an external cavity and measured with a frequency comb (Menlo Systems FC1500-250-WG), in procedures described in more detail in Chapters 2 and 3, as well as in Ref. [121]. Its output is switched on for typically 1 to 20 μs using an acousto-optic modulator immediately after the first laser pulse.

The two Rydberg-excitation lasers are focused to beam-waist radii of ~70 μm and intersect at right angles in the ~100 μm-diameter ultracold Cs atom cloud (the short-pulse laser travelling along the laboratory x axis and the long-pulse laser along the z axis, as defined in Section 2.1).

Transitions are detected by monitoring spontaneously produced ions and field-ionised Rydberg atoms, which are extracted with a slowly rising electric field (rise time ~1 μs) towards a multichannel-plate (MCP) detector. The pulsed electric field is delayed with respect to the second laser pulse. The Cs^+ ions produced by spontaneous ionisation or pulsed field ionisation (PFI) are detected mass-selectively. The spectra discussed in this chapter are obtained by monitoring the Cs^+-ion yield as a function of the frequency of the long-pulse UV laser.

Stray electric and magnetic fields are compensated to below 25 mV/cm and 20 mG, respectively, for all experiments described in this chapter, as described in Section 2.7.

6.3 High-resolution spectroscopy of $ns_{1/2}(n+1)s_{1/2}$ pair resonances

An example of a spectrum recorded with the resonant two-colour excitation scheme described above is presented in Fig. 6.2 where it is compared to the one-colour two-photon spectrum recorded in the same spectral region, but with the pulsed UV laser (see Chapter 5). The spectral resolution is ~6 MHz (see Fig. 6.2b)), almost two orders of magnitude better than in the spectrum recorded with the short-pulse UV laser (see Fig. 6.2a)). The $32s_{1/2}33s_{1/2}$ resonance is studied here from the intermediate $6s_{1/2}32p_{3/2}$ level using the narrow-bandwidth low-intensity UV laser (frequency ν' in Eq. 6.1) in the second step of the resonant

$$32s_{1/2}33s_{1/2} \xleftarrow{\nu'} 6s_{1/2}32p_{3/2} \xleftarrow{\nu} 6s_{1/2}6s_{1/2} \tag{6.5}$$

two-photon transition. In the experiments, a few atoms are resonantly excited to $32p_{3/2}$ Rydberg states using the short-pulse UV laser before excitation with the narrow-bandwidth UV laser, the frequency of which is scanned on the low-frequency side of the atomic $32p_{3/2} \leftarrow 6s_{1/2}$ transition. The interacting Rydberg-atom-pair states excited in this way are observed to decay to Cs^+ ions, just like the pair states excited with one-colour intense UV-laser pulses (see Chapter 5). The signals of spontaneously formed Cs^+ ions are therefore the signature of the excitation of interacting Rydberg-atom-pair states in spectral regions free of atomic resonances. The signals are, in first approximation and in a certain range of experimental conditions, proportional to the number of initially excited seed Rydberg atoms. To compensate for intensity and frequency fluctuations of the pulse-amplified laser and, consequently, to increase the signal-to-noise ratios, the Cs^+-ion signals are divided by the signals resulting from pulsed field ionisation of seed Rydberg atoms in all spectra of the type presented in Fig. 6.2b).

The improvement in the spectral resolution is, primarily, the result of using a laser with a much smaller bandwidth and a weaker intensity for the second excitation step in Eq. 6.5 and, secondly, of actively populating the long-lived intermediate, singly excited level. Therefore, the spectral resolution is independent of the resolution of the first excitation step (leading to the generation of the seed Rydberg atoms), similar to the case of UV-millimetre-wave resonances desribed in Section 3.1, and the photoassociation occurs in a one-photon transition (see also Eq. (6.2)). In the spectrum depicted

in Fig. 6.2a), the signal is plotted as a function of the detuning corresponding to $2\times\nu_{\mathrm{UV}}$ to account for the two-photon excitation process. In contrast, the spectrum shown in Fig. 6.2b) obtained with the sequential two-photon excitation scheme is plotted as a function of the detuning corresponding to ν_{UV}.

The asymmetry of the $32s_{1/2}33s_{1/2}$ resonance in Fig. 6.2b), with a sharp edge corresponding closely to the position of the pair-dissociation asymptote and a red-degraded line shape resulting from pair excitation to the attractive molecular curves, is much better resolved using the sequential excitation scheme. The comparison of the two spectra also reveals that the shift of the resonance peak in the spectrum of Fig. 6.2a) is the result of the convolution of the asymmetric line shape function with the 130-MHz-broad Gaussian laser-line-shape function. However, the improved resolution does not only enable a better characterisation of resonances observed before, but also enables the observation of additional resonances, *e.g.*, those visible in Fig. 6.2b) at detunings above -500 MHz, which could not be detected in the one-colour experiments.

The experimental spectrum in Fig. 6.2b) is accurately reproduced over a broad spectral range around the $32s_{1/2}33s_{1/2}$ Rydberg-atom-pair resonance by a spectrum simulated using Eq. (6.2), which takes into account the resonant one-photon excitation of the pair state from the intermediate $32p_{3/2}6s_{1/2}$ level. However, the intensity of the simulated spectrum is systematically too weak at small detunings (down to about -1.5 GHz) from the atomic $32p_{3/2} \leftarrow 6s_{1/2}$ resonance. The observation of larger-than-expected signals in the experiment at frequencies just below the atomic transition frequency suggests that the second laser pulse excites more than one atom per seed atom. This form of "aggregation" of Rydberg-atom excitation has been referred to as "avalanche" excitation in previous work [237] and is discussed in more detail in Section 6.5.

In the next section, a special type of interacting Rydberg-atom-pair resonances originating from bound levels in long-range potential wells is presented. These pair resonances referred to as "bound macrodimers" in the literature were predicted theoretically [229] but proved to be rather elusive experimentally.

6.4 Bound long-range states of interacting Rydberg atoms

In this section, experimental and theoretical evidence for the existence of bound Rydberg macrodimers of Cs is presented. The bound states are formed via two-colour three-photon photoassociation of ultracold cesium atoms following the procedures outlined above, under conditions where the effects of external electric and magnetic fields can be neglected. The observed photoassociation resonances are unambigu-

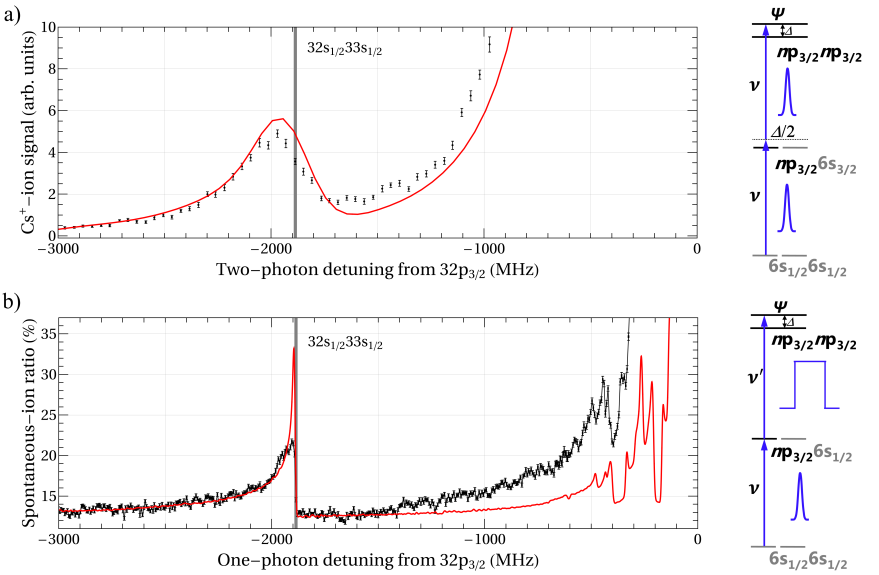

Figure 6.2: Comparison of spectra measured in the same frequency range and similar samples of ultracold Cs atoms, but with different laser-excitation pulse shapes and intensities. The spectrum in a) was recorded with a 4.4-ns-long pulsed UV laser (pulse energy of ~10 μJ, peak power 2 kW), and the vertical grey bar denotes the position of the $32s_{1/2}33s_{1/2}$ dissociation asymptote. The spontaneous Cs^+-ion yield is plotted against the two-photon ($2 \times \nu_{UV}$) detuning from the $32p_{3/2}32p_{3/2}$ asymptote. The spectrum in b) was recorded with a cw single-mode UV laser, after resonant excitation of a few $32p_{3/2}$ "seed" Rydberg atoms. The signal corresponds to the average number of Rydberg-atom pairs per "seed" atom and is obtained as the ratio of Cs^+-ion signals resulting from the spontaneous ionisation of the sample to Cs^+ ions arising from the pulsed field ionisation of the seed Rydberg atoms. The two red curves in a) and b) are simulated spectra using the model described in Section 5.1 and Section 6.1, respectively.

ously linked to long-range potential minima, which are calculated on the basis of the detailed model of the long-range multipole-multipole interactions presented in Section 5.1 (see also Ref. [65]).

6.4.1 Prediction of bound Rydberg macrodimers

On the basis of this potential model, a computational search for long-range wells in the potentials of interacting Cs Rydberg atoms was conducted. Long-range potential minima were identified for states correlated to many different pair-dissociation asymptotes. However, the predictions of simpler few-level models, *e.g.*, such as models only including the different fine-structure components of a single $nln'l'$ level (see Ref. [230]), could not be confirmed by the calculations based on extended basis sets.

The high pair-state density is the reason for both the ubiquitous occurrence of potential minima and for the failure of simpler models to predict the positions of these potential minima. The calculations with extensive basis sets reveal also the importance of higher-order terms in the multipole expansion of the long-range interaction (just as it was already shown for the one-colour two-photon excitation in Chapter 5.3.3). A truncation to only dipole-dipole interactions turns out to be completely inadequate for accurate predictions (to about 2 MHz) of long-range potential wells of the type discussed here.

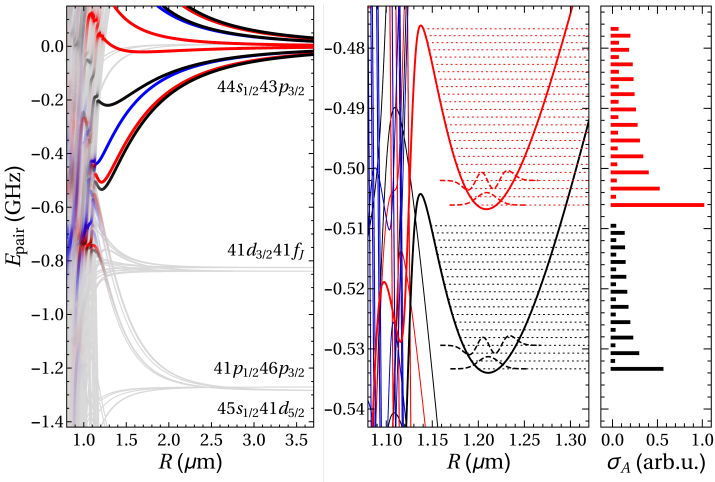

Figure 6.3: Potential-energy functions of two Cs Rydberg atoms in the vicinity of the $43p_{3/2}44s_{1/2}$ dissociation asymptote. The colour shading indicates the $43p_{3/2}44s_{1/2}$ character of the interacting Rydberg-atom-pair states, with 1% denoted by full colour. Black, red, and blue potentials functions correspond to $\Omega = 0$, $\Omega = 1$, and $\Omega = 2$ molecular states (see text for details). Calculated vibrational levels are presented in the middle panel as dashed horizontal lines. The right-hand-side panel indicates calculated intensity distributions.

The investigation presented in the following concentrates on molecular states correlated to $np_{3/2}n's_{1/2}$ dissociation asymptotes. These states have already attracted theoretical and experimental attention because the always-resonant "excitation-hopping" dipole-dipole coupling of the type $n's_{1/2}np_{3/2} \leftrightarrow np_{3/2}n's_{1/2}$ could be used to model interacting spins [213–215, 238]. In Cs, potential minima have been found, *e.g.*, for the states correlated to the $44s_{1/2}43p_{3/2}$ and the $44p_{3/2}45s_{1/2}$ dissociation asymptotes. The calculated potential curves of the molecular states correlated to the $44s_{1/2}43p_{3/2}$ dissociation asymptote together with the positions of predicted vibrational states (dashed lines in the middle panel of Fig. 6.3) supported by the long-range

wells is presented in Fig. 6.3. The analysis of the potential functions reveals that the always-resonant dipole-dipole interaction is the reason for the level splittings at long range and, consequently, the shift of some potential functions to lower energies. The potential minima result, however, from interactions with lower-lying functions correlated to the $41p_{1/2}46p_{3/2}$ and the $45s_{1/2}41d_{5/2}$ dissociation asymptotes. The interactions leading to the avoided crossings are therefore dipole-quadrupole interactions.

The vibrational states and eigenenergies of the selected potentials were calculated using the mapped Fourier-grid method [175]. The expected intensity modulation of even and odd v vibrational levels (see right-hand-side panel in Fig. 6.3) is a result of photoassociation from an ultracold sample, with corresponding thermal de Broglie wavelengths much larger than the oscillations of the vibrational wavefunctions. Transitions to odd v levels are expected to be very weak because of the odd number of nodes of the vibrational wavefunction and the partial cancellation of contributions from regions where the vibrational function has opposite sign. The relevant vibrational spacing between adjacent even-v levels is predicted to be $2 \times 1.4\,\mathrm{MHz}$, which makes it almost possible to resolve these states in the experiments described here.

The long-range Rydberg-atom-pair states correlated to the $44s_{1/2}43p_{3/2}$ pair-dissociation asymptote depicted in Fig. 6.3 are almost ideal candidates for an experimental investigation because *i*) the equilibrium internuclear distances are close to 1 μm, which corresponds to the maximum of the nearest-neighbour-distribution in the ultracold gas, *ii*) the molecular functions have mainly $44s_{1/2}43p_{3/2}$ character near the potential minima (see colour shading of PECs in Fig. 6.3) and are therefore optically accessible, *iii*) the potentials are steep, resulting in vibrational spacings of $\sim 1.4\,\mathrm{MHz}$ (see right-hand-side panel in Fig. 6.3), and *iv*) the wells are isolated from other potential curves to which they could strongly couple.

6.4.2 Experimental spectra of bound Rydberg macrodimers

Experimental spectra recorded in the vicinity of the $44s_{1/2}43p_{3/2}$ dissociation asymptote are presented in Fig. 6.4. To obtain these spectra, the frequency of the pulsed visible laser was tuned to the two-photon $44s_{1/2} \leftarrow 6s_{1/2}$ resonance to generate $44s_{1/2}$ seed atoms and the long-pulse UV laser was scanned on the low-frequency side of the atomic $43p_{3/2} \leftarrow 6s_{1/2}$ transition. First, the spontaneous-ion signal is displayed as a function of the UV-laser frequency without any $44s_{1/2}$ seed Rydberg atoms (see Fig. 6.4a)). This measurement represents the expected background signal in the three-photon experiment. This background signal is small and structureless at detunings below $-500\,\mathrm{MHz}$. A set of resonances at a detuning of around $-500\,\mathrm{MHz}$ is attributed

to the excitation of "butterfly-like" long-range Rydberg molecules [a] (see also the qualitative discussion of these unusual molecular states in Chapter 4). The increase of the background signal at detunings above −500 MHz is assumed to result from one-colour (UV) two-photon excitation of Rydberg-atom pairs, as observed in Chapter 5.

The spectra shown in Figs. 6.4b), c) and d) were recorded with both lasers, in a time sequence schematically shown in Fig. 6.1d). In this sequence, the two laser pulses do not overlap in time, the UV laser is switched on for 5 μs following the first visible laser pulse, and the electric field is pulsed after an additional PFI delay of 5 μs. The integrated ion signal resulting from the PFI of $44s_{1/2}$ seed Rydberg atoms is presented in the spectrum displayed in Fig. 6.4b). The fluctuations and drifts of this signal are primarily due to the slow drifts of the intensity of the pulsed visible laser. However, the reduced signal strengths at detunings of about −740 MHz and −500 MHz correlate to the resonances observed in the Cs^+-ion signal. The signal corresponding to spontaneously produced Cs^+ ions, which are detected in a separate TOF channel, is given in Fig. 6.4c). With the seed atoms present, the UV-laser spectrum of the spontaneously formed ions reveals several additional resonances and an increased, frequency-independent background signal when compared to the spectrum shown in Fig. 6.4a). In order to normalise the Cs^+-ion signal, the background signal measured without the seed Rydberg atoms (see Fig. 6.4a) is subtracted. The resulting difference spectrum is then normalised by division with the PFI seed signal (see Fig. 6.4b)) at each experimental cycle. The resulting ratio is averaged over several experimental cycles at each frequency step. The resulting spectrum is displayed in Fig. 6.4d), where it is compared to a simulated spectrum (red trace) that was convoluted with a Gaussian line-shape function of 6 MHz full width at half maximum. All resonances in the experimental spectrum are reproduced by the simulation and can be assigned to single Rydberg-atom-pair resonances. The three resonances above −600 MHz arise from the three potential wells corresponding to different states with molecular angular-momentum-projection quantum numbers Ω (see the potential functions shown in black for $\Omega = 0$, in red for $\Omega = 1$, and in blue for $\Omega = 2$ in Fig. 6.3). The resonances below −600 MHz arise from the potential maxima resulting from the same avoided crossings and which occur at an internuclear separation of ∼1 μm, as depicted in Fig. 6.3. Unfortunately, the predicted vibrational series in each of the potential wells could not be resolved because the linewidth of 6 MHz exceeds the calculated vibrational spacings of 1.4 MHz.

Similar long-range potential minima are predicted on the low-frequency side of

[a] This assignment is enabled by the observation that the molecules decay to molecular Cs_2^+ ions, which was empirically found to be characteristic of Cs_2 long-range Rydberg molecules (see Chapter 4.6).

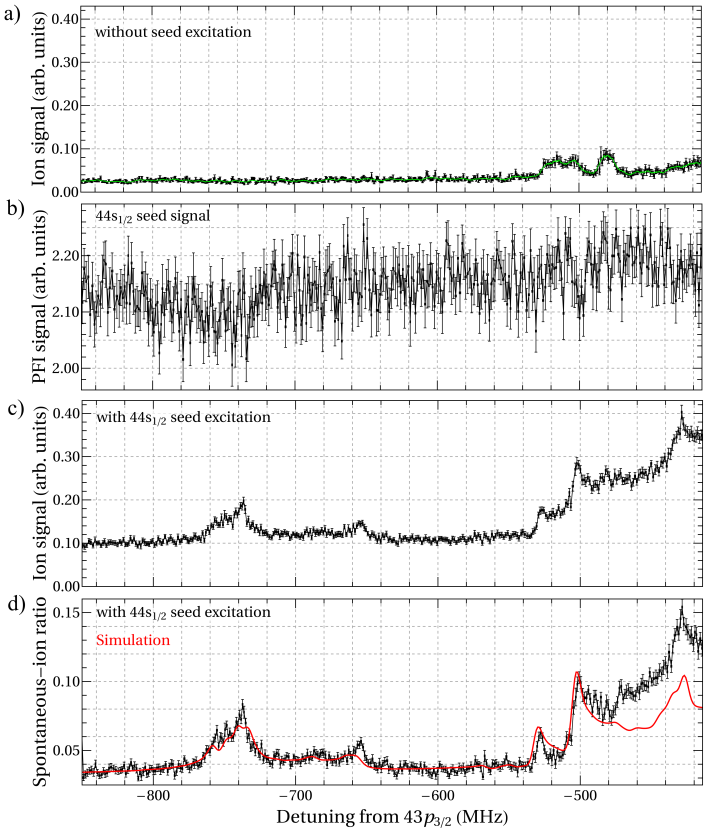

Figure 6.4: UV-laser spectra on the low-frequency side of the $43p_{3/2} \leftarrow 6s_{1/2}$ transition in an ultracold sample of Cs atoms. (a) Spectrum measured with the UV laser only. (b) Spectrum obtained by monitoring the PFI signal of $44s_{1/2}$ seed Rydberg atoms. (c) Spectrum of the spontaneous-ion signal recorded following excitation of a few atoms to the $44s_{1/2}$ Rydberg state with the first laser pulse. (d) Same spectrum as (c) but after subtraction of the background signal depicted in trace (a) and normalisation by division with the PFI signal of the seed atoms depicted in trace (b). The solid red line represents a simulated spectrum (see text for details).

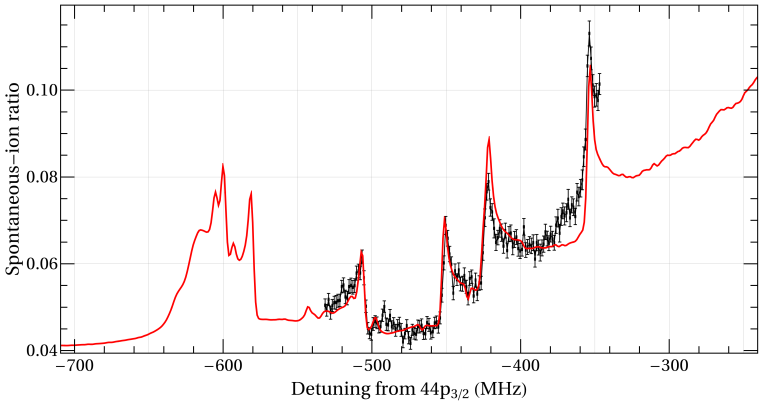

Figure 6.5: UV-laser spectra recorded on the low-frequency side of the $44p_{3/2} \leftarrow 6s_{1/2}$ transition following seed excitation of a few Cs atoms to $45s_{1/2}$ Rydberg states. The spectrum represented by black dots was measured with a 2-µs-long UV pulse and a pulsed-field-ionisation delay of 12 µs and is an average over several measurements in this region. The simulated spectrum is shown as a solid red line.

the $44p_{3/2}45s_{1/2}$ dissociation asymptote. Further improvements of the measurement conditions (mainly lower "seed" atom density, shorter, 2-µs-long UV pulses for photoassociation) resulted in the experimental spectrum presented as a black trace in Fig. 6.5. This spectrum is quantitatively reproduced by the simulated line-shape function (red line in Fig. 6.5, calculated using Eq. (6.2)) which include the convolution with a Gaussian function of 3 MHz full width at half maximum. A width of 3 MHz represents the limit of the experimental resolution given by the finite width of the laser (∼1.5 MHz), and the thermal width of the $Cs(6s_{1/2}) + Cs(6s_{1/2})$ continuum (∼1 MHz) at a temperature of ∼40 µK. Because the potential shapes are very similar to those in the energy region below the $43p_{3/2}44s_{1/2}$ dissociation asymptote, the spectrum recorded on the low-frequency side of the $44p_{3/2}45s_{1/2}$ has the same overall appearance as the spectrum measured on the low-frequency side of the $43p_{3/2}44s_{1/2}$ dissociation asymptote. Resonances with red-degraded line shapes are attributed to attractive branches of the long-range potentials, whereas repulsive states and potential wells result in blue-degraded line shapes. The blue-degraded resonances located at detunings of −450 MHz, −425 MHz and −355 MHz can be directly linked to the $\Omega = 0, 1$ and 2 potential wells, respectively. The resonances at −507 MHz and below −583 MHz originate from the potential maxima of the lower branches of the avoided crossings, which are adiabatically correlated to lower-lying dissociation asymptotes.

The quantitative agreement of the experimental observations with the potential model is a strong indication for the observation of bound macrodimers. Surprisingly, also these bound macrodimers are found to decay to Cs^+ ions within less than 10 μs. Whereas the decay of Rydberg-atom-pair states excited to attractive potential functions can be understood in a Penning-ionisation model (see Section 5.3.5), the calculated potentials presented in Fig. 6.3 indicate that Penning ionisation cannot occur in the bound macrodimers.

6.4.3 On the lifetime of bound Rydberg macrodimers

In the following, an experimental investigation relying on the delayed PFI technique, and two theoretical investigations are presented with the aim to reveal the influence of different decay channels on the lifetime of bound macrodimers. The experimental investigation of the decay mechanism and lifetimes of the molecular resonances was complicated by the very small signals, typically ten times weaker than the seed-Rydberg-atom signals.

The experimental results are shown in Fig. 6.6, where two photoassociation spectra are compared to the simulated spectra. Both spectra were measured following the excitation of a few $45s_{1/2}$ seed Rydberg atoms with a 2-μs-long UV pulse the frequency of which was tuned below the atomic $44p_{3/2} \leftarrow 6s_{1/2}$ resonance. The spectrum in black was recorded with a PFI delay of 12 μs, whereas no PFI delay was applied in the measurement of the spectrum depicted in grey. Two different effects are revealed by comparing the two spectra. The first effect is a larger flat signal in the black trace. This offset in the signals of Cs^+ ions can originate from spontaneous ionisation of the $45s_{1/2}$ seed atoms during the 12 μs delay because it is completely independent of the frequency of the UV laser. An interaction-induced ionisation of the seed Rydberg atoms is unlikely because, firstly, their density is only $\sim 5 \cdot 10^7\,\mathrm{cm}^{-3}$, corresponding to an average nearest-neighbour separation of more than 15 μm and, secondly, all potential curves correlated to $ns_{1/2}ns_{1/2}$ asymptotes are repulsive and Penning ionisation is suppressed. An upper limit for the ionisation rate resulting from collisions with hot atoms from the background gas can be estimated as 250 Hz, which, though significant, is too small to explain the observed effect. One can speculate that secondary processes, such as those initiated by ions produced by these collisions, could lead to the ionisation of more Rydberg atoms and account for the observed signal. More likely is a contribution from radiatively decaying seed atoms to which the ion signals are normalised.

The second effect, which is more relevant in the context of bound macrodimers, is revealed when the experimental spectra are compared to the simulated spectra (solid lines in Fig. 6.6). Resonances originating from bound states, *e.g.*, those observed at

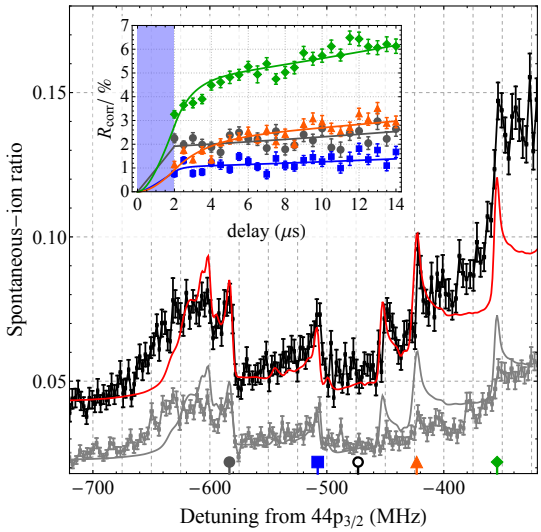

Figure 6.6: Ratio of spontaneous-ion to PFI signals as function of the detuning of the UV laser (2 μs pulse length) from the $44p_{3/2} \leftarrow 6s_{1/2}$ transition when $45s_{1/2}$ seed atoms are present. Ions were extracted after a delay of 0 (gray points) and 12 μs (black points). The spectrum simulated for a linewidth of 5 MHz (vertically scaled and offset) is shown as solid red and gray lines for comparison. The inset shows the measured ratios (circles, squares, triangles, and diamonds) as a function of the extraction delay at the fixed laser detunings marked by the corresponding symbol on the frequency axis. A time-dependent background signal (measured at the frequency indicated by an open circle) was subtracted from all curves. Solid curves show the fit of a rate-equation model to the data, the light-blue shaded region indicates the UV-excitation pulse.

detunings of −450 MHz, −425 MHz and −355 MHz, are much stronger in the spectrum recorded with the PFI delay than in the spectrum recorded without PFI delay. Resonances originating from potential maxima at short internuclear separations, in a region of much higher molecular state density, *e.g.*, at −583 MHz and −507 MHz, are observed with similar intensities in both spectra. These results indicate that the bound macrodimers decay more slowly into Cs^+ ions than the macrodimers excited to attractive potential functions.

The dynamics of the Cs^+-ion formation was also studied by varying the PFI delay at fixed UV-laser frequencies corresponding to the positions of the different molecular resonances. The inset of Fig. 6.6 depicts measurements of the background-corrected spontaneous-ion ratios R_{corr} as a function of the extraction delay for different UV-laser detunings together with results of a rate-equation model for the decay and formation processes of seed atoms and macrodimers. The free parameters of this model, the

photoassociation and ionization rates at a given detuning, are determined from a fit of the model to the data. The model reveals that the apparent increase of the curves observed for all detunings results from the normalization to the PFI signal, which decreases with time due to radiative decay (and to a much lesser extend due to ionization) of the initial seed atoms. The fitted relative photoassociation rates are in good agreement with the intensities calculated on the basis of Eq. (5.9). The fitted ionization rates exceed 3 MHz at the positions of the resonances located at detunings of -583 MHz and -507 MHz. Significantly lower ionization rates of about 0.6(1) and 1.0(1) MHz are obtained for the resonances at detunings of -421 and -355 MHz, respectively, which correspond to bound macrodimers. Although the corresponding lifetimes of less than 2 μs are much shorter than expected [229, 239], they are still considerably longer than at the positions of potential maxima, which we consider a further indication of the bound nature of these states.

Considering the high density of electronic states in the energy range of the Rydberg-atom-pair states, it might not be surprising that the observed macrodimers autoionise on the microsecond timescale. Two possible ionisation mechanisms are investigated theoretically in the following: *i*) direct, electronic transitions in which one Rydberg atom of the interacting pair state is transferred into the (ionisation) continuum while the other Rydberg atom is de-excited into a more strongly bound state, and *ii*) a vibrational autoionisation process, where the decay of the bound macrodimer is caused by non-adiabatic couplings to molecular states with open ionisation channels.

The first mechanism is reminiscent of inter-Coulombic decay (ICD) [240, 241] which was observed on fast time scales in such diverse systems as neon clusters [242], in water and hydroxide [243], and in water dimers [244, 245]. In the context of Rydberg atoms, this mechanism was discussed by Amthor *et al.* [246] in a perturbative treatment of the Rydberg-Rydberg interaction. Here, the model of Ref. [246] is extended by expanding the pair-state wavefunction at the equilibrium position of the macrodimer potential (performed for the $\Omega = 0$ state correlated to the $43p_{3/2}44s_{1/2}$ pair-dissociation asymptote, see Fig. 6.3) in a basis including more than 1000 pair-dissociation asymptotes with contributions from atomic Rydberg states in the range from $n = 30$ to $n = 200$. The ICD rates for each of the basis states were estimated using the model of Amthor *et al.* (see, in particular, Eq. 2 in Ref. [246]). The total rate for the ICD-type autoionisation process was then found by incoherent summation. The resulting rate is only of the order of 10 mHz, corresponding to a lifetime of 10 s, and is thus completely negligible in comparison to the experimentally observed decay rates of $\sim$1 MHz and even to the rates of radiative decay by fluorescence to the electronic ground state. The model includes implicitly ICD-type ionisation following a cascade of electronic Rydberg-Rydberg pair-state transitions, a process which was speculated to be the mechanism of the fast ionisation of a Rydberg gas observed

experimentally [223]. This modeling clearly shows that electronic auto-ionisation of interacting Rydberg atoms, either directly or following a cascade of electronic transitions, can be neglected in the range of the internuclear separations of the Rydberg-atom pairs considered here.

The role of the second mechanism, which is vibrational autoionisation through non-adiabatic couplings, was investigated by calculating the radial non-adiabatic-coupling matrix elements [247]

$$H_{1,\nu_1;2,\nu_2}(\mathrm{cm}^{-1}) = -\frac{16.8576}{\mu(\mathrm{amu})}\left\langle \xi^{ad}_{\nu_1} \left| \left\langle \Phi^{ad}_1 \left| \frac{\partial^2}{\partial R^2} \right| \Phi^{ad}_2 \right\rangle_r (\mathrm{\AA}^{-2}) \right| \xi^{ad}_{\nu_2} \right\rangle_R - \frac{33.7152}{\mu(\mathrm{amu})}\left\langle \xi^{ad}_{\nu_1} \left| \left\langle \Phi^{ad}_1 \left| \frac{\partial}{\partial R} \right| \Phi^{ad}_2 \right\rangle_r (\mathrm{\AA}^{-1}) \right| \frac{d}{dR}\xi^{ad}_{\nu_2} \right\rangle_R (\mathrm{\AA}^{-1}) \quad (6.6)$$

between the bound states in the macrodimer potential (performed again for the $\Omega = 0$ state correlated to the $43p_{3/2}44s_{1/2}$ pair-dissociation asymptote) with normalised vibrational wavefunctions ξ_{ν_1} and electronic wavefunctions Φ_1, and the energetically open continuum states with energy-normalised wavefunctions ξ_{ν_2} and electronic wavefunctions Φ_2. In this calculation, the pair-state basis consisted of all Rydberg-atom-pair asymptotes with $\Delta n < 2$ and detunings below 10 GHz relative to the $43p_{3/2}44s_{1/2}$ pair-dissociation asymptote. The total rates for non-adiabatic transitions were found to range from 10 mHz for $v = 0$ to 100 Hz for $v = 10$ and are thus also too small to explain the experimentally observed decay rates.

The role of the molecular rotation and rovibrational couplings were not investigated explicitly. The fact that the couplings (leading to the existence of minima in the considered Born-Oppenheimer potential curves) are of dipole-quadrupole nature (and thus require a coupling between electronic and rotational degrees of freedom) might indicate the possible importance of rovibrational couplings. However, the quasi-degeneracy of rotational energy levels discussed in the context of the dipole-quadrupole interaction (see Chapter 5.3.2) renders a significant contribution from rovibrational dissociation unlikely.

In the experiments, many seed Rydberg atoms are excited in the ultracold atom cloud and even though the seed-Rydberg-atom density is low, the long-range interaction of the bound macrodimers with all or just the nearest seed Rydberg atom could induce the fast decay. The effect of the background seed-Rydberg atoms on the atomic $43p_{3/2} \leftarrow 6s_{1/2}$ transition was studied under the same conditions that were used to photoassociate the bound macrodimers correlated to the $43p_{3/2}44s_{1/2}$ pair-dissociation asymptote. The only difference was the reduced UV-laser intensity to avoid saturation broadening of the atomic transition. The results of this experiment are presented in Fig. 6.7. A clear broadening of the atomic Rydberg resonance (black trace) is observed with increasing seed-Rydberg-atom density (green and red traces).

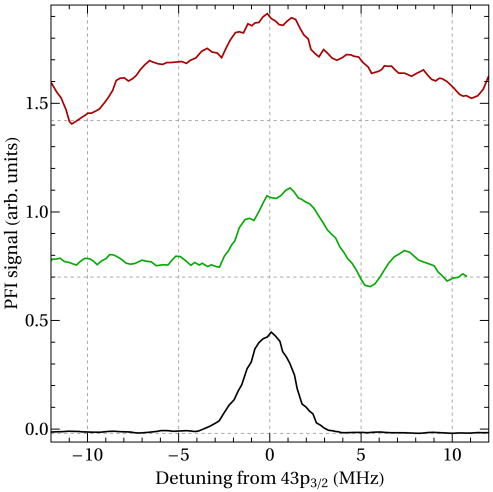

Figure 6.7: UV-laser spectra of the $43p_{3/2} \leftarrow 6s_{1/2}$ transition without any seed Rydberg atoms present in the ultracold Cs atom sample (black) trace and with a few Cs atoms excited to the $44s_{1/2}$ state prior to the application of the UV-laser pulse (green and red traces). The total UV-laser-independent offset results from pulsed field ionisation of the seed Rydberg atoms excited with a pulse-amplified diode laser. Consequently, the spectrum presented in red was recorded with twice the density of seed Rydberg atoms compared to the spectrum presented in green.

The broadening is taken as an indication of the significant interaction of $43p_{3/2}$ Rydberg atoms with all $44s_{1/2}$ seed Rydberg atoms and is about 3 MHz for the densities (see green trace in Fig. 6.7) used also in the excitation of the bound macrodimers. The influence of the seed Rydberg atoms on the decay of the bound macrodimers could therefore be of relevance, but further experimental investigations are required to draw definitive conclusions.

6.5 Observation of Rydberg-excitation aggregates

To study the effect of the off-resonant sequential "avalanche" Rydberg excitation and the formation of Rydberg-atom aggregates in more detail, the region near the atomic $42p_{3/2} \leftarrow 6s_{1/2}$ transition in Cs (see Fig. 6.8) was investigated. At this value of n, the energy spacing between $np_{3/2}np_{3/2}$ and $ns_{1/2}(n+1)s_{1/2}$ Rydberg-atom-pair states is only $12.5 \cdot h$ MHz, leading to significant state-mixing and level shifts already at large internuclear separations [224]. The relevant potential curves are depicted in Fig. 6.9. In the experiment, the frequency of the short-pulse UV laser was tuned to

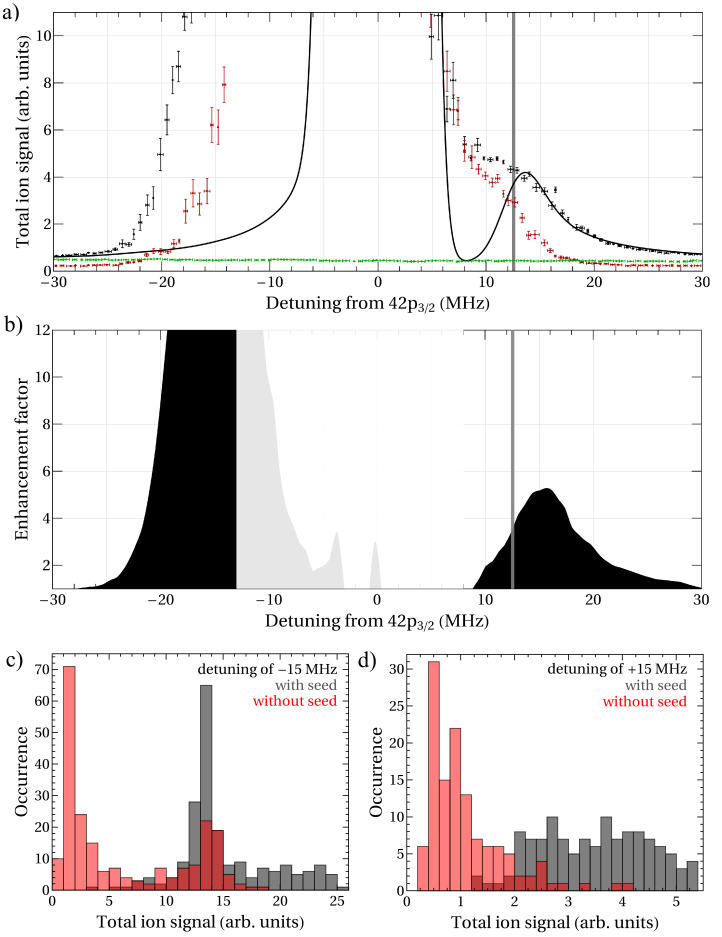

Figure 6.8: a) Two-colour UV-laser spectrum recorded in the vicinity of the atomic $42p_{3/2} \leftarrow 6s_{1/2}$ transition (black dots). The green dots represent the background signal caused by the short-pulse UV laser alone with its frequency fixed at the position of the $42p_{3/2} \leftarrow 6s_{1/2}$ transition. The spectrum obtained without any seed Rydberg atoms, *i.e.* without the short-pulse laser, is presented as dark red dots. The vertical grey bar indicates the asymptotic energy of the $42s_{1/2}43s_{1/2}$ pair state. The full line represents a spectrum calculated with the model of the multipole-multipole interactions between Rydberg atoms (see Section 3.1). b) Difference between the two-colour spectrum and the long-pulse UV-laser spectrum presented as black and red dots in a), respectively, divided by the seed Rydberg signal (green dots in a)) as a function of the laser detuning from the $42p_{3/2} \leftarrow 6s_{1/2}$ transition (black). The counting distributions at detunings of −15 MHz and +15 MHz for the excitation without (red bars) and with (black bars) seed Rydberg atoms are presented in panels c) and d), respectively.

the position of the $42p_{3/2} \leftarrow 6s_{1/2}$ transition. Consequently, the potential curves needed to describe the excitation with the long-pulse UV laser are correlated to the $Cs(42p_{3/2}) + Cs(42p_{3/2})$ and the $Cs(42s_{1/2}) + Cs(43s_{1/2})$ dissociation asymptotes (see left-hand-side panel of Fig. 6.9). The molecular potential curves that correlate with the $42s_{1/2}43s_{1/2}$ functions are repulsive and the dipole-dipole $42p_{3/2}42p_{3/2} - 42s_{1/2}43s_{1/2}$ interaction implies the occurrence of a weak resonance with a blue-degraded line shape close to the position of the $42s_{1/2}43s_{1/2}$ asymptote on the high-frequency side of the atomic $42p_{3/2} \leftarrow 6s_{1/2}$ transition. The dipole-dipole interaction also implies that the molecular functions correlated to the $42p_{3/2}42p_{3/2}$ Rydberg-atom-pair state are attractive and lead to a strong red-degraded molecular resonance on the low-frequency side of the $42p_{3/2} \leftarrow 6s_{1/2}$ atomic resonance.

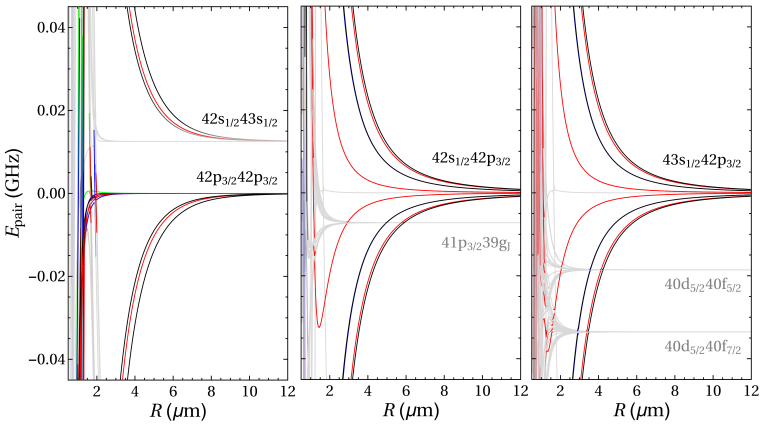

Figure 6.9: Long-range potential-energy curves in an energy rage of $\pm 40 \cdot h$ MHz around the $42p_{3/2}42p_{3/2}$ (left-hand side), the $42s_{1/2}42p_{3/2}$ (middle) and the $43s_{1/2}42p_{3/2}$ (right-hand side) Rydberg-pair-dissociation asymptotes. The colour shading of the molecular potential curves represent the admixture of the asymptotic level which is placed at the origin of the energy scale. Full colour denotes 1 % character of the specific asymptotic state, and black and red traces indicate molecular states with $\Omega = 0$ and 1, respectively.

The experimental spectra are presented in Fig. 6.8a). The frequency-independent signal presented in green was measured with the short-pulse UV laser alone and corresponds to the pulsed field ionisation of the "seed" $42p_{3/2}$ Rydberg atoms. The red trace was measured with the long-pulse UV laser alone, and the black trace was recorded with both lasers. As explained in the experimental section, the lasers did not overlap in time, and the second laser pulse was applied immediately after the first laser pulse. In the spectrum shown in black, a partially resolved resonance is observed on the high-frequency side of the atomic resonance, close to the position of

the $42s_{1/2}43s_{1/2}$ asymptote (see vertical grey line in Fig. 6.8a)). This resonance is also observed in the simulated spectrum (solid black trace in Fig. 6.8a)), that was obtained on the basis of the potential functions depicted in the left-hand-side panel of Fig. 6.9. In the experimental trace, the resonance is not as well resolved as in the simulation because of partial overlap with the broadened atomic transition.

Whenever the experimental black trace in Fig. 6.8a) is larger than the sum of the spectra shown in green and red, the additional signal can unambiguously be attributed to the two-colour two-photon excitation of Rydberg-atom-pair states. The additional Rydberg excitations are visualised in Fig. 6.8b), which depicts the difference between the spectrum measured with and without seed Rydberg atoms normalised to the seed-Rydberg-atom signal. This spectrum represents the enhancement factor of the photoexcitation probability induced by the seed Rydberg atoms. When this factor becomes greater than two, more than one additional Rydberg atom is excited for each seed Rydberg atom, which is indicative of an aggregation of Rydberg excitations. At the $42s_{1/2}43s_{1/2}$ pair resonance on the high-frequency side of the atomic transition, enhancement factors up to 4 are observed. The excitation of the $42s_{1/2}43s_{1/2}$ pair resonance therefore facilitates additional Rydberg excitations during the 15-µs-long UV-laser pulse. An exact theoretical description of the dynamics of that process is difficult and would require the calculation of few-body–Rydberg-atom states, which is beyond the scope of this investigation. The relevant potentials for the excitation of a third Rydberg atom close to a Rydberg-atom-pair state will, however, resemble those depicted for $42s_{1/2}42p_{3/2}$ and $43s_{1/2}42p_{3/2}$ Rydberg-atom-pair states states in Fig. 6.9. The always-resonant $ns_{1/2}n'p_{3/2} \leftrightarrow n'p_{3/2}ns_{1/2}$ dipole-dipole interaction in these dimers gives rise to long-range interactions (detunings of 15 MHz correspond to internuclear distances of $\sim 5\,\mu m$), and leads to the formation of small Rydberg aggregates after the initial pair-state excitation. The state mixing induced by this interaction will also strongly modify the interactions in the $42s_{1/2}43s_{1/2}$ pair state. Consequently, on the high-frequency side of the atomic transition, the system should be described as a three- or few-body state with the p character fully "delocalised" over all interacting Rydberg atoms. The experimental data indicates that these interactions lead to the formation of small Rydberg aggregates, with enhancement factors much smaller than observed on the low-frequency side of the atomic $42p_{3/2} \leftarrow 6s_{1/2}$ transition (see Fig. 6.8b)).

On the low-frequency side, the pair states carry mainly $42p_{3/2}42p_{3/2}$ character. The very large enhancement factors of much more than 10 for detunings between -10 and -15 MHz correspond to an excitation avalanche. Each $42p_{3/2}$ Rydberg atom excited with the long-pulse UV laser also acts as an additional seed atom facilitating the excitation of further neighbouring ground-state atoms, which results in a spatially correlated many-body state [232]. This process is also observed with the long-pulse

laser alone as revealed already by the underestimation of the signals at detunings between -20 and -10 MHz in the simulated spectra (compare red dots and solid black line in Fig. 6.8a)). The counting distributions recorded at detunings of -15 and $+15$ MHz also reveal this effect of the excitation avalanche. The counting distribution measured without seed atoms is shown in red in Fig. 6.8c) and d) and is bimodal for the Rydberg excitation at a detuning of -15 MHz. In this case, the majority of the experimental cycles leads to the formation of only a few Rydberg-atom pairs, but a few cycles give rise to an ionisation signal that is more than 10 times stronger, and of the same strength as observed when the short-pulse UV laser is turned on. The conditions for an excitation avalanche are thus only occasionally realised. It appears that not all seed atoms are effective in inducing an excitation avalanche, but that those that are effective lead to very similar enhancement of the excitation. The behaviour is reminiscent of that of a saturable autocatalytic process, and suggests that the process terminates when the entire sample has been excited. Assuming that the initial excitation occurs at the centre of the 30-μm-diameter cloud of ultracold Cs atoms and taking a facilitation radius of 5 μm for a detuning of -15 MHz (see Fig. 6.9a), the estimated enhancement factor corresponding to the avalanche excitation of the entire sample is ~ 100. At a positive detuning of $+15$ MHz, the counting distributions do not reveal any sign of an excitation avalanche, even though the enhancement factor of ~ 4 indicates the formation of small Rydberg-atom aggregates. Additional experimental and theoretical work is clearly needed to fully understand these intriguing observations.

6.6 Conclusions & Outlook

A sequential two-colour excitation scheme has been applied to study interacting Rydberg-atom-pair states. The results presented in this chapter demonstrate that a spectral resolution of 3 MHz can be achieved, which is almost two orders of magnitude better compared to corresponding one-colour two-photon excitation schemes. The possibility of accessing pair states of Rydberg atoms in different angular-momentum states (such as nsnp pair states, by preparing the seed Rydberg atoms using a two-photon transition) has been successfully demonstrated. Finally, the two-colour excitation scheme was applied to study the formation of larger Rydberg aggregates under conditions where the excitation of many atoms is facilitated by a single or only very few seed Rydberg atoms.

The unprecedented resolution of 3 MHz enabled the observation of bound macrodimers consisting of two cesium atoms in high Rydberg states. The macrodimers correlate to Cs $n\mathrm{p}_{3/2}$ + Cs $((n+1)\mathrm{s}_{1/2})$ dissociation asymptotes and are observed at the

positions of avoided crossings between long-range van der Waals potential curves. The lower, repulsive and the upper, bound molecular states are clearly resolved in the experiments. The bound macrodimers are distinguished from repulsive molecular states by means of their behaviour with respect to spontaneous ionisation. The experimental results are in agreement with simulations based on a detailed model of the long-range multipole-multipole interactions of Rydberg-atom-pair states. Calculations of vibrational levels in these long-range potentials were performed, but the vibrational states could not be resolved in the experiments. The next important step towards an unambiguous observation of metastable bound quantum states in long-range potentials correlated to Rydberg-atom-pair states would be to resolve these vibrational series. Lower temperatures, higher atom densities and narrower-bandwidth laser radiation are required to achieve this goal.

Finally, the situation is similar to the situation encountered in the experiments on long-range Rydberg molecules described in Chapter 4: The adiabatic potential model accounts very accurately (to about $\sim 2\,\mathrm{MHz}$) for the positions of the experimentally observed resonances, but fails to explain the fast ($1\,\mu\mathrm{s}$ timescale) decay of the long-range molecular states observed experimentally.

Chapter 7

Conclusions & Outlook

In this thesis, high-resolution spectroscopy of ultracold and dense gas-phase samples of Cs using narrow-bandwidth laser radiation and millimetre waves has been used to investigate interactions between Cs Rydberg atoms and with their environment with unprecendented precision and accuracy.

A prerequisite for the investigation of the effects of such interactions is a thorough characterisation of the properties of the isolated (noninteracting) atoms. The first part of this thesis, summarised in Chapters 2 and 3 was therefore devoted to precision spectroscopic measurements of the properties of the Rydberg states of Cs.

In the first studies of the Rydberg-energy-level structure of the Cs atom, the precision and accuracy limits of spectroscopic investigations of high-n Rydberg states of Cs were established in the same apparatus used later for studying the interactions. Millimetre-wave transitions between Rydberg states were recorded at a resolution (full width at half maximum of the observed lines) of 17 kHz (Section 3.1). This resolution is a factor of three better than what was achieved in a molecular beam [114] where the transit time of the atoms limits the interaction time with the radiation and thus the spectral resolution. Transit-time broadening and Doppler broadening were found to be negligible for the ultracold samples used in this work. As in comparable experiments in ultracold Rb [248, 249], the resolution of the spectroscopic measurements presented here was limited at high n values by the impossibility to exactly compensate inhomogeneous electric and magnetic stray fields and by the natural linewidths of the transitions at low n values.

Higher resolution requires a reduced inhomogeneity of the stray fields, which in the future could be achieved using a different experimental geometry in which the photoexcitation region is located farther away from any (especially electrically insulating) surfaces (see, *e.g.*, the experiments on very-high-n Rydberg states in Ref. [250]). However, in setups used to generate dense samples of ultracold atoms, the large magnetic-field gradient of the MOT imposes restrictions on the geometry of the exper-

imental geometry. Higher resolution, which always implies longer coherence times, can also be achieved in transitions involving states which are insensitive to external stray fields, *e.g.* transitions from the ground state to $k = 0$ states of Rydberg-Stark manifolds, $(n+1)\mathrm{s} \leftarrow n\mathrm{s}_{1/2}$ two-photon transitions with very small differential Stark and Zeeman shifts, or transitions involving long lived, low-n Rydberg states.

The possibility to accurately measure absolute frequencies in the optical regime using a frequency comb was exploited in the measurement of $n\mathrm{p}_J \leftarrow 6\mathrm{s}_{1/2}$ transitions to $n\mathrm{p}_{3/2}$ and $n\mathrm{p}_{1/2}$ Rydberg states of Cs. In these experiments (see Section 3.2), each transition frequency was determined to an accuracy and precision of better than 100 kHz. Extrapolation of the Rydberg series in a global fit of the Rydberg-Ritz formula yielded $E_{\mathrm{I,Cs}} = hc \cdot 31\,406.467\,732\,5(14)\,\mathrm{cm}^{-1}$, the most accurately determined value of an ionisation energy so far in any atom other than hydrogen and an improvement in precision compared to the previous value by two order of magnitude [121, 122]. Improved values of the quantum defects and their energy dependence could also be derived.

A further significant improvement of the level of precision and accuracy of the determination of the ionisation energy in Cs will require the improvement of many experimental parameters, in particular a reduction of the laser bandwidth and a reduction of the temperature of the sample (to avoid limitations by the Doppler broadening). The measurement presented here should rather inspire other experiments to achieve a similar level of precision in lighter atoms or molecules, where the measurements of ionisation energies can challenge theoretical calculations [161, 163, 164, 251], which cannot reach the required accuracy in Cs containing 55 electrons.

These precision measurements formed the starting point of the experiments that led to the main scientific results presented in this thesis: the detection and characterisation of two types of metastable long-range molecules arising from the interactions between a Cs Rydberg atom and another Cs atom located in its vicinity. The first type of such molecules consists of long-range Rydberg molecules correlated to $\mathrm{Cs}(n\mathrm{p}_{3/2}) + \mathrm{Cs}(6\mathrm{s}_{1/2}, F = 3, 4)$ dissociation asymptotes. The binding in these long-range Rydberg molecules results from the low-energy s-wave scattering of the Rydberg electron off the ground-state atom. The second type of molecules consists of bound macrodimers, made of two weakly interacting Rydberg atoms correlated to $n\mathrm{p}_{3/2}(n+1)\mathrm{s}_{1/2}$ asymptotes. For comparison with the experimental results, bound states in long-range potential wells were also investigated theoretically for both the interaction of a Rydberg atom and a ground-state atom and for the long-range multipole-multipole interaction between two Rydberg atoms.

The long-range Rydberg molecules bound by low-energy electron-neutral-atom scattering had been observed prior to this work in several systems [40–50], and lifetimes comparable to the radiative lifetimes of the correlated atomic Rydberg states

had been observed [170, 171]. The experiments presented in this thesis contribute two important new observations to the characterisation of these exotic molecules: Firstly, the effect of the singlet channel in the electron-Cs scattering on the molecular binding was observed experimentally (see Chapter 4 and Ref. [167]) by exploiting the mixing between singlet and triplet scattering channels induced by the hyperfine interaction of the ground-state atom [39]. This mixing leads to the formation of bound states with F-dependent binding energies. By comparing the measured binding energies to those predicted using an s-wave-scattering potential model, the value of $a_{S,0} = -3.5 \pm 0.4\ a_0$ for the zero-energy singlet scattering length for electron-Cs scattering could be determined for the first time on the basis of experimental data. The second important contribution concerns the decay of these molecular states. All long-range Rydberg molecules were detected *via* the rapid (lifetimes below 1 µs at $n = 33$) decay into molecular Cs_2^+ ions. Whereas the potential model based on s-wave scattering of the Rydberg electron off the ground-state atom accounts for the binding energies of the vibrational ground states of the long-range Rydberg molecules, the fast decay (as well as the occurrence of further molecular resonances) could not be unambiguously explained. Possible explanations discussed in this thesis are effects of p-wave scattering, enhanced by the presence of low-energy p-wave-scattering shape resonances in the $e^- + Cs$ scattering [178], and the coupling to molecular Rydberg series converging to high vibrational levels of the Cs_2^+ ion. The inclusion of the p-wave scattering in the model in conjunction with further systematic experimental investigations of the lifetimes of the long-range Rydberg molecules for different electronic and vibrational states and states associated with different dissociation thresholds has the potential to resolve some of the open questions raised by the results presented here.

The bound Rydberg macrodimers, contrary to the established long-range Rydberg molecules, had not been unambiguously identified before this thesis, even though resonances of interacting Rydberg-atom-pair states had been observed [58–65]. Indirect evidence of bound macrodimers was found in pairs of Cs Rydberg atoms at n values around 66 in the presence of an electric field [63]. In the course of this thesis, two different excitation schemes were applied to study the interactions in Rydberg-atom-pair states. In the first set of experiments, interacting-Rydberg-atom-pair resonances were observed following excitation with an intense pulsed UV laser. The resonances were excited in one-colour two-photon transitions at a resolution of 130 MHz and were classified as belonging to the following categories:

1. Resonances correlated to $ns_{1/2}(n+1)s_{1/2}$ pair-dissociation asymptotes (see Section 5.3.1). These resonances result primarily from the dipole-dipole interaction with the optically accessible $np_{3/2}np_{3/2}$ pair states.

2. Resonances correlated to $ns_{1/2}(n-3)f_j$ and $(n+1)s_{1/2}(n-4)f_j$ pair-dissociation asymptotes (see Section 5.3.2). These resonances are an effect of the dipole-quadrupole interaction with the optically accessible $np_{3/2}np_{3/2}$ pair states. The occurrence of the dipole-quadrupole interaction between two atoms in isotropic space (with negligible external fields) is surprising at first because the dipole-quadrupole interaction does not conserve the electronic parity of the pair state. Consequently, its observation betrayed the coupling of electronic and nuclear degrees of freedom in long-range Rydberg-atom-pair states. The coupling was shown to be facilitated by the quasi-degeneracy of rotational levels of the collision complex.

3. Window resonances at the positions of avoided level crossings between potential functions correlated to $(n-4)f_j(n-3)f_j$ and $np_{3/2}np_{3/2}$ pair-dissociation asymptotes (see Section 5.3.3). The accurate modelling of the positions of these avoided level crossings required the inclusion of terms up to the octupole-octupole interaction in the long-range-interaction Hamiltonian operator. The effects of these higher-order terms had typically been neglected in previous treatments of interactions between ultracold Rydberg atoms, but were found to be dominant here.

4. Resonances resulting from potential maxima correlated to $ns_{1/2}(n+1)s_{1/2}$ pair-dissociation asymptotes (see Section 5.3.1).

These pair resonances were detected *via* spontaneously formed Cs^+ ions. The dynamics and the mechanism of the spontaneous ionisation of Rydberg-atom pairs with attractive long-range potential functions could be quantitatively understood: Penning ionsation was shown to occur after acceleration of the two Rydberg atoms towards each other followed by Auger-type ionisation in regions close to the LeRoy radius, where orbital overlap becomes significant (see Section 5.3.5). Similar processes, though with smaller rates, can occur when atom pairs are excited to repulsive potential functions. The difference is that ionising collisions occur after the dissociation of the initial Rydberg-atom pair with other Rydberg atoms [228].

In a second set of experiments (see Chapter 6) aimed at investigating Rydberg-atom-pair states at a higher spectral resolution, a sequential, resonant excitation scheme involving, in the first step, the generation of a small number of Rydberg atoms (called seed Rydberg atoms) and, using a second, frequency-detuned laser, the excitation of neighbouring atoms to form Rydberg-atom-pair states. In these experiments, resonances detuned by several hundred MHz from $np_{3/2}n's_{1/2}$ pair-dissociation asymptotes (with $n = 44, 45$) could be observed at a resolution of ~ 3 MHz and directly linked to potential wells by a detailed model of the interaction potentials.

Even though the adiabatic potential model also predicted vibrational levels in these long-range wells, the corresponding molecular resonances were found to rapidly decay to Cs^+ ions with estimated decay rates of ~4 MHz. Further experimental and theoretical studies are required to clarify whether the observed decay is related to a general instability and bound macrodimers do not exist in the form in which they are predicted [229] or to establish the specific decay mechanism.

Experimentally, it would be advantageous in the future to investigate the seeded excitation of Rydberg macrodimers and aggregates in a dual-species experiment. In this case, the seed Rydberg atoms could be prepared from one atom type and distinguished from additionally excited Rydberg atoms of the other type by means of their ion time of flight to the detector. This measurement of interacting Rydberg macrodimers would be background free, and would enable the measurements at lower values of the principal quantum number than was possible in the studies presented in this thesis. Indeed, at lower n values, the potential wells are also predicted but could not be observed so far because of insufficient experimental sensitivity. The observation of these states would, however, enable the resolution of the vibrational levels in the long-range potential wells using the current laser system, which would be a direct indication of the existence of metastable bound macrodimers. Finally, the observation of an Rydberg-excitation avalanche was observed and interpreted using the concept of a facilitation radius and a facilitated volume.

The motivation and basis for many scientific applications (see, *e.g.*, Refs. [25, 114, 252]) of Rydberg states are their long lifetimes scaling as n^3 with the principal quantum number. In the case of Cs, the lifetimes of np Rydberg states are longer than 100 μs for $n > 30$, even including 300-K-blackbody-radiation-induced transitions [73]. However, in the experimental studies presented in this thesis, atomic Rydberg states, interacting Rydberg-atom-pair states and long-range Rydberg molecules were often detected *via* their ionic decay products. The ionisation rates for interacting, molecular states were found to be on the order of 1 MHz, much faster than the ionisation rates of a low-density Rydberg gas. Consequently, the spontaneous formation of ions on sub-microsecond timescales was used as a sensitive tool for the detection of molecular resonances. However, the spontaneous ionisation of the ultracold Rydberg gas was observed also in low-density samples produced by resonant Rydberg excitation and was used to detect atomic Rydberg transitions to states that would not have field ionised in our experimental setup (see Section 3.2). Ionisation of resonantly excited Rydberg atoms can be induced by blackbody radiation, collision with ground-state atoms and with other Rydberg atoms. It can be concluded that long coherence times with high Rydberg states can presumably only be exploited under very-low-density conditions and when inhomogeneous broadenings induced by stray fields are small. Several aspects of the ionisation mechanism remain poorly understood and further

experimental and theoretical work in this direction would be desirable.

Appendix A

Units and Constants

Constants

Table A.1: List of the fundamental constants used in this dissertation (from Ref. [253]).

Quantity	Symbol	Value	Unit
Speed of light (vacuum)	c, c_0	299 792 458	$\mathrm{m\,s^{-1}}$
Electric constant	ε_0	8.854 187 817...$\times 10^{-12}$	$\mathrm{A\,s\,(V\,m)^{-1}}$
Planck constant	h	6.626 069 57(29)$\times 10^{-34}$	J s
	$\hbar = \frac{h}{2\pi}$	1.054 571 726(47)$\times 10^{-34}$	J s
Elementary charge	e	1.602 176 565(35)$\times 10^{-19}$	C
Rydberg constant	$R_\infty = \frac{\alpha^2 m_e c}{2h}$	109 737.315 685 39(55)	$\mathrm{cm^{-1}}$
Bohr radius	$a_0 = \frac{4\pi\varepsilon_0\hbar^2}{m_e e^2}$	0.529 177 210 92(17)$\times 10^{-10}$	m
Bohr magneton	$\mu_\mathrm{B} = \frac{e\hbar}{2m_e}$	9.274 009 68(20)$\times 10^{-24}$	$\mathrm{J\,T^{-1}}$
Electron rest mass	m_e	9.109 382 91(40)$\times 10^{-31}$	kg
Proton rest mass	m_p	1.672 621 777(74)$\times 10^{-27}$	kg
Neutron rest mass	m_n	1.674 927 351(74)$\times 10^{-27}$	kg
Constant of Avogadro	N_A	6.022 141 29(27)$\times 10^{23}$	$\mathrm{mol^{-1}}$
Boltzmann constant	k, k_B	1.380 648 8(13)$\times 10^{-23}$	$\mathrm{J\,K^{-1}}$

Atomic units

Table A.2: List of atomic units (from Ref. [253]).

Quantity	Symbol	Value	Unit
Electric charge	e	$1.602\,176\,565(35)\times10^{-19}$	C
Mass	m_e	$9.109\,382\,91(40)\times10^{-31}$	kg
Action	$\hbar$	$1.054\,571\,726(47)\times10^{-34}$	$\mathrm{J\,s^{-1}}$
Length	a_0	$0.529\,177\,210\,92(17)\times10^{-10}$	m
Energy	E_h	$4.359\,744\,17(75)\times10^{-18}$	J
Time	$\frac{\hbar}{E_\mathrm{h}}$	$2.418\,884\,326\,505(16)\times10^{-17}$	s
Force	$\frac{E_\mathrm{h}}{a_0}$	$8.238\,722\,5(14)\times10^{-8}$	N
Velocity	$\frac{a_0 E_\mathrm{h}}{\hbar}$	$2.187\,691\,263\,3(73)\times10^{6}$	$\mathrm{m\,s^{-1}}$
Electric potential	$\frac{E_\mathrm{h}}{e}$	27.211 384 5(23)	V
Electric field	$\frac{E_\mathrm{h}}{a_0 e}$	$5.142\,206\,42(44)\times10^{11}$	$\mathrm{V\,m^{-1}}$

Energy equivalents

Table A.3: List of energy equivalents [253].

	$\frac{E}{hc}$ / $\mathrm{cm^{-1}}$	$\frac{E}{h}$ / GHz
$E = 1$ J	$5.034\,117\,20(86)\times10^{22}$	$1.509\,190\,37(26)\times10^{24}$
$\frac{E}{hc} = 1\ \mathrm{cm^{-1}}$	1	29.979 245 8
$\frac{E}{h} = 1$ GHz	0.033 356 409 ...	1
$E = 1$ eV	8 065.544 45(69)	$2.417\,989\,40(21)\times10^{5}$
$E = 1\,E_\mathrm{h}$	$2.194\,746\,313\,705(15)\times10^{5}$	$6.579\,683\,920\,721(44)\times10^{6}$

Appendix B

Matrix elements of the long-range multipole-multipole-interaction Hamiltonian

In this appendix, expressions for the matrix elements of the atomic multipoles contributing to V_{inter} (see Eq. (5.2)) are derived in the product basis $|n_\text{A} l_\text{A} j_\text{A} \omega_\text{A}, n_\text{B} l_\text{B} j_\text{B} \omega_\text{B}\rangle$. The full form of the Hamiltonian operator of the long-range interaction between two neutral atoms A and B including dipole-dipole, dipole-quadrupole and quadrupole-quadrupole contributions is

$$\begin{aligned} V'_{\text{inter}} = &- \frac{1}{R^3} Q^\text{A}_{1,0} Q^\text{B}_{1,0} \\ &- \frac{1}{\sqrt{2}R^3} (Q^\text{A}_{1,-1} Q^\text{B}_{1,1} + Q^\text{A}_{1,1} Q^\text{B}_{1,-1}) \\ &+ \frac{\sqrt{3}}{R^4} (Q^\text{A}_{1,-1} Q^\text{B}_{2,1} - Q^\text{A}_{2,-1} Q^\text{B}_{1,1} \\ &+ \frac{3}{R^4} (Q^\text{A}_{1,0} Q^\text{B}_{2,0} - Q^\text{A}_{2,0} Q^\text{B}_{1,0}) \\ &\quad + Q^\text{A}_{1,1} Q^\text{B}_{2,-1} - Q^\text{A}_{2,1} Q^\text{B}_{1,-1}) \\ &+ \frac{6}{R^5} Q^\text{A}_{2,0} Q^\text{B}_{2,0} \\ &+ \frac{2\sqrt{6}}{R^5} (Q^\text{A}_{2,-1} Q^\text{B}_{2,1} + Q^\text{A}_{2,1} Q^\text{B}_{2,-1}) \\ &+ \frac{\sqrt{6}}{R^5} (Q^\text{A}_{2,-2} Q^\text{B}_{2,2} + Q^\text{A}_{2,2} Q^\text{B}_{2,-2}). \end{aligned} \tag{B.1}$$

The matrix elements of an atomic multipole

$$Q_{L,\omega}(\vec{r}) = \sqrt{\frac{4\pi}{2L+1}} r^L Y_{L,\omega}(\hat{r}) \tag{B.2}$$

in this basis are given by

$$\begin{aligned}&\langle n_i' l_i' j_i' \omega_i' |\, \hat{Q}_{L,\omega}(\vec{r}) \,| n_i l_i j_i \omega_i \rangle \\ &= \sqrt{\frac{4\pi}{2L+1}}\, \langle n_i' l_i' j_i' |\, \hat{r}^L \,| n_i l_i j_i \rangle\, \langle l_i' j_i' \omega_i' |\, \hat{Y}_{L,\omega}(\hat{r}) \,| l_i j_i \omega_i \rangle\,, \end{aligned} \tag{B.3}$$

where the radial matrix elements

$$\begin{aligned}&\langle n_i' l_i' j_i' |\, \hat{r}^L \,| n_i l_i j_i \rangle \equiv R_{n_i l_i j_i}^{n_i' l_i' j_i' L} \\ &= \int \Psi^*_{n_i' l_i' j_i'}(r) r^L \Psi_{n_i l_i j_i}(r)\, dr \end{aligned} \tag{B.4}$$

are evaluated numerically using the Numerov method [115] and a model core potential [254]. The angular matrix elements are evaluated using the analytical expressions [255]

$$\begin{aligned}&\langle l_i' j_i' \omega_i' |\, \hat{Y}_{L,\omega}(\hat{r}) \,| l_i j_i \omega_i \rangle \\ &= (-1)^{j_i + l_i' + L + \frac{1}{2}} \sqrt{(2j_i+1)(2l_i+1)} \\ &\times \begin{Bmatrix} l_i & \frac{1}{2} & j_i \\ j_i' & L & l_i' \end{Bmatrix} \sqrt{\frac{2L+1}{4\pi}}\, C^{l_i' 0}_{l_i 0, L 0}\, C^{j_i' \omega_i'}_{j_i \omega_i, L\omega}\,, \end{aligned} \tag{B.5}$$

where $C^{l_i' \omega_i'}_{l_i \omega_i, L\omega}$ are the Clebsch-Gordan coefficients and $\begin{Bmatrix} j_1 & j_2 & j_3 \\ j_4 & j_5 & j_6 \end{Bmatrix}$ is Wigner's 6-j symbol.

As an example, the full expression for the matrix elements of the lowest-order term in the multipole expansion, the dipole-dipole interaction, is given here:

$$\begin{aligned}&\langle n_A' l_A' j_A' \omega_A', n_B' l_B' j_B' \omega_B' |\, \hat{V}_{\mathrm{dd}} \,| n_A l_A j_A \omega_A, n_B l_B j_B \omega_B \rangle \\ &= (-1)^{j_A + j_B + l_A' + l_B'} R^{-3} R^{n_A' l_A' j_A' \, 1}_{n_A l_A j_A}\, R^{n_B' l_B' j_B' \, 1}_{n_B l_B j_B} \\ &\times \sqrt{(2j_A+1)(2j_B+1)(2l_A+1)(2l_B+1)} \\ &\times \Big(C^{j_A' \omega_A'}_{j_A \omega_A, 1 1}\, C^{j_B' \omega_B'}_{j_B \omega_B, 1 -1} + \\ &+ 2 C^{j_A' \omega_A'}_{j_A \omega_A, 1 0}\, C^{j_B' \omega_B'}_{j_B \omega_B, 1 0} + C^{j_A' \omega_A'}_{j_A \omega_A, 1 -1}\, C^{j_B' \omega_B'}_{j_B \omega_B, 1 1} \Big) \\ &\times C^{l_A' 0}_{l_A 0, 1 0}\, C^{l_B' 0}_{l_B 0, 1 0} \begin{Bmatrix} l_A & \frac{1}{2} & j_A \\ j_A' & L & l_A' \end{Bmatrix} \begin{Bmatrix} l_B & \frac{1}{2} & j_B \\ j_B' & L & l_B' \end{Bmatrix}. \end{aligned} \tag{B.6}$$

List of Figures

List of Tables

Bibliography

[1] T. W. Hänsch and A. L. Schawlow: "Cooling of gases by laser radiation", *Optics Communications* **13** (1), 68 (1975).

[2] D. Wineland and H. Dehmelt: "Proposed $10^{14}\ \Delta\nu < \nu$ laser fluorescence spectroscopy on TI^{+} mono-ion oscillator III", in "Bulletin of the American Physical Society", volume 20, 637–637 (1975).

[3] D. J. Wineland and W. M. Itano: "Laser cooling of atoms", *Phys. Rev. A* **20**, 1521 (1979).

[4] E. L. Raab, M. Prentiss, A. Cable, S. Chu and D. E. Pritchard: "Trapping of Neutral Sodium Atoms with Radiation Pressure", *Phys. Rev. Lett.* **59**, 2631 (1987).

[5] A. Aspect, E. Arimondo, R. Kaiser, N. Vansteenkiste and C. Cohen-Tannoudji: "Laser Cooling below the One-Photon Recoil Energy by Velocity-Selective Coherent Population Trapping", *Phys. Rev. Lett.* **61**, 826 (1988).

[6] C. Monroe, W. Swann, H. Robinson and C. Wieman: "Very cold trapped atoms in a vapor cell", *Phys. Rev. Lett.* **65**, 1571 (1990).

[7] M. Kasevich and S. Chu: "Laser cooling below a photon recoil with three-level atoms", *Phys. Rev. Lett.* **69**, 1741 (1992).

[8] I. Mourachko, D. Comparat, F. de Tomasi, A. Fioretti, P. Nosbaum, V. M. Akulin and P. Pillet: "Many-Body Effects in a Frozen Rydberg Gas", *Phys. Rev. Lett.* **80**, 253 (1998).

[9] W. R. Anderson, J. R. Veale and T. F. Gallagher: "Resonant Dipole-Dipole Energy Transfer in a Nearly Frozen Rydberg Gas", *Phys. Rev. Lett.* **80**, 249 (1998).

[10] W. Vassen, C. Cohen-Tannoudji, M. Leduc, D. Boiron, C. I. Westbrook, A. Truscott, K. Baldwin, G. Birkl, P. Cancio and M. Trippenbach: "Cold and trapped metastable noble gases", *Rev. Mod. Phys.* **84**, 175 (2012).

[11] E. S. Shuman, J. F. Barry and D. DeMille: "Laser cooling of a diatomic molecule", *Nature* **467** (7317), 820 (2010).

[12] M. T. Hummon, M. Yeo, B. K. Stuhl, A. L. Collopy, Y. Xia and J. Ye: "2D Magneto-Optical Trapping of Diatomic Molecules", *Phys. Rev. Lett.* **110**, 143001 (2013).

[13] V. Zhelyazkova, A. Cournol, T. E. Wall, A. Matsushima, J. J. Hudson, E. A. Hinds, M. R. Tarbutt and B. E. Sauer: "Laser cooling and slowing of CaF molecules", *Phys. Rev. A* **89**, 053416 (2014).

[14] J. R. Rydberg: "XXXIV. On the structure of the line-spectra of the chemical elements", *Philos. Mag. Series 5* **29** (179), 331 (1890).

[15] T. F. Gallagher: *Rydberg Atoms*, Cambridge University Press (2005).

[16] R. F. Stebbings and F. B. Dunning (eds.): *Rydberg States of Atoms and Molecules*, Cambridge University Press, Cambridge (1983).

[17] J.-P. Connerade: *Highly Excited Atoms*, Cambridge University Press, Cambridge (1998).

[18] S. Haroche: "Nobel Lecture: Controlling photons in a box and exploring the quantum to classical boundary*", *Rev. Mod. Phys.* **85** (3), 1083 (2013).

[19] J. M. Raimond, M. Brune and S. Haroche: "Manipulating quantum entanglement with atoms and photons in a cavity", *Rev. Mod. Phys.* **73**, 565 (2001).

[20] C. Guerlin, E. Brion, T. Esslinger and K. Mølmer: "Cavity quantum electrodynamics with a Rydberg-blocked atomic ensemble", *Phys. Rev. A* **82**, 053832 (2010).

[21] T. Peyronel, O. Firstenberg, Q.-Y. Liang, S. Hofferberth, A. V. Gorshkov, T. Pohl, M. D. Lukin and V. Vuletić: "Quantum nonlinear optics with single photons enabled by strongly interacting atoms", *Nature* **488** (7409), 57 (2012).

[22] Y. O. Dudin and A. Kuzmich: "Strongly Interacting Rydberg Excitations of a Cold Atomic Gas", *Science* **336** (6083), 887 (2012).

[23] D. Maxwell, D. J. Szwer, D. Paredes-Barato, H. Busche, J. D. Pritchard, A. Gauguet, K. J. Weatherill, M. P. A. Jones and C. S. Adams: "Storage and Control of Optical Photons Using Rydberg Polaritons", *Phys. Rev. Lett.* **110**, 103001 (2013).

[24] D. Tiarks, S. Baur, K. Schneider, S. Dürr and G. Rempe: "Single-Photon Transistor Using a Förster Resonance", *Phys. Rev. Lett.* **113**, 053602 (2014).

[25] M. D. Lukin, M. Fleischhauer, R. Côté, L. M. Duan, D. Jaksch, J. I. Cirac and P. Zoller: "Dipole Blockade and Quantum Information Processing in Mesoscopic Atomic Ensembles", *Phys. Rev. Lett.* **87**, 037901 (2001).

[26] M. Saffman, T. G. Walker and K. Mølmer: "Quantum information with Rydberg atoms", *Rev. Mod. Phys.* **82**, 2313 (2010).

[27] H. Weimer, M. Müller, I. Lesanovsky, P. Zoller and H. P. Büchler: "A Rydberg quantum simulator", *Nat. Phys.* **6** (5), 382 (2010).

[28] G. Pupillo, A. Micheli, M. Boninsegni, I. Lesanovsky and P. Zoller: "Strongly Correlated Gases of Rydberg-Dressed Atoms: Quantum and Classical Dynamics", *Phys. Rev. Lett.* **104**, 223002 (2010).

[29] H. Weimer, M. Müller, H. P. Büchler and I. Lesanovsky: "Digital quantum simulation with Rydberg atoms", *Quantum Information Processing* **10** (6), 885 (2011).

[30] E. Urban, T. A. Johnson, T. Henage, L. Isenhower, D. D. Yavuz, T. G. Walker and M. Saffman: "Observation of Rydberg blockade between two atoms", *Nat Phys* **5** (2), 110 (2009).

[31] A. Gaëtan, Y. Miroshnychenko, T. Wilk, A. Chotia, M. Viteau, D. Comparat, P. Pillet, A. Browaeys and P. Grangier: "Observation of collective excitation of two individual atoms in the Rydberg blockade regime", *Nat Phys* **5** (2), 115 (2009).

[32] T. Wilk, A. Gaëtan, C. Evellin, J. Wolters, Y. Miroshnychenko, P. Grangier and A. Browaeys: "Entanglement of Two Individual Neutral Atoms Using Rydberg Blockade", *Phys. Rev. Lett.* **104** (1), 010502 (2010).

[33] D. Jaksch, J. I. Cirac, P. Zoller, S. L. Rolston, R. Côté and M. D. Lukin: "Fast Quantum Gates for Neutral Atoms", *Phys. Rev. Lett.* **85**, 2208 (2000).

[34] L. Isenhower, E. Urban, X. L. Zhang, A. T. Gill, T. Henage, T. A. Johnson, T. G. Walker and M. Saffman: "Demonstration of a Neutral Atom Controlled-NOT Quantum Gate", *Phys. Rev. Lett.* **104** (1), 010503 (2010).

[35] M. A. Baig, M. S. Mahmood, M. Akram and J. Hormes: "Inner-shell and double excitation spectrum of caesium involving 5p and 6s subshells", *Journal of Physics B: Atomic, Molecular and Optical Physics* **29** (17), 3871 (1996).

[36] E. Amaldi and E. Segrè: "Effetto della Pressione Sui Termini Elevati Degli Alcalini", *Il Nuovo Cimento* **11** (3), 145 (1934).

[37] E. Fermi: "Sopra lo Spostamento per Pressione delle Righe Elevate delle Serie Spettrali", *Il Nuovo Cimento* **11** (3), 157 (1934).

[38] C. H. Greene, A. S. Dickinson and H. R. Sadeghpour: "Creation of Polar and Nonpolar Ultra-Long-Range Rydberg Molecules", *Phys. Rev. Lett.* **85**, 2458 (2000).

[39] D. A. Anderson, S. A. Miller and G. Raithel: "Angular-momentum couplings in long-range Rb_2 Rydberg molecules", *Phys. Rev. A* **90**, 062518 (2014).

[40] V. Bendkowsky, B. Butscher, J. Nipper, J. P. Shaffer, R. Löw and T. Pfau: "Observation of ultralong-range Rydberg molecules", *Nature* **458** (7241), 1005 (2009).

[41] V. Bendkowsky, B. Butscher, J. Nipper, J. B. Balewski, J. P. Shaffer, R. Löw, T. Pfau, W. Li, J. Stanojevic, T. Pohl and J. M. Rost: "Rydberg Trimers and Excited Dimers Bound by Internal Quantum Reflection", *Phys. Rev. Lett.* **105** (16), 163201 (2010).

[42] W. Li, T. Pohl, J. M. Rost, S. T. Rittenhouse, H. R. Sadeghpour, J. Nipper, B. Butscher, J. B. Balewski, V. Bendkowsky, R. Löw and T. Pfau: "A Homonuclear Molecule with a Permanent Electric Dipole Moment", *Science* **334** (6059), 1110 (2011).

[43] J. B. Balewski, A. T. Krupp, A. Gaj, D. Peter, H. P. Büchler, R. Löw, S. Hofferberth and T. Pfau: "Coupling a single electron to a Bose-Einstein condensate", *Nature* **502** (7473), 664 (2013), letter.

[44] A. Krupp, A. Gaj, J. Balewski, P. Ilzhöfer, S. Hofferberth, R. Löw, T. Pfau, M. Kurz and P. Schmelcher: "Alignment of D-State Rydberg Molecules", *Physical Review Letters* **112** (14), 143008 (2014).

[45] A. Gaj, A. T. Krupp, J. B. Balewski, R. Löw, S. Hofferberth and T. Pfau: "From molecular spectra to a density shift in dense Rydberg gases", *Nat Commun* **5** (2014), article.

[46] D. Anderson, S. Miller and G. Raithel: "Photoassociation of Long-Range nD Rydberg Molecules", *Physical Review Letters* **112** (16), 163201 (2014).

[47] D. Booth, S. T. Rittenhouse, J. Yang, H. R. Sadeghpour and J. P. Shaffer: "Production of trilobite Rydberg molecule dimers with kilo-Debye permanent electric dipole moments", *Science* **348** (6230), 99 (2015).

[48] T. Manthey, T. Niederprüm, O. Thomas and H. Ott: "Dynamically probing ultracold lattice gases via Rydberg molecules", *New Journal of Physics* **17** (10), 103024 (2015).

[49] B. J. DeSalvo, J. A. Aman, F. B. Dunning, T. C. Killian, H. R. Sadeghpour, S. Yoshida and J. Burgdörfer: "Ultra-long-range Rydberg molecules in a divalent atomic system", *Phys. Rev. A* **92**, 031403 (2015).

[50] F. Böttcher, A. Gaj, K. M. Westphal, M. Schlagmüller, K. S. Kleinbach, R. Löw, T. C. Liebisch, T. Pfau and S. Hofferberth: "Observation of mixed singlet-triplet Rb_2 Rydberg molecules", *Phys. Rev. A* **93**, 032512 (2016).

[51] G. Vitrant, J. M. Raimond, M. Gross and S. Haroche: "Rydberg to plasma evolution in a dense gas of very excited atoms", *J. Phys. B* **15** (2), L49 (1982).

[52] T. F. Gallagher, K. A. Safinya, F. Gounand, J. F. Delpech, W. Sandner and R. Kachru: "Resonant Rydberg-atom - Rydbert-atom collisions", *Phys. Rev. A* **25** (4), 1905 (1982).

[53] M. P. Robinson, B. L. Tolra, M. W. Noel, T. F. Gallagher and P. Pillet: "Spontaneous Evolution of Rydberg Atoms into an Ultracold Plasma", *Phys. Rev. Lett.* **85** (21), 4466 (2000).

[54] W. Li, P. J. Tanner and T. F. Gallagher: "Dipole-Dipole Excitation and Ionization in an Ultracold Gas of Rydberg Atoms", *Phys. Rev. Lett.* **94**, 173001 (2005).

[55] T. E. Lee, H. Häffner and M. C. Cross: "Antiferromagnetic phase transition in a nonequilibrium lattice of Rydberg atoms", *Phys. Rev. A* **84**, 031402 (2011).

[56] C. Carr, R. Ritter, C. G. Wade, C. S. Adams and K. J. Weatherill: "Nonequilibrium Phase Transition in a Dilute Rydberg Ensemble", *Phys. Rev. Lett.* **111**, 113901 (2013).

[57] N. Malossi, M. M. Valado, S. Scotto, P. Huillery, P. Pillet, D. Ciampini, E. Arimondo and O. Morsch: "Full Counting Statistics and Phase Diagram of a Dissipative Rydberg Gas", *Phys. Rev. Lett.* **113**, 023006 (2014).

[58] S. M. Farooqi, D. Tong, S. Krishnan, J. Stanojevic, Y. P. Zhang, J. R. Ensher, A. S. Estrin, C. Boisseau, R. Côté, E. E. Eyler and P. L. Gould: "Long-Range Molecular Resonances in a Cold Rydberg Gas", *Phys. Rev. Lett.* **91** (18), 183002 (2003).

[59] J. STANOJEVIC, R. CÔTÉ, D. TONG, S. M. FAROOQI, E. E. EYLER and P. L. GOULD: "Long-range Rydberg-Rydberg interactions and molecular resonances", *Eur. Phys. J. D* **40** (1), 3 (2006).

[60] J. STANOJEVIC, R. CÔTÉ, D. TONG, E. E. EYLER and P. L. GOULD: "Long-range potentials and (n-1)d+ns molecular resonances in an ultracold Rydberg gas", *Phys. Rev. A* **78** (5), 052709 (2008).

[61] A. SCHWETTMANN, K. R. OVERSTREET, J. TALLANT and J. P. SHAFFER: "Analysis of long-range Cs Rydberg potential wells", *Journal of Modern Optics* **54** (16-17), 2551 (2007).

[62] K. R. OVERSTREET, A. SCHWETTMANN, J. TALLANT and J. P. SHAFFER: "Photoinitiated collisions between cold Cs Rydberg atoms", *Phys. Rev. A* **76** (1), 011403 (2007).

[63] K. R. OVERSTREET, A. SCHWETTMANN, J. TALLANT, D. BOOTH and J. P. SHAFFER: "Observation of electric-field-induced Cs Rydberg atom macrodimers", *Nat. Phys.* **5** (8), 581 (2009).

[64] J. DEIGLMAYR, H. SASSMANNSHAUSEN, P. PILLET and F. MERKT: "Observation of Dipole-Quadrupole Interaction in an Ultracold Gas of Rydberg Atoms", *Phys. Rev. Lett.* **113**, 193001 (2014).

[65] H. SASSMANNSHAUSEN, F. MERKT and J. DEIGLMAYR: "Pulsed excitation of Rydberg-atom-pair states in an ultracold Cs gas", *Phys. Rev. A* **92**, 032505 (2015).

[66] W. C. STWALLEY, Y.-H. UANG and G. PICHLER: "Pure Long-Range Molecules", *Phys. Rev. Lett.* **41**, 1164 (1978).

[67] H. R. THORSHEIM, J. WEINER and P. S. JULIENNE: "Laser-induced photoassociation of ultracold sodium atoms", *Physical Review Letters* **58** (23), 2420 (1987).

[68] A. FIORETTI, D. COMPARAT, A. CRUBELLIER, O. DULIEU, F. MASNOU-SEEUWS and P. PILLET: "Formation of Cold Cs_2 Molecules through Photoassociation", *Phys. Rev. Lett.* **80**, 4402 (1998).

[69] F. MASNOU-SEEUWS and P. PILLET: "Formation of ultracold molecules ($T \leq 200$ μK) via photoassociation in a gas of laser-cooled atoms", in B. B. WALTHER and HERBERT (eds.), "Advances In Atomic, Molecular, and Optical Physics", volume 47, 53–127, Academic Press (2001).

[70] K. M. Jones, E. Tiesinga, P. D. Lett and P. S. Julienne: "Ultracold photoassociation spectroscopy: Long-range molecules and atomic scattering", *Rev. Mod. Phys.* **78**, 483 (2006).

[71] L. Hollberg and J. L. Hall: "Measurement of the Shift of Rydberg Energy Levels Induced by Blackbody Radiation", *Phys. Rev. Lett.* **53** (3), 230 (1984).

[72] I. I. Beterov, D. B. Tretyakov, I. I. Ryabtsev, A. Ekers and N. N. Bezuglov: "Ionization of sodium and rubidium nS, nP, and nD Rydberg atoms by blackbody radiation", *Phys. Rev. A* **75** (5), 052720 (2007).

[73] V. D. Ovsiannikov, I. L. Glukhov and E. A. Nekipelov: "Rates of blackbody radiation-induced transitions from Rydberg states of alkali atoms", *J. Phys. B* **44** (19), 195010 (2011).

[74] D. J. Wineland, R. E. Drullinger and F. L. Walls: "Radiation-Pressure Cooling of Bound Resonant Absorbers", *Phys. Rev. Lett.* **40**, 1639 (1978).

[75] W. Neuhauser, M. Hohenstatt, P. Toschek and H. Dehmelt: "Optical-Sideband Cooling of Visible Atom Cloud Confined in Parabolic Well", *Phys. Rev. Lett.* **41**, 233 (1978).

[76] H. J. Metcalf and P. van der Straten: "Laser Cooling and Trapping", Graduate Texts in Contemporary Physics, Springer New York (1999).

[77] G. C. Bjorklund, M. D. Levenson, W. Lenth and C. Ortiz: "Frequency modulation (FM) spectroscopy", *Appl. Phys. B* **32**, 145 (1983).

[78] B. P. Anderson and M. A. Kasevich: "Loading a vapor-cell magneto-optic trap using light-induced atom desorption", *Phys. Rev. A* **63**, 023404 (2001).

[79] G. Reinaudi, T. Lahaye, Z. Wang and D. Guéry-Odelin: "Strong saturation absorption imaging of dense clouds of ultracold atoms", *Optics Letters* **32** (21), 3143 (2007).

[80] W. Petrich, M. H. Anderson, J. R. Ensher and E. A. Cornell: "Behavior of atoms in a compressed magneto-optical trap", *Journal of the Optical Society of America B* **11** (8), 1332 (1994).

[81] C. G. Townsend, N. H. Edwards, C. J. Cooper, K. P. Zetie, C. J. Foot, A. M. Steane, P. Szriftgiser, H. Perrin and J. Dalibard: "Phase-space density in the magneto-optical trap", *Phys. Rev. A* **52**, 1423 (1995).

[82] S. Chandrasekhar: "Stochastic Problems in Physics and Astronomy", *Rev. Mod. Phys.* **15**, 1 (1943).

[83] R. GRIMM, M. WEIDEMÜLLER and Y. B. OVCHINNIKOV: "Optical Dipole Traps for Neutral Atoms", in B. B. WALTHER and HERBERT (eds.), "Adv. At. Mol. Opt. Phys.", volume 42, 95, Academic Press (2000).

[84] J. TALLANT, D. BOOTH and J. P. SHAFFER: "Photoionization rates of Cs Rydberg atoms in a 1064-nm far-off-resonance trap", *Phys. Rev. A* **82**, 063406 (2010).

[85] T. R. O'BRIAN, J.-B. KIM, G. LAN, T. J. MCILRATH and T. B. LUCATORTO: "Verification of the ponderomotive approximation for the ac Stark shift in Xe Rydberg levels", *Phys. Rev. A* **49**, R649 (1994).

[86] A. FELINGER: *Data Analysis and Signal Processing in Chromatography/ Data Handling in Science and Technology*, volume 21, Elsevier, Amsterdam, the Netherlands (1998).

[87] T. G. WALKER and M. SAFFMAN: "Consequences of Zeeman degeneracy for the van der Waals blockade between Rydberg atoms", *Phys. Rev. A* **77** (3), 032723 (2008).

[88] M. M. SALOUR: "Powerful dye laser oscillator-amplifier system for high resolution and coherent pulse spectroscopy", *Opt. Comm.* **22** (2), 202 (1977).

[89] U. HOLLENSTEIN, H. PALM and F. MERKT: "A broadly tunable extreme ultraviolet laser source with a 0.008 cmâĹŠ1 bandwidth", *Review of Scientific Instruments* **71** (11) (2000).

[90] T. HÄNSCH and B. COUILLAUD: "Laser frequency stabilization by polarization spectroscopy of a reflecting reference cavity", *Optics Communications* **35** (3), 441 (1980).

[91] M. SCHÄFER, M. ANDRIST, H. SCHMUTZ, F. LEWEN, G. WINNEWISSER and F. MERKT: "A 240 to 380 GHz millimetre wave source for very high resolution spectroscopy of high Rydberg states", *J. Phys. B* **39** (4), 831 (2006).

[92] B. G. LINDSAY, K. A. SMITH and F. B. DUNNING: "Control of long-term output frequency drift in commercial dye lasers", *Rev. Sci. Instr.* **62** (6), 1656 (1991).

[93] S. M. JAFFE, M. ROCHON and W. M. YEN: "Increasing the frequency stability of single-frequency lasers", *Rev. Sci. Instr.* **64** (9), 2475 (1993).

[94] W. Z. ZHAO, J. E. SIMSARIAN, L. A. OROZCO and G. D. SPROUSE: "A computer-based digital feedback control of frequency drift of multiple lasers", *Rev. Sci. Instr.* **69** (11), 3737 (1998).

[95] K. Matsubara, S. Uetake, H. Ito, Y. Li, K. Hayasaka and M. Hosokawa: "Precise Frequency-Drift Measurement of Extended-Cavity Diode Laser Stabilized with Scanning Transfer Cavity", *Jap. J. Appl. Phys.* **44** (1A), 229 (2005).

[96] R. W. P. Drever, J. L. Hall, F. V. Kowalski, J. Hough, G. M. Ford, A. J. Munley and H. Ward: "Laser phase and frequency stabilization using an optical resonator", *Appl. Phys. B* **31** (2), 97 (1983).

[97] D. Haubrich and R. Wynands: "A modified commercial Ti:sapphire laser with 4 kHz rms linewidth", *Opt. Comm.* **123** (4–6), 558 (1996).

[98] B. Sanguinetti, H. O. Majeed, M. L. Jones and B. T. H. Varcoe: "Precision measurements of quantum defects in the $n\mathrm{P}_{3/2}$ Rydberg states of ^{85}Rb", *J. Phys. B* **42** (16), 165004 (2009).

[99] T. Udem, J. Reichert, R. Holzwarth and T. W. Hänsch: "Absolute Optical Frequency Measurement of the Cesium D_1 Line with a Mode-Locked Laser", *Phys. Rev. Lett.* **82** (18), 3568 (1999).

[100] S. A. Diddams, D. J. Jones, J. Ye, S. T. Cundiff, J. L. Hall, J. K. Ranka, R. S. Windeler, R. Holzwarth, T. Udem and T. W. Hänsch: "Direct Link between Microwave and Optical Frequencies with a 300 THz Femtosecond Laser Comb", *Phys. Rev. Lett.* **84**, 5102 (2000).

[101] D. J. Jones, S. A. Diddams, J. K. Ranka, A. Stentz, R. S. Windeler, J. L. Hall and S. T. Cundiff: "Carrier-Envelope Phase Control of Femtosecond Mode-Locked Lasers and Direct Optical Frequency Synthesis", *Science* **288** (5466), 635 (2000).

[102] T. Udem, R. Holzwarth and T. W. Hansch: "Optical frequency metrology", *Nature* **416** (6877), 233 (2002).

[103] P. Kubina, P. Adel, F. Adler, G. Grosche, T. W. Hänsch, R. Holzwarth, A. Leitenstorfer, B. Lipphardt and H. Schnatz: "Long term comparison of two fiber based frequency comb systems", *Opt. Expr.* **13** (3), 904 (2005).

[104] J. P. Marangos: "Electromagnetically induced transparency", *Journal of Modern Optics* **45** (3), 471 (1998).

[105] M. Fleischhauer, A. Imamoglu and J. P. Marangos: "Electromagnetically induced transparency: Optics in coherent media", *Rev. Mod. Phys.* **77**, 633 (2005).

[106] K.-J. Boller, A. Imamoğlu and S. E. Harris: "Observation of electromagnetically induced transparency", *Phys. Rev. Lett.* **66**, 2593 (1991).

[107] A. K. Mohapatra, T. R. Jackson and C. S. Adams: "Coherent Optical Detection of Highly Excited Rydberg States Using Electromagnetically Induced Transparency", *Phys. Rev. Lett.* **98**, 113003 (2007).

[108] A. Tauschinsky, R. M. T. Thijssen, S. Whitlock, H. B. van Linden van den Heuvell and R. J. C. Spreeuw: "Spatially resolved excitation of Rydberg atoms and surface effects on an atom chip", *Phys. Rev. A* **81**, 063411 (2010).

[109] D. Petrosyan, J. Otterbach and M. Fleischhauer: "Electromagnetically Induced Transparency with Rydberg Atoms", *Phys. Rev. Lett.* **107**, 213601 (2011).

[110] G. Günter, M. Robert-de Saint-Vincent, H. Schempp, C. S. Hofmann, S. Whitlock and M. Weidemüller: "Interaction Enhanced Imaging of Individual Rydberg Atoms in Dense Gases", *Phys. Rev. Lett.* **108**, 013002 (2012).

[111] M. G. Littman, M. L. Zimmerman and D. Kleppner: "Tunneling Rates for Excited States of Sodium in a Static Electric Field", *Phys. Rev. Lett.* **37**, 486 (1976).

[112] H. C. Straub, M. A. Mangan, B. G. Lindsay, K. A. Smith and R. F. Stebbings: "Absolute detection efficiency of a microchannel plate detector for kilo-electron volt energy ions", *Review of Scientific Instruments* **70** (11) (1999).

[113] T. F. Gallagher, L. M. Humphrey, W. E. Cooke, R. M. Hill and S. A. Edelstein: "Field ionization of highly excited states of sodium", *Phys. Rev. A* **16**, 1098 (1977).

[114] A. Osterwalder and F. Merkt: "Using High Rydberg States as Electric Field Sensors", *Phys. Rev. Lett.* **82** (9), 1831 (1999).

[115] M. L. Zimmerman, M. G. Littman, M. M. Kash and D. Kleppner: "Stark structure of the Rydberg states of alkali-metal atoms", *Phys. Rev. A* **20** (6), 2251 (1979).

[116] P. Goy, J. M. Raimond, G. Vitrant and S. Haroche: "Millimeter-wave spectroscopy in cesium Rydberg states. Quantum defects, fine- and hyperfine-structure measurements", *Phys. Rev. A* **26**, 2733 (1982).

[117] R. Kaiser, N. Vansteenkiste, A. Aspect, E. Arimondo and C. Cohen-Tannoudji: "Mechanical Hanle effect", *Z. Phys. D* **18**, 17 (1991).

[118] D. A. Steck: "Cesium D Line Data", (2003).

[119] T. Bergeman, G. Erez and H. J. Metcalf: "Magnetostatic trapping fields for neutral atoms", *Phys. Rev. A* **35**, 1535 (1987).

[120] T. VOGT, M. VITEAU, A. CHOTIA, J. ZHAO, D. COMPARAT and P. PILLET: "Electric-field induced dipole blockade with Rydberg atoms", *Phys. Rev. Lett.* **99**, 073002 (2007).

[121] J. DEIGLMAYR, H. HERBURGER, H. SASSMANNSHAUSEN, P. JANSEN, H. SCHMUTZ and F. MERKT: "Precision measurement of the ionization energy of Cs i", *Phys. Rev. A* **93**, 013424 (2016).

[122] K.-H. WEBER and C. J. SANSONETTI: "Accurate energies of nS , nP , nD , nF , and nG levels of neutral cesium", *Phys. Rev. A* **35**, 4650 (1987).

[123] F. MERKT and H. SCHMUTZ: "Very high resolution spectroscopy of high Rydberg states of the argon atom", *The Journal of Chemical Physics* **108** (24) (1998).

[124] E. ARIMONDO, M. INGUSCIO and P. VIOLINO: "Experimental determinations of the hyperfine structure in the alkali atoms", *Rev. Mod. Phys.* **49**, 31 (1977).

[125] V. GERGINOV, A. DEREVIANKO and C. E. TANNER: "Observation of the Nuclear Magnetic Octupole Moment of ^{133}Cs", *Phys. Rev. Lett.* **91**, 072501 (2003).

[126] F. SCHWABL: *Quantum mechanics*, Springer Berlin (2007).

[127] G. BELIN, L. HOLMGREN and S. SVANBERG: "Hyperfine Interaction, Zeeman and Stark Effects for Excited States in Cesium", *Phys. Scr.* **14** (1), 39 (1976).

[128] P. TSEKERIS, J. FARLEY and R. GUPTA: "Measurement of the hyperfine structure of the $8^2P_{\frac{1}{2}}$ state of ^{87}Rb and the $9^2P_{\frac{1}{2}}$ state of ^{133}Cs", *Phys. Rev. A* **11**, 2202 (1975).

[129] P. TSEKERIS, R. GUPTA, W. HAPPER, G. BELIN and S. SVANBERG: "Determination of hyperfine structure of highly excited S states in alkali atoms using a CW dye laser", *Phys. Lett. A* **48** (2), 101 (1974).

[130] G. BELIN and S. SVANBERG: "Laser spectroscopy investigation of the hyperfine structure of highly excited $^2P_{3/2}$ states in alkali atoms", *Phys. Lett. A* **47** (1), 5 (1974).

[131] S. RYDBERG and S. SVANBERG: "Investigation of the $n\ ^2P_{3/2}$ Level Sequence in the Cs I Spectrum by Level Crossing Spectroscopy", *Phys. Scr.* **5** (4), 209 (1972).

[132] J. FARLEY, P. TSEKERIS and R. GUPTA: "Hyperfine-structure measurements in the Rydberg S and P states of rubidium and cesium", *Phys. Rev. A* **15**, 1530 (1977).

[133] H. Bucka, H. Kopfermann and E. W. Otten: "Bestimmung der Kernquadrupolmomente der radioaktiven Isotopen $Cs^{1}35$ und $Cs^{1}37$", *Ann. Phys.* **459**, 39 (1959).

[134] H. Bucka and G. von Oppen: "Hyperfeinstruktur und Lebensdauer des $8^2P_{3/2}$-Terms im Cs I-Spektrum", *Ann. Phys.* **465**, 119 (1962).

[135] I. I. Ryabtsev and D. B. Tret'yakov: "Microwave spectroscopy of the Zeeman effect in Rydberg atoms of sodium", *Optics and Spectroscopy* **90** (2), 145 (2001).

[136] C. C. Finlay, S. Maus, C. D. Beggan, T. N. Bondar, A. Chambodut, T. A. Chernova, A. Chulliat, V. P. Golovkov, B. Hamilton, M. Hamoudi, R. Holme, G. Hulot, W. Kuang, B. Langlais, V. Lesur, F. J. Lowes, H. Lühr, S. Macmillan, M. Mandea, S. McLean, C. Manoj, M. Menvielle, I. Michaelis, N. Olsen, J. Rauberg, M. Rother, T. J. Sabaka, A. Tangborn, L. Tøffner-Clausen, E. Thébault, A. W. P. Thomson, I. Wardinski, Z. Wei and T. I. Zvereva: "International Geomagnetic Reference Field: the eleventh generation", *Geophysical Journal International* **183** (3), 1216 (2010).

[137] K. Müller-Dethlefs and E. W. Schlag: "Chemical Applications of Zero Kinetic Energy (ZEKE) Photoelectron Spectroscopy", *Angew. Chem. (int. ed. engl.)* **37** (10), 1346 (1998).

[138] F. Merkt, S. Willitsch and U. Hollenstein: "High-resolution Photoelectron Spectroscopy", in M. Quack and F. Merkt (eds.), "Handbook of High-Resolution Spectroscopy", volume 3, 1617–1654, John Wiley & Sons, Chichester (2011).

[139] J. Berkowitz: *Photoabsorption, photoionization and photoelectron spectroscopy*, Academic Press, New York (1979).

[140] C.-Y. Ng: "Vacuum Ultraviolet Spectroscopy and Chemistry by Photoionization and Photoelectron Methods", *Ann. Rev. Phys. Chem.* **53**, 101 (2002).

[141] B. Ruscic: "Photoionization mass spectroscopic studies of free radicals in gas phase: Why and how", in R. M. Mohan (ed.), "Research Advances in Physical Chemistry", volume 1, 39–75, Global, Trivandrum, India (2000).

[142] C. Blondel, W. Chaibi, C. Delsart, C. Drag, F. Goldfarb and S. Kröger: "The electron affinities of O, Si, and S revisited with the photodetachment microscope", *Eur. Phys. J. D* **33** (3), 335 (2005).

[143] G. Herzberg and Ch. Jungen: "Rydberg series and ionization potential of the H_2 molecule", *J. Mol. Spectrosc.* **41** (3), 425 (1972).

[144] C. J. SANSONETTI, K. L. ANDREW and J. VERGES: "Polarization, penetration, and exchange effects in the hydrogenlike nf and ng terms of cesium", *J. Opt. Soc. Am.* **71** (4), 423 (1981).

[145] C.-J. LORENZEN and K. NIEMAX: "Precise quantum defects of nS, nP and nD Levels in Cs I", *Z. Phys. A* **315** (2), 127 (1984).

[146] M. S. O'SULLIVAN and B. P. STOICHEFF: "Doppler-free two-photon absorption spectrum of cesium", *Can. J. Phys.* **61** (6), 940 (1983).

[147] J. M. RAIMOND, M. GROSS, C. FABRE, S. HAROCHE and H. H. STROKE: "Laser measurement of intensity ratio anomalies in principal series doublets of caesium Rydberg states: does the D1 line vanish?", *J. Phys. B* **11** (24), L765 (1978).

[148] H. SASSMANNSHAUSEN, F. MERKT and J. DEIGLMAYR: "High-resolution spectroscopy of Rydberg states in an ultracold cesium gas", *Phys. Rev. A* **87**, 032519 (2013).

[149] T. F. GALLAGHER: *Rydberg Atoms*, Cambridge University Press (2005).

[150] C. BAHRIM, U. THUMM and I. I. FABRIKANT: "^3S_e and ^1S_e scattering lengths for e- + Rb, Cs and Fr collisions", *J. Phys. B* **34** (6), L195 (2001).

[151] T. F. GALLAGHER and P. PILLET: "Dipole-Dipole Interactions of Rydberg Atoms", in E. ARIMONDO (ed.), "Adv. At. Mol. Opt. Phys.", volume 56, 161–218, Academic Press (2008).

[152] W. RITZ: "On a New Law of Series Spectra", *Astrophysical Journal* **28**, 237 (1908).

[153] P. J. MOHR, B. N. TAYLOR and D. B. NEWELL: "The 2014 CODATA Recommended Values of the Fundamental Physical Constants (Web Version 7.0). This database was developed by J. Baker, M. Douma, and S. Kotochigova. National Institute of Standards and Technology, Gaithersburg, MD 20899", (2015).

[154] CIAAW: "Atomic weights of the elements 2015", (2015).

[155] G. W. F. DRAKE and R. A. SWAINSON: "Quantum defects and the 1/ \textit{n} dependence of Rydberg energies: Second-order polarization effects", *Phys. Rev. A* **44** (9), 5448 (1991).

[156] C. SEILER, S. D. HOGAN, H. SCHMUTZ, J. A. AGNER and F. MERKT: "Collisional and Radiative Processes in Adiabatic Deceleration, Deflection, and Off-Axis Trapping of a Rydberg Atom Beam", *Phys. Rev. Lett.* **106** (7), 073003 (2011).

[157] M. Motsch, P. Jansen, J. A. Agner, H. Schmutz and F. Merkt: "Slow and velocity-tunable beams of metastable He_2 by multistage Zeeman deceleration", *Phys. Rev. A* **89** (4), 043420 (2014).

[158] D. Z. Kandula, C. Gohle, T. J. Pinkert, W. Ubachs and K. S. E. Eikema: "Extreme Ultraviolet Frequency Comb Metrology", *Phys. Rev. Lett.* **105** (6), 063001 (2010).

[159] A. Cingöz, D. C. Yost, T. K. Allison, A. Ruehl, M. E. Fermann, I. Hartl and J. Ye: "Direct frequency comb spectroscopy in the extreme ultraviolet", *Nature* **482** (7383), 68 (2012).

[160] J. Liu, E. J. Salumbides, U. Hollenstein, J. C. J. Koelemeij, K. S. E. Eikema, W. Ubachs and F. Merkt: "Determination of the ionization and dissociation energies of the hydrogen molecule", *J. Chem. Phys.* **130** (17), 174306 (2009).

[161] K. Piszczatowski, G. Łach, M. Przybytek, J. Komasa, K. Pachucki and B. Jeziorski: "Theoretical Determination of the Dissociation Energy of Molecular Hydrogen", *J. Chem. Theo. Comp.* **5** (11), 3039 (2009).

[162] K. Pachucki and J. Komasa: "Rovibrational levels of HD", *Phys. Chem. Chem. Phys.* **12** (32), 9188 (2010).

[163] K. Pachucki and J. Komasa: "Accurate adiabatic correction in the hydrogen molecule", *J. Chem. Phys.* **141** (22), 224103 (2014).

[164] D. Sprecher, C. Jungen, W. Ubachs and F. Merkt: "Towards measuring the ionisation and dissociation energies of molecular hydrogen with sub-MHz accuracy", *Faraday Discuss.* **150** (0), 51 (2011).

[165] S. D. Hogan and F. Merkt: "A New Perspective on the Binding Power of an Electron", *ChemPhysChem* **10** (17), 2931 (2009).

[166] J. Tallant, S. T. Rittenhouse, D. Booth, H. R. Sadeghpour and J. P. Shaffer: "Observation of Blueshifted Ultralong-Range Cs_2 Rydberg Molecules", *Physical Review Letters* **109** (17), 173202 (2012).

[167] H. Sassmannshausen, F. Merkt and J. Deiglmayr: "Experimental Characterization of Singlet Scattering Channels in Long-Range Rydberg Molecules", *Phys. Rev. Lett.* **114**, 133201 (2015).

[168] M. A. Bellos, R. Carollo, J. Banerjee, E. E. Eyler, P. L. Gould and W. C. Stwalley: "Excitation of Weakly Bound Molecules to Trilobitelike Rydberg States", *Phys. Rev. Lett.* **111**, 053001 (2013).

[169] T. Niederprüm, O. Thomas, T. Eichert, C. Lippe, J. Pérez-Ríos, C. Greene and H. Ott: "Observation of pendular butterfly Rydberg molecules", *arXiv:1602.08400* (2016).

[170] B. Butscher, V. Bendkowsky, J. Nipper, J. B. Balewski, L. Kukota, R. Löw, T. Pfau, W. Li, T. Pohl and J. M. Rost: "Lifetimes of ultralong-range Rydberg molecules in vibrational ground and excited states", *Journal of Physics B: Atomic, Molecular and Optical Physics* **44** (18), 184004 (2011).

[171] F. Camargo, J. D. Whalen, R. Ding, H. R. Sadeghpour, S. Yoshida, J. Burgdörfer, F. B. Dunning and T. C. Killian: "Lifetimes of ultra-long-range strontium Rydberg molecules", *Phys. Rev. A* **93**, 022702 (2016).

[172] M. D. Gregoire, I. Hromada, W. F. Holmgren, R. Trubko and A. D. Cronin: "Measurements of the ground-state polarizabilities of Cs, Rb, and K using atom interferometry", *Phys. Rev. A* **92**, 052513 (2015).

[173] A. Omont: "On the theory of collisions of atoms in rydberg states with neutral particles", *Journal de Physique* **38** (11), 1343 (1977).

[174] I. I. Fabrikant: "Interaction of Rydberg atoms and thermal electrons with K, Rb and Cs atoms", *Journal of Physics B: Atomic and Molecular Physics* **19** (10), 1527 (1986).

[175] V. Kokoouline, O. Dulieu, R. Kosloff and F. Masnou-Seeuws: "Mapped Fourier methods for long-range molecules: Application to perturbations in the Rb_2 (0_u^+) photoassociation spectrum", *The Journal of Chemical Physics* **110** (20), 9865 (1999).

[176] F. M. Penning: "Über Ionisation durch metastabile Atome", *Naturwissenschaften* **15** (40), 818 (1927).

[177] F. Mohler and C. Boeckner: "Effects of gases on photoionization of caesium by line absorption", *Bureau of Standards Journal of Research* **5**, 399 (1930).

[178] M. Scheer, J. Thøgersen, R. C. Bilodeau, C. A. Brodie, H. K. Haugen, H. H. Andersen, P. Kristensen and T. Andersen: "Experimental Evidence that the $6s6p^3P_J$ States of Cs^- Are Shape Resonances", *Phys. Rev. Lett.* **80**, 684 (1998).

[179] G. F. Gribakin and V. V. Flambaum: "Calculation of the scattering length in atomic collisions using the semiclassical approximation", *Phys. Rev. A* **48**, 546 (1993).

[180] W. Kołos and L. Wolniewicz: "Nonadiabatic Theory for Diatomic Molecules and Its Application to the Hydrogen Molecule", *Rev. Mod. Phys.* **35**, 473 (1963).

[181] T. Sharp: "Potential-energy curves for molecular hydrogen and its ions", *Atomic Data and Nuclear Data Tables* **2**, 119 (1970).

[182] P. Quadrelli, K. Dressler and L. Wolniewicz: "Nonadiabatic coupling between the EF+GK+H $^1\Sigma_g^+$, $I\,^1\Pi_g$, and $^1\Delta_g$ states of the hydrogen molecule. Calculation of rovibronic structures in H_2, HD, and D_2", *The Journal of Chemical Physics* **92** (12) (1990).

[183] S. C. Ross and C. Jungen: "Multichannel quantum-defect theory of double-minimum $^1\Sigma_g^+$ states in H_2. I. Potential-energy curves", *Phys. Rev. A* **49**, 4353 (1994).

[184] S. C. Ross and C. Jungen: "Multichannel quantum-defect theory of double-minimum $^1\Sigma_g^+$ states in H_2. II. Vibronic-energy levels", *Phys. Rev. A* **49**, 4364 (1994).

[185] R. H. Lipson and R. W. Field: "Toward a global and causal understanding of the unusual Rydberg state potential energy curves of the heteronuclear rare gas dimers", *The Journal of Chemical Physics* **110** (22) (1999).

[186] E. Kleimenov, O. Zehnder and F. Merkt: "Spectroscopic characterization of the potential energy functions of Ne_2 Rydberg states in the vicinity of the $Ne(^1S_0)$ + Ne(4p) dissociation limits", *Journal of Molecular Spectroscopy* **247** (1), 85 (2008).

[187] N. Spiess: Ph.D. thesis, Fachbereich Chemie, Universität Kaiserslautern (1989), unpublished.

[188] A. Jraij, A. Allouche, M. Korek and M. Aubert-FrÃ‰con: "Theoretical electronic structure including spin-orbit effects of the alkali dimer cation", *Chemical Physics* **310** (1-3), 145 (2005).

[189] G. Herzberg and C. Jungen: "Rydberg series and ionization potential of the H_2 molecule", *J. Mol. Spec.* **41**, 425 (1972).

[190] E. L. Hamilton, C. H. Greene and H. R. Sadeghpour: "Shape-resonance-induced long-range molecular Rydberg states", *Journal of Physics B: Atomic, Molecular and Optical Physics* **35** (10), L199 (2002).

[191] N. Samboy and R. Côté: "Rubidium Rydberg macrodimers", *J. Phys. B* **44** (18), 184006 (2011).

[192] R. J. Le Roy: "Energy levels of a diatomic near dissociation", in R. F. Barrow, D. A. Long and D. J. Millen (eds.), "Molecular Spectroscopy", volume 1, 113–176, Royal Society of Chemistry, Cambridge (1973).

[193] J. O. Hirschfelder and W. J. Meath: "The Nature of Intermolecular Forces", *Adv. Chem. Phys.* **12**, 3 (1967).

[194] A. Dalgarno: "New Methods for Calculating Long-Range Intermolecular Forces", *Adv. Chem. Phys.* **12**, 143 (1967).

[195] M. R. Flannery, D. Vrinceanu and V. N. Ostrovsky: "Long-range interaction between polar Rydberg atoms", *J. Phys. B* **38** (2), S279 (2005).

[196] A. Schwettmann, J. Crawford, K. R. Overstreet and J. P. Shaffer: "Cold Cs Rydberg-gas interactions", *Phys. Rev. A* **74** (2), 020701 (2006).

[197] C. Ates, T. Pohl, T. Pattard and J. M. Rost: "Antiblockade in Rydberg Excitation of an Ultracold Lattice Gas", *Phys. Rev. Lett.* **98**, 023002 (2007).

[198] T. Amthor, C. Giese, C. S. Hofmann and M. Weidemüller: "Evidence of Antiblockade in an Ultracold Rydberg Gas", *Phys. Rev. Lett.* **104**, 013001 (2010).

[199] B. Vermersch, A. W. Glaetzle and P. Zoller: "Magic distances in the blockade mechanism of Rydberg p and d states", *Phys. Rev. A* **91**, 023411 (2015).

[200] T. G. Walker and M. Saffman: "Zeros of Rydberg-Rydberg Föster interactions", *Journal of Physics B: Atomic, Molecular and Optical Physics* **38** (2), S309 (2005).

[201] S. Ravets, H. Labuhn, D. Barredo, T. Lahaye and A. Browaeys: "Measurement of the angular dependence of the dipole-dipole interaction between two individual Rydberg atoms at a Förster resonance", *Phys. Rev. A* **92**, 020701 (2015).

[202] P. Schausz, M. Cheneau, M. Endres, T. Fukuhara, S. Hild, A. Omran, T. Pohl, C. Gross, S. Kuhr and I. Bloch: "Observation of spatially ordered structures in a two-dimensional Rydberg gas", *Nature* **491** (7422), 87 (2012).

[203] K. M. Maller, M. T. Lichtman, T. Xia, Y. Sun, M. J. Piotrowicz, A. W. Carr, L. Isenhower and M. Saffman: "Rydberg-blockade controlled-not gate and entanglement in a two-dimensional array of neutral-atom qubits", *Phys. Rev. A* **92**, 022336 (2015).

[204] A. M. Hankin, Y.-Y. Jau, L. P. Parazzoli, C. W. Chou, D. J. Armstrong, A. J. Landahl and G. W. Biedermann: "Two-atom Rydberg blockade using direct 6S to nP excitation", *Phys. Rev. A* **89**, 033416 (2014).

[205] D. Barredo, S. Ravets, H. Labuhn, L. Béguin, A. Vernier, F. Nogrette, T. Lahaye and A. Browaeys: "Demonstration of a Strong Rydberg Blockade in Three-Atom Systems with Anisotropic Interactions", *Phys. Rev. Lett.* **112**, 183002 (2014).

[206] T. Gallagher: "Resonant collisional energy transfer between Rydberg atoms", *Physics Reports* **210** (5), 319 (1992).

[207] T. Vogt, M. Viteau, J. Zhao, A. Chotia, D. Comparat and P. Pillet: "Dipole Blockade at Förster Resonances in High Resolution Laser Excitation of Rydberg States of Cesium Atoms", *Phys. Rev. Lett.* **97**, 083003 (2006).

[208] I. I. Ryabtsev, D. B. Tretyakov, I. I. Beterov and V. M. Entin: "Observation of the Stark-Tuned Förster Resonance between Two Rydberg Atoms", *Phys. Rev. Lett.* **104**, 073003 (2010).

[209] J. M. Nipper: *Interacting Rydberg atoms: Coherent control at Förster resonances and polar homonuclear molecules*, Ph.D. thesis, Universität Stuttgart (2012).

[210] J. Nipper, J. B. Balewski, A. T. Krupp, B. Butscher, R. Löw and T. Pfau: "Highly Resolved Measurements of Stark-Tuned Förster Resonances between Rydberg Atoms", *Phys. Rev. Lett.* **108**, 113001 (2012).

[211] S. Ravets, H. Labuhn, D. Barredo, L. Béguin, T. Lahaye and A. Browaeys: "Coherent dipole–dipole coupling between two single Rydberg atoms at an electrically-tuned Förster resonance", *Nature Physics* **10** (12), 914 (2014).

[212] F. Robicheaux, J. V. Hernández, T. Topçu and L. D. Noordam: "Simulation of coherent interactions between Rydberg atoms", *Phys. Rev. A* **70**, 042703 (2004).

[213] S. Wüster, C. Ates, A. Eisfeld and J. M. Rost: "Newton's Cradle and Entanglement Transport in a Flexible Rydberg Chain", *Phys. Rev. Lett.* **105**, 053004 (2010).

[214] H. Schempp, G. Günter, S. Wüster, M. Weidemüller and S. Whitlock: "Correlated Exciton Transport in Rydberg-Dressed-Atom Spin Chains", *Phys. Rev. Lett.* **115**, 093002 (2015).

[215] D. Barredo, H. Labuhn, S. Ravets, T. Lahaye, A. Browaeys and C. S. Adams: "Coherent Excitation Transfer in a Spin Chain of Three Rydberg Atoms", *Phys. Rev. Lett.* **114**, 113002 (2015).

[216] T. Förster: "Zwischenmolekulare Energiewanderung und Fluoreszenz", *Annalen der Physik* **437** (1-2), 55 (1948).

[217] F. MERKT and M. QUACK: "Molecular Quantum Mechanics and Molecular Spectra, Molecular Symmetry, and Interaction of Matter with Radiation", in M. QUACK and F. MERKT (eds.), "Handbook of High-Resolution Spectroscopy", volume 1, 1 – 5, John Wiley & Sons, Chichester (2011).

[218] D. TONG, S. M. FAROOQI, E. G. M. VAN KEMPEN, Z. PAVLOVIC, J. STANOJEVIC, R. CÔTÉ, E. E. EYLER and P. L. GOULD: "Observation of electric quadrupole transitions to Rydberg nd states of ultracold rubidium atoms", *Phys. Rev. A* **79**, 052509 (2009).

[219] Y. YU, H. PARK and T. F. GALLAGHER: "Microwave Transitions in Pairs of Rb Rydberg Atoms", *Phys. Rev. Lett.* **111**, 173001 (2013).

[220] J. HAN and T. F. GALLAGHER: "Field ionization of the frozen Rydberg gas", *Phys. Rev. A* **77**, 015404 (2008).

[221] T. POHL, T. PATTARD and J. M. ROST: "Plasma formation from ultracold Rydberg gases", *Phys. Rev. A* **68**, 010703 (2003).

[222] W. LI, M. W. NOEL, M. P. ROBINSON, P. J. TANNER, T. F. GALLAGHER, D. COMPARAT, B. LABURTHE TOLRA, N. VANHAECKE, T. VOGT, N. ZAHZAM, P. PILLET and D. A. TATE: "Evolution dynamics of a dense frozen Rydberg gas to plasma", *Phys. Rev. A* **70**, 042713 (2004).

[223] P. J. TANNER, J. HAN, E. S. SHUMAN and T. F. GALLAGHER: "Many-Body Ionization in a Frozen Rydberg Gas", *Phys. Rev. Lett.* **100**, 043002 (2008).

[224] M. VITEAU, A. CHOTIA, D. COMPARAT, D. A. TATE, T. F. GALLAGHER and P. PILLET: "Melting a frozen Rydberg gas with an attractive potential", *Phys. Rev. A* **78**, 040704 (2008).

[225] A. REINHARD, K. C. YOUNGE, T. C. LIEBISCH, B. KNUFFMAN, P. R. BERMAN and G. RAITHEL: "Double-Resonance Spectroscopy of Interacting Rydberg-Atom Systems", *Phys. Rev. Lett.* **100**, 233201 (2008).

[226] F. ROBICHEAUX, M. M. GOFORTH and M. A. PHILLIPS: "Simulations of prompt many-body ionization in a frozen Rydberg gas", *Phys. Rev. A* **90**, 022712 (2014).

[227] T. AMTHOR, M. REETZ-LAMOUR, S. WESTERMANN, J. DENSKAT and M. WEIDEMÜLLER: "Effect of van der Waals Interactions Observed in Real Time in an Ultracold Rydberg Gas", *Phys. Rev. Lett.* **98**, 023004 (2007).

[228] T. AMTHOR, M. REETZ-LAMOUR, C. GIESE and M. WEIDEMÜLLER: "Modeling many-particle mechanical effects of an interacting Rydberg gas", *Phys. Rev. A* **76**, 054702 (2007).

[229] C. Boisseau, I. Simbotin and R. Côté: "Macrodimers: Ultralong Range Rydberg Molecules", *Phys. Rev. Lett.* **88** (13), 133004 (2002).

[230] M. Kiffner, H. Park, W. Li and T. F. Gallagher: "Dipole-dipole-coupled double-Rydberg molecules", *Phys. Rev. A* **86** (3), 031401 (2012).

[231] M. Kiffner, W. Li and D. Jaksch: "Magnetic Monopoles and Synthetic Spin-Orbit Coupling in Rydberg Macrodimers", *Phys. Rev. Lett.* **110**, 170402 (2013).

[232] I. Lesanovsky and J. P. Garrahan: "Out-of-equilibrium structures in strongly interacting Rydberg gases with dissipation", *Phys. Rev. A* **90**, 011603 (2014).

[233] A. Bambini, P. R. Berman, R. Buffa, E. J. Robinson and M. Matera: "Laser-induced collisional energy transfer", *Physics Reports* **238** (5), 245 (1994).

[234] H. Schempp, G. Günter, M. Robert-de Saint-Vincent, C. S. Hofmann, D. Breyel, A. Komnik, D. W. Schönleber, M. Gärttner, J. Evers, S. Whitlock and M. Weidemüller: "Full Counting Statistics of Laser Excited Rydberg Aggregates in a One-Dimensional Geometry", *Phys. Rev. Lett.* **112**, 013002 (2014).

[235] A. Hu, T. E. Lee and C. W. Clark: "Spatial correlations of one-dimensional driven-dissipative systems of Rydberg atoms", *Phys. Rev. A* **88**, 053627 (2013).

[236] A. Urvoy, F. Ripka, I. Lesanovsky, D. Booth, J. P. Shaffer, T. Pfau and R. Löw: "Strongly Correlated Growth of Rydberg Aggregates in a Vapor Cell", *Phys. Rev. Lett.* **114**, 203002 (2015).

[237] C. Simonelli, M. M. Valado, G. Masella, L. Asteria, E. Arimondo, D. Ciampini and O. Morsch: "Seeded excitation avalanches in off-resonantly driven Rydberg gases", *arXiv:1602.01257* (2016).

[238] G. Günter, H. Schempp, M. Robert-de Saint-Vincent, V. Gavryusev, S. Helmrich, C. S. Hofmann, S. Whitlock and M. Weidemüller: "Observing the Dynamics of Dipole-Mediated Energy Transport by Interaction-Enhanced Imaging", *Science* **342** (6161), 954 (2013).

[239] L. G. Marcassa and J. P. Shaffer: "Chapter Two - Interactions in Ultracold Rydberg Gases", in P. R. B. Ennio Arimondo and C. C. Lin (eds.), "Adv. At. Mol. Opt. Phys.", volume 63, 47–133, Academic Press (2014).

[240] L. S. Cederbaum, J. Zobeley and F. Tarantelli: "Giant Intermolecular Decay and Fragmentation of Clusters", *Phys. Rev. Lett.* **79**, 4778 (1997).

[241] R. Santra, J. Zobeley, L. S. Cederbaum and N. Moiseyev: "Interatomic Coulombic Decay in van der Waals Clusters and Impact of Nuclear Motion", *Phys. Rev. Lett.* **85**, 4490 (2000).

[242] S. Marburger, O. Kugeler, U. Hergenhahn and T. Möller: "Experimental Evidence for Interatomic Coulombic Decay in Ne Clusters", *Phys. Rev. Lett.* **90**, 203401 (2003).

[243] E. F. Aziz, N. Ottosson, M. Faubel, I. V. Hertel and B. Winter: "Interaction between liquid water and hydroxide revealed by core-hole de-excitation", *Nature* **455** (7209), 89 (2008).

[244] T. Jahnke, H. Sann, T. Havermeier, K. Kreidi, C. Stuck, M. Meckel, M. Schöffler, N. Neumann, R. Wallauer, S. Voss, A. Czasch, O. Jagutzki, A. Malakzadeh, F. Afaneh, T. Weber, H. Schmidt-Böcking and R. Dörner: "Ultrafast energy transfer between water molecules", *Nat Phys* **6** (2), 139 (2010).

[245] M. Mucke, M. Braune, S. Barth, M. Förstel, T. Lischke, V. Ulrich, T. Arion, U. Becker, A. Bradshaw and U. Hergenhahn: "A hitherto unrecognized source of low-energy electrons in water", *Nat Phys* **6** (2), 143 (2010).

[246] T. Amthor, J. Denskat, C. Giese, N. N. Bezuglov, A. Ekers, L. S. Cederbaum and M. Weidemüller: "Autoionization of an ultracold Rydberg gas through resonant dipole coupling", *The European Physical Journal D* **53** (3), 329 (2009).

[247] H. Lefebvre-Brion and R. W. Field: "Chapter 3 - Terms Neglected in the Born-Oppenheimer Approximation", in "The Spectra and Dynamics of Diatomic Molecules", 87–231, Academic Press, San Diego (2004).

[248] W. Li, I. Mourachko, M. W. Noel and T. F. Gallagher: "Millimeter-wave spectroscopy of cold Rb Rydberg atoms in a magneto-optical trap: Quantum defects of the *ns* , *np* , and *nd* series", *Phys. Rev. A* **67**, 052502 (2003).

[249] J. Han, Y. Jamil, D. V. L. Norum, P. J. Tanner and T. F. Gallagher: "Rb nf quantum defects from millimeter-wave spectroscopy of cold ^{85}Rb Rydberg atoms", *Phys. Rev. A* **74**, 054502 (2006).

[250] S. Ye, X. Zhang, T. C. Killian, F. B. Dunning, M. Hiller, S. Yoshida, S. Nagele and J. Burgdörfer: "Production of very-high-n strontium Rydberg atoms", *Phys. Rev. A* **88**, 043430 (2013).

[251] K. Pachucki and J. Komasa: "Leading order nonadiabatic corrections to rovibrational levels of H_2, D_2, and T_2", *J. Chem. Phys.* **143** (3), 034111 (2015), wOS:000358429800011.

[252] Z. Liao, M. Al-Amri, T. Becker, W. P. Schleich, M. O. Scully and M. S. Zubairy: "Atom lithography with subwavelength resolution via Rabi oscillations", *Phys. Rev. A* **87**, 023405 (2013).

[253] P. J. Mohr, B. N. Taylor and D. B. Newell: "CODATA recommended values of the fundamental physical constants: 2010", *Rev. Mod. Phys.* **84** (4), 1527 (2012).

[254] M. Marinescu, H. R. Sadeghpour and A. Dalgarno: "Dispersion coefficients for alkali-metal dimers", *Phys. Rev. A* **49** (2), 982 (1994).

[255] D. Varshalovich, A. N. Moskalev and V. K. Khersonskii: *Quantum Theory of Angular Momentum*, World Scientific Publishing, Singapore (1988).

Publications

Articles

1. N. Hansen, P. Kraus, H. Saßmannshausen, T. Timmerscheidt and W. van Gunsteren
   “An effective force field for molecular dynamics simulations of dimethyl sulfone”
   MOLECULAR PHYSICS, **109** (22), 2593 (2011).

2. S. D. Hogan, P. Allmendinger, H. Saßmannshausen, H. Schmutz, and F. Merkt
   “Surface-Electrode Rydberg-Stark Decelerator”
   PHYSICAL REVIEW LETTERS **108** (6), 063008 (2012).

3. H. Saßmannshausen, F. Merkt, and J. Deiglmayr
   “High-resolution spectroscopy of Rydberg states in an ultracold cesium gas”
   PHYSICAL REVIEW A **87** (3), 032519 (2013).

4. J. Deiglmayr, H. Saßmannshausen, P. Pillet, and F. Merkt
   “Observation of Dipole-Quadrupole Interaction in an Ultracold Gas of Rydberg Atoms”
   PHYSICAL REVIEW LETTERS **113** (19), 193001 (2014).

5. H. Saßmannshausen, F. Merkt, and J. Deiglmayr
   “Experimental Characterization of Singlet Scattering Channels in Long-Range Rydberg Molecules”
   PHYSICAL REVIEW LETTERS **114** (13), 133201 (2015).

6. H. Saßmannshausen, F. Merkt, and J. Deiglmayr
   “Pulsed excitation of Rydberg-atom-pair states in an ultracold Cs gas”
   PHYSICAL REVIEW A **92** (3), 032505 (2015).

6. J. Deiglmayr, H. Herburger, H. Saßmannshausen, P. Jansen, H. Schmutz, and F. Merkt
   “Precision measurement of the ionization energy of Cs I”
   PHYSICAL REVIEW A **93** (1), 013424 (2016).

8. H. Saßmannshausen, J. Deiglmayr, and F. Merkt
   "Exotic Chemistry with Ultracold Rydberg Atoms"
   CHIMIA **70** (4), 263 (2013).

9. H. Saßmannshausen, J. Deiglmayr, and F. Merkt
   "Long-range Rydberg molecules, Rydberg macrodimers and Rydberg aggregates in an ultracold Cs gas"
   accepted for publication in EPJ ST (2016).

10. H. Saßmannshausen and J. Deiglmayr
    "Observation of Rydberg-Atom Macrodimers: Micrometer-Sized Diatomic Molecules"
    PHYSICAL REVIEW LETTERS **117** (8), 083401 (2016).

Talks

1. "Millimetre-wave spectroscopy on high Rydberg states of ultracold cesium"
   COHERENCE School and Young Excited Atomix (YEA) Meeting on Fundamentals of Rydberg Atoms and Molecules, Pisa, Italy, September 16 – 20, 2012

2. "Spectroscopy of ultracold Rydberg atoms in the interacting and non-interacting regimes"
   International School on Ultracold Rydberg Physics, Max Planck Institute for the Physics of Complex Systems, Dresden, Germany, July 1 – 5, 2013

3. "Exotic chemistry with ultracold Rydberg atoms"
   Physical Chemistry Colloquium, ETH Zurich, Switzerland, April 14, 2015

4. "Photoassociation upon Rydberg excitation of ultracold Cs atoms"
   COHERENCE Final Conference: International Conference on Rydbergs at Durham (iCoRD), Durham, Great Britain, June 28 – July 3, 2015

5. "Molecular resonances in the Rydberg-excitation spectrum of an ultracold Cs gas"
   Workshop: Correlation and Order in Rydberg Gases, Lorentz Center in Leiden, Netherlands, May 30 – June 3, 2016

6. "Rydberg-atom macrodimers and aggregates"
   Quantum Science and Technology Lunch Seminar, ETH Zurich, September 1, 2016

Poster presentations

1. “Decelerating and trapping Rydberg atoms close to surfaces”
   2nd NCCR QSIT General Meeting, Arosa, Switzerland, February 1, 2012.

2. “High-resolution spectroscopy of ultracold cesium atoms”
   ITN COHERENCE Lecture Series of Chris Greene on Atomic, Molecular and Optical Physics, Heidelberg, Germany, June 25, 2012.

3. “High-resolution spectroscopy of ultracold cesium atoms”
   ITN COHERENCE Workshop: Coherence and Decoherence in Rydberg Systems, Gif-sur-Yvette, France, July 19 – 20, 2012.

4. “High-resolution spectroscopy of ultracold Rydberg atoms”
   Fall Meeting of the Swiss Chemical Society (SCS), ETH Zurich, Switzerland, September 13, 2012

5. “High-resolution spectroscopy of ultracold Rydberg atoms”
   ITN COHERENCE School and Young Excited Atomix (YEA) Meeting on Fundamentals of Rydberg Atoms and Molecules, Pisa, Italy, September 16 – 20, 2012

6. “High-resolution spectroscopy of ultracold cesium atoms”
   3rd NCCR QSIT General Meeting, Arosa, Switzerland, January 30 – February 1, 2013

7. “High-resolution spectroscopy of ultracold cesium atoms”
   RQI - Winter School on Rydberg Physics and Quantum Information, Obergurgl, Austria, February 10 – 15, 2013

8. “High-resolution spectroscopy of Rydberg states in an ultracold cesium gas”
   International Workshop on Ultracold Rydberg Physics, Max Planck Institute for the Physics of Complex Systems, Dresden, Germany, July 8 – 12, 2013

9. “Spectroscopy of ultracold Rydberg atoms in the interacting and non-interacting regimes”
   Fall Meeting of the Swiss Chemical Society (SCS), EPFL Lausanne, Switzerland, September 6, 2013

10. “Ultracold Rydberg atoms: From high-resolution spectroscopy to the study of many-body interactions”
    Leopoldina-Symposium “Spectroscopy and Molecular Dynamics at the Limit”, ETH Zurich, Switzerland, September 11 – 13, 2013

11. “Probing Rydberg physics by high-resolution spectroscopy”
    Winter Graduate School on Atomic, Molecular and Optical Physics: Ultracold Rydberg Physics, Biosphere 2, Tucson, USA, January 7 – 12, 2014

12. “Probing Rydberg physics by high-resolution spectroscopy”
    4th NCCR QSIT General Meeting, Arosa, Switzerland, February 5 – 7, 2014

13. “Observation of dipole-dipole and dipole-quadrupole interactions between pairs of ultracold cesium Rydberg atoms”
    ITN COHERENCE Workshop on Ultracold Rydberg Physics, Granada, Spain, September 10 – 12, 2014

14. “Rydberg atoms and molecules in the gas phase - from precision spectroscopy to many-body interactions”
    4th NCCR QSIT Site Visit, ETH Zurich, Switzerland, November 6 – 7, 2014

15. “Rydberg atoms and exotic quantum states”
    5th NCCR QSIT General Meeting, Arosa, Switzerland, January 7 – 9, 2015

16. “Observation of singlet-scattering channels in long-range Rydberg dimers”
    XXIXth International Conference on Photonic, Electronic and Atomic Collisions (ICPEAC), Toledo, Spain, July 22 – 28, 2015

17. “Photoassociation of cesium atoms upon Rydberg excitation in a dense ultracold gas”
    Fall Meeting of the Swiss Chemical Society (SCS), EPFL Lausanne, Switzerland, September 4, 2015

18. “Long-range interactions in an ultracold Rydberg gas”
    6th NCCR QSIT General Meeting, Arosa, Switzerland, February 3 – 5, 2016

19. “Photoassociation of cesium atoms upon Rydberg excitation in a dense ultracold gas”
    Fall Meeting of the Swiss Chemical Society (SCS), University of Zurich, Switzerland, September 15, 2016

Danksagung

Auch wenn nur mein Name auf dem Umschlag steht, so ist dieses Werk doch ein Produkt der Zusammenarbeit mit vielen talentierten und lieben Menschen. An dieser Stelle bedanke ich mich daher ganz herzlich bei allen, die mich in den vergangenen fünf Jahren unterstützt und zum Gelingen dieser Arbeit beigetragen haben:

Prof. Dr. Frédéric Merkt für weit mehr als nur die Möglichkeit meine Dissertation in deiner Arbeitsgruppe durchführen zu können. Was ist dieses «weit mehr»? Zum einen sind das deine unermüdliche Begeisterung für die exakte Wissenschaft, die sich immer wieder auch auf mich übertragen hat, deine beispielhafte Genauigkeit bei der Betreuung meiner wissenschaftlichen Arbeit und beim gemeinsamen Verfassen jeglicher Publikationen und für die Freiheit, die du mir bei der Wahl der Experimente immer gewährt hast. Zum anderen sind das die vielen Dinge abseits des wissenschaftlichen Arbeitsalltags, welche die Zeit in deiner Gruppe zu einer wundervollen gemacht haben: die jährlichen Skiausflüge nach St. Luc, Herbstwanderungen, Weihnachtsfeiern bei dir zu Hause und die gemeinschaftlichen Laborputztage mit abschliessendem Fondue.

Bessere Rahmenbedingungen für ein Doktorat als in deiner Gruppe kann man sich nicht vorstellen.

Prof. Dr. Tilman Esslinger danke ich herzlich für die Übernahme des Koreferates.

Dr. Johannes Deiglmayr für die vielen Dinge, die ich im Labor, vor dem Computer und beim Kaffee trinken von dir gelernt habe und für die Übernahme des zweiten Koreferats. Ohne deine hervorragende wissenschaftliche Betreuung, deine legendären Fähigkeiten im Labor, dein vollständiges Wissen über Atomphysik und deine Mathematica- und LabView-Kunst wäre es zu dieser Dissertation nicht gekommen. Die Arbeit mit dir war ein großes Vergnügen.

Prof. Dr. Pierre Pillet for your interest in our experiments, many valuable suggestions and for the discussions we had during your stay at ETH Zurich in spring 2014, which

were so important for the interpretation of the Rydberg-atom-pair resonances.

Josef «Seppi Agners» Agner für deine stets verständlichen und sinnvollen Kommentare (auch zu späterer Stunde). Dass du die Experimente oftmals besser als die Doktoranden verstehst, sagt bereits viel über dein Talent aus, und deine Beiträge als Mechaniker waren herausragend. An deine Rufe «lunch!» und «b. o'c.!» werde ich mich erinnern.

Hansjürg Schmutz für unersätzbare Entwicklungen jeglicher vom Experiment geforderten elektronischen Schaltungen und Baugruppen. Die von dir organisierte Wanderung zum Atomkraftwerk war auch ein Highlight (nach anfänglichem Nebel wurde das Wetter immer strahlender).

Dr. Urs Hollenstein für deine konzeptuell bereits fest mit deinem Namen verbundene ständige Hilfsbereitschaft (am Ringlaser, beim Erstellen neuer Übungsaufgaben, bei sämtlichen Formatierungsproblemen, und so weiter und so weiter...), die lustigen Fondue-Abende bei dir zu Hause und die Organisation einer schönen Wanderung mit einem grandiosen Finale in Gommiswald.

Iréne Müller, Iréne Urbanek, Sandra Jörimann und Christa Leumann für das Übernehmen aller administrativer Tätigkeiten.

Allen Kollegen und Freunden aus der Merkt-Gruppe:
Dr. Christa Haase für die schöne gemeinsame Zeit zu Beginn meines Doktorats in E209 und auch bei Velotouren. Ich hoffe wir werden irgendwann nochmal Lebowski's Lieblingsgetränk trinken, den gleichnamigen Film schauen und übers Leben reden.
Dr. Michael Motsch ebenfalls für die gute Zeit in E209 und bei Velotouren und dein umfangreiches Wissen, das du gerne geteilt hast.
Maximilian Beyer einfach nur für deine menschlich nette Art, die interessanten wissenschaftlichen Diskussionen und W.-G.A.-Abende.
Ugo «Soft hands» Jacovella for elephants (maybe less), baseball, table football, an amazing trip to Paris and some «truc» freely adapted from Captain Cousteau.
Luca Semeria (for your skiis that were part of the best vacation ever) and Dr. Ondřej Tkáč for the excellent atmosphere in the office in the last years.
Pitt Allmendinger für die tolle gemeinsame Zeit auf Konferenzen (inklusive Sonnenaufgängen und Frühstück), Kartenrunden bei dir und die Ausflüge innerhalb Zürichs.
Dr. Paul «Paolopedia» Jansen für interessante Touren mit dem Schiff und über Land, sowie die guten Gespräche in Kaffeepausen und beim «b. o'c.».
Matija Žeško for directing my attention towards Croatia (it is a great country!) and for an excellent organisation in the desert (saving tens of thirsty people).

Katharina Höveler für die Motivation zum Training.
Auch allen Ehemaligen für die herzliche Aufnahme in der Gruppe: Dr. Katrin Dulitz, Dr. Alex Wiederkehr, Dr. Konstantina Vasilatou, Dr. Christian Seiler, Prof. Dr. Stephen Hogan (particularly also for the skiing boots!), Dr. Daniel Sprecher, Dr. Monika Grütter, Dr. Lorena Piticco, Dr. Sandro Mollet, Dr. Bérenger Gans, Prof. Dr. Clément Lauzin, Dr. Martin Schäfer. Michael Peper als meinem Nachfolger wünsche ich alles Gute!

The organisers and members of the finished COHERENCE network. It was a huge success and I consider myself very fortunate that I had the possiblity to be a part of it. I learned a lot and I had a fantastic time at every single event.

Meinen lieben Eltern, meiner Schwester und meinem Bruder und meinen Großeltern danke ich sehr herzlich für ihre immerwährende Unterstützung, in jeder Lage, zu jeder Zeit! Manchmal war es besonders wichtig, denn von jenem Tag der Entscheidung unterm Kirschbaum führt eine gerade Linie bis hierher. Danke für Euer Vertrauen!